

## INFORMATION TO USERS

This manuscript has been reproduced from the microfilm master. UMI films the text directly from the original or copy submitted. Thus, some thesis and dissertation copies are in typewriter face, while others may be from any type of computer printer.

The quality of this reproduction is dependent upon the quality of the copy submitted. Broken or indistinct print, colored or poor quality illustrations and photographs, print bleedthrough, substandard margins, and improper alignment can adversely affect reproduction.

In the unlikely event that the author did not send UMI a complete manuscript and there are missing pages, these will be noted. Also, if unauthorized copyright material had to be removed, a note will indicate the deletion.

Oversize materials (e.g., maps, drawings, charts) are reproduced by sectioning the original, beginning at the upper left-hand corner and continuing from left to right in equal sections with small overlaps. Each original is also photographed in one exposure and is included in reduced form at the back of the book.

Photographs included in the original manuscript have been reproduced xerographically in this copy. Higher quality 6" x 9" black and white photographic prints are available for any photographs or illustrations appearing in this copy for an additional charge. Contact UMI directly to order.

# U·M·I

University Microfilms International  
A Bell & Howell Information Company  
300 North Zeeb Road, Ann Arbor, MI 48106-1346 USA  
313/761-4700 800/521-0600



**Order Number 9325447**

**A computer-aided engineering system for process design in sheet  
metal forming**

**Ahmetoglu, Mustafa Ali, Ph.D.**

**The Ohio State University, 1993**

**U·M·I**  
300 N. Zeeb Rd.  
Ann Arbor, MI 48106





**A COMPUTER-AIDED ENGINEERING SYSTEM FOR  
PROCESS DESIGN IN SHEET METAL FORMING**

A Dissertation

Presented in Partial Fulfillment of the Requirements for  
the Degree Doctor of Philosophy in the Graduate  
School of the Ohio State University

by

Mustafa Ali Ahmetoglu, BSc. ME., M. S.

\* \* \* \* \*

The Ohio State University  
1993

Dissertation Committee

Dr. Taylan Altan

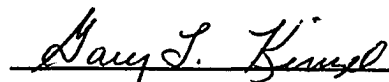
Dr. Gary L. Kinzel

Dr. Rajiv Shivpuri

Approved by



Taylan Altan, Co-Advisor  
Department of Industrial and System Engineering



Gary L. Kinzel, Co-Advisor

To my wife, Eser Tufekci,  
for her understanding and support

## ACKNOWLEDGMENT

I express my deep gratitude and sincere appreciation to my advisors Prof. Taylan Altan, and Prof. Gary L. Kinzel for their guidance and encouragement throughout this research. Their enthusiasm and constructive criticism have served as the inspiration for improvement. Their kindness in academic as well as personal matters has made my stay in Columbus most pleasant.

My gratitude is extended to Prof. Rajiv Shivpuri and Prof. Glenn Daehn for their careful review of this manuscript and for providing me with helpful suggestions, and to Professor R. Allen Miller for many stimulating discussions.

Thanks are also due to my wife, Eser Tufekci, for being the light in my life, and to my parents, Emine and Haydar Ahmetoglu, and my sisters, Nilgün and Elif, for their love, encouragement, and continuous support. I love them.

At last, but not the least, I would like to thank all the people who, during the last 30 years, taught me something and helped my personal and academic growth. Without them, I would not be here writing these sentences.

## VITA

- January 20, 1963 . . . . Born - Istanbul, Türkiye
- 1984 . . . . . BSc., Mechanical Engineering, Istanbul  
Technical University, Istanbul, Türkiye
- 1986 . . . . . MS., Mechanical Engineering, University of  
Michigan, Michigan
- 1987 . . . . . MS., Industrial and Operations Engineering,  
University of Michigan, Michigan

## FIELDS OF STUDY

Major Field: Industrial and System Engineering  
Sheet Metal Forming, Taylan Altan, Rajiv Shivpuri  
Mechanical Design and Stress Analysis, Gary Kinzel  
Knowledge-Base Systems, R. Allen Miller

## TABLE OF CONTENTS

DEDICATION .....	ii
ACKNOWLEDGMENTS.....	iii
VITA.....	iv
LIST OF TABLES.....	ix
LIST OF FIGURES.....	xii

<u>Chapter</u>	<u>Page</u>
I INTRODUCTION .....	1
II LITERATURE REVIEW AND RESEARCH OBJECTIVES.....	6
2.1 Computer Aided Engineering Systems in Sheet Metal Forming.....	6
2.2 Process Sequence Design.....	13
2.3 Analysis of Sheet Metal Forming Processes .....	15
2.4 Objectives and Scope of the Current Research.....	21
III TECHNICAL BACKGROUND ON SHEET METAL FORMING PROCESSES.....	26
3.1 Geometries of Deeply Recessed Parts .....	26
3.2 Sheet Forming Operations .....	29
3.2.1 Bending.....	29
3.2.2 Stretch Forming.....	33
3.2.3 Deep Drawing.....	35

3.3	Multi-Stage Forming Operations.....	36
3.3.1	Direct Redrawing.....	36
3.3.2	Reverse Redrawing.....	38
3.4	Process Variables in Stamping.....	40
3.5	Failure Limits.....	50
IV	BLANK HOLDER DESIGN AND FORCE CONTROL TO IMPROVE THE PART QUALITY.....	54
4.1	Deep Drawing with Blank Holder .....	54
4.2	Effects of Blank Holder Force (BHF) and Pressure (BHP) .....	59
4.2.1	Rigid Blank Holders.....	61
4.2.2	Flexible Blank Holders .....	67
4.2.3	Estimation of Blank Holder Pressure.....	69
4.3	Control of Blank Holder Force (BHF) .....	71
4.3.1	Use of Fracture Limit for BHF Control.....	72
4.3.2	Use of Punch Force for BHF Control.....	73
V	SIMULATION OF AXISYMMETRIC AND PLANE-STRAIN SHEET METAL FORMING PROCESSES.....	77
5.1	Theory of Plasticity.....	78
5.2	Equilibrium Equations Based on General Tool Profiles .....	80
5.3	Rigid Plasticity.....	87
5.4	Material Behavior .....	87
5.5	Friction.....	88
5.6	Contact Boundary.....	88
5.7	Bending Correction.....	89
5.8	Drawbead and Blank Holder Force Models .....	91
5.9	Prediction of Stresses, Strains, and Punch Force .....	93
5.10	Numerical Examples .....	95
5.10.1	Analysis of Axisymmetric Deep Drawing Operations.....	96
5.10.2	Analysis of Plane-Strain Deep Drawing Operations.....	103

VI	DEEP DRAWING AND REVERSE REDRAWING OF ROUND CUPS IN MULTI-ACTION ERC/NSM PRESS.....	112
6.1	Multi-Action ERC/NSM Press.....	114
6.2	Material Properties.....	120
6.3	Deep Drawing.....	122
6.4	Reverse Redrawing.....	131
6.5	Failure Evaluation.....	138
6.5.1	Failure Criteria.....	141
6.5.2	Verification of the Failure Criteria with Experiments.....	147
VII	DEEP DRAWING OF ROUND CUPS IN 160 TON DOUBLE ACTION HYDRAULIC MINSTER PRESS.....	166
7.1	Specifications of The Minster Press.....	166
7.2	Material Properties and Process Conditions.....	170
7.2.1	Materials.....	170
7.2.2	Strain Measurements.....	172
7.2.3	Lubrication.....	173
7.3	Deep Drawing of Round Cups.....	175
7.4	Effect of BHF on The Failure of Sheet Metal Products.....	214
7.4.1	Fracture.....	214
7.4.2	Wrinkling.....	232
7.5	Optimum BHF to Improve The Drawability.....	243
7.5.1	Punch Force Control Method.....	244
7.5.2	Radial Stress Control Method.....	251
7.5.3	Thickness Strain Control Method.....	254
7.5.4	Experiments and Comparison with Simulation Results.....	257
VIII	SUMMARY AND CONCLUSIONS.....	271
8.1	Analysis of Deep Drawing and Redrawing.....	271
8.2	Failure Evaluation.....	272
8.3	BHF Control in Sheet Metal Forming.....	272

8.4	Deep Drawing experiments.....	273
8.5	Future Work.....	273
8.6	Summary of Research Contributions.....	275
LIST OF REFERENCES.....		278
APPENDICES		
A.	PLASTICITY EQUATIONS BASED ON HILL'S OLD THEORY.....	289
B.	EQUILIBRIUM EQUATIONS FOR GENERAL PUNCH PROFILE.....	294
C.	DESCRIPTION OF THE ANALYSIS MODULE.....	300
D.	EQUILIBRIUM AND VOLUME CONSTANCY EQUATIONS FOR PLANE-STRAIN GEOMETRIES.....	306
E.	ANALYSIS OF REDRAWING.....	311
F.	TOOL DESIGN FOR MULTI-STEP DEEP DRAWING EXPERIMENTS IN ERC/NSM PRESS.....	315
G.	TOOL DESIGN FOR DEEP DRAWING EXPERIMENTS IN MINSTER PRESS.....	355



## LIST OF TABLES

<u>Table</u>	<u>Page</u>
3.1 List of sheet metal forming process variables .....	45
5.1 Material properties and process conditions for deep drawing of Deep Drawing Quality Steel .....	96
5.2 Material properties and process conditions for deep drawing of AA1100-O .....	100
5.3 Material properties and process conditions for plane-strain punch stretching simulation .....	103
5.4 Material properties and process conditions for deep drawing by flat bottom square punch .....	108
6.1 Aluminum alloys which were used in the experiments .....	112
6.2 Specifications of ERC/NSM press .....	112
6.3 R values for AA 1100-O .....	120
6.4 K and n values for aluminum alloys .....	121
6.5 Yield and ultimate tensile strengths for aluminum alloys .....	122
6.6 Material properties and process conditions for deep drawing of AA1100-O .....	123
6.7 Material properties and process conditions for deep drawing of AA3104-H19 .....	126
6.8 Material properties and process conditions for deep drawing and reverse redrawing of AA3104-H19 .....	134
6.9 Material properties and process conditions for deep drawing and reverse redrawing of AA1100-O .....	136
6.10 Critical buckling stresses for aluminum alloys .....	146
6.11 Material properties, process conditions, and definition of failure criteria for deep drawing and reverse redrawing of AA3104-H19 .....	148

6.12	Material properties, process conditions, and definition of failure criteria for deep drawing and reverse redrawing of AA3104-H19 .....	152
6.13	Material properties, process conditions, and definition of failure criteria for deep drawing and reverse redrawing of AA1100-O.....	157
6.14	Material properties, process conditions, and definition of failure criteria for deep drawing and reverse redrawing of AA1100-O.....	161
6.15	Material properties, process conditions, and definition of failure criteria for deep drawing and reverse redrawing of AA3104-H19 .....	162
7.1	Specifications of the 1-DPA-160-10 Minster/Tranemo hydraulic press.....	167
7.2	Materials which are used in the experiments.....	171
7.3	Material properties.....	171
7.4	Friction coefficients used in the simulations.....	175
7.5	Summary of material properties, and process conditions for deep drawing of AA 1100-O .....	178
7.6	Summary of material properties, and process conditions for deep drawing of AA 2024-O .....	184
7.7	Summary of material properties, and process conditions for deep drawing of HSG steel .....	190
7.8	Summary of material properties, and process conditions for deep drawing of UV steel .....	208
7.9	Summary of material properties, and process conditions for deep drawing of IF steel .....	209
7.10	Material properties.....	211
7.11	Parameters to approximate Forming Limit Diagrams .....	216
7.12	Summary of material properties, FLD parameters, and process conditions for deep drawing of HSG steel.....	217
7.13	Predicted, and measured cup heights at fracture for HSG steel.....	219
7.14	Summary of material properties, FLD parameters, and process conditions for deep drawing of UV steel.....	223
7.15	Predicted, and measured cup heights at fracture for UV steel.....	223
7.16	Summary of material properties, FLD parameters, and process conditions for deep drawing of IF steel.....	226

7.17	Predicted, and measured cup heights at fracture for IF steel.....	226
7.18	Material properties, FLD parameters, and sheet thicknesses for HSG, IF, and UV steel.....	228
7.19	Summary of material properties, and process conditions for deep drawing of AA 1100-O .....	232
7.20	Summary of material properties, and process conditions for deep drawing of HSG steel .....	247
7.21	Results of constant BHF experiments.....	259
F.1	$R_p/t$ ratios used in the experiments.....	320
F.2	Recommended draw ratios .....	323
F.3	Design Parameters used in Multi-Stage Tool Design for Aluminum Alloys .....	325
F.4	Maximum punch forces required in the first stage (deep drawing).....	329
F.5	Maximum punch forces required in the second stage (reverse redrawing).....	330
F.6	Specifications of electro servomotors .....	345
F.7	CircuitPac hydraulic power unit .....	349
G.1	Recommendations for punch and die profile radii.....	358
G.2	Design parameters used in the deep drawing tool design.....	361
G.3	Specifications of LM Pressure Transducer .....	374
G.4	Specifications of string potentiometer.....	376

## LIST OF FIGURES

<u>Table</u>	<u>Page</u>
2.1 Conventional die design method.....	7
2.2 A CAE system concept for sheet metal forming.....	10
2.3 General scheme of integrated CAD/CAM system for deep drawing.....	11
2.4 Process sequence to draw a round cup.....	14
2.5 CAE system architecture.....	23
2.6 Interactions between different modules of the CAE system.....	24
3.1 Shape classification of sheet metal parts .....	27
3.2 Sheet metal forming processes.....	30
3.3 Forces applied during bending.....	32
3.4 Stresses during bending.....	32
3.5 Deformation during stretch forming.....	34
3.6 Direct redrawing of round cups.....	37
3.7 Reverse redrawing in a double action press.....	39
3.8 Stretch-draw sheet forming operations.....	41
3.9 Stamping in a single action press.....	43
3.10 Deep drawing of large non-symmetric parts .....	47
3.11 Maximum possible draw ratio versus part size.....	47
3.12 The sketch of wrinkling and formability limits and the "drawability window" in deep drawing.....	51
3.13 The effect of steel strength on wrinkling and fracture limits.....	51
3.14 The effect of blank size and die profile radius on wrinkling and fracture limits.....	53
3.13 Forming limits for gasoline tank made by deep drawing process .....	53
4.1 Deep drawing using a cylindrical punch.....	55

4.2	Different regions in deep drawing operation.....	56
4.3	Failure types in deep drawing of round cups.....	57
4.4	Use of drawbeads; a) conventional, b) locking, c) combined.....	60
4.5	Layout of drawbeads for a car door tooling.....	60
4.6	Failure modes in panel forming.....	62
4.7	Typical sheet thickness distribution in deep drawing of round cups.....	62
4.8	Material thickness variation in two different sections in drawing a non-axisymmetric part.....	64
4.9	Increase in sheet thickness in deep drawing rectangular parts with different blank shape .....	66
4.10	Flexible blankholder for deep drawing rectangular parts.....	68
4.11	Illustration of "fracture limit" variable blankholding force method.....	74
4.12	Conical cup geometry and the orientation of tangential force.....	74
4.13	Tangential force distribution for deep drawing a conical cup using different blankholding force .....	76
4.14	Variation of binder force as a result of closed loop control.....	76
5.1	General axisymmetric tool profile.....	81
5.2	General plane-strain tool profile.....	83
5.3	General geometry and different zones in a deep drawing operation .....	84
5.4	Different zones in a direct redrawing operation.....	85
5.5	Different zones in a reverse redrawing operation .....	86
5.6	Clearance between punch and die.....	90
5.7	Restraining force due to either blankholder or drawbead.....	92
5.8	Blankholder force variations that can be used in SHEET_FORM.....	94
5.9	Tool geometry for deep drawing of DDQS.....	97
5.10	Strain distributions for deep drawing of DDQS.....	99
5.11	Tool geometry for deep drawing of AA1100-O .....	100
5.12	Punch force and strain distributions in deep drawing of AA1100-O using a blankholding force of 6.8 kN .....	101

5.13	Punch force and strain distributions in deep drawing of AA1100-O using a blankholding force of 12.4 kN .....	102
5.14	Plane-strain stretch forming using cylindrical punch.....	104
5.15	Deformed sheet geometry at punch travels of 7 mm, 15 mm, and 35 mm .....	106
5.16	Stretch forming of sheet metal using cylindrical punch.....	106
5.17	Plane-strain deep drawing using cylindrical punch.....	107
5.18	Deep drawing using flat bottom square punch.....	109
5.19	Deep drawing using flat bottom square punch.....	110
6.1	Deformed cups from the multi-stage forming experiments.....	113
6.2	ERC/NSM multi-action servo press with deep draw tooling.....	116
6.3	Geometry of the tooling used in the 1st stage (deep drawing) operation .....	118
6.4	Geometry of the tooling used in the 2nd stage (reverse redrawing) operation .....	119
6.5	Geometry of the cup at two different punch travels (0.575" and 0.94") during the first stage, deep drawing, operation.....	124
6.6	Punch force in the deep drawing of AA1100-O.....	124
6.7	Radial strain distribution for deep drawing of AA1100-O at the punch travel of 0.575".....	125
6.8	Radial strain distribution for deep drawing of AA1100-O at the punch travel of 0.94".....	125
6.9	Radial strain distribution for deep drawing of AA3104-H19 at the punch travel of 0.875".....	128
6.10	Circumferential strain distribution for deep drawing of AA3104-H19 at the punch travel of 0.94".....	128
6.11	Draw-in during a deep drawing process.....	129
6.12	Comparison of the predicted outer flange radia, $r_f$ , to experimentally measured radia at punch travels of 0.3", 0.7", 1.0" .....	130
6.13	Comparison of experimentally measured maximum punch forces with predicted maximum punch forces for AA3104-H19 .....	130

6.14	Measured upper and lower punch forces during the first stage (deep drawing) and second stage (reverse redrawing) forming operations.....	132
6.15	Radial strain distribution for reverse redrawing of AA3104-H19 at the punch travel of 1.5".....	135
6.16	Circumferential strain distribution for reverse redrawing of AA3104-H19 at the punch travel of 1.5".....	135
6.17	Deformed cup geometries at two different punch travels during the reverse redrawing operation.....	137
6.18	Punch force distribution for reverse redrawing of AA1100-O.....	137
6.19	Radial strain distribution for reverse redrawing of AA1100-O at the punch travel of 1.5".....	139
6.20	Circumferential strain distribution for reverse redrawing of AA1100-O at the punch travel of 1.5".....	139
6.21	Fracture and wrinkling in deep drawing of aluminum alloys.....	140
6.22	Wrinkling in reverse redrawing of AA3104-H19.....	142
6.23	Initial (guess) forming limit diagram for AA1100-O.....	144
6.24	Effect of BHF on wrinkling in deep drawing AA3104-H19.....	150
6.25	Fracture and wrinkling limits for deep drawing of AA3104-H19 under dry friction conditions.....	151
6.26	Effect of BHF on wrinkling in deep drawing AA3104-H19.....	154
6.27	Deep drawing of AA3104-H19 to the height of 0.42" and 0.75" using BHF of 2.0 kip.....	155
6.28	Wrinkling limit for deep drawing of AA3104-H19 using water dilutable oil based lubricant.....	156
6.29	Wrinkling and fracture limits for deep drawing of 0.020" thick AA1100-O using machine oil.....	158
6.30	Wrinkling and fracture limits for deep drawing of 0.032" thick AA1100-O using machine oil.....	160
6.31	Effect of draw ratio on fracture limit.....	163
6.32	Wrinkling and fracture limits for draw ratio of 2.2.....	165
7.1	The 1-DPA-160-10 Minster/Tranemo hydraulic press, and overall dimensions.....	168

7.2	A sample round blank with circle grids etched on its surface for strain measurements.....	174
7.3	Tool geometry for deep drawing of round cups in Minster press .....	176
7.4	A sample cup formed in the experiments .....	177
7.5	Comparison of FDM predictions with the measurements in deep drawing of AA1100-O .....	180
7.6	Comparison of FDM predictions with the measurements in deep drawing of AA1100-O .....	182
7.7	Comparison of FDM predictions with the measurements in deep drawing of AA1100-O .....	183
7.8	Comparison of FDM predictions with the measurements in deep drawing of AA2024-O .....	186
7.9	Comparison of FDM predictions with the measurements in deep drawing of AA2024-O .....	187
7.10	Comparison of measured punch force distributions for different thicknesses used in deep drawing of AA2024-O .....	189
7.11	Comparison of radial and strain distributions for different thicknesses used in deep drawing of AA2024-O .....	189
7.12	Comparison of FDM predictions with the measurements in deep drawing of HSG steel .....	191
7.13	Comparison of FDM predictions with the measurements in deep drawing of HSG steel .....	192
7.14	Comparison of radial strain distributions obtained using different initial blank diameters in deep drawing of HSG steel.....	194
7.15	Comparison of punch force versus stroke diagrams for different initial blank diameters in deep drawing of HSG steel.....	195
7.16	Comparison of punch force versus stroke diagrams for different initial blank diameters in deep drawing of HSG steel.....	197
7.17	Comparison of radial strain distributions for different initial blank diameters in deep drawing of HSG steel.....	197
7.18	BHF variations used in the evaluation of SHEET_FORM .....	198
7.19	Comparison of FDM predictions with measurements in deep drawing of HSG steel .....	200



7.20	Comparison of FDM predictions with measurements in deep drawing of HSG steel .....	201
7.21	Comparison of punch force versus stroke diagram for different BHF variations in deep drawing of HSG steel .....	202
7.22	Comparison of the resulting strain distributions using constant BHF=85.0 kN and the BHF variations shown in Figure 7.18.....	204
7.23	Comparison of FDM predictions with measurements in deep drawing of UV steel .....	206
7.24	The effect of different draw ratios on the punch force versus stroke diagram in deep drawing of UV steel.....	207
7.25	Comparison of FDM predictions with measurements in deep drawing of UV steel .....	210
7.26	The effect of material parameters on the punch force versus stroke diagram.....	213
7.27	The effect of material parameters on the radial strain distribution.....	213
7.28	Fracture in deep drawn cups from HSG steel.....	218
7.29	The respective domains of wrinkling and tearing in deep drawing of round cups.....	220
7.30	Forming limit diagrams for deep drawing HSG steel blank.....	222
7.31	Forming limit diagrams for deep drawing UV steel blank.....	224
7.32	Forming limit diagrams for deep drawing IF steel blank.....	227
7.33	Comparison of failure heights for different draw ratios for different materials.....	229
7.34	Wrinkling in deep drawing AA1100-O. Blank diameter is 279.4 mm, BHF is 6.4 kN.....	233
7.35	Wrinkling in deep drawing AA1100-O. Blank diameter is 254.0 mm, BHF is 6.4 kN and 113.7 kN.....	235
7.36	Schematic diagram of deep drawing conical shapes, and the corresponding stress distribution.....	238
7.37	BHF variations used in the experiments to study the wrinkling.....	240
7.38	Wrinkling due to variations in BHF .....	241
7.39	Forces acting on the sheet metal during a deep drawing operation.....	245
7.40	BHF variation predicted based on punch force control method.....	249

7.41	Punch force profile using constant 200kN, and variable BHF based on punch force control method together with the optimum punch force distribution calculated from the Equation 7.5.....	249
7.42	Punch force distributions using constant 400 kN, and variable BHF based on punch force control method together with the optimum punch force distribution calculated from Equation 7.5.....	250
7.43	Punch force distributions using the BHF variations shown in Figure 7.40 together with the optimum punch force distribution calculated from the Equation 7.5.....	250
7.44	BHF variations predicted based on radial stress control method .....	252
7.45	Maximum radial stress vs. punch travel using constant 200 kN, and variable BHF based on radial stress control method together with the critical radial stress calculated from the Equation 7.4 .....	252
7.46	Maximum radial stress vs. punch travel using constant 400 kN, and variable BHF based on radial stress control method together with the critical radial stress calculated from the Equation 7.4 .....	253
7.47	Maximum radial stress distributions using the BHF variations shown in Figure 7.44 together with the critical radial stress calculated from the Equation 7.4.....	253
7.48	BHF variations predicted based on maximum thickness strain control method .....	255
7.49	Maximum thickness strain vs. punch travel using constant 200 kN, and variable BHF based on thickness strain control method together with the maximum desirable thickness strain.....	255
7.50	Maximum thickness strain vs. punch travel using constant 400 kN, and variable BHF based on thickness strain control method together with the maximum desirable thickness strain.....	256
7.51	BHF variation predictions based on punch force, maximum radial stress, and maximum thickness strain control methods with an initial BHF of 200 kN.....	256
7.52	BHF variation predictions based on punch force, maximum radial stress, and maximum thickness strain control methods with an initial BHF of 400 kN.....	258

7.53	Punch force and BHF distributions measured during the deep drawing of HSG steel .....	261
7.54	Estimated BHF variations for deep drawing of high strength steel .....	261
7.55	Punch force and BHF distributions measured during the deep drawing of HSG steel together with the predicted ones.....	263
7.56	Punch force and BHF distributions measured during the deep drawing of UV steel .....	265
7.57	Punch force and BHF distributions measured during the deep drawing of UV steel .....	265
7.58	Punch force and BHF distributions measured during the deep drawing of IF steel .....	267
7.59	Punch force and BHF distributions measured during the deep drawing of IF steel .....	267
7.60	Punch force and BHF distributions measured during the deep drawing of IF steel .....	268
7.61	Punch force and BHF distributions measured during the deep drawing of IF steel .....	270
7.62	Punch force and BHF distributions measured during the deep drawing of IF steel .....	270
B.1	Flat bottomed punch geometry .....	298
C.1	General geometry and different zones in a deep drawing operation .....	305
F.1	Final cup geometry.....	317
F.2	Process sequence for the experiments .....	319
F.3	Tool arrangement for deep drawing .....	327
F.4	Principles of draw and reverse redraw operations.....	327
F.5	Geometry of a reverse redrawing tooling .....	331
F.6	Assembly drawing of the tooling used in the experiments .....	333
F.7	First stage die assembly, and the positioning of the hollow loadcell for the blankholder force measurements .....	334
F.8	Second stage blankholder assembly, and the positioning of the "button" loadcell for blankholder force measurements.....	336
F.9	Open position of the dies.....	338

F.10	Clamp position of the dies.....	339
F.11	Position of the tooling after the first stage, deep draw, operation.....	340
F.12	Clamp position before the reverse redrawing operation.....	341
F.13	Position of the tooling after the reverse redrawing operation.....	343
F.14	Pneumatic circuit of ERC/NSM press.....	346
F.15	Hydraulic circuit for the blankholder action in reverse redrawing operation on ERC/NSM press.....	348
F.16	Pneumatic circuit for the ejector on the draw/reverse redraw tooling.....	351
F.17	Draw/reverse redraw tooling with loadcells in place.....	352
G.1	Axisymmetric cup geometry.....	357
G.2	Assembly drawing of the die set for deep drawing of a round cup in Minster press.....	364
G.3	Orientation of the supporting cushion pins.....	367
G.4	Open position of the tooling.....	370
G.5	Clamp position of the tooling.....	371
G.6	Formed position of the tooling.....	372
G.7	200 ton loadcell for measuring punch load in deep drawing tooling on Minster press.....	377
G.8	40 ton loadcell for measuring blankholder force in deep drawing tooling on Minster press.....	377

## CHAPTER I

### INTRODUCTION

Sheet metal forming is an essential part of the modern industry. It is required in the manufacture of wide range of goods including automobiles, aircraft, and consumer products. Designing sheet metal forming dies is still an art requiring people with special skills and knowledge. It is a trial-and-error process based upon past experience. Prototype dies are machined and tried out, and if they do not work they are re-machined and tried again. This trial-and-error process, sometimes involving clay or wood models, has required lead times in the automotive industry up to four years in order to meet production schedules. In order to overcome this inefficiency, a scientific approach should be taken to design sheet metal forming dies.

The application of CAD/CAM is a relatively new development in sheet metal forming. This is because of the complexities involved in modeling sheet metal forming processes. However, the advantages to be gained by the application of methods of Computer-Aided Engineering are so significant in this area that it can no longer be ignored.

CAE techniques can be applied to sheet metal forming processes in several ways:

- a) At the design stage, the plastic deformation required to form a certain shape is analyzed to predict the severity of forming operations and to determine the sheet metal properties required to allow this deformation without failure,
- b) In the tool design stage, modeling of the forming process is necessary to determine, in deep drawing for example, how the blank holder should be designed to control the flow of the sheet into the die cavity,
- c) In the process design stage, modeling can be used to determine the optimum process parameters, such as blank holder force in deep drawing, etc., in order to reduce the cost of the process, and save time energy,
- c) In multi-stage forming operations, modeling can be used to find optimal intermediate geometries of the part at each stage,
- d) If the tooling is available and the part is already in the production, modeling together with experimental data can be used to analyze sheet failure and determine how to overcome it.

CAE techniques can also be applied to analyze sheet metal parts as structures to determine the strength, stiffness and energy absorption during collapse but this application is not considered in this study.

The overall objective of this research is to develop a CAE system for the process sequence design for sheet metal components. In this study, only axisymmetric and plane-strain geometries are considered. However, the methods developed are general, and similar techniques can be applied to

more complex geometries. The CAE system outlined in Section 2.4 has two main components. These are: (a) the knowledge-based expert system module (symbolic module), and (b) the process-modeling analysis module (numeric module). The symbolic module includes available domain expertise in the form of "if .... then" rules. The numerical module simulates metal forming operations using the finite difference method. These modules should be integrated for the automatic process sequence design.

The research to develop the outlined CAE system was initiated at Battelle Columbus Laboratories where a Finite Difference based analysis program, DEEPDW, for simple axisymmetric deep drawing process was developed. Sitaraman has continued to work on the project as part of his Ph.D. dissertation, [Sitaraman, 1989a]. He has developed the analysis program, SHEET\_FORM, to analyze single step deep drawing and stretch forming processes with different axisymmetric punch geometries. He has also developed a knowledge-based expert system, ASFEX, for process sequence design in axisymmetric sheet metal forming processes.

All the work involved in the current study is related to the analysis program. SHEET\_FORM has been modified so that the number of geometries that can be analyzed using SHEET\_FORM is increased (including plane-strain sections, direct and reverse redrawing operations, etc.), strain and stress predictions can be evaluated against failure, both a constant and variable blank holder force (BHF) as a function of punch travel can be used in the simulations and the BHF can be optimized to increase the attainable cup

height. Several experiments have been conducted to verify the results of the analysis module.

This document is organized into eight chapters, and provides a general review of sheet metal forming technology and analysis together with the results of the experimental studies. It includes a survey of current industrial practices, findings from a literature review, and a detailed explanation of the current study on developing a computer-aided engineering system for process sequence design for sheet metal forming. Chapter 2 provides a review of the CAE systems used in sheet metal forming industry. A summary of the analysis techniques, and objectives and scope of the current research is also provided in Chapter 2. Chapter 3 presents a general background on sheet metal forming processes. An extensive review of the technology in blank holder design and force control is summarized in Chapter 4. The details of the formulation for the analysis of deep drawing and stretch forming processes using the Finite Difference Method (FDM) is given in Chapter 5. A preliminary comparison of SHEET\_FORM with the experiments and FEM solutions found in the literature is also provided in Chapter 5. Chapter 6 summarizes the multi-stage deep drawing experiments conducted in the ERC/NSM press, and compares the theoretical results with the experimental measurements. Details of the failure evaluation module, and the verification of its results against experiments are also provided in Chapter 6. Chapter 7 provides the details of the experiments conducted in 160 ton single action hydraulic press. The comparison of the strain and force predictions with the experimental measurements from these experiments are also given in



Chapter 7. Details of the method to predict the optimum blank holder force variation as a function of punch travel, and its verification with the experiments are also provided in Chapter 7. Chapter 8 provides a summary and the concluding remarks, identifies research contributions of this work, and presents an outline of the future work.

## **CHAPTER II**

### **LITERATURE REVIEW AND RESEARCH OBJECTIVES**

#### **2.1. Computer Aided Engineering Systems in Sheet Metal Forming**

Conventional die design methods involve several steps starting from part design to the manufacture of the dies for production, Figure 2.1. It requires experience and involves trial-and-error processes that cost substantial amounts of time and money. To reduce the amount of time and money invested in die design and to shorten the lead times to meet production schedules, a scientific approach should be taken to the design and manufacture of the dies. An integrated Computer Aided Engineering (CAE) system for die design that can be applied to certain families of parts could be used to reduce the amount of trial-and-error and thus result in quantifiable cost and time savings.

Initial studies utilizing CAE techniques were concentrated on the modeling of the forming processes, and several methods were developed for process



simulation. These methods are summarized in Section 2.3. In parallel with process modeling efforts, several expert systems were developed to automate die design processes during recent years. Two of these expert systems are FORMEX, for cold forging, [Sevenler, et al., 1986], and AGMPO, for deep drawing, [Eshel, et al., 1985]. Both of these expert systems can be used to design process sequences for axisymmetrical parts. The next generation of CAE systems will include both process modeling and die design expert systems to simulate the trial-and-error procedure currently used in the industry, [Sitaraman, et al., 1989b]. In several examples from industry, initial attempts to computerize die design methodology and integrate it with CAM have already proven to be largely successful. Fujitsu LTD., Tokyo, has shortened the manufacturing process and set-up time by about 75% using their Integrated CAD/Sheet Metal manufacturing system, [Sfiligoj, 1983]. Hitachi LTD. has developed a CAD system for progressive dies which has resulted in an 80% reduction in die design time, [Murakami, et al., 1980].

Toyota Motor Corporation has developed an "integrated" CAD/CAM/CAE system for the design of sheet metal forming dies, [Takahashi, et al., 1988, Okamoto, et al., 1988]. This system is capable of designing, evaluating, and modifying the die design to improve the technological level. Toyota Motor Corporation reports that their "integrated" CAD/CAM/CAE system has already resulted in a 50% reduction in man-hours in die design by employing powerful geometric functions to design die faces and to evaluate press forming feasibility, a 30% reduction in man-hours in the manufacture of die faces by eliminating measuring work for model fabrication and the preparation of NC processing data, and a 30% reduction in man-hours in die

tryout and modifications by understanding press forming severity and by upgrading press die accuracy.

Karima has proposed a knowledge-based system in sheet metal forming, [Karima, et al., 1987]. The system design is based on manipulating the knowledge to determine what action to take to achieve the desired goals, keeping in perspective the various design constraints. A typical system for process modeling in sheet metal forming consists of the properties of the material before and after the deformation, the deformation zone, conditions at the material/tool interface, tooling characteristics, and auxiliary equipment as illustrated in Figure 2.2. A CAE system should have the capabilities of blank development, predicting metal flow, and load displacement curves for irregularly shaped parts.

Karima, 1989, suggests that a hybrid system for process planning in sheet metal forming should have several modules such as prediction module, which mathematically predicts the result of stamping for a known geometry of blank, tooling, material properties, lubrication and boundary conditions, etc., and design module, which helps the designers to design the process sequence and the blank shape in order to form the desired product.

Tisza, 1987, describes a CAD/CAM system for developing tools for the manufacture of sheet metal components having axisymmetric and rectangular cross sections. The system would be modular as shown in Figure 2.3. It would consist primarily of a Geometric Description Module for reading in the object geometry, a Blank Module for determining the optimum shape,

## CAE SYSTEM

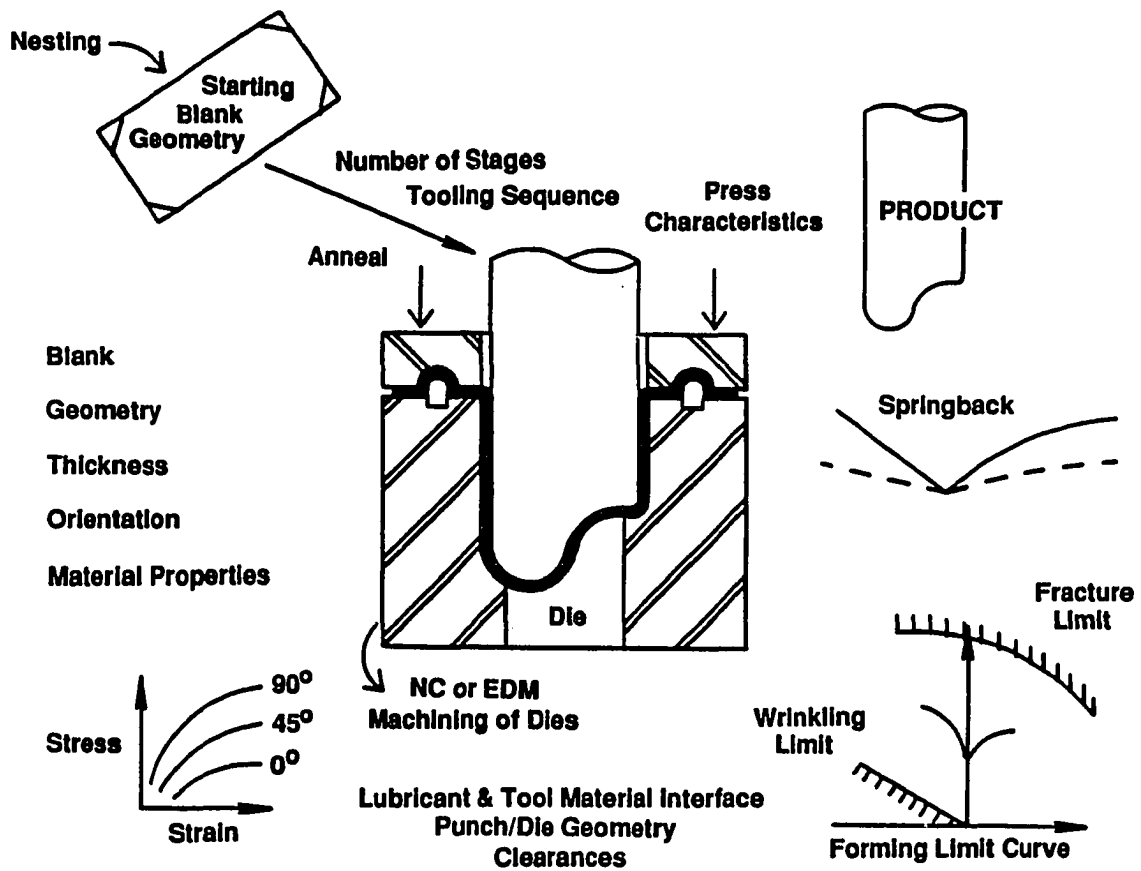


Figure 2.2: A CAE system concept for sheet metal forming, [Karima, 1987].

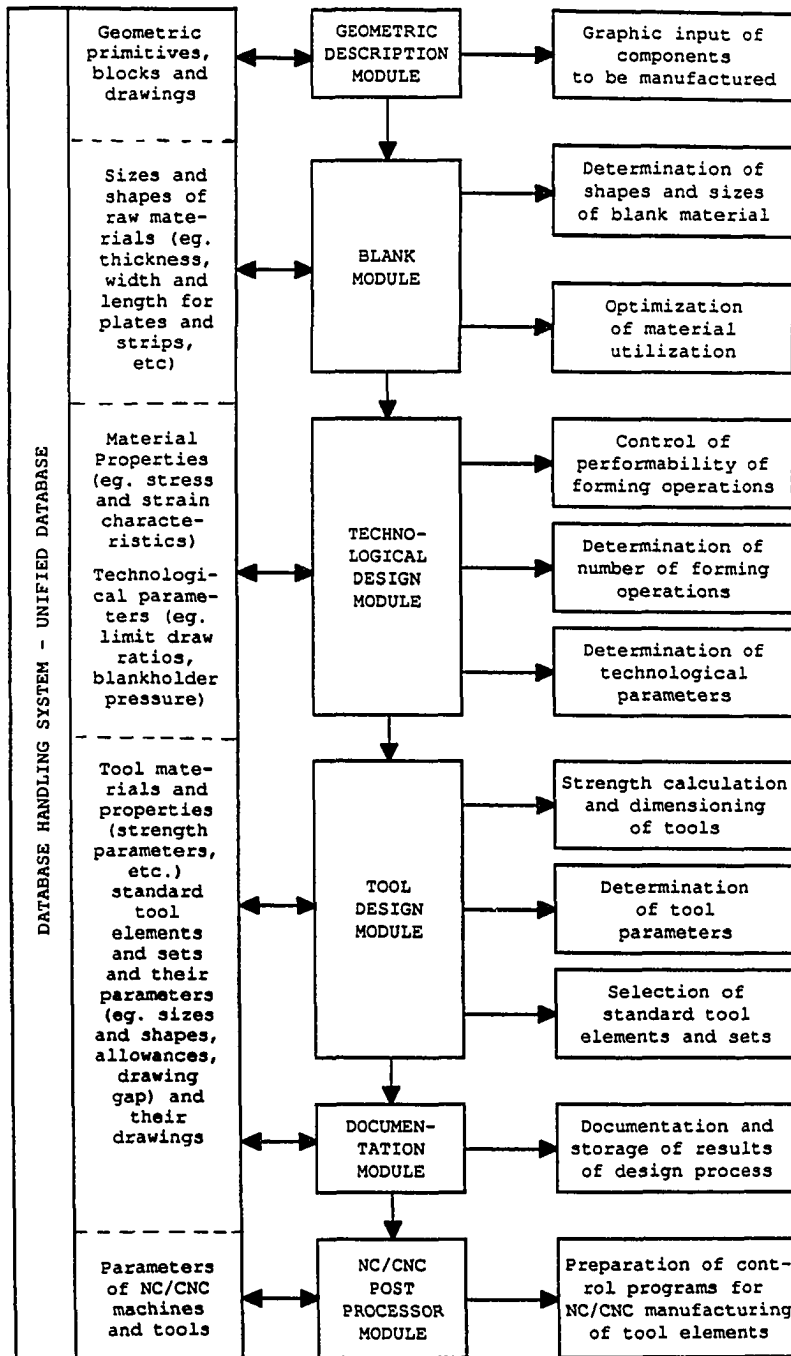


Figure 2.3: General scheme of integrated CAD/CAM system for deep drawing, [Tizsa, 1987].

size, and nesting of blanks, a Technological Design Module for designing process sequence based on empirical rules and technological parameters, a Tool Design Module for designing the tools and selecting a tool of standard size, and a NC/CNC Post Processor Module for preparing control programs for NC/CNC manufacturing of tool elements. Applying this system, the time and labor required for design and manufacturing can be reduced.

An integrated CAE system for auto-body press tool design is developed by Makinouchi, et al., 1991. The objective of the CAE system is to predict forming defects in stamping operations by simulating the forming process using 2-D and 3-D Finite Element codes. The system consists of five modules. These are: 1) CAD module to describe the tool geometry, 2) data base module to provide experimental data, 3) pre-processor module to generate the mesh for FE simulations, 4) simulation module including two elasto-plastic FE codes, and 5) post-processor to display the results using computer graphics. The CAE system was applied to several sheet metal forming processes successfully, however, it needs to be further verified.

A CAD/CAE system is described by Aita, et al, 1992. The analysis of a sheet metal forming process starts from the description of the tool geometries using CAD data. The system consists of several modules including a CAD/Mesh Generator, Forming Simulation Module, Post-Processor, and Design and Manufacturing Module. For accurate analysis and successful optimization of the tool geometries, interaction is provided between different modules of the system.



An integrated CAE system was developed for the design of progressive dies by Adachi, et al, 1983. Starting from the product specifications, the system designs the tooling, and creates the NC program to manufacture the dies. This system can reduce the design time by 40% as compared to the conventional die design.

## **2.2. Process Sequence Design**

When a cup is to be drawn from a flat blank the number of required drawing operations must be determined. If the deformation required to form the cup is within practical limits, e.g. shallow cups, then the cup can be formed in one operation. These forming limits are available in the literature [Lange, 1985]. If a relatively deep cup is formed, then usually two or more operations are required. Figure 2.4 shows a process sequence used to form an axisymmetric part.

A die designer has to determine the number and the geometry of necessary successive forming operations and design the dies accordingly. The number of operations required usually depends on the sheet metal quality, its thickness, the geometry of the dies, amount of thinning and ironing, and the ratio of the initial sheet thickness to the diameter of the cup. If a sheet metal blank is drawn too deeply in one operation, then the pressure required to form the flat sheet into a cylindrical shape will exceed the tensile strength of the metal in the wall of the drawn cup and fracture will occur.

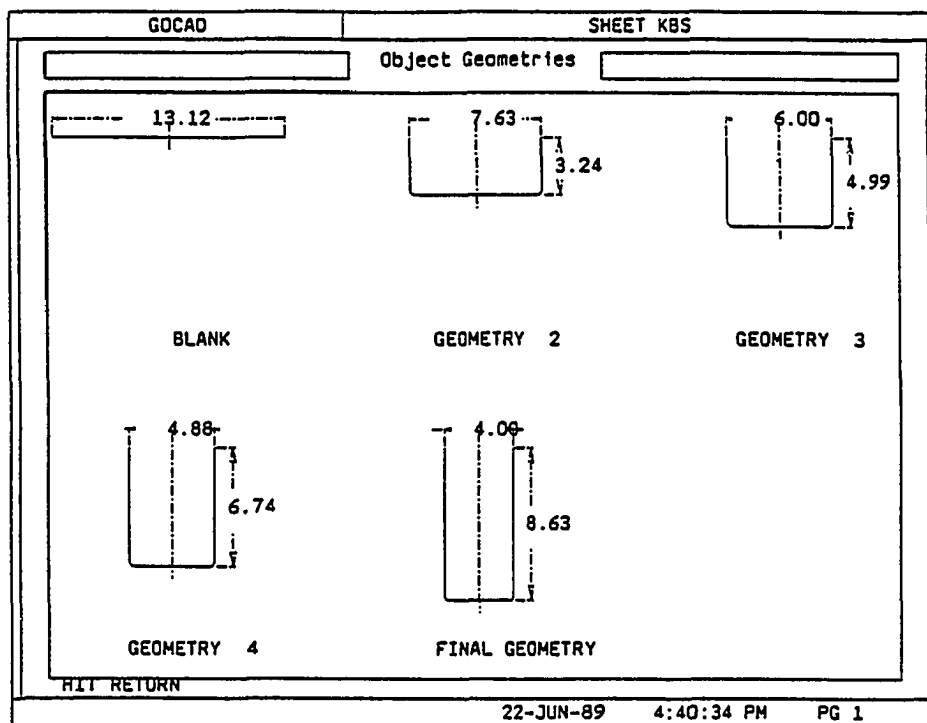


Figure 2.4: Process sequence to draw a round cup, [Sitaraman, 1989a].

If the drawn part is too deep in proportion to its diameter, then redrawing is required. In this case, the die designer has to determine the number of necessary forming operations and design the dies for these successive operations. If the dies for successive operations require abrupt changes in the shape of the metal or excessive reduction in diameter, then, the metal will be over-stressed during forming and will fracture. On the other hand, the cost of tooling may be excessive if too many redrawing operations are used.

### **2.3. Analysis of Sheet Metal Forming Processes**

Predicting the stress and strain distributions during and after a forming operation is one of the major concerns in sheet metal forming. For better product design, improved product quality, and efficiency in die design, stresses and strains should be predicted prior to any die try-out and production. Die designer should check whether it is feasible to make the part with a particular shape and from a given material before manufacturing the dies.

The major objective of modeling sheet metal forming processes is to provide the necessary information for the design and control of these processes without requiring expensive die tryouts. Thus modeling techniques should be capable of determining the effects of various process parameters upon metal-flow and potential failure in the deforming material. Analysis technique should also be efficient in computation and the results should be within an acceptable degree of accuracy.

Mathematical or computer modeling of sheet metal forming processes involves many difficulties due to complex shapes of the workpieces, modeling material behavior, and modeling friction conditions existing at the interface between the tool and the workpiece. Due to these difficulties, it is impossible to model sheet metal forming processes exactly. This is why process modeling techniques represent simplifications of the actual processes.

Analytical methods used to model sheet metal forming operations are usually divided into two types. One type includes both drawing and stretch forming. In this type, variations of strain and stress through the thickness of the sheet are usually neglected. In the other type, bending is dominant, therefore, variations in stress and strain through the thickness must be taken into consideration. Usually, a forming operation includes both types of deformation. To include both types in modeling an actual operation, it is necessary to divide the problem into two parts. Both types should be solved separately and the results should be combined.

The general approach to develop a model for a forming process involves several steps and may be summarized, in simplified terms, as follows. The first step is to classify the problem according to whether a bending or stretching/drawing type of solution is applicable, and then express the strains in terms of geometry by making simplifying assumptions about either geometry or strain distribution. The second step is to select a constitutive model and a flow rule to characterize the material behavior and yield surface. The third step is to write the equations of equilibrium for the forming forces

and the stresses that will occur inside the sheet metal during the forming operation. Finally, the equations of equilibrium must be solved such that both the stress and the velocity boundary conditions are satisfied.

The history of process modeling is more than fifty years old, and it can be attributed to the work done by Sachs, Swift, and Hill in the analysis of stretch forming and deep drawing of axisymmetric cups employing hemispherical shaped punches, [Sachs, 1934; Swift, 1939; Hill, 1950]. Computer based modeling techniques have been developed and increasingly used to simulate sheet metal forming processes over the past three decades due to advances made in computational facilities. Several approximate methods have been suggested for the analysis of forming processes. Some of these methods are the finite element method (FEM), the finite difference method (FDM), slip-line field approach, upper bound technique, etc. Among these methods, FEM is used widely because of its flexibility and ability to obtain a detailed solution and closeness of its solution to the exact one. Application of FDM is usually limited to simple geometries, such as hemispherical or flat-bottomed cylindrical punch.

The finite difference technique is limited to simple geometries since it is not practical to model the surface and contact conditions for complicated geometries using FDM. However, this method gives fast and reasonably accurate results for simple axisymmetric or plane strain geometries. Woo has pioneered the work in the application of finite-differences to the deep drawing of cylindrical cups by taking into consideration the stretch forming of

the material over the punch head, [Woo, 1968]. Woo's analysis was based on the incremental theory of plasticity. The predicted stresses and strains compared well with experimental results, however, anisotropy effects were not included in the analysis. The work by Vemuri, et al., 1986, based on Woo's approach, predicted stresses and strains in deep drawing of a cylindrical cup taking the effect of normal anisotropy into consideration.

Significant work has also been done in the analysis of stretch forming. Using a finite difference technique, Woo has analyzed stretch forming of an isotropic Misses material over a hemispherical punch under axisymmetric conditions using FDM [Woo, 1965]. Kaftanoglu and Alexander, 1970, have developed a comprehensive analysis for axisymmetric punch stretching taking the effects of anisotropy, friction, non-linear strain hardening, and pre-strain into account. They have reported good agreement between theoretical predictions and experimental results with ferrous and non-ferrous materials employing hemispherical and ellipsoidal punches. For varying frictional conditions, they observed through their analysis that the location of the plastic instability point moves away from the punch with increasing coefficient of friction as found earlier by experiments. They have reported that the instability criterion based on 'Strain Propagation' was the best in successfully predicting the onset of instability rather than 'Maximum Load' or 'Maximum Pressure' criteria. Kim's semi-empirical analysis, based on Woo's method, used Hill's new yield function to predict stresses and strains in an axisymmetric stretch forming analysis over a hemispherical punch [Kim, et al., 1984]. Their analysis uses the friction coefficient as a variable to match the

theoretical and experimental thickness strains at the pole. The experimental thickness strains measured elsewhere in the cup were found to be less than their analytically-predicted values which they attribute to possible draw-in during experiments and to errors in measurements.

FEM has found a wider application because of its ability to model complex-shaped geometries and boundary conditions. FEM has been used to solve actual metal forming problems starting in the 1960's by Marcal, et al., 1967, Yamada, et al., 1968, and Zienkiewicz, et al., 1969. A systematic survey of the developments and applications of FEM on process modeling of sheet metal forming has been given by Wafi, 1982.

For simple applications (such as the analysis of deep drawing and stretch forming of cylindrical or hemispherical cups, and analysis of simple plane strain section), FDM results are compatible with FEM results. In these applications, FEM does not have an advantage over FDM. It is easy to introduce boundary conditions and solve the equilibrium equations, therefore, FDM gives faster results with the same accuracy as FEM. However, as the geometry gets complicated (i.e., if there are several draw and redraw operations which introduce several hard to determine neutral points where the sheet metal does not flow), it gets very difficult to describe the metal flow and solve the equilibrium equations to reach a convergent solution. Compared to FDM, it is easy to describe the complicated boundary conditions in FEM, and therefore, FEM is widely used in the analysis of complicated sheet metal forming operations.

The majority of sheet metal components are formed in more than one forming operations depending on the severity of deformation. Therefore, it is especially important to be able to analyze stresses and strains in multi-step forming processes. In an incremental deformation, true strains can be added at each increment. As a result, the analysis of multi-stage forming operations is relatively straight forward. Several investigators have studied multi-step sheet metal forming processes. Gerdeen, 1984, has used the deformation theory of plasticity and analyzed multi-step forming operations using a rigid-plastic material model. In that analysis, a closed form solution to the problem was presented which required a prior knowledge of the thickness strain distribution. It is claimed that the strain in any stage does not depend on the deformation path, and the strain in any stage can be found depending on the current geometry and the original shape, [Gerdeen, 1984]. The force, required to deform the metal from one stage to the next one, depends on the change in the strain between these two stages. Reissner, et al., 1987, has studied deep drawing of two part cans using the finite difference method. He employed a rigid plastic model with normal anisotropy and isotropic work hardening. The workpiece was divided into several zones and the analysis was carried out using Woo's method. Majlessi, et al., 1987, has studied multi-step sheet metal forming processes under axisymmetric conditions using the finite element method. He employed membrane elements and the deformation theory of plasticity. The assumption of proportional loading in each step of forming was examined and the results were compared with experiments.



## 2.4. Objectives and Scope of the Current Research

Industrial visits, literature survey, and discussions with die design experts during the research initiation phase indicate that despite the advances made in modeling and understanding better the sheet metal forming processes, almost all die design experts still rely on rules of thumb and experience for designing dies. To our knowledge, no expert systems are currently being used for die designing in industry. But many companies expressed keen interest in either developing or acquiring a practical expert system which would help them achieve substantial time, energy, and cost savings in die design by improving standardization, optimizing number of die stations, improving material savings, reducing tool wear, and also enhancing production rate. In addition to being a permanent and confidential source of expertise, such a system would serve as a valuable consultant for die design experts and as a dependable training aid for beginners. One ultimate goal for many automobile industries today is to develop a fully Computer Integrated Manufacturing (CIM) system in which everything from conceptual design to die tryout, from product design to final inspection could be carried out by maintaining a central, unified database. Such a system, according to experts, would most likely be operational in industries by the mid-nineties. They also point out that a workable expert system for die designing is an important stage in developing such a CIM system.

A CAE system for die design in sheet metal forming would be used in the design stage and help die designers to reduce the number of trial-and-error

steps involved in conventional die design techniques. To solve the problems involved in conventional method, and at the same time, obtain high quality geometric models of the sheet metal forming dies, geometric models should be created, evaluated, and modified in the design stage. Once the required quality of the geometric model is obtained, the sheet metal forming dies can be manufactured by NC machines based on the final geometric model.

The main objective of the current study is to develop a CAE system for an automatic process sequence design for the manufacture of sheet metal components. The main components for the CAE system is shown in Figure 2.5. The Knowledge-Based Expert System Module and Process Modeling Analysis Module should interact with each other during the design and decision making processes. The input to the CAE system is the final sheet metal object geometry that needs to be manufactured and the process parameters, and the output from the system is the process sequence design including intermediate object geometries and the optimum process parameters.

The interaction between different modules of the CAE system is shown in Figure 2.6. Given the desired cup geometry and the estimated process parameters, the CAE system will come up with the process sequence to form the cup. In designing the process sequence, the CAE system will utilize two features. One of them is the knowledge base and the other one is the analysis routine. The system will first use the knowledge base to design the initial process sequence and then run the analysis routine to check the strain values

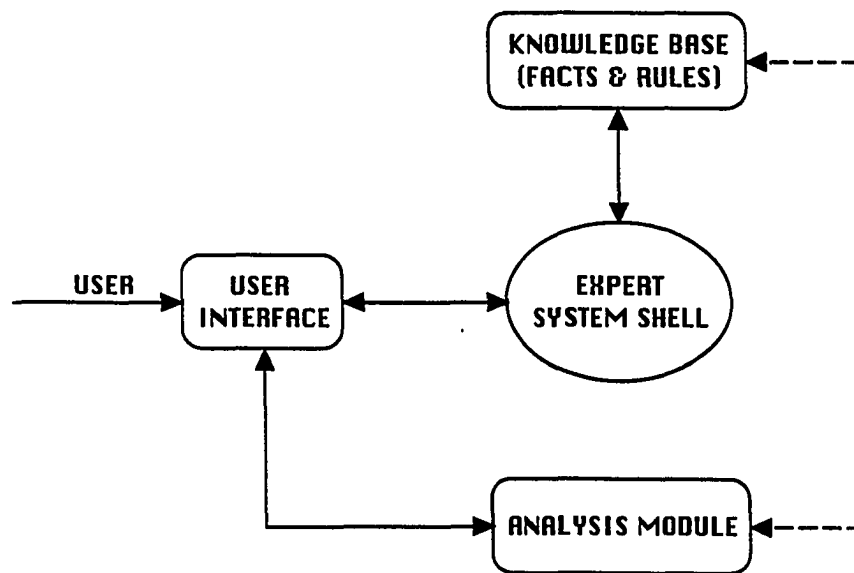


Figure 2.5: CAE system architecture, [Sitaraman, 1989a].

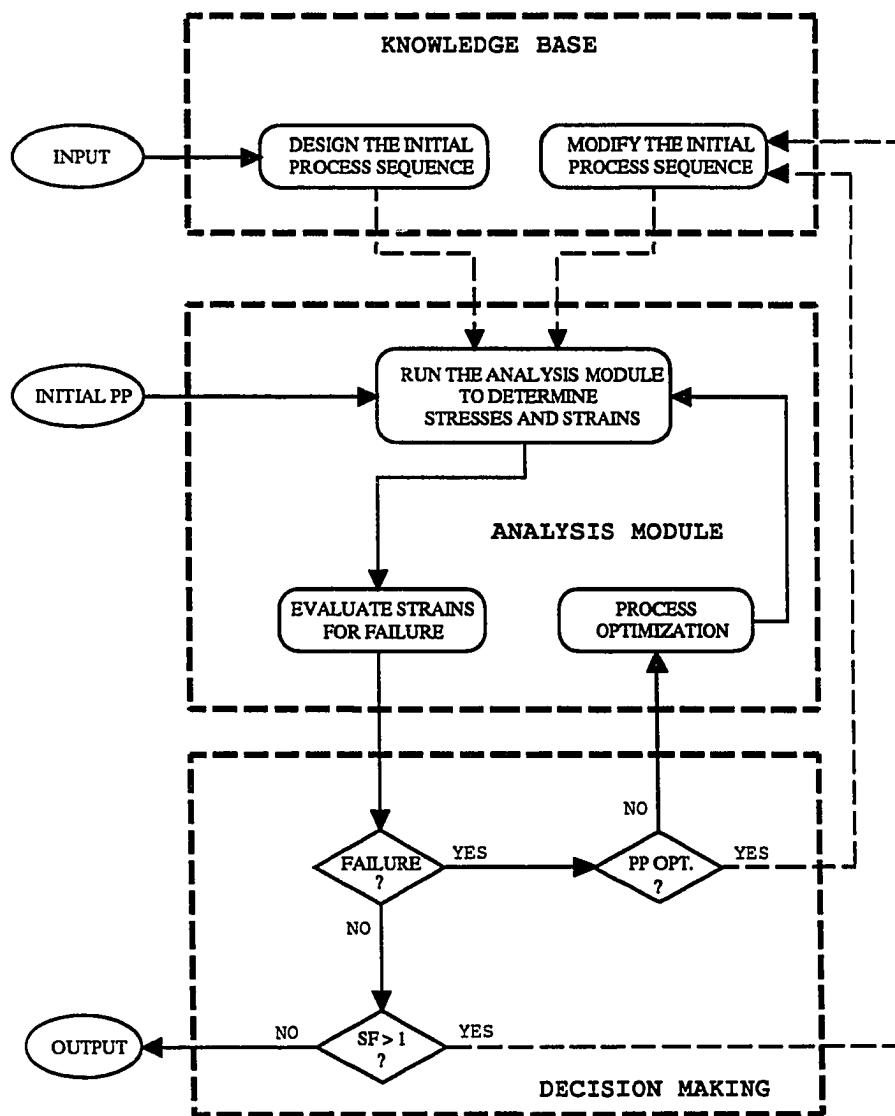


Figure 2.6: Interactions between different modules of the CAE system.

PP: process parameters

SF: safety factor. If  $SF > 1$ , then, process design is too conservative and it should be modified.

at each stage designed. The analysis module will formulate the mechanics of metal forming and predict stresses and strains. If the strain values indicate a failure at a certain stage, then, the system will modify the design of that stage. The knowledge-base system for the process sequence design of axisymmetric geometries has been completed and tested against several test cases by Sitaraman, 1989b.

All the work involved in this study is related to the analysis model. Interactions between the knowledge base system and the analysis module, as shown in Figure 2.6, are not provided. Dashed lines in Figures 2.5 and 2.6 show the missing links in the overall CAE system. The expert system and the analysis modules run separately. A designer must first run the expert system to obtain a preliminary process sequence based on empirical design guidelines. Then, he/she would run the analysis program to verify the formability of the workpiece.

During the period of this study, the analysis module has been improved so that it can be used to analyze more complex geometries, to determine failure, i.e. fracture and/or wrinkling, and to optimize the process conditions. Several experiments have been conducted to study the deep drawing process and to verify the results of the analysis module. In a follow up project, the link between the knowledge-base system and the analysis module will be developed.

## CHAPTER III

### TECHNICAL BACKGROUND ON SHEET METAL FORMING PROCESSES

#### 3.1. Geometries of Deeply Recessed Parts

In automobile and aircraft industry, a large number of non-symmetrical, difficult-to-produce sheet metal components are required. A shape classification of these parts according to Sachs is given in Figure 3.1. The subject of this dissertation is deeply recessed parts with straight or tapered walls.

Different sections in a deeply recessed part may be classified into three groups according to their geometry. These are axisymmetric, plane-strain, and general 3-D sections. Each of these sections should be studied separately because they have minor differences in their deformation processes.

Axisymmetric cup forming operation applies to drawing of parts having a circular cross section, i.e., from the top view, all contours appear as circles. This is called a cupping operation. If not fully axisymmetric, some sections of a

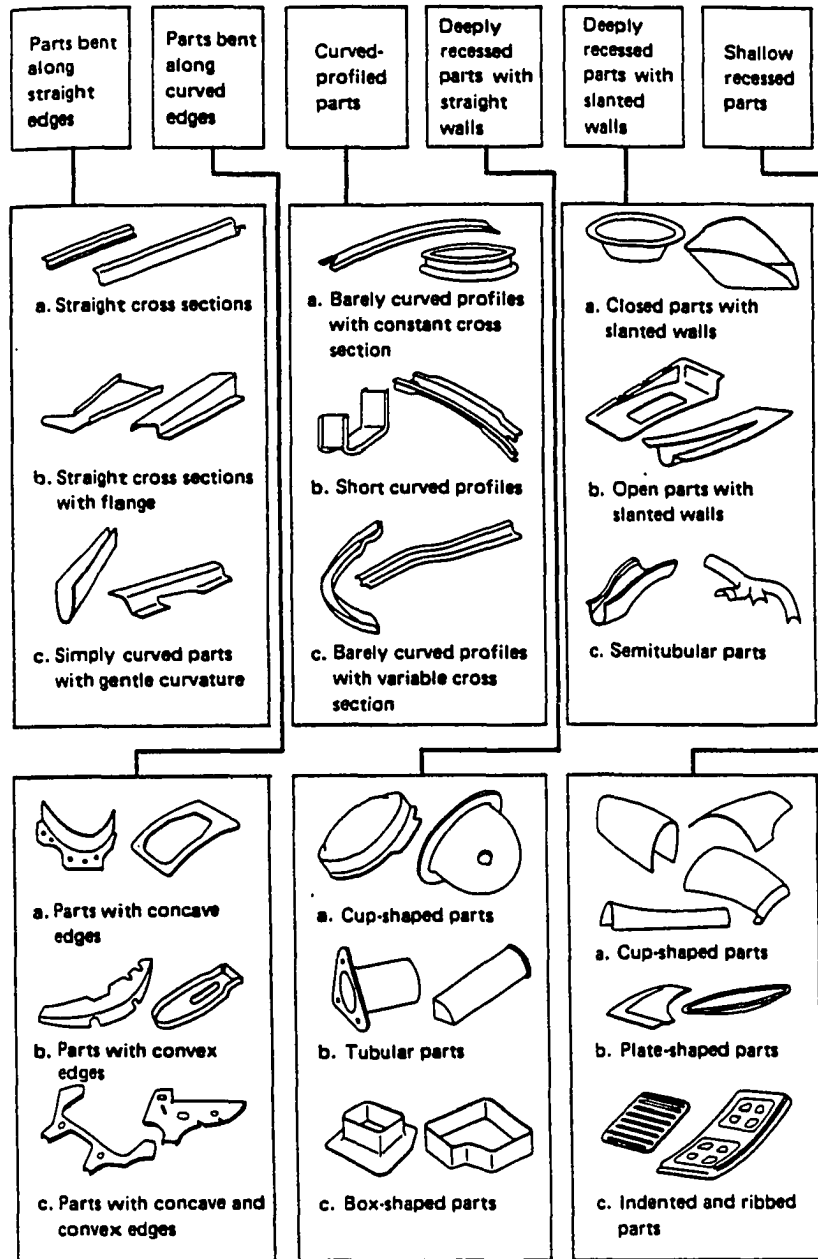


Figure 3.1: Shape classification of sheet metal parts, [Lange, 1985].

deeply recessed part may be approximated as axisymmetric. Because of the circular shape, the stresses and strains throughout the section are axially symmetric during the drawing. An axisymmetric section can be formed into a desired section in one or more stages depending on the severity of the forming operation. Limiting Drawing Ratios for round cups (i.e., the diameter of starting blank versus the diameter of drawn cup) which are readily available in the literature [Lange, 1985] can be used to design the process sequence for these sections.

Some sections in a deeply recessed part can be classified as plane-strain. These are the sections in the middle of a long part where the end effects can be neglected. In these sections, depending on the orientation and the magnitude of the clamping forces, strains are close to zero in the length direction.

In many cases, some sections of a workpiece does not have a regular shape (i.e., sections can not be classified as axisymmetric or plane-strain). The contour of these parts changes irregularly causing a wide variation in the stresses and strains. Wrinkling or excess of metal may occur in one section, while excess thinning of metal may cause tears in other sections. Forming of this kind of shapes has the highest tooling and production cost and results in greatest amount of scrap. The number of trials which are necessary to establish the shape and dimensions of the blank and intermediate forming stages can be quite large.



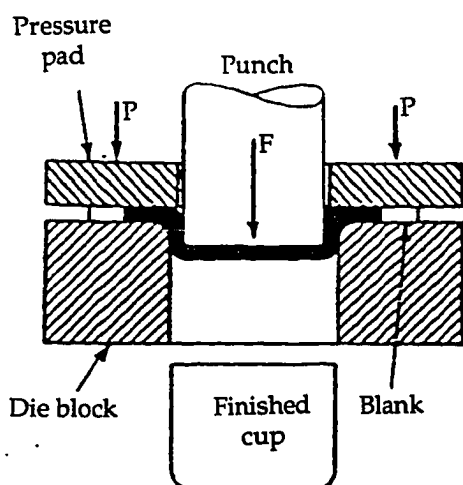
## **3.2. Sheet Forming Operations**

There are several sheet metal forming processes that are commonly practiced in the industry. These processes are shown in Figure 3.2. Production of sheet metal components which are classified in Figure 3.1 may require a combination of these forming processes. Most commonly used operations to form deeply recessed parts are bending, deep drawing, and stretch forming.

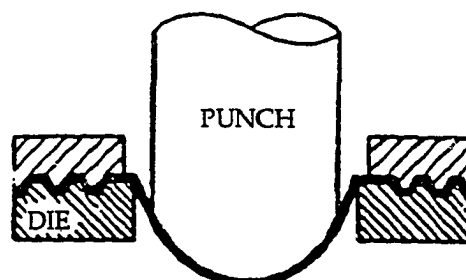
### **3.2.1. Bending**

Bending is a method of producing shapes by stressing metal beyond its yield strength, but not past its ultimate tensile strength. Die bending involves bending of the sheet between punch and die until the workpiece contacts the sides of the die. The forces applied during bending are in opposite directions, just as in the cutting of sheet metal. Bending forces, however, are spread farther apart, resulting in plastic distortion of metal without failure. Bending forces during V-die bending and Single-die bending are shown in Figure 3.3.

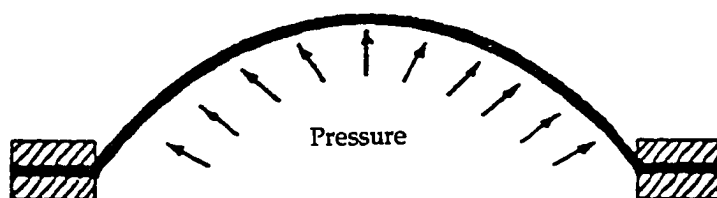
During bending, the material is locally stressed at the bend radii along a line. The stress distribution on a sheet metal, after bending, is shown in Figure 3.4. The metal outside of the bend radius has been stretched, indicating that a tensile stress has been applied. The metal on the inside of the bend radius has been placed under a compressive stress. Therefore, if fracture occurs in



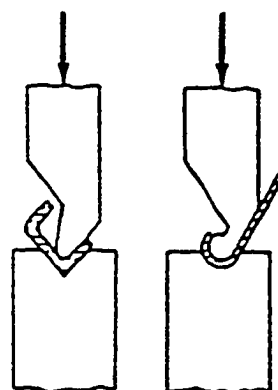
a) Deep Drawing



b) Stretch Forming

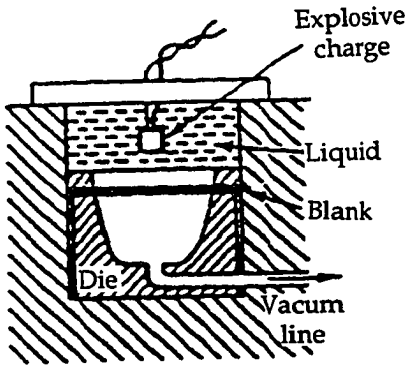


c) Hydrostatic Bulging

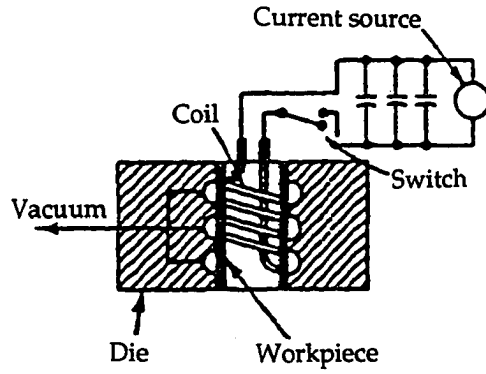


d) Brake Bending

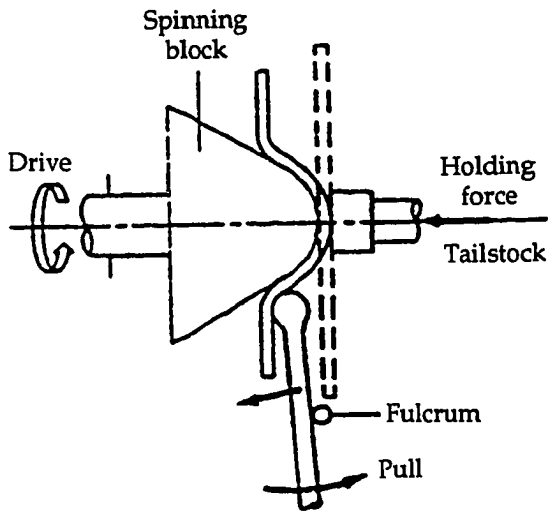
Figure 3.2: Sheet metal forming processes, [Redecop, et al., 1986].



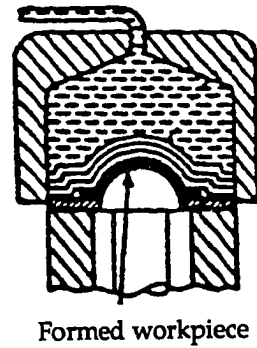
e) Explosive Forming



f) Electromagnetic Forming



g) Spinning



h) Hydroforming

Figure 3.2: Continued, [Redecop, et al., 1986].

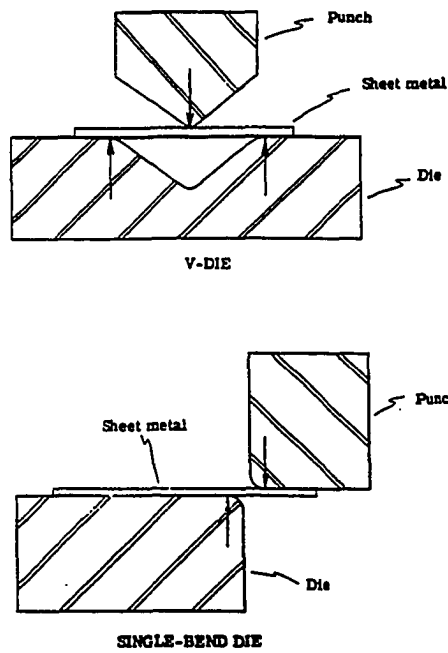


Figure 3.3: Forces applied during bending, [Eary, et al., 1974].

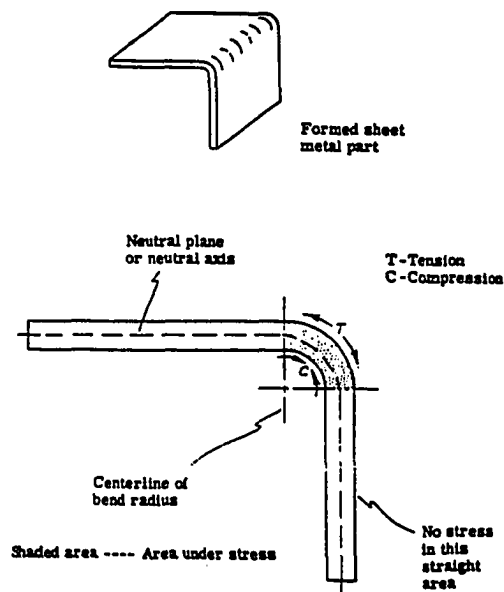


Figure 3.4: Stresses during bending, [Eary, et al., 1974].

bending, it will occur at the outside of the bend, and if wrinkling occurs, it will occur at the inside of the bend.

### 3.2.2. Stretch Forming

"Stretch forming is a method that combines controlled stretching and bending of sheet metal blanks, roll-formed sections, and extrusions around form blocks (dies) to produce accurately contoured parts without wrinkles", [TMEH, 1984]. Stretch forming operation is shown in Figure 3.5. Application of stretching prior to or during bending operations, prevents wrinkling and reduces the effect of springback.

Some advantages of stretch forming are increased tensile strength and hardness. The metal is stressed under tension and so there is little springback or buckling in the stretch formed parts. Since the sheet metal is stressed above the yield strength prior to the punch stroke, the pressure required to form the metal is less than the pressure required in similar deep drawing operations, and because the pressure is low, the die can be made lighter. This will reduce the tooling costs. Also in stretch forming operations, scrap cost will tend to be low because trimming operations can be reduced by 50%, [TMEH, 1984].

Stretch forming is used for forming body panels, such as doors, roofs, or fenders for trucks, busses, and special vehicles, and in the aircraft industry. In

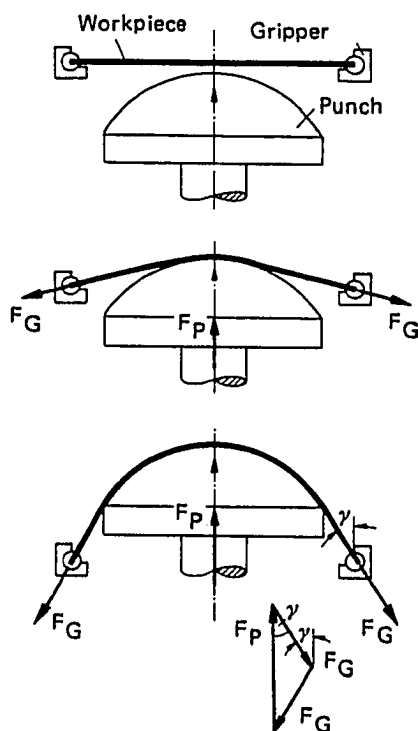


Figure 3.5: Deformation during stretch forming, [Lange, 1985].

these latter applications, formed sheet metal components with very large surface areas are sometimes required. For these applications, special forming machines are used because of the necessary machine size.

### 3.2.3. Deep Drawing

"Deep drawing is a cold forming process which forms a flat sheet of metal into a deeply recessed part having a wall thickness essentially the same as that of the blank", [TMEH, 1984]. Major elements of a deep drawing operation is shown in Figure 3.2a.

In deep drawing operation, thickness change is not desired. Usually the thickness of the final product is the same as the thickness of the initial blank. Therefore the surface area of the final product is the same as that of the initial blank. This is often used to determine the blank size to form a certain shape.

Major failure modes in deep drawing operations are wrinkling and tearing. Wrinkling may occur in the flange or in the side wall of the cup if the clearance between the die and the punch is high. Wrinkling can be prevented by applying restraining forces to the sheet metal to control the metal flow during the deformation. Bending of sheet metal over the die corner radius introduces some restraining to the flow of metal into the die cavity. If the metal is thick this restraining would be enough to form the part, but in most cases a blankholder is required to obtain extra restraining forces. If the

blankholder force is large fracture may occur in the unsupported region between the die and the punch corner profiles. The material is stretched and the maximum tensile stress and rupture may occur in this region close to the punch corner profile. The metal must have a combination of strength and ductility to avoid rupture, and blankholding force should be controlled during the process.

### **3.3. Multi-Stage Forming Operations**

If the depth of a cup to be manufactured by drawing exceeds its diameter, the cup must be produced in a multi-stage operation. Beginning with a flat blank, the sheet metal is transformed into one or more intermediate shapes before it reaches the desired shape and dimensions. The maximum percent reduction in a redrawing operation, i.e., the ratio of drawn cup diameter to redrawn cup diameter, depends on the ductility of the metal and the design of the part.

#### **3.3.1. Direct Redrawing**

Redrawing of a cup is illustrated in Figure 3.6. During redrawing, the cup first sits on top of the lower die while the punch and the blank holder fit inside of the cup. The wall thickness of the blank holder is limited by the percent reduction of the redraw. Therefore, if the percent reduction in the draw



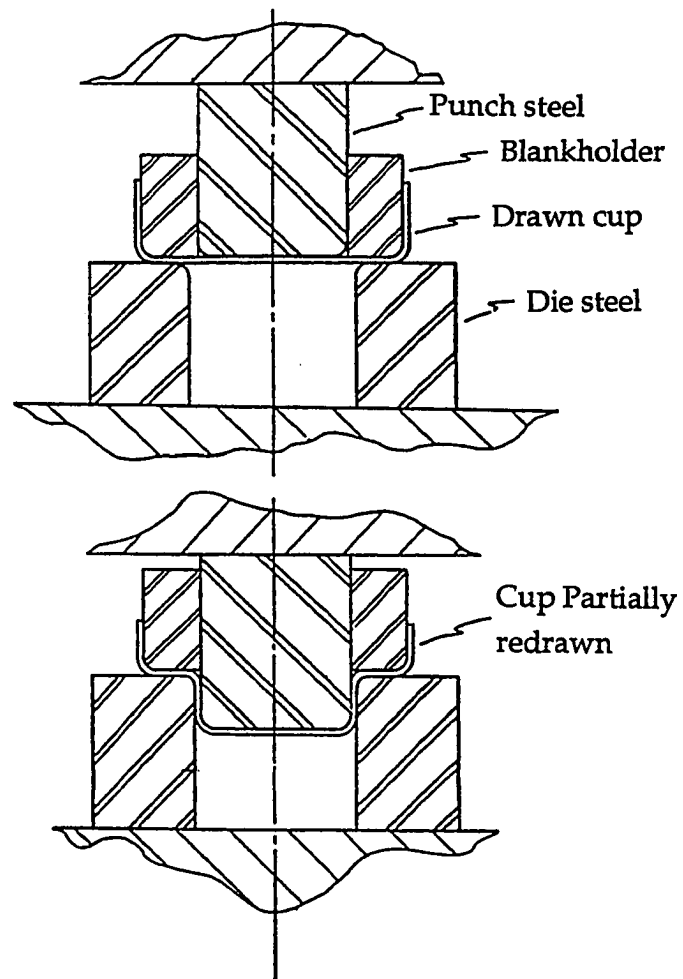


Figure 3.6: Direct redrawing of round cups, [Eary, et al., 1974].

diameter (i.e., diameter of drawn cup versus diameter of redrawn cup) is not large, the blank holder can not be used for redrawing.

During redrawing, the sheet metal is bent at the radii in a direction opposite to that of drawing. The reverse bending of the metal in this manner causes more work hardening and a reduction in ductility. In order to restore the initial ductility, annealing may be required between certain drawing stages.

### **3.3.2. Reverse Redrawing**

During reverse redrawing, Figure 3.7, the material is bent at the radii in the same direction as it is during drawing. Thus less work hardening of metal occurs, so the number of annealing stages between draws is less than that for redrawing.

The major disadvantage of reverse redrawing is the limitation on wall thickness of the die steel. The smaller the percent reduction, i.e., the smaller the difference between the diameter of the drawn cup and the diameter of the reverse redrawn cup, the thinner must be the die wall. But there is no restriction on the sizes and the shape of the blank holder, so good control and prevention of wrinkles can be obtained.

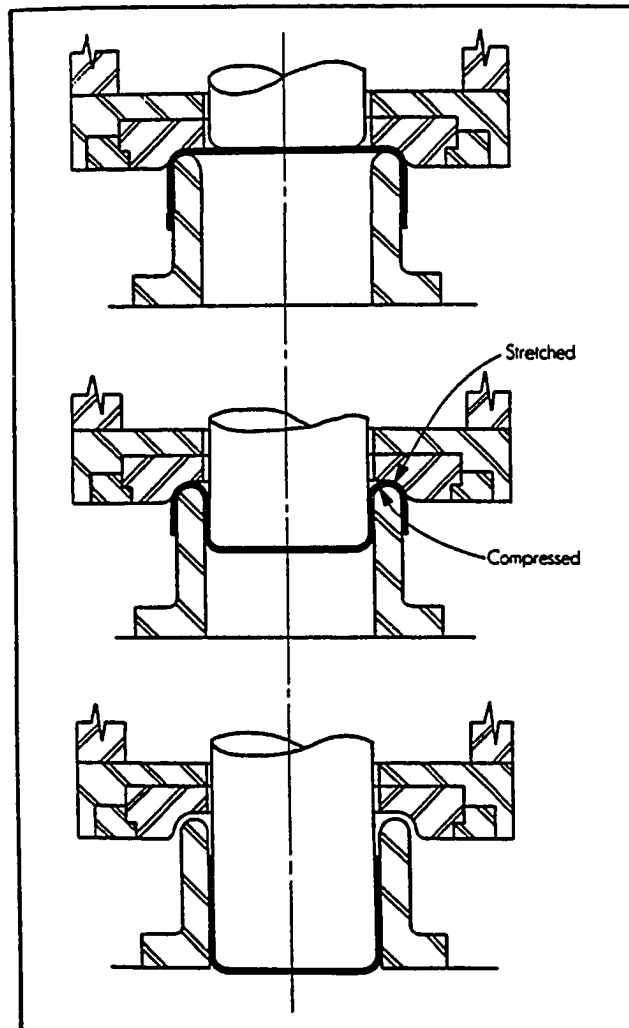
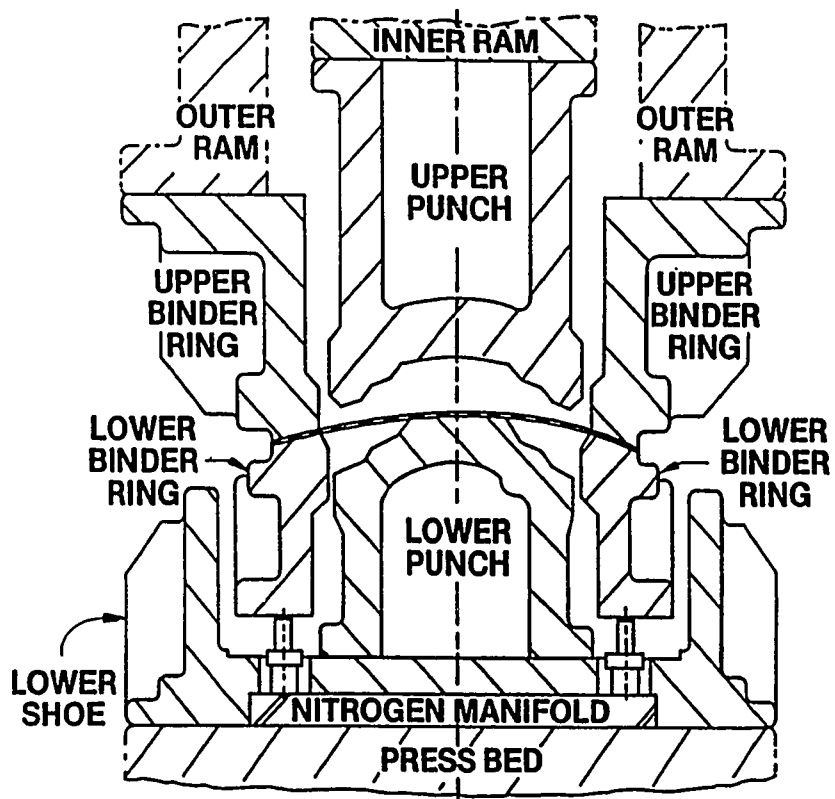


Figure 3.7: Reverse redrawing in a double action press, [TMEH, 1984].

### 3.4. Process Variables in Stamping

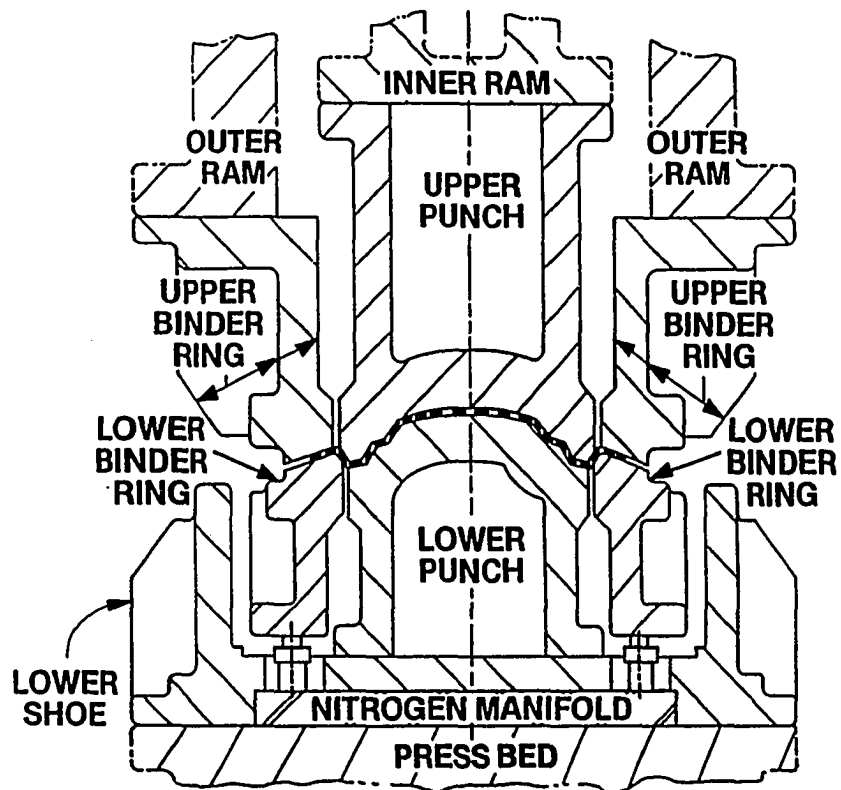
A typical stamping operation using a double action press (where the ram has two motions, one for the blank holder and the other for the punch or die) is illustrated in Figure 3.8. After the blank is placed on the lower binder ring, the upper binder ring moves towards the sheet which is then held between the upper and lower binders or blank holders, Figure 3.8a. Both the lower and upper binder rings continue to move downward and stretch the sheet over the lower punch or male die. The upper die moves downward to form the final shape of the panel, Figure 3.8b. A stamping operation which is performed in a single action press is shown in Figure 3.9. In a single action press, the upper binder ring and the upper die are attached to the ram. In the first stage, the sheet metal is clamped between the upper and lower binder rings, Figure 3.9a, then, at the second stage, both the upper and lower binder rings move downward to form the sheet around the stationary lower punch, Figure 3.9b. In both single and double action presses, metal flow can be controlled during the forming process either by varying the Blank Holder Force (BHF), the Blank Holder Pressure (BHP), or by selectively lubricating the blank.

Automotive stamping operations involve a large number of process variables, as listed in Table 3.1, [Siekirk, 1988], including the appropriate inclinations of the part geometry and the binder surfaces. The following major factors that influence metal flow have been summarized recently by Siegert in the foreword of the proceedings of a recent conference held at the Technical University of Stuttgart, [Siegert 1991]:



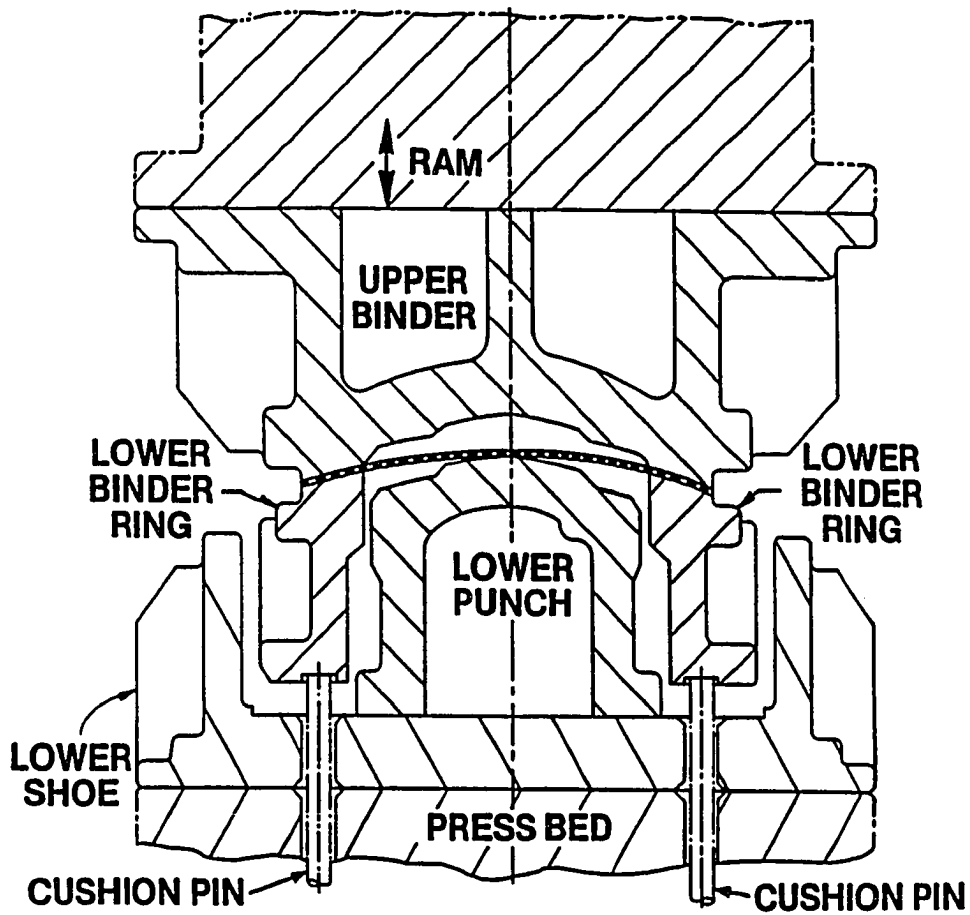
a) binder wrap position

Figure 3.8: Stretch-draw sheet forming operations, [Pool, 1990].



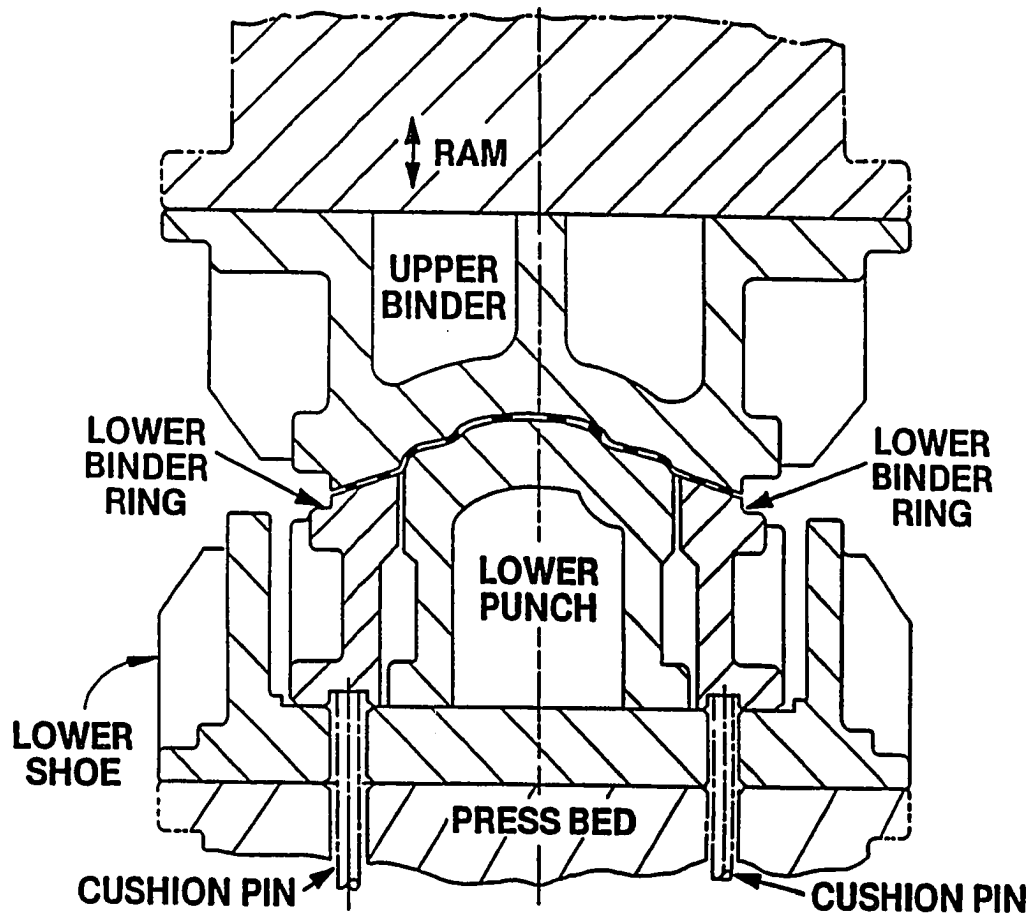
b) closed or formed position

Figure 3.8: Continued, [Pool, 1990].



a) binder wrap position

Figure 3.9: Stamping in a single action press, [Pool, 1990].



b) closed or formed position

Figure 3.9: Continued, [Pool, 1990].



**Table 3.1: List of Sheet Metal Forming Process Variables, [Siekirk, 1988].****BLANK VARIABLES**

- 1) Dimensions
- 2) Location in die
- 3) Edge condition

**LUBRICATION**

- 4) Type
- 5) Coating thickness and distribution

**PRESS VARIABLES**

- 6) Punch guidance
- 7) Punch speed (as a function of press stroke)
- 8) Binder force and its variation around the binder ring
- 9) Counter balance pressure
- 10) Rigidity

**WORK MATERIAL VARIABLES**

- 11) Thickness (normal and thickness profile)
- 12) Mechanical properties
- 13) Surface topography
- 14) Coating and surface chemistry

**DIE VARIABLES**

- 15) Guidance
- 16) Alignment; (i.e., position in press)
- 17) Surface finish
- 18) Material
- 19) Draw beads (change with wear)
- 20) Hardness
- 21) Punch radii (change with wear)
- 22) Surface coatings and surface chemistry
- 23) Profile radii (change with wear)
- 24) Rigidity

**MISCELLANEOUS VARIABLES**

- 25) Dirt in the die or on the blank
- 26) Blank pre-bend position (affect blank location)

**INTERACTIVE VARIABLES**

- 27) Work material temperature
- 28) Die temperature
- 29) Atmospheric conditions (temperature, humidity)
- 30) Shims on stop blocks (affect binder load distribution)

- Shape and size of the blank. Larger blanks require higher forming and friction forces. As a result, higher punch loads are needed for draw and stretch forming.
- Draw beads. The draw force increases with increasing number of draw beads where local friction and bending require more energy and force. In limiting cases, material flow may be fully stopped in the die flange or blank holder area by "locking" the motion of the sheet metal so that only stretching occurs. The positioning and various designs of draw beads are schematically illustrated in Figure 3.10, [Siegert, et al., 1991].
- Lubrication and Friction. The amount and selective distribution of the lubricant over the blank surface influences the value of the local friction between the sheet material and the blank holder as well as between the sheet and the dies. As a result material flow is locally influenced.

The influence of lubrication is especially significant when forming large stampings. In deep drawing the total forming force,  $F_t$ , can be considered to have two components: a) the force necessary to overcome friction,  $F_f$ , and b) the force necessary to perform plastic deformation,  $F_d$ , i.e.,  $F_t = F_f + F_d$ . Experiments conducted for producing round cups demonstrated that the friction component,  $F_f$ , of the total drawing force increases with increasing punch diameter, [Doege, 1987]. As a result, the maximum possible draw ratio (initial blank diameter / cup diameter) decreases with increasing cup size, Figure 3.11.

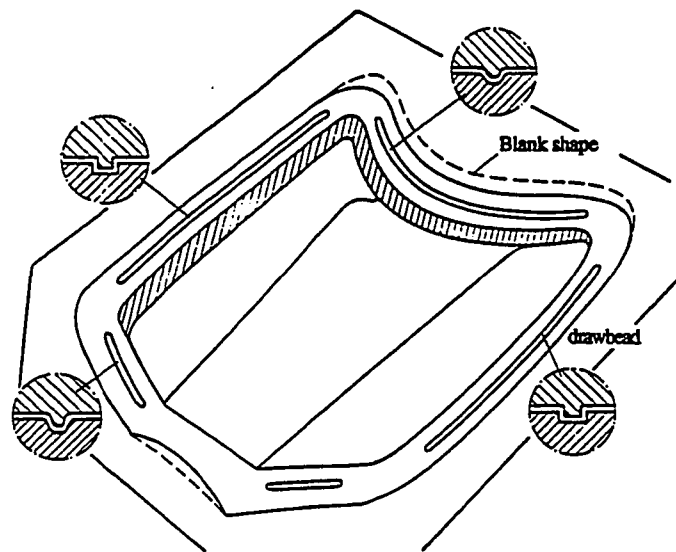


Figure 3.10: Deep drawing of large non-symmetric parts, [Siegert, et al., 1991].

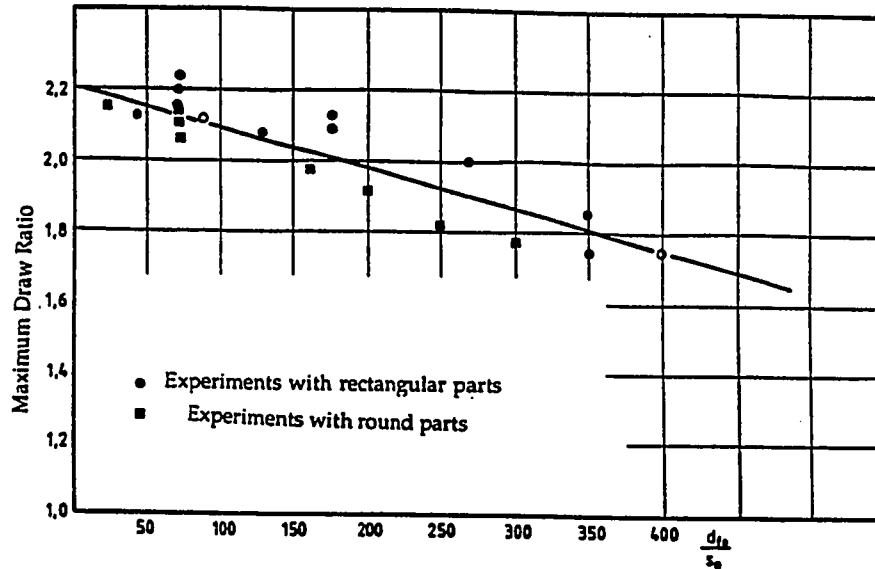


Figure 3.11: Maximum possible draw ratio versus part size, [Doege, 1987].  
 $d_{f0}$ =cup diameter (fictious calculated value for rectangular parts),  
 $s_0$ =blank thickness

- Blank holder and Punch Velocities. In single action presses, the velocity of the binder or blank holder is particularly important. A sudden impact of the upper blank holder ring upon the blank may damage the lubricant film and the surface characteristics of the sheet material. As a result, friction between the sheet and the blank holder may increase. In mechanical double action presses, the binder velocity is controlled by the press drive which is designed to reduce this sudden impact effect. The draw velocity influences mainly the friction conditions. With increasing draw velocity, the friction in the flange is reduced provided the adverse effect of the initial binder-blank contact upon the lubricant film is eliminated. As a result, drawability improves with increasing speed of the draw punch. With increasing forming speed, the strain rate also increases. However, at the cold forming conditions that are present in most stamping operations the influence of strain rate upon the flow stress of the sheet material is usually negligible and the friction effects are more important.
- Blank Holder Surface Pressure. Control of the BHF locally, i.e., around the binder ring, influences friction and local material flow. For a given die and blank geometry, sheet material and lubrication, the metal flow in stamping, i.e., stretching and/or deep drawing, is mainly controlled by the restraining force generated by the BHF and/or the draw beads. On one hand the BHF must be large enough to allow stretching and prevent wrinkling especially at the corners of a stamping, and on the other hand, the BHF must not be so large that the material is "drawn" in with excessive local thinning or tearing.

The local BHP (around the periphery of the binder ring) may be influenced by "adjusting" locally the gap between the blank holder ring and the die flange surface. At locations where this gap is small, the surface pressure and consequently the surface friction increase and material flow is retarded. At locations with a larger gap the opposite situation occurs and material flow is enhanced. In attempting to control the material flow by adjusting the blank holder gap, it is well to consider that the gap is also influenced by the elastic deflections of the tooling and the press. In addition, in large production runs some tool wear occurs. Thus, the dimensions of the draw beads and of the binder surface change, requiring continuous die maintenance and adjustment to maintain the reproducibility in production, especially if the dies are not always used in the same press, [Siegert, 1991].

It is possible to control the material flow by controlling the BHP without using the conventional "adjustment" of the blank holder-die gap. The BHP can be controlled by focusing different amounts of force to specific areas of the blank holder. Thus, the entire die-blank holder system is elastically deformed to modify and control the BHP and gap locally. This approach is practical and being used in the modern installations with large mechanical single action transfer presses. For this purpose, the first (draw) station of such presses are equipped with a hydraulic multi-point cushion system.

Many stamping operations require that the BHP be controlled both spatially around the binder ring and temporally, i.e., as a function of the ram stroke. In addition, it is necessary to consider that in a mechanical press the binder

ring touches the blank at a relatively high speed (200 to 300 mm/sec). This "impact" generates noise, results in a peak force, and may cause a breakdown of the lubricant film on the blank surface. Consequently, an ideal draw cushion system, used in the first station of a large single action transfer press, must satisfy the following requirements, [Schneider, 1987]:

- a) vibration-free control of the BHF at the start of and during the drawing process
- b) control of a constant or variable BHF during the process
- c) independent and direct control of the BHF on several (four, six or eight) locations of the die
- d) controlled upstroke of the die after drawing is completed.

### **3.5. Failure Limits**

The BHF must be sufficiently large to prevent excessive wrinkling (or buckling) but not too large to cause tearing (or splitting or fracture). Therefore, for a certain part geometry, there is a "drawability window" in which the blank holding force can be adjusted. This "drawability window" is illustrated for deep drawing in Figure 3.12. The adjustment window is between points (A) and (C). The actual size of the "drawability window" depends on many factors including the tooling geometry, the blank geometry, thickness, and blank holder type, and sheet material. The higher the draw depth and/or the thinner the material and/or lower the material quality, the more critical the severity of drawing and the narrower the "drawability

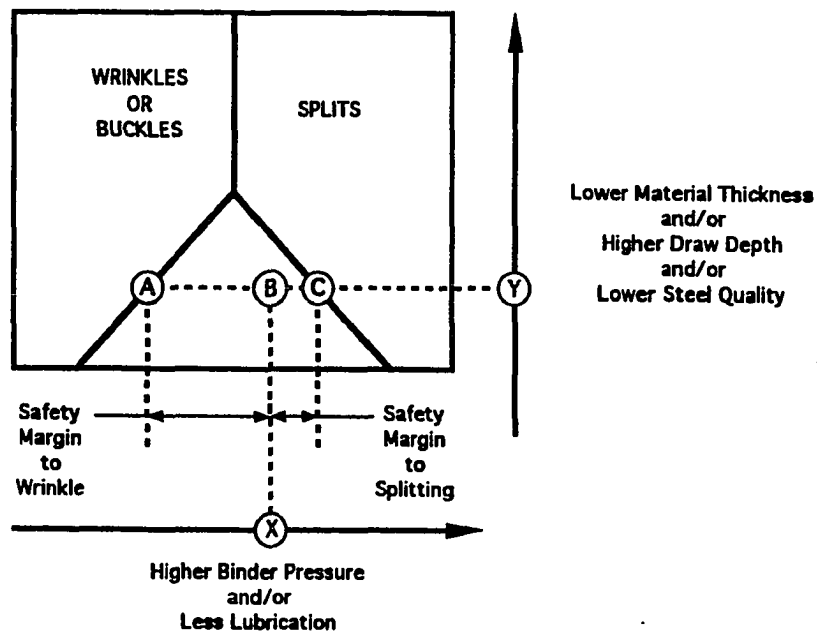


Figure 3.12: The sketch of wrinkling and formability limits and the "drawability window" in deep drawing, [Patrishkoff, 1991].

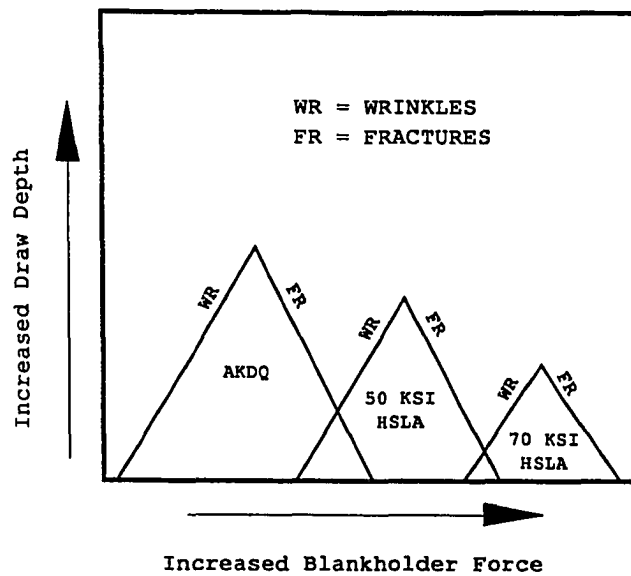


Figure 3.13: The effect of steel strength on wrinkling and fracture limits, [Patrishkoff, 1991].

window". At low blank holding forces, the cup height is limited by a tendency to wrinkling (A), while at high blank holding forces, the cup height is limited by fracture (C) at the unsupported region closer to the punch nose. For a certain draw depth (Y), the drawability window is shown between points (A) and (C) in Figure 3.12. With a blank holder pressure of (X), the blank is in the safety zone (B) for the draw depth of (Y). Safety margins at (B) are (A-B) for wrinkling and (B-C) for fracture. The effect of steel strength on the wrinkling and fracture limits is shown in Figure 3.13. The blank holder force should be adjusted for different grades of steel to produce good parts which are free of wrinkling and fracture for different grades of steel. Higher blank holder forces should be used to reduce wrinkling for higher yield strength steels, [Patrishkoff, 1991]. The effects of the blank size and the die profile radius on the wrinkling and fracture limits are shown in Figure 3.14. The safety zone represented by the triangular area between wrinkling and fracture limits moves to the right or left, as shown in Figure 3.14, depending on the blank size or die profile radius. Changes in both the blank size and the die profile radius require adjustment in the blank holder force, [Patrishkoff, 1991].

Another way of illustrating the drawability window is given in Figure 3.15, for a specific example, namely deep drawing one half of a fuel tank, [Siegert, et al., 1990].



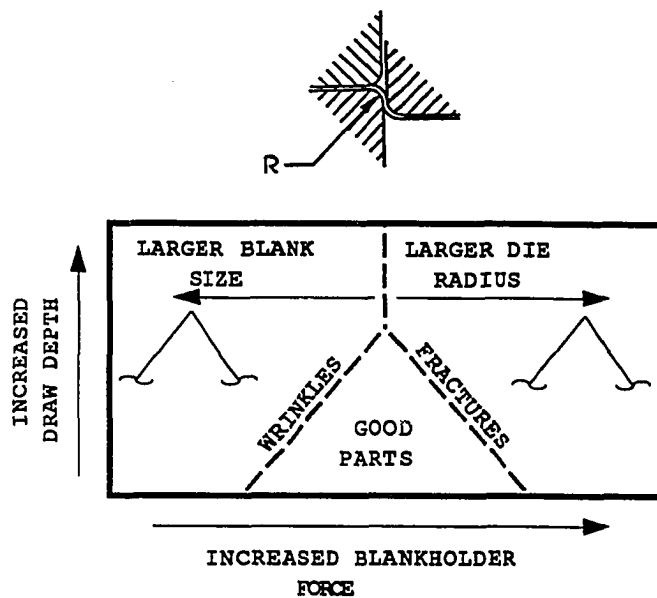


Figure 3.14: The effect of blank size and die profile radius on wrinkling and fracture limits, [Patrishkoff, 1991].

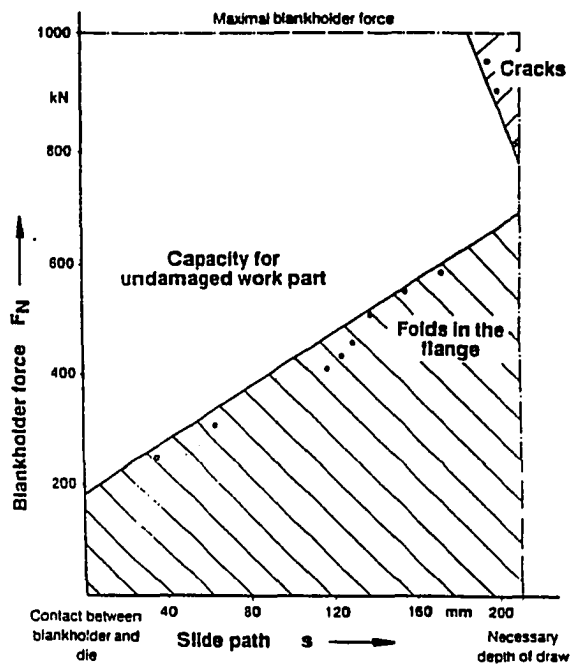


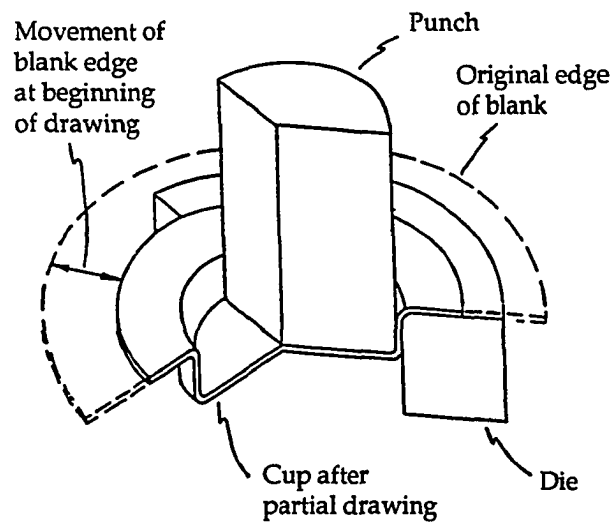
Figure 3.15: Forming limits for gasoline tank made by deep drawing process, [Siegert, et al., 1990].

## CHAPTER IV

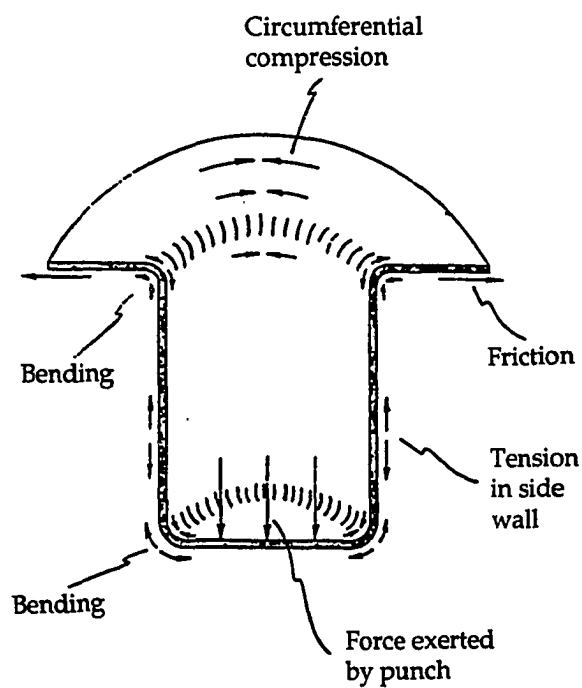
### BLANK HOLDER DESIGN and FORCE CONTROL to IMPROVE THE PART QUALITY

#### 4.1. Deep Drawing with Blank Holder

In a deep drawing operation, a flat metal blank is placed between a die cavity and a movable punch, (Figure 3.2a). As the punch moves into the die cavity, the metal blank is forced through the die and formed into the desired shape, (Figure 4.1a). Corners of the die cavity and punch are rounded to prevent cutting of sheet metal and the space provided between the punch and the die cavity allows space for the full thickness of sheet metal. During drawing, the sheet metal is subjected to undesired stress and strain distributions. As the shape of the sheet metal blank is gradually changed from a planar form to a cylindrical shape, the sheet metal under the blank holder is stressed in tension in a radial direction and stressed in compression in a circumferential direction (Figure 4.1b). Under the effect of these stresses, the metal may wrinkle in the flange area (Figure 4.3a), region A-B-C in Figure 4.2, and tear in the wall area (Figure 4.3b), region D-E in Figure 4.2.



a) cut-away view of draw die



b) forces during deep drawing

Figure 4.1: Deep drawing using a cylindrical punch, [Eary, et al., 1974].

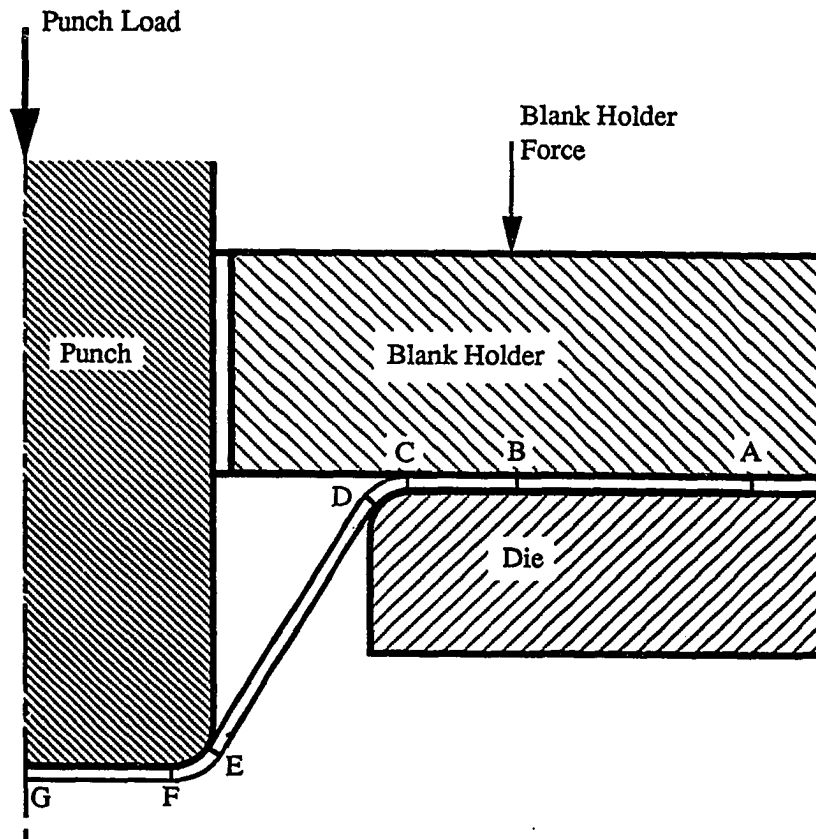
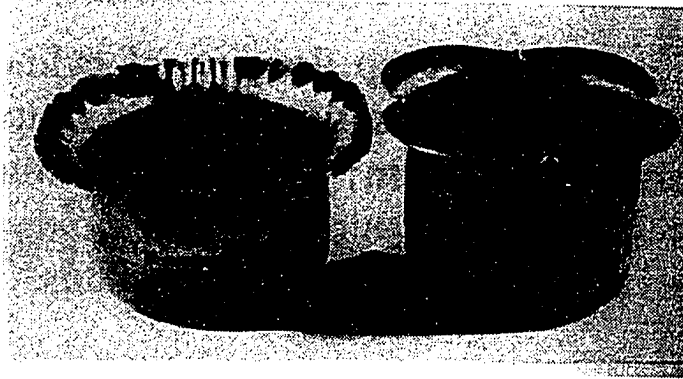
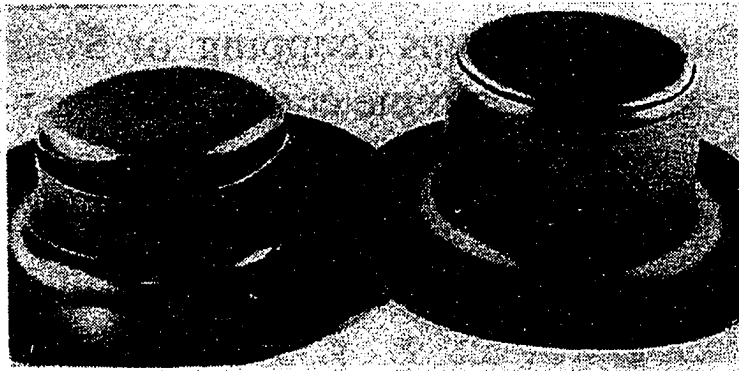


Figure 4.2: Different regions in deep drawing operation.

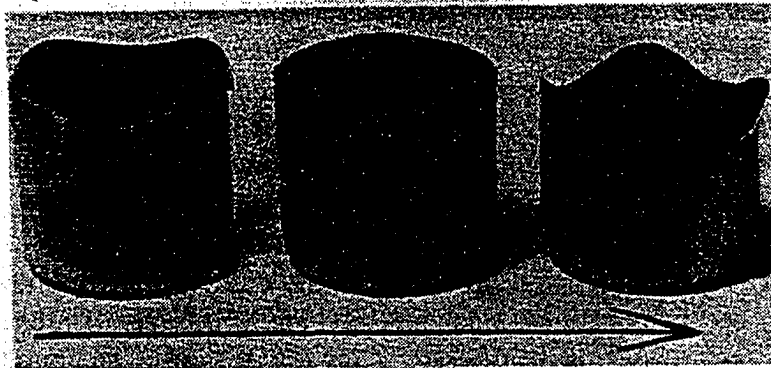
- A-B: Radial drawing of the flange between die and the blankholder with friction resistance present at the interface.
- B-C: Radial drawing of sheet not in contact with the blankholder.
- C-D: Radial drawing and bending over the die corner radius.
- D-E: Unbending and straightening to form the wall of the cup.
- E-F: Bending, sliding, and stretching over the punch profile.
- F-G: Bi-axial tensile stretching of the sheet over the bottom surface of the punch.



a) Wrinkling in a partially drawn cup due to insufficient blankholder force.



b) Tearing of the cup wall at the bottom.



c) Earing behavior of cups made from three different copper sheets.  
Arrow indicates rolling direction of the sheet.

Figure 4.3: Failure types in deep drawing of round cups, [Hosford, et al., 1983].

Another problem in the drawing operation is called earing. Earing is the result of anisotropic behavior of the sheet metal. Anisotropy is the difference in metal properties, measured along axes in different directions [Sitaraman, 1989b]. When a circular metal blank is drawn the response of the blank in the direction of rolling may be different from that at an angle to the direction of rolling. If the metal is anisotropic, the blank flange will develop thickened portions along predictable radial lines as the blank is compressed when being drawn into the die cavity. The number of thickened portions and the degree of thickening along the circumference of a drawn round cup is a function of the anisotropic properties of the metal and the severity of drawing. In addition to the non-uniformity in thickness circumferentially, the wall thickness of the cup varies from the top to bottom. The "ears" are extensions beyond the rim of the cup of the thinner portions between the thickened portions along the circumference (Figure 4.3c).

There are several ways to prevent wrinkling and reduce earing in sheet metal forming operations. One way is to do the operation in several steps. But this will increase the tooling cost. Another method is to use pressure pads or blankholders and reduce the number of steps to form the sheet metal. The use of pressure pads or blankholders around the die opening can reduce or eliminate the formation of wrinkles. If the portion of tooling around the die opening can be used to apply a clamping pressure on the blank flange to hold it flat without reducing its thickness and allowing it to move into the die opening, a sheet metal cup can be formed without any wrinkling.

In some cases, blank holders can not create enough restraining force. In these cases, drawbeads are used to provide an extra restraining on the metal flow, as seen in Figure 4.4. Drawbeads are widely used in forming of non-symmetric parts that might normally have some areas of wrinkling and some areas of excessive stretching. A drawbead is made up of a rib-like projection from one surface of the tooling, and a groove just opposite, into which the drawbead fits. The shape of the bead and of the groove may vary from semi-cylindrical to rectangular. The drawbeads are placed in areas around the blank where sheet metal is drawn in more readily. This restricts the material flow from this area while encouraging the material flow from the areas of excessive wrinkling. More than one row of drawbeads can be used if necessary. An example of drawbead placement and typical drawbead design for a non-symmetric part can be seen in the Figure 4.5, [Lange, 1985].

#### **4.2. Effects of Blank Holder Force (BHF) and Pressure (BHP)**

As discussed in the previous section, blank holders are used to control the metal flow during deformation and to prevent wrinkling. If the wrinkling is expected to be severe, then blank holders should be used throughout the forming process, i.e., a blank holder should contact the blank before the deformation starts and be removed after the forming process is completed.

In forming of large autobody panels, wrinkling is caused by non-uniform stretching in the long plane sections, [Yoshida, et al., 1979]. Drawbeads are

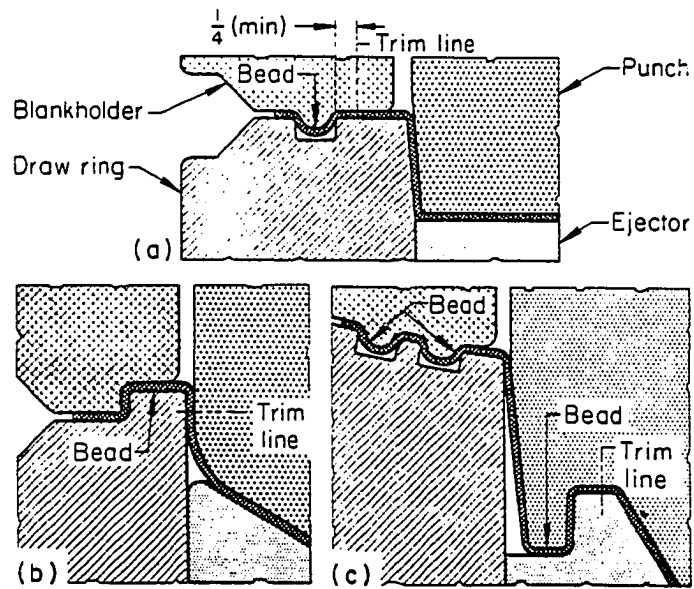


Figure 4.4: Use of drawbeads; a) conventional, b) locking, c) combined. Dimensions are given in inches, [ASM, 1988].

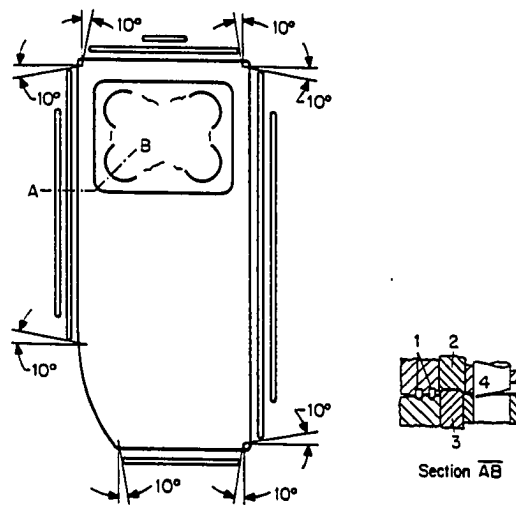


Figure 4.5: Layout of drawbeads for a car door tooling, [Lange, 1985].



usually used to control the tension in the material and the amount of draw-in during the forming process. The deformation controlled by drawbeads and several forming defects that may occur in panel forming are shown in Figure 4.6, [Furubayashi, et al., 1988]. During the deformation, sheet metal is repeatedly bent and unbent while passing through the drawbeads causing a considerable amount of reduction in thickness.

In the drawing of round cups, wrinkling occurs either in the flange of the workpiece or in the wall region as in the case of conical cups due to high compressive stresses in the circumferential direction. The severity of wrinkling in round cups can be estimated based on the ratio of sheet thickness to punch diameter, [Eary, et al., 1974]. If this ratio is greater than 0.025, the part can be drawn without using a blank holder. Also, it has been suggested that the use of a blank holder is not necessary if the radial length of the contact area between die and blank does not exceed a certain multiple of the metal thickness for a given drawing ratio, [Lange, 1985].

#### **4.2.1. Rigid Blank Holders**

The simplest blank holder is a "rigid" one. A "rigid" blank holder does not adjust to the thickness changes that occur on the sheet metal during the deformation. This is why the gap between die and the blank holder surfaces should be adjusted carefully. The rigid blank holder touches the sheet metal where the thickness is maximum and applies pressure only at these points,

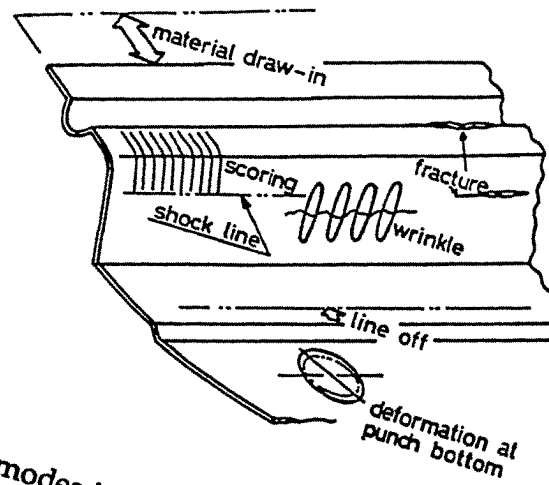


Figure 4.6: Failure modes in panel forming, [Furubayashi, et al., 1988].

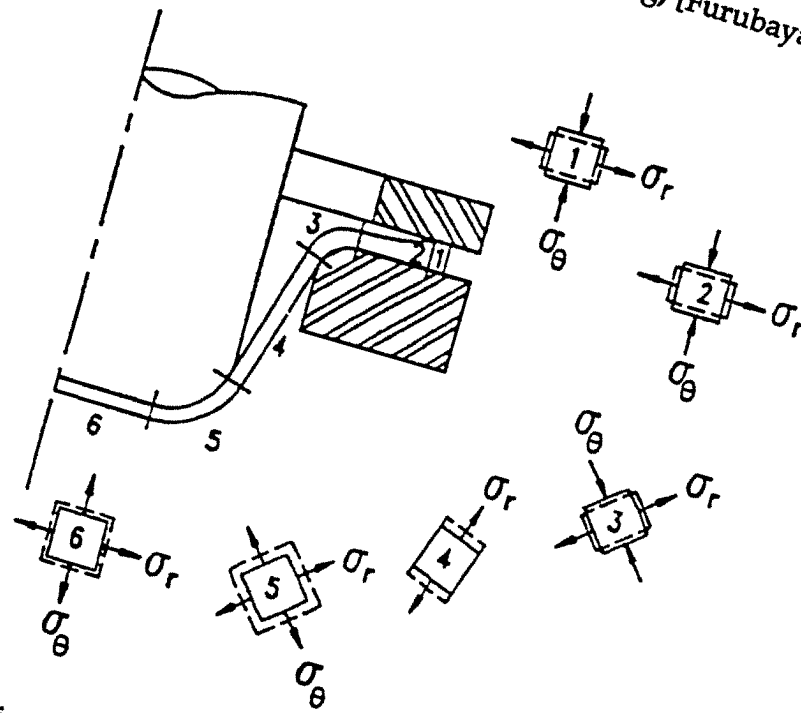


Figure 4.7: Typical sheet thickness distribution in deep drawing of round cups, [Karima, et al., 1989].

Figures 4.7 and 4.8, [Karima, et al., 1989]. Since the maximum compressive stresses in the circumferential direction occur at these locations, the blank holder pressure should be concentrated on these points. Often it is necessary to allow a certain percentage of thickening of the blank and an increase in the workpiece-blank holder contact area. To obtain a uniform pressure distribution, the locations of increased thickness in the sheet metal are determined, and the blank holder is ground at these locations to increase the clearance (or the gap) between the die and the blank holder locally.

#### **a- Thickening of blank in drawing of round cups**

Different zones which occur during the forming process of an axisymmetrical shell are shown in Figure 4.7. Zones 1 and 2 correspond to the flange which is between the die and the blank holder. The largest compressive stresses in the circumferential direction occur at the outer rim. This is why sheet metal thickens and wrinkling occurs this region. Because of the thickness variation in the flange, material is in contact with the blank holder only at Zone 1, and the largest blank holder effect is expected at this region. The actual blank holder pressure is a maximum at the outer edge and decreases to zero at the interface between Zones 1 and 2. It should be noted that the assumption of a "rigid" tool surfaces in Figure 4.7 is somewhat unrealistic. The blank holder and possibly the die elastically deform and present a complex contact surface between the tools and the blank.

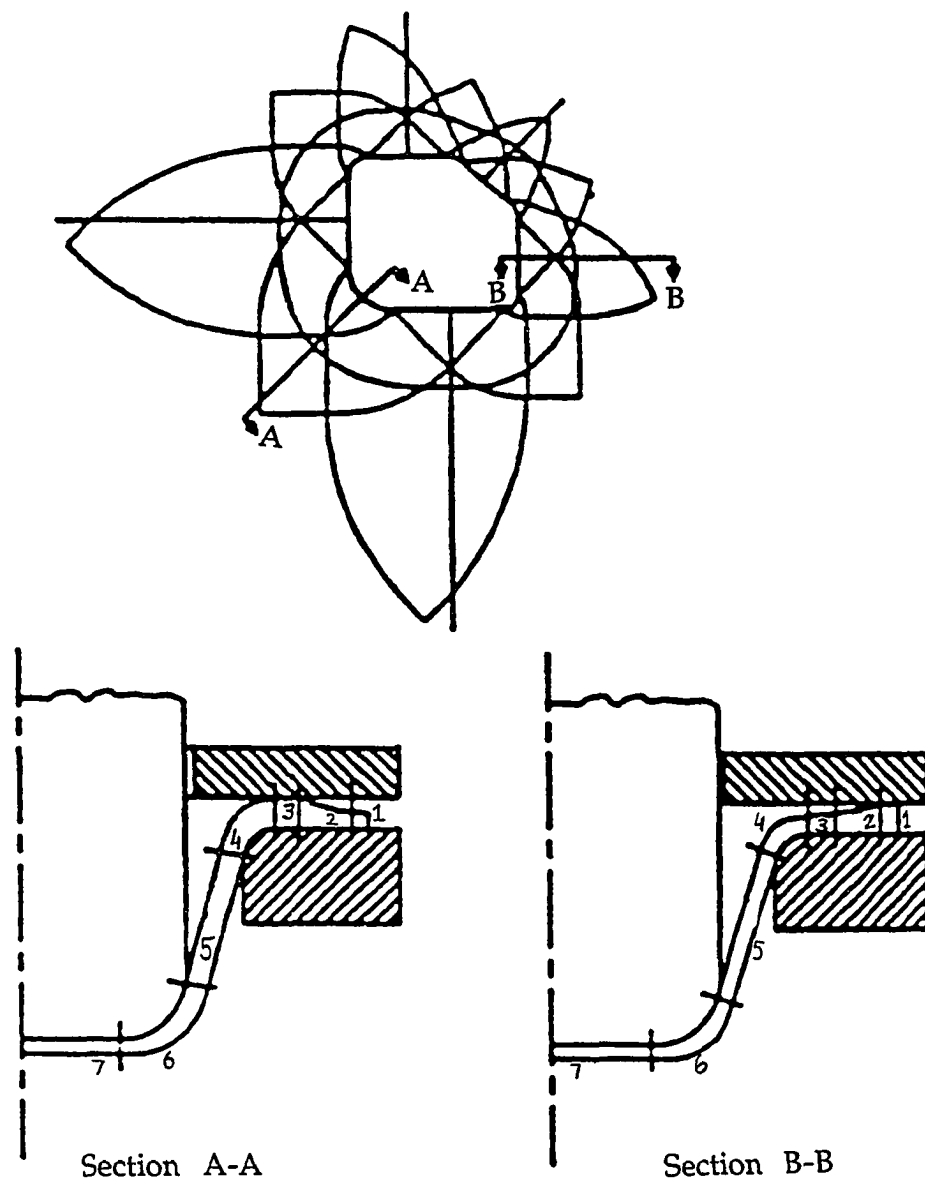


Figure 4.8: Material thickness variation in two different sections in drawing a non-axisymmetric part, [Karima, et al., 1989].

In forming an axisymmetrical cup, Figure 4.7, the maximum compressive stresses and thickening occur at Zone 1, and maximum thinning occur at Zone 5. Therefore, wrinkling may occur at Zone 1 and fracture may occur at Zone 5. The blank holding force has a direct effect on both wrinkling and fracture. Increasing the blank holding force will prevent wrinkling but also cause increased radial stresses and possible fracture in Zone 5. This is why the blank holding force should be adjusted carefully between two limits not to cause wrinkling and fracture as discussed earlier.

#### **b- Thickening of blank in drawing rectangular parts**

The different deformation zones which occur during deep drawing of a "rectangular" part are shown in Figures 4.8 and 4.9. Two different thickness distributions can be seen in different sections of a deforming shell, [Doege, et al., 1987]. These are at the corner and in the middle of the side walls. At the corner (Section A-A), there are seven zones, [Karima, et al., 1989]. Zone 1 is rigid, and maximum thickening occurs at Zone 3. In the middle of the side walls (Section B-B), there are seven zones, too. In this section, maximum thickening occurs at Zone 1, and Zone 3 is the rigid zone where there is no deformation and thickening. Maximum compressive hoop stresses occur at the areas of maximum thickening. If there are no hoop stresses, then there is no danger of wrinkling. Therefore, wrinkling is severe at the locations of maximum thickening. Thus in drawing "rectangular" parts, a blank holding pressure is required only near the inner corner radii and at the outer periphery of the straight sections.

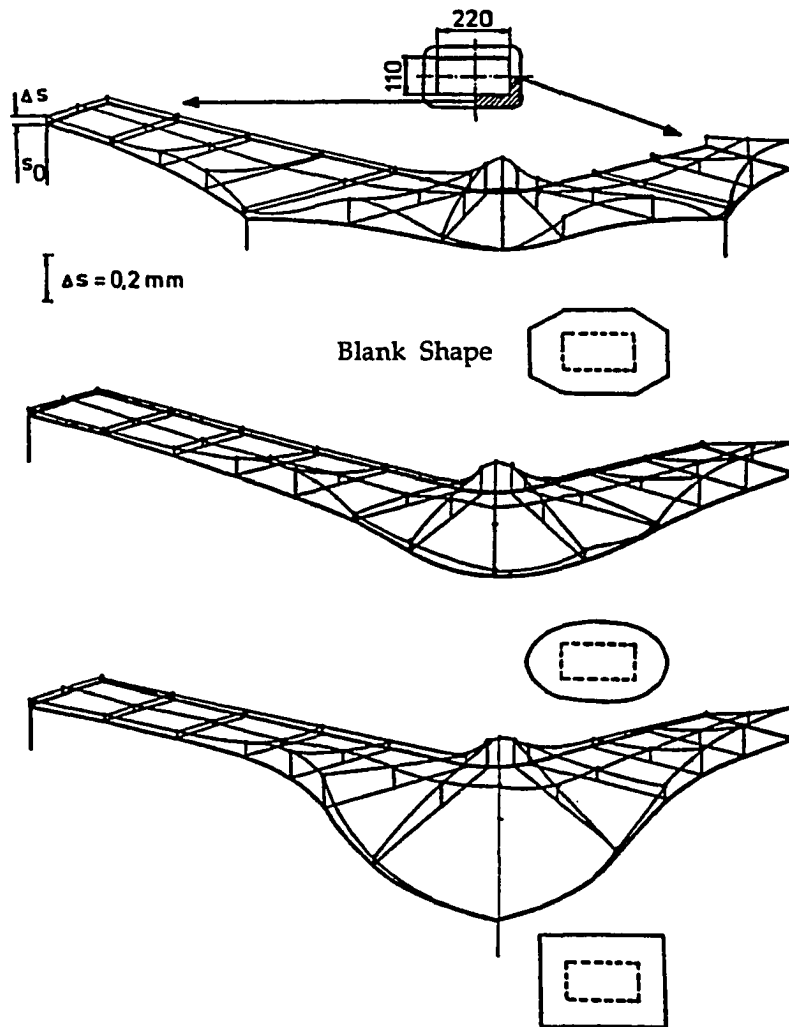


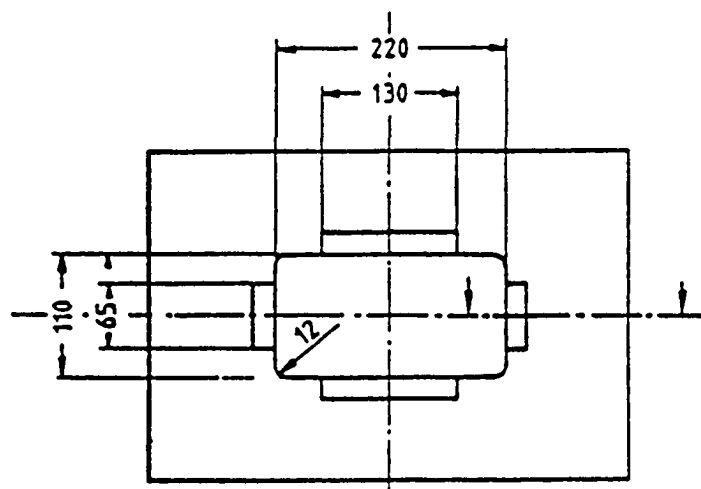
Figure 4.9: Increase in sheet thickness in deep drawing rectangular parts with different blank shape, [Doege, et al., 1987].

(Material: St 14.03, sheet thickness: 1 mm, blankholder pressure:  $2.5 \text{ N/mm}^2$ , draw ratio=1.8)

#### 4.2.2. Flexible Blank Holders

Compared to rigid blank holders, better results should be expected from flexible or "elastic" blank holders. Due to variations in the sheet metal thickness that occur during drawing, the rigid blank holder adjusts itself to the maximum sheet thickness and does not apply pressure where the sheet metal is thinner, and small wrinkles may occur at these regions. Using flexible blank holders, the contact area between the sheet metal and blank holder can be increased and the blank holder force can be applied more evenly upon the blank during the deformation. Flexible blank holders can completely suppress the wrinkles and improve the appearance of the sheet metal surface. A flexible blank holder design was suggested by researchers in Hannover, Figure 4.10. In this design, an elastomer consisting of a polyurethane sheet was used. The elastomer was prestressed several times with a high load before it was used. Pressure bars were arranged within the straight sides of the blank holder to achieve a higher local surface pressure in these zones, [Doege, et al., 1987].

Despite its simplicity and apparent advantages, the "flexible" blank holder designs, such as that seen in Figure 4.10, have not been widely used.



Arrangement of pressure bars

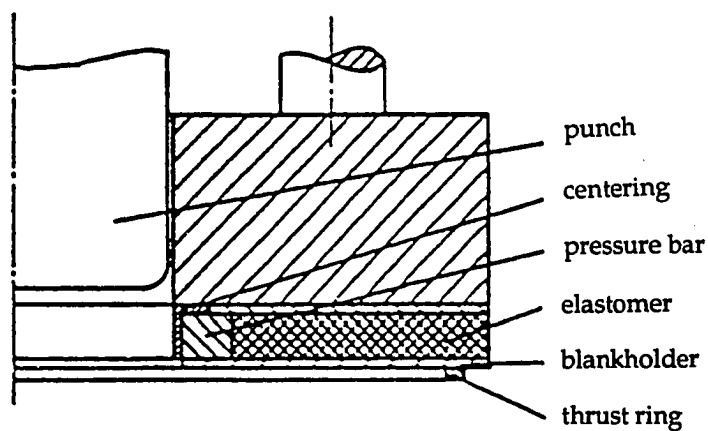


Figure 4.10: Flexible blankholder for deep drawing rectangular parts, [Doege, 1987].



### 4.2.3. Estimation of Blank Holder Pressure

It is useful to estimate the blank holder pressure necessary to prevent wrinkling and tearing in order to select the appropriate press for a given operation, [Doege, 1987].

In a recent study conducted by Sommer, [Sommer, 1986], the blank holder pressure is given as

$$p_{NA} = km \left( \frac{A_0}{A_{st}} - 1 \right) \sigma_m \quad (4.1)$$

- where
- $p_{NA}$  : blank holder pressure at start
  - $A_0$  : plan area of the sheet blank
  - $A_{st}$  : plan area of the punch
  - $k = \frac{1 + (r_{max} - r_{min})}{r_m n_m} 0.49 \times 10^{-3}$  , material factor
  - $r_{max}$ : maximum r-value in blank plane
  - $r_{min}$ : minimum r-value in blank plane
  - $r_m$  : average perpendicular anisotropy,  $r_m = (r_0 + 2r_{45} + r_{90}) / 4$
  - $n_m$ : average strain hardening exponent,  $n_m = (n_0 + 2n_{45} + n_{90}) / 4$
  - $m = 1 + \left( \frac{d_{f_0}}{t_0} - 175 \right) \frac{0.17}{100}$  , shape factor
  - $d_{f_0}$  : fictious equivalent punch diameter (calculated for a rectangular punch)
  - $t_0$  : original sheet thickness
  - $\sigma_m$  : tensile strength

$A_0/A_{st}$  corresponds to the draw ratio,  $\beta$  which is equal to the blank diameter/punch diameter in drawing of round cups. As expected from Equation 4.1, the initial BHF increases linearly with increasing draw ratio. Similarly, experimental studies also show that the BHF increases with increasing tensile strength,  $\sigma_m$ , as well as with increasing relative part size, i.e.,  $d_{f0}/t_0$ .

If drawbeads are used to restrain metal flow, the restraining force that is necessary to form the material around the bead and the normal force that is necessary to keep the drawbead closed through out the forming process must be estimated. Current calculation methods usually do not distinguish between these two forces and, thus, result in higher static load in the nitrogen cylinders used to keep the beads closed. As a result, coupled with dynamic loads caused by the impact of upper and lower blank holder, the total BHF can exceed the capacity of the blank holder slide and damage the tooling. One solution to this problem is to separate the forming forces and the normal forces in the calculations and lower the static nitrogen cylinder force. This will reduce the dynamic forces due to impact. Herderich reported an experimental procedure to determine empirical equations in order to calculate the restraining force and the normal force as a function of bead geometry, sheet thickness, and material properties, [Herderich, 1990].

### 4.3. Control of Blank Holder Force (BHF)

There are three methods of controlling the blank holder force in a deep drawing process, [Karima, et al., 1989]. These are;

1) Pressure control which is the case in the hydraulic presses or hydraulic cushions where the blank holder force is preset before the experiments. The blank holding action can be obtained by means of an outer slide in double action presses or by using a die cushion in single action presses. In either case, the blank holding force can be adjusted by controlling the pressure on the outer slide or cushion. In modern presses, it is possible to program these pressures before the drawing starts. Pressure is usually varied either linearly or stepwise as a function of time or slide position.

2) Initial force control which is the case with spring and rubber actuated blank holders in single action mechanical presses. In this case, the blank holder force increases with drawing, and is given by

$$F_b = F_{b0} + K_{bh}[(t - t_0) + \text{ram travel}] \quad (4.2)$$

where  $F_{b0}$  : initial blank holder force

$t$  : current sheet thickness

$t_0$  : initial sheet thickness

$K_{bh}$  : blank holder stiffness constant

3) Initial gap set-up which is typical in double action presses. In this case, depending on the relative stiffness of blank holder and press, the resulting blank holder force could increase or decrease during drawing. In

this case the blank holder force is calculated by solving the following set of equations.

$$F_{\text{press}} = F_b + F_d \quad (4.3)$$

$$F_b = K_{\text{bh}} \cdot h \cdot \left( 1 + \frac{t - t_0}{h} - \frac{d}{h} \right) \quad (4.4)$$

where  $F_d$  : drawing force  
 $h$  : ram travel  
 $d$  : deflection of the press under loading

#### 4.3.1. Use of Fracture Limit for BHF Control

A method for active BHF control was suggested by Manabe, et al., 1987. This method monitors the punch load as a measure of maximum stresses that occur in the sheet metal during the deformation, and reduces the BHF to prevent fracture while applying enough BHF to prevent wrinkling. This is why it is called the "fracture limit variable blank holding force method" and is based on the idea that both the stress state in the sheet metal and the punch load are affected by the BHF. An increase in the BHF will prevent wrinkling but since it will also increase the tensile stresses in the workpiece, too much increase in the BHF may cause tearing. This is why there should be an upper limit to the BHF. Tangential forces which causes tensile stresses in the cup wall close to the punch nose are directly proportional to the punch load. The proportionality constant can be determined from the cup wall angle. By

controlling the punch load, it is possible to control the tangential forces and tensile stresses in the cup. Manabe suggests that if the punch load is less than the fracture load of the metal, so are the tensile forces in the cup wall. The main objective is to control the blank holding force so that the punch force will stay constant at a value slightly less than the load necessary to fracture the sheet metal, Figure 4.11. To achieve this objective, the BHF is varied during the process. In Figure 4.11, the punch load and BHF distributions are plotted against the current drawing ratio, i.e. the ratio of the current flange outer diameter to the die opening diameter. The current drawing ratio is a maximum in the beginning and decreases during the forming operation.

Other methods can be used to control the blank holding force based on the wrinkling limit rather than the fracture limit in the BHF calculation. According to this method, the BHF can be set to the minimum value that will keep the wrinkling height constant and suppress the growth of wrinkling.

#### **4.3.2. Use of Punch Force for BHF Control**

Hardt, et al, presented two methods for controlling the blank holding force, [Hardt, et al., 1990]. These methods are based on determining the optimum punch force distribution or normalized average thickness distribution. In these methods, a real-time control loop and adaptive control of the BHF are used. Experiments using conical dies were performed and the tangential force,  $F_t$ , illustrated in Figure 4.12, was measured in each experiment. The tangential force distributions corresponding to different constant BHF's were

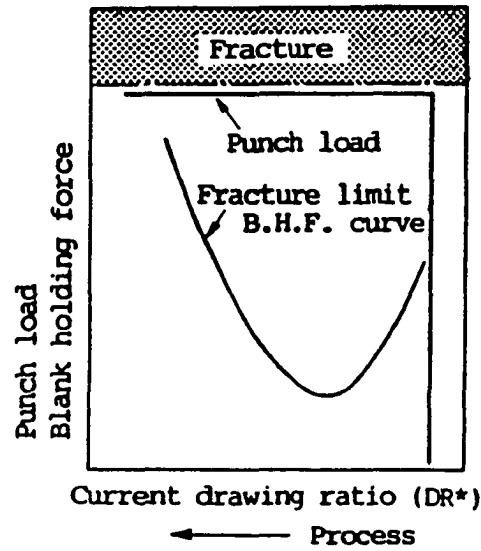


Figure 4.11: Illustration of "fracture limit" variable blankholding force method, [Manabe, et al., 1987].

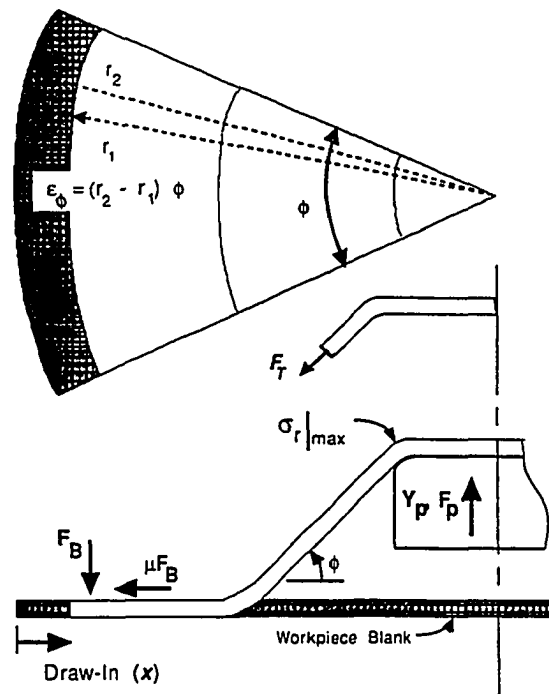


Figure 4.12: Conical cup geometry and the orientation of tangential force,  $F_t$ , [Hardt, et al., 1990].

determined for a given part geometry. Results of these experiments for five different blank holding forces are shown in Figure 4.13. The tangential force distribution, corresponding to the blank holding force which allows the maximum punch travel without fracture or wrinkling, is selected as the optimum and later used in the control system as a target trajectory. Starting from any constant blank holding force, the control system measures the tangential force and modifies the blank holding force to obtain the target tangential force trajectory, Figure 4.14. Once the target is reached, the blank holding force stays constant until the end of the deformation. Although this method may improve the quality of drawn sheet metal cups, it requires preliminary experiments to determine the target for the control system. It is also different than the other blank holding control methods in that it is based on the idea of determining the optimum constant blank holding force during the preliminary experiments. Subsequently, this constant blank holding force is maintained during the forming process by using a control system.

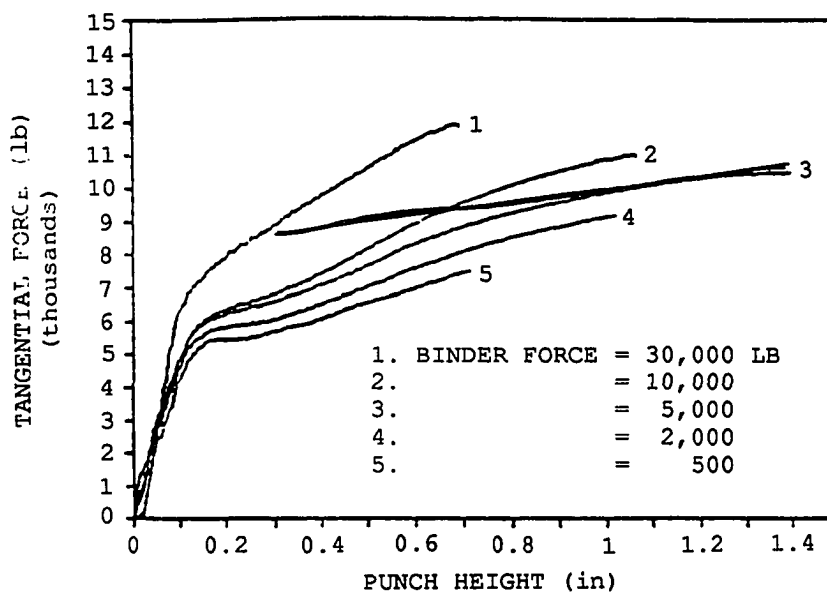


Figure 4.13: Tangential force distribution for deep drawing a conical cup using different blankholding force, [Hardt, et al., 1990].

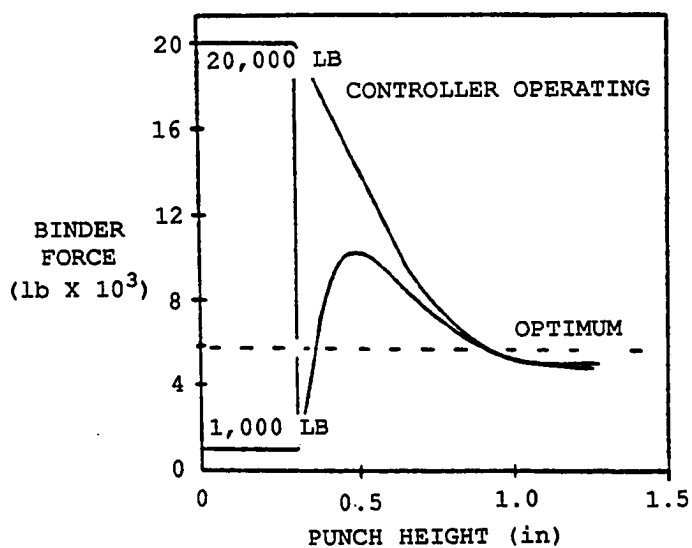


Figure 4.14: Variation of binder force as a result of closed loop control, [Hardt, et al., 1990].



## CHAPTER V

### SIMULATION OF AXISYMMETRIC AND PLANE-STRAIN SHEET METAL FORMING PROCESSES

Based on earlier work, conducted at the ERC for net shape manufacturing, [Sitaraman, 1989a], an interactive computer aided design system, SHEET\_FORM, was developed to analyze axisymmetric and plane-strain deep drawing and stretch forming processes. A detailed description of the analysis module is given in Appendix C. The input to the system includes important process and material variables such as blank diameter, sheet thickness, punch diameter, die opening diameter, die and punch profile radius, blankholder force, sheet metal-tool interface friction, anisotropy value, and strain hardening exponent. The output from the system includes the punch load-displacement variations, and the distribution of radial, circumferential, and thickness stress-strain values along the length of the cup at any stroke of the punch. A constant blankholding force as well as a variable blankholding force as a function of punch displacement can be simulated during the analysis process. SHEET\_FORM is implemented in FORTRAN and runs on both VAX/VMS and PC/DOS operating system and uses PLTPAK, developed at The Ohio State University, for graphics.

### 5.1. Theory of Plasticity

Hill's [Hill, 1948; Hill, 1950] theory (commonly known as Hill's 'old' theory) of anisotropic plasticity, based on modifications to von Mises quadratic yield function and its associated flow rule, is probably the most widely used theory today, [Wagoner, 1980]. Assuming isotropy in the plane of the sheet, the theory requires only one anisotropy parameter, the average anisotropy factor  $R$ . Isotropic hardening is assumed indicating that all plastic properties are considered uniform and homogeneous in the material, and the effect of hydrostatic stress is not included. However, this 'old' theory has been able to predict the plastic behavior of most of the materials with reasonable success except for materials such as rimmed steel, zinc, copper, and 70/30 brass sheet which have an average anisotropy factor less than 1. A newer version of Hill's theory [Hill, 1979] involves two anisotropy parameters,  $R$  and  $M$ , and has been increasingly used today.

Based on Hill's 'old' theory (Appendix A) it can be shown that

$$\begin{aligned}\sigma_2 - \sigma_1 &= \frac{(1+R)\bar{\sigma}}{(1+2R)d\bar{\epsilon}} [2d\epsilon_2 + d\epsilon_3] \\ \sigma_3 - \sigma_1 &= \frac{(1+R)\bar{\sigma}}{(1+2R)d\bar{\epsilon}} [d\epsilon_2 + (1+R)d\epsilon_3] \\ d\bar{\epsilon}^2 &= \left( \frac{1+R}{1+2R} \right) [2d\epsilon_2^2 + (1+R)d\epsilon_3^2 + 2d\epsilon_2 d\epsilon_3]\end{aligned}\tag{5.1}$$

where  $\sigma_1$ ,  $\sigma_2$ , and  $\sigma_3$  are principal Cauchy stresses, and  $d\epsilon_1$ ,  $d\epsilon_2$ , and  $d\epsilon_3$  are principal strain increments.  $d\bar{\epsilon}$  is the equivalent strain increment, and  $R$  is the average anisotropy factor. The elastic part of strain increment is neglected

in these equations, and therefore, the total strain increment is equal to the plastic strain increment.

In axisymmetric deformation,  $\sigma_1 = \sigma_r$ ,  $\sigma_2 = \sigma_\theta$ , and  $\sigma_3 = \sigma_t$  are principal radial, circumferential, and thickness stresses respectively.  $d\varepsilon_1 = d\varepsilon_r$ ,  $d\varepsilon_2 = d\varepsilon_\theta$ , and  $d\varepsilon_3 = d\varepsilon_t$  are principal radial, circumferential, and thickness strain increments respectively. In axisymmetric deformations, thickness and circumferential strains at a node can be defined as

$$d\varepsilon_t = \ln\left(\frac{t}{t_0}\right) \quad d\varepsilon_\theta = \ln\left(\frac{r}{r_0}\right) \quad (5.2)$$

where  $t$  is the current sheet thickness  
 $t_0$  is the initial thickness of blank  
 $r$  is the current radius of a point  
 $r_0$  is the original radius of a point

Volume constancy is satisfied by

$$\varepsilon_r + \varepsilon_\theta + \varepsilon_t = 0 \quad (5.3)$$

Based on Equation 5.3, the radial strain can be found as

$$\varepsilon_r = -(\varepsilon_\theta + \varepsilon_t) \quad (5.4)$$

In plane-strain deformations, it is assumed that there is no deformation in the circumferential direction, i.e.,  $d\varepsilon_\theta = 0$ .

In this case, Equations 5.1 and 5.4 becomes

$$\begin{aligned}\sigma_2 - \sigma_1 &= \frac{(1+R)\bar{\sigma}}{(1+2R)d\bar{\epsilon}} [d\epsilon_3] \\ \sigma_3 - \sigma_1 &= \frac{(1+R)\bar{\sigma}}{(1+2R)d\bar{\epsilon}} [(1+R)d\epsilon_3] \\ d\bar{\epsilon}^2 &= \left( \frac{1+R}{1+2R} \right) [(1+R)d\epsilon_3^2]\end{aligned}\tag{5.5}$$

$$\epsilon_r = -\epsilon_t\tag{5.6}$$

## 5.2. Equilibrium Equations Based on General Tool Profiles

The equilibrium equation for a general, axisymmetric punch profile shown in Figure 5.1 can be written as (Appendix B)

$$\frac{1}{r'}(\sigma_r t) \frac{dr'}{d\alpha} + \frac{d}{d\alpha}(\sigma_r t) = \frac{\sigma_\theta \rho'_1 t}{r'} (\cos\alpha + \mu \sin\alpha) + \sigma_r \mu t\tag{5.3}$$

where  $\mu$  : friction coefficient

$t$  : thickness of the material

$$\rho'_1 = \rho_1 + \frac{t}{2}$$

$$r' = r + \frac{t}{2} \sin\alpha$$

and also the punch pressure  $p$  can be evaluated using the expression

$$p = \frac{t}{\rho_1 r} [\sigma_1 r + \sigma_2 \rho_1 \sin\alpha]\tag{5.4}$$



For the general plane-strain punch profile shown in Figure 5.2, the equilibrium equation can be written as (Appendix B)

$$\frac{d(\sigma_1 t)}{d\theta} = \mu(\sigma_1 t) \quad (5.5)$$

where  $\mu$  : friction coefficient

$\theta$  : contact angle at the punch nose

and the punch pressure can be evaluated from the expression

$$P = \frac{\sigma_1 t}{\rho} \quad (5.6)$$

There are six regions which needs to be considered separately in the analysis of a deep drawing operation. These regions are shown in Figure 5.3. Deformation modes in each of these regions are explained in Appendix C (Section C.1). Equilibrium and geometric equations are different in each of these regions. These equations for axisymmetric geometries can be found in Sitaraman, 1989b. For plane-strain deep drawing operations, the equilibrium and volume constancy equations are summarized in Appendix D.

In direct and reverse redrawing, there are two more regions to be included in the analysis (Figures 5.4 and 5.5). Deformation modes in each of these regions are explained in Appendix C (Sections C.2 and C.3). Equilibrium and volume constancy equations for these regions are given in Appendix E.



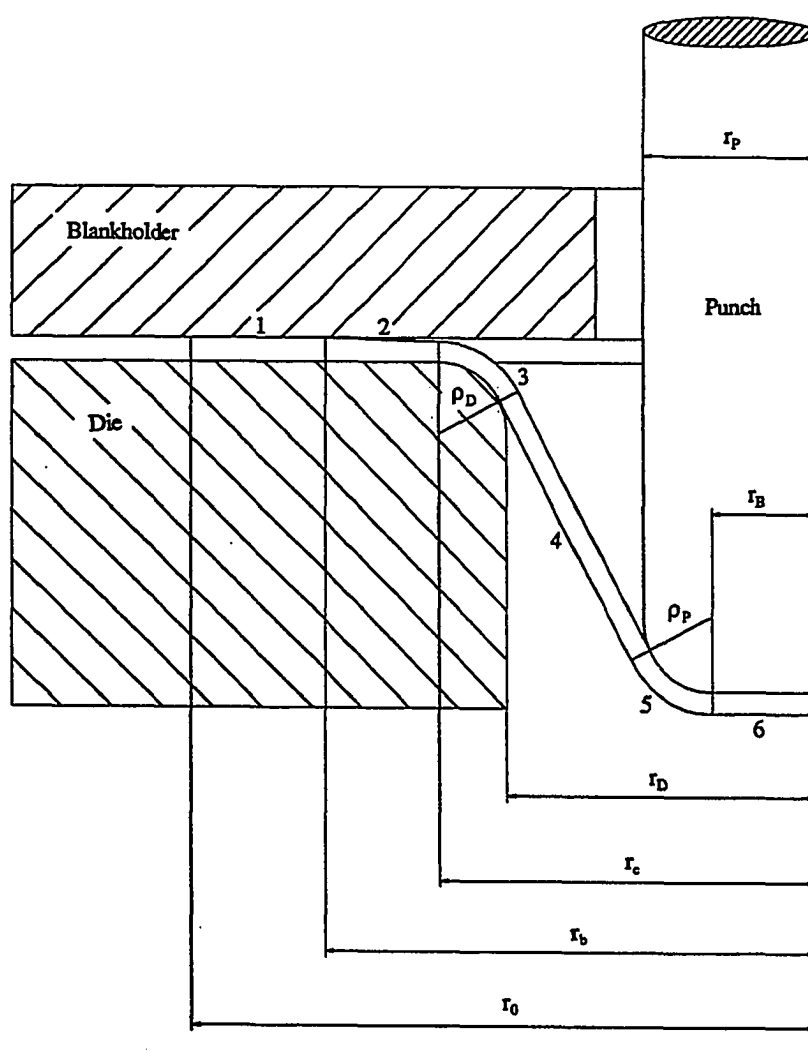


Figure 5.3: General geometry and different zones in a deep drawing operation.



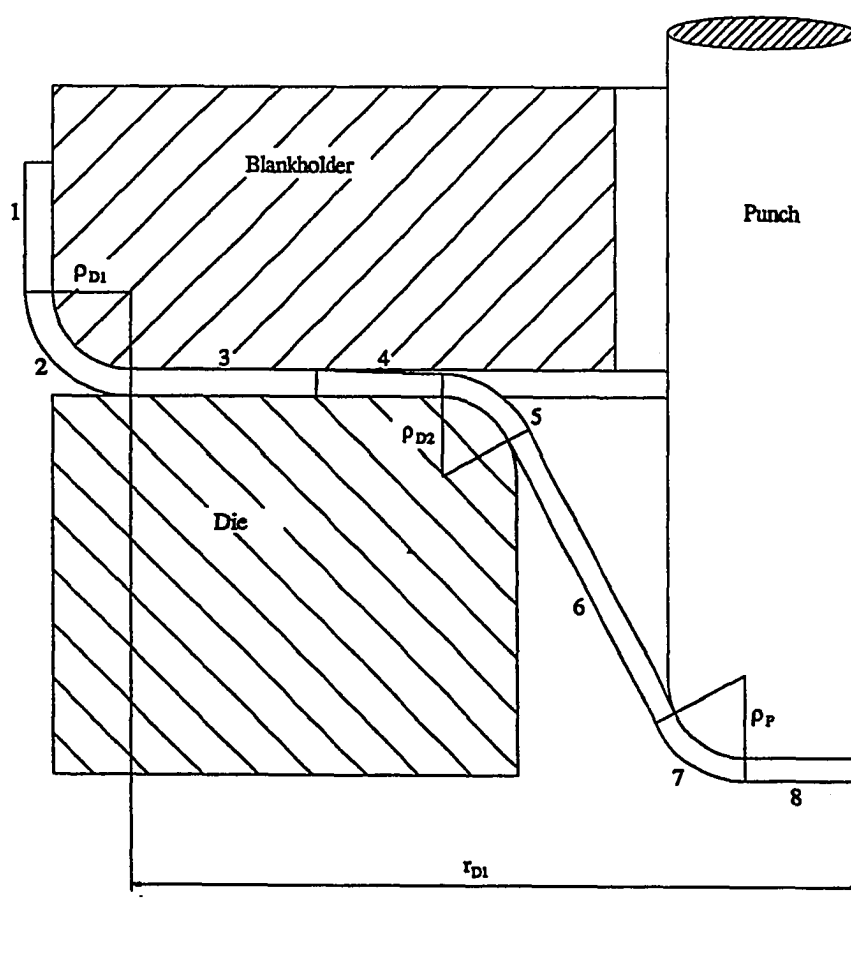


Figure 5.4: Different zones in a direct redrawing operation.



### 5.3. Rigid Plasticity

SHEET\_FORM assumes the material to be rigid plastic neglecting elastic strain component. This assumption is valid in most of the metal forming operations where the elastic strain component is significantly small and thus negligible compared to the plastic strain component. This approach has been successfully employed by investigators such as Kobayashi and Kim [Kobayashi, 1978] and Wang [Wang, 1982a and b]. The alternative approaches such as elastic-plastic and elastoplastic are CPU time expensive and have been pursued by researchers to solve the unloading problem with a rigid plastic material, to determine residual stresses, and to estimate springback.

### 5.4. Material Behavior

The material is assumed to obey the Swift's power law hardening equation.

$$\bar{\sigma} = K(\bar{\epsilon} + \epsilon_0)^n \quad (5.7)$$

where  $\bar{\epsilon}$  is the total equivalent strain  
 $\epsilon_0$  is the initial strain  
 $K$  is strain-hardening coefficient  
 $n$  is strain-hardening exponent.

$\bar{\epsilon}$  can be computed by summing the equivalent strain increments as

$$\bar{\epsilon} = \int d\bar{\epsilon} = \sum d\bar{\epsilon}_i \quad (5.8)$$

### 5.5. Friction

The tools (the punch and the dies) are assumed to be rigid when compared to the workpiece undergoing deformation. The interface friction between the workpiece and the tools is modeled using modified Coulomb friction theory. In the modified Coulomb friction theory, the friction coefficient,  $\mu$ , is expressed as a function of relative movement of the workpiece node with respect to the tool, and the tangential friction force,  $F_t$ , can be estimated from the normal force,  $F_n$ , as

$$F_t = \mu f(\Delta u_t) F_n \quad (5.9)$$

where  $0 \leq f(\Delta u_t) \leq 1$

### 5.6. Contact Boundary

The contact boundary, the node at which the workpiece leaves the punch or die surface, can be determined by looking at the sign of the normal force  $F_n$ . Typically, the normal force is non-negative or acting out of the tool surface. When normal force is negative or the direction of the normal force is toward the tool surface, the workpiece nodes for which  $F_n < 0$  are released from the tool surface and treated as free or unsupported nodes.

In the analysis of plane-strain geometries, a second condition based on the geometry and relative positions of punch and die is used to determine the

separation point from the punch and die surfaces. For a given punch travel, the node at which the workpiece leaves the punch or die surface can be determined by solving the following equation for separation angle,  $\phi$ , of the sheet from the punch

$$\rho_p + \rho_d + t_N = x \sin \phi + (\rho_p + \rho_d + t_N - z) \cos \phi \quad (5.10)$$

where  $\rho_p$ : punch corner radius  
 $\rho_d$ : die corner radius  
 $t_N$ : sheet thickness at the pole  
 $x$ : horizontal distance between the punch and the die centers of curvatures (Figure 5.6).

### 5.7. Bending Correction

When the sheet is drawn or stretched over a curved surface, there is additional tensile (compressive) straining on the convex (concave) surface. The current analysis estimates stresses and strains along the mid-surface of the sheet, and therefore, is not capable of predicting local perturbation in the strain distribution at the locations of curvatures. According to bending theory, the increment in true strain on the outer and inner surfaces of the sheet over the midplane of the sheet can be determined using

$$\Delta \epsilon = \ln \left( 1 \pm \frac{t}{2\rho} \right) \quad (5.11)$$

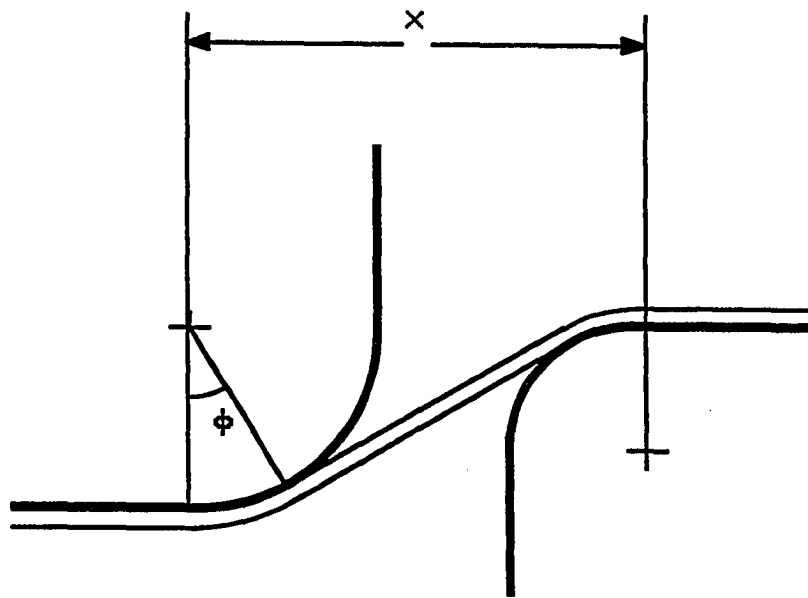


Figure 5.6: Clearance between punch and die.

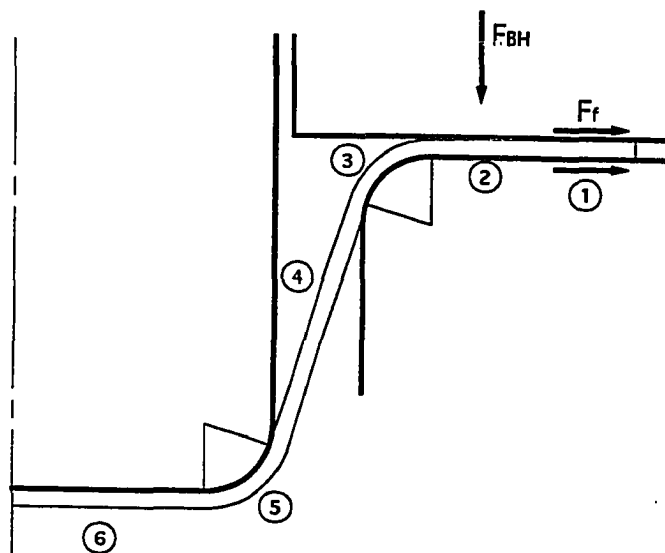
where  $\rho$  is the local radius of curvature  
 $t$  is sheet thickness  
 $+$  is for the outer surface of the sheet and,  
 $-$  is for the inner surface of the sheet

### 5.8. Drawbead and Blank Holder Force Models

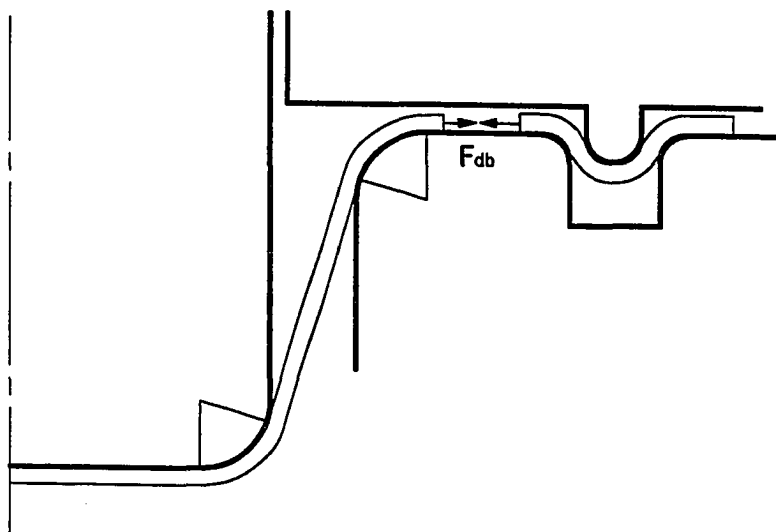
In a deep drawing operation, restraining forces are applied to the sheet metal by means of either a blank holder or a drawbead. Both methods can be simulated in SHEET\_FORM.

Deep drawing of a round cup using a rigid blank holder is shown in Figure 5.7a. Due to the axisymmetric nature of deformation, thickening occurs in the outer edge of the flange in Zone 1 in Figure 5.7a. Sheet metal is in contact with the blank holder only at this region. Friction occurs at sheet/blankholder and sheet/die interfaces, and the blank holder force,  $F_{bh}$ , which is in normal direction to the sheet plane, is converted to in-plane frictional restraining force,  $F_f$ .

Deep drawing of a round cup using a drawbead is shown in Figure 5.7b. Sheet metal is bent around a bead to create the restraining force. The drawbead force,  $F_{db}$ , is modeled as a traction force at the sheet boundary. There is no blankholder contact zone such as Zone 1 in Figure 5.7a.



a) Blankholder force.



b) Drawbead force.

Figure 5.7: Restraining forces in deep drawing.



Similar zones exist in deep drawing of plane-strain sections. There is no thickening at the outer edge of the flange, Zone 1, as in the case of deep drawing of a round cup. However, in Zone 1, the sheet metal blank is under the compression of the blankholder force, and thinning occurs in this region.

In modern stamping presses, the blank holder force can be varied during the forming process in order to prevent fracture and wrinkling and improve the drawability, [Ahmetoglu, et al., 1992a]. In SHEET\_FORM, the blank holding force can be varied stepwise, linearly, or as a continuous function with respect to the punch travel, Figure 5.8.

### **5.9. Prediction of Stresses, Strains, and Punch Force**

SHEET\_FORM is based on the Finite Difference Method, uses incremental deformation theory, and assumes that the material is rigid-plastic. The sheet material is further assumed to be isotropic in the plane of the sheet, and anisotropic in the normal or the thickness direction. Hill's "old" yield function is used to define the yield surface, and Hollomon's power-law equation is used to describe the hardening curve of the material. The tool-workpiece interface friction condition is modeled using the modified Coulomb friction law..

One half of the sheet metal blank is modeled during the simulation. The blank is divided into  $N$  elements of equal length. For  $N$  elements, there are

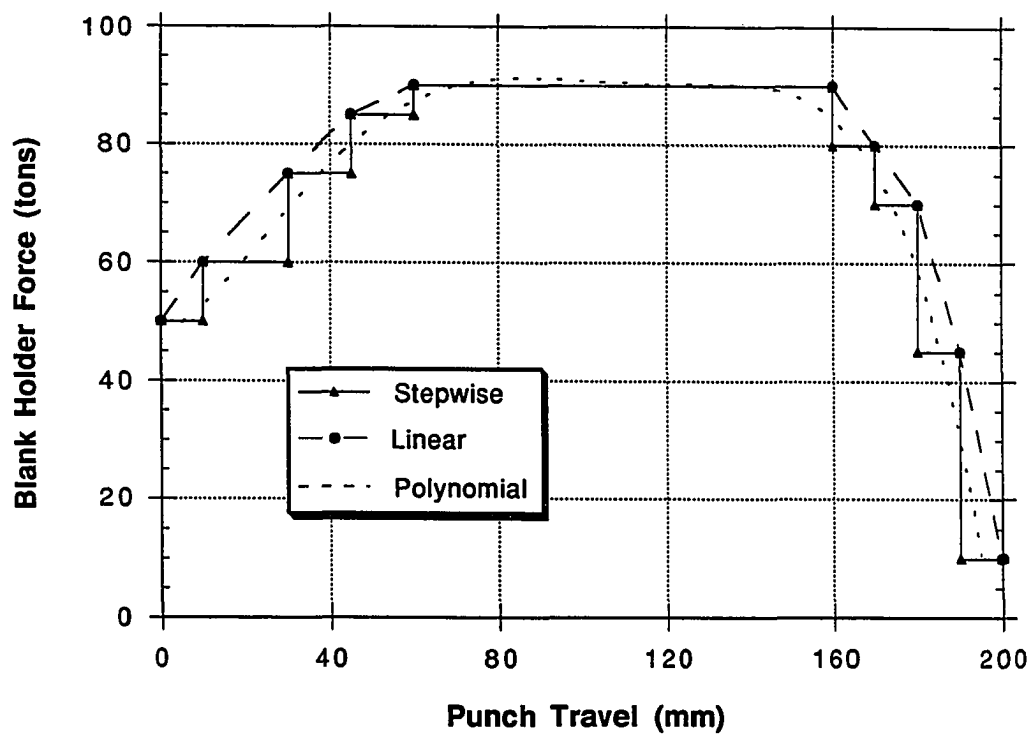


Figure 5.8: Blankholder force variations that can be used in SHEET\_FORM.

$N+1$  boundaries or nodes. The deep drawing process is modeled stage by stage as a quasistatic process, and for a given stage  $J$  of the punch displacement, all strains and stresses throughout the workpiece at the end of the previous stage  $J-1$  are known. The stress and strain distributions in the workpiece at the current stage during the deformation are determined by solving the equilibrium, geometry, and constitutive equations simultaneously. At any stage, the punch force required to draw the sheet can be determined from the knowledge of stresses in the sheet at the beginning of Zone 4 (see Figure 5.3) because this zone serves as a link for transmitting the punch force to the flange compression.

### **5.10. Numerical Examples**

In this section, results will be presented from the preliminary tests to compare different modules of the analysis program, SHEET\_FORM, with experiments and other analysis results available in the literature. Results will be displayed for deep drawing of axisymmetric and plane-strain geometries. Since there was no data readily available in the literature, the redrawing module is tested against the experiments conducted in ERC/NSM laboratories as part of this study. These results will be shown in Chapter VII.

### 5.10.1. Analysis of Axisymmetric Deep Drawing Operations

#### Deep Drawing Quality Steel

Deep drawing of a round cup (Figure 5.9) is formed from Deep Drawing Quality Steel. The process parameters are summarized in Table 5.1. Strain predictions are compared with experimental measurements as well as an elastic-plastic FEM solution, [Saran, et al., 1990c].

**Table 5.1: Material properties and process conditions for deep drawing of Deep Drawing Quality Steel**

<u>Material Properties and Blank Dimensions</u>		
$\bar{R}$ (Anisotropy Factor)	=	1.65
K (Strain-Hardening Coeff.)	=	547 MPa
n (Strain-Hardening Exp.)	=	0.18
Blank Diameter	=	200 mm
Blank Thickness	=	0.70 mm
<u>Process Conditions</u>		
Lubrication	=	oil based lube.
Blankholder Force	=	80 kN
Cup Height	=	31.5 mm

The blank diameter used was 200 mm, and the vertical blankholder force was 80 kN. During the simulation, an effective friction coefficient of  $\mu=0.22$  was

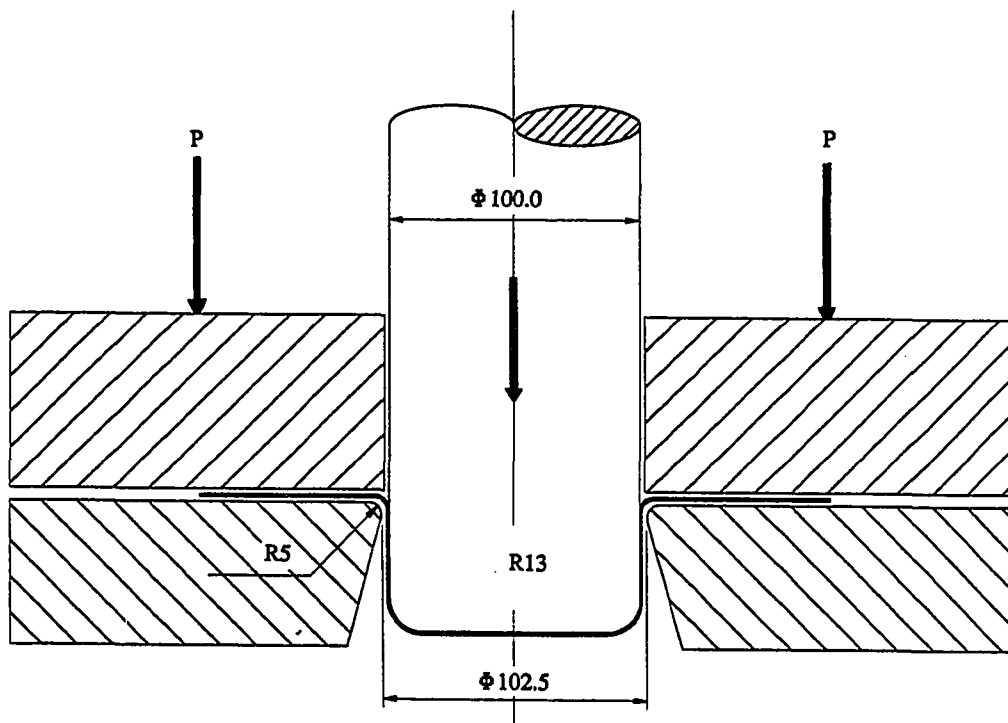
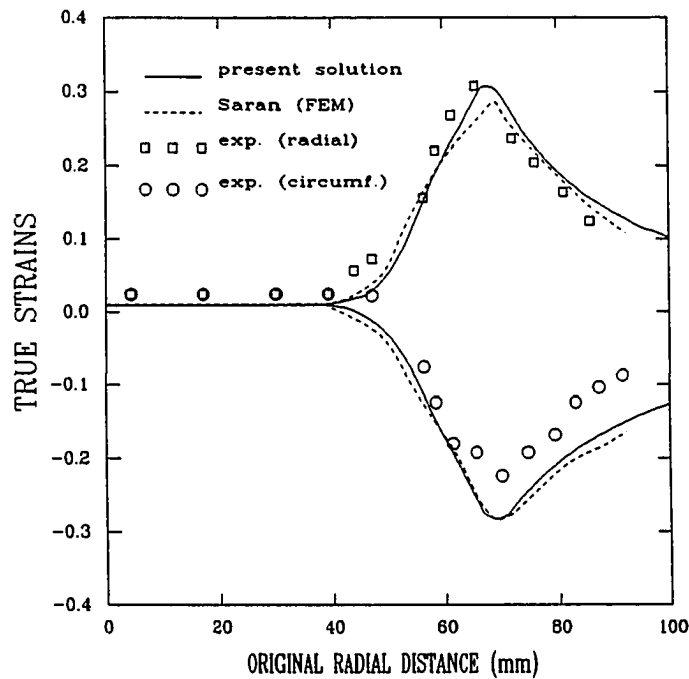


Figure 5.9: Tool geometry for deep drawing of DDQS.

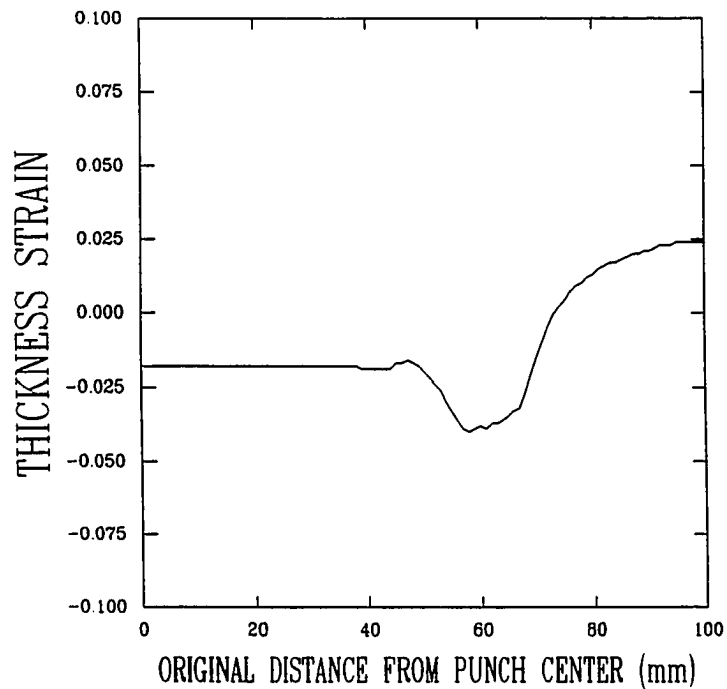
used in all of the contacting surfaces. Radial and circumferential strains are plotted as a function of the original radial distance in Figure 5.10a. Strain distributions predicted by the finite difference solution is in reasonably good agreement with the experimental measurements and elastic-plastic FEM solution. The thickness strain distribution is also plotted as a function of the original radial distance in Figure 5.10b. The largest absolute thickness strain occurs near the punch nose.

### Aluminum Alloy

Deep drawing experiments using AA1100-O was conducted by Yossifon, et al, 1990, in the ERC/NSM laboratories. The tool geometry for these experiments is shown in Figure 5.11. Process parameters are summarized in Table 5.2. Round blanks of 90 mm diameter are formed using constant blank holder forces of 6.8 kN and 12.4 kN. Friction conditions are simulated using a friction coefficient of  $\mu=0.1$ . Radial and circumferential strains predicted using SHEET\_FORM is compared with experiments in Figures 5.12a and 5.13a, and the experimental and theoretical results of the punch forces versus punch stroke are shown in Figures 5.12b and 5.13b for 6.8 kN and 12.4 kN blank holder forces respectively. Good agreement between the punch force results are obtained in the early stages of the punch stroke. Towards the end of the punch stroke, the experimental punch forces are higher, probably as a result of the flange upsetting effect near the end of the stroke.



a) Radial and circumferential strain.



b) Thickness strain.

Figure 5.10: Strain distributions in deep drawing of DDQS. FEM and experiment results are taken from Saran, et al., 1990c.

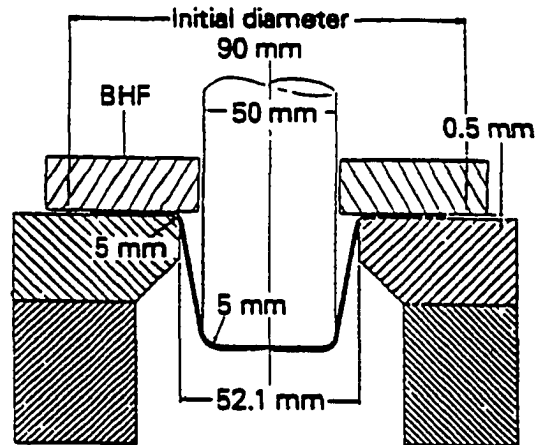
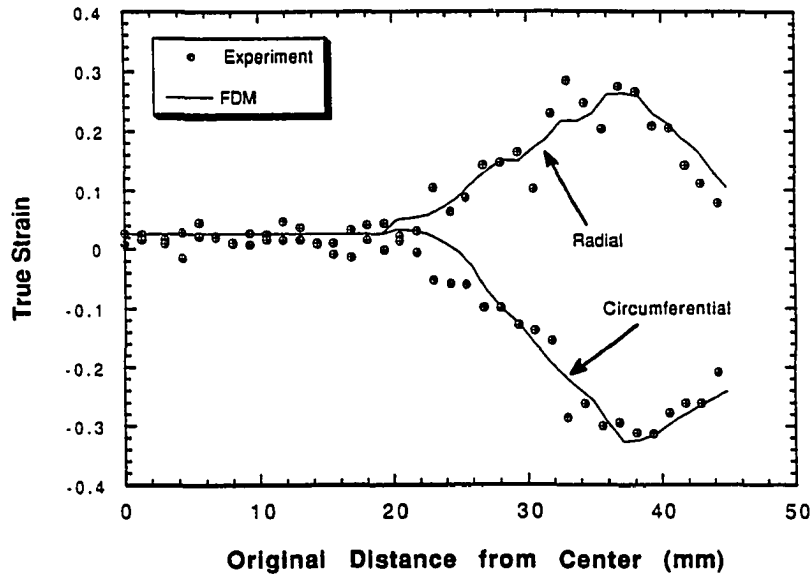


Figure 5.11: Tool geometry for deep drawing of AA1100-O.

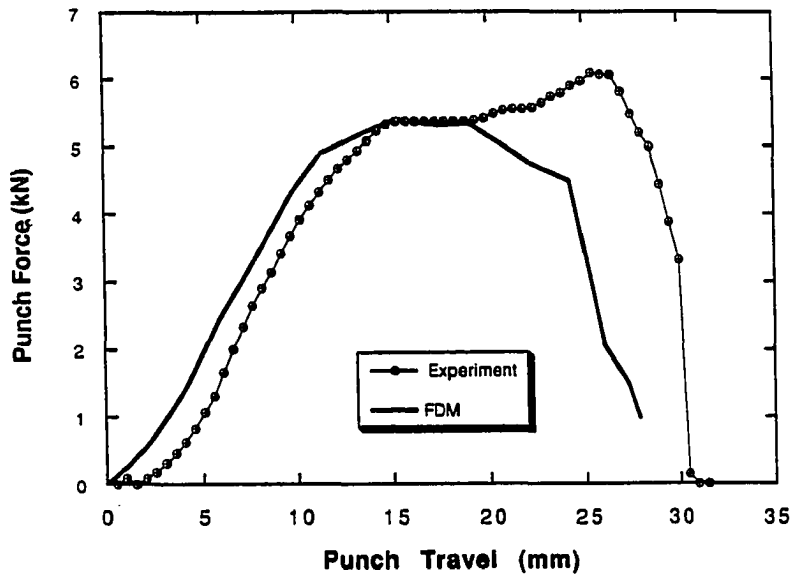
Table 5.2: Material properties and process conditions for deep drawing of AA1100-O

<u>Material Properties and Blank Dimensions</u>		
$\bar{R}$ (Anisotropy Factor)	=	0.80
K (Strain-Hardening Coeff.)	=	130 MPa
n (Strain-Hardening Exp.)	=	0.215
Blank Diameter	=	90 mm
Blank Thickness	=	0.82 mm
<u>Process Conditions</u>		
Lubrication	=	moly grease
Blankholder Force	=	6.8 kN, 12.4 kN
Cup Height	=	19.8 mm, 28.3 mm



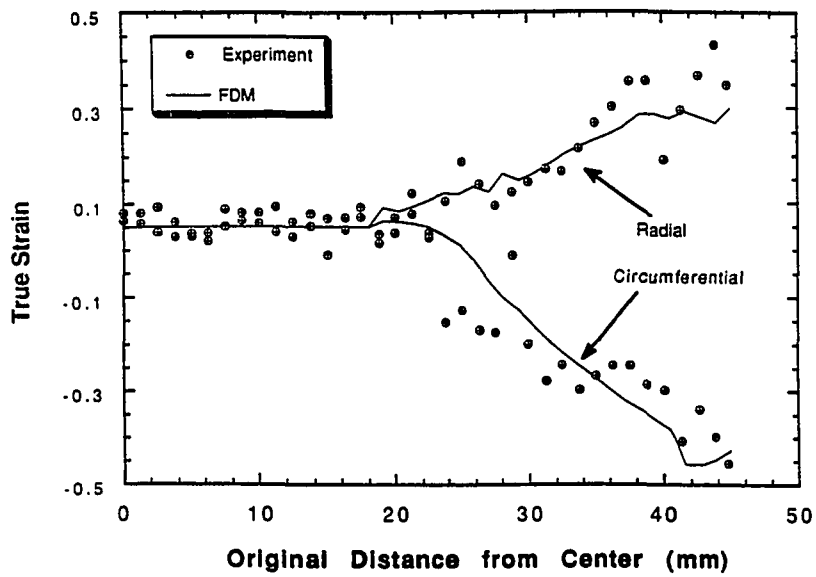


a) Radial and circumferential strain distributions.

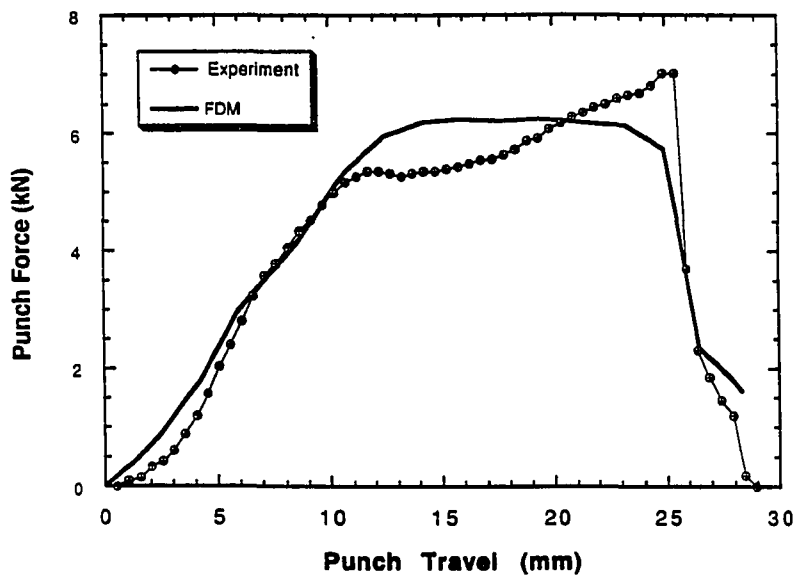


b) Punch force distributions.

Figure 5.12: Deep drawing of AA1100-O using a blankholding force of 6.8 kN. Experiments are taken from Yossifon, et al., 1990.



a) Radial and circumferential strain distributions.



b) Punch force distributions.

Figure 5.13: Deep drawing of AA1100-O with a blankholding force of 12.4 kN. Experiments are taken from Yossifon, et al., 1990.

### 5.10.2. Analysis of Plane-Strain Deep Drawing Operations

#### Cylindrical punch stretching

Plane-strain punch stretching using a cylindrical punch was analyzed and the results compared with existing solutions. The problem geometry (Figure 5.14) and the process parameters are summarized in Table 5.3. Due to symmetry, only the right half of the geometry was used for the simulation and for displaying the results.

**Table 5.3: Material properties and process conditions for plane-strain punch stretching simulation**

<u>Material Properties and Blank Dimensions</u>		
$\bar{R}$ (Anisotropy Factor)	=	1.0
K (Strain-Hardening Coeff.)	=	585 MPa
n (Strain-Hardening Exp.)	=	0.216
Blank Width	=	118.36 mm
Blank Thickness	=	1.0 mm
<u>Process Conditions</u>		
Lubrication	=	perfectly lubricated
Blankholder Force	=	6.8 kN, 12.4 kN
Punch Travel	=	20.0 mm, 40.0 mm

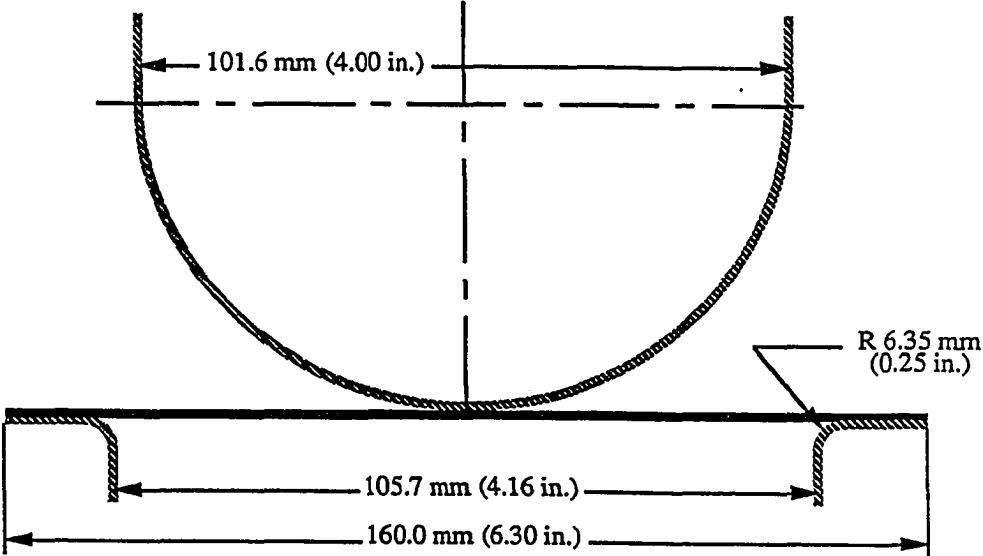


Figure 5.14: Plane-strain stretch forming using cylindrical punch.

In the simulations, sheet metal was clamped at a distance of 59.18 mm from the axis of symmetry. It was also assumed that sheet metal was perfectly lubricated, i.e., there was no friction at the blank-die and blank-punch interfaces. Under this assumption, an exact solution is readily available. The deformed sheet metal geometry is shown at three different punch heights in Figure 5.15. The strain results obtained by numerical analysis for two punch depths of 20 mm and 40 mm are shown in Figure 5.16. Results are in full agreement with the exact solution.

#### Cylindrical punch deep drawing

A deep drawing process using the same tools shown in Figure 5.14 and the same material parameters summarized in Table 5.3 was simulated. In this case, a 80.0 mm wide sheet metal blank was used in the simulation. A horizontal drawbead force ( $F_d$ ) of 300 kN was applied at the edge of the blank. This example was also simulated by both Frey, et al., 1987, and Saran, et al., 1990a, using an FEM membrane formulation. A friction coefficient of  $\mu=0.3$  was used at the die-blank and punch-blank interfaces in order to compare. Figure 5.17 shows the results of the current analysis in comparison with the previous solutions for two different punch travels. Results are in good agreement with the existing solutions.

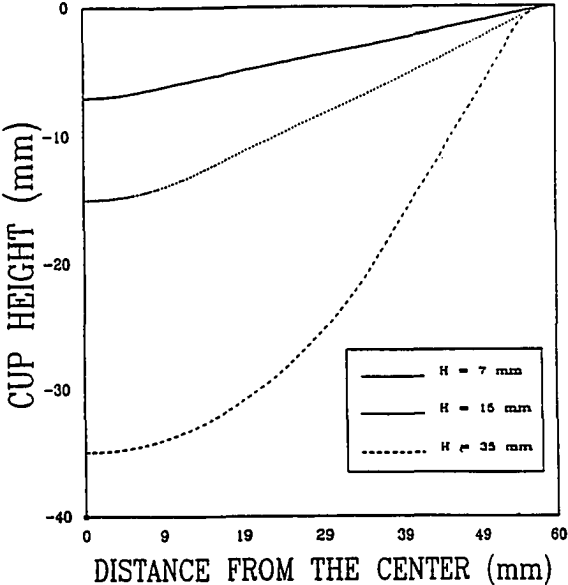


Figure 5.15: Deformed sheet geometry at punch travels of 7 mm, 15 mm, and 35 mm.

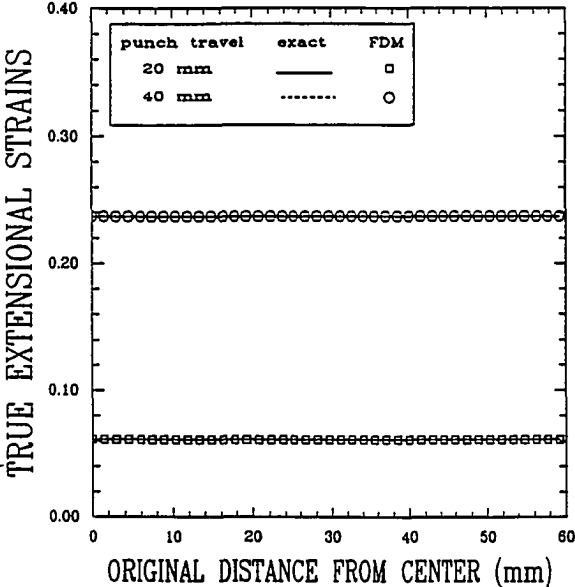


Figure 5.16: Stretch forming of sheet metal using cylindrical punch. Comparison with exact solution at punch travels of 20 mm, and 40 mm. ( $\mu=0.0$ )

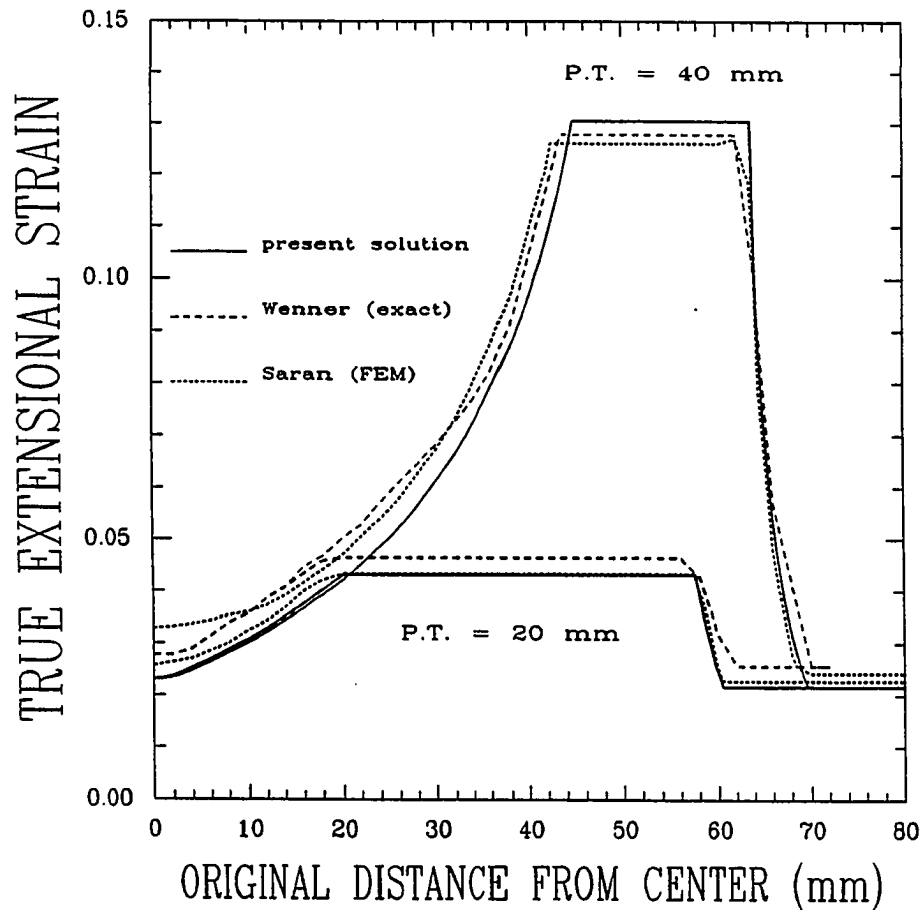


Figure 5.17: Plane-strain deep drawing using cylindrical punch. Comparison with FEM and exact solution. FEM and exact solution are taken from Saran, et al., 1990a, and Frey, et al., 1987, respectively. ( $\mu=0.3$  was used by all for comparison)

### Square punch deep drawing

Another comparison is also made by existing experimental data for plane-strain draw case, [Wang, et al., 1990]. The tool geometry is shown in Figure 5.18, and material parameters are summarized in Table 5.4.

**Table 5.4: Material properties and process conditions for deep drawing by flat bottom square punch**

<u>Material Properties and Blank Dimensions</u>		
$\bar{R}$ (Anisotropy Factor)	=	1.92
K (Strain-Hardening Coeff.)	=	598 MPa
n (Strain-Hardening Exp.)	=	0.23
Blank Width	=	150.0 mm
Blank Thickness	=	1.0 mm
<u>Process Conditions</u>		
Lubrication	=	dry friction
Drawbead Force	=	290 N/mm
Punch Travel	=	15.0 mm

A friction coefficient of  $\mu=0.25$  and a horizontal drawbead force of  $F_d=290$  N/mm were used in the experiments. This problem was simulated by Saran, et al., 1990b, using a FEM membrane formulation. Figure 5.19 shows the



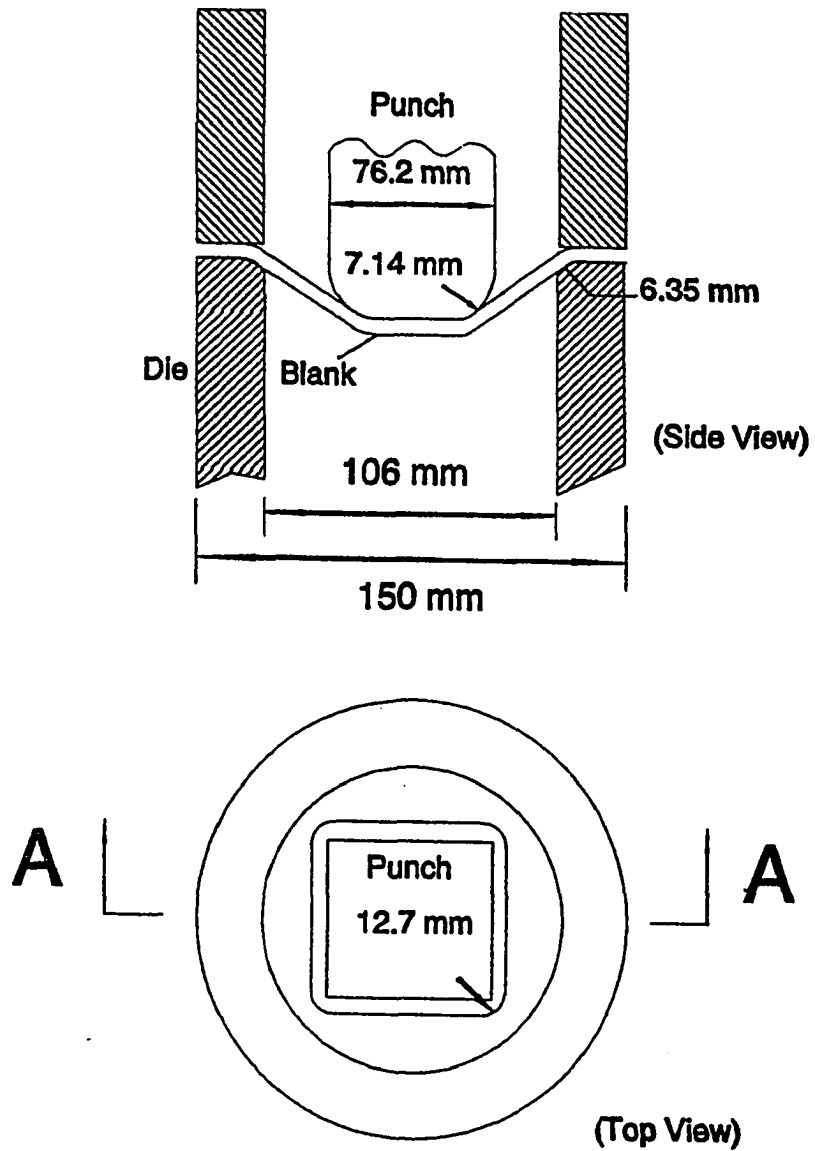


Figure 5.18: Deep drawing using flat bottom square punch. Tool geometry and deformed sheet shape. (Saran, et al., 1990b)

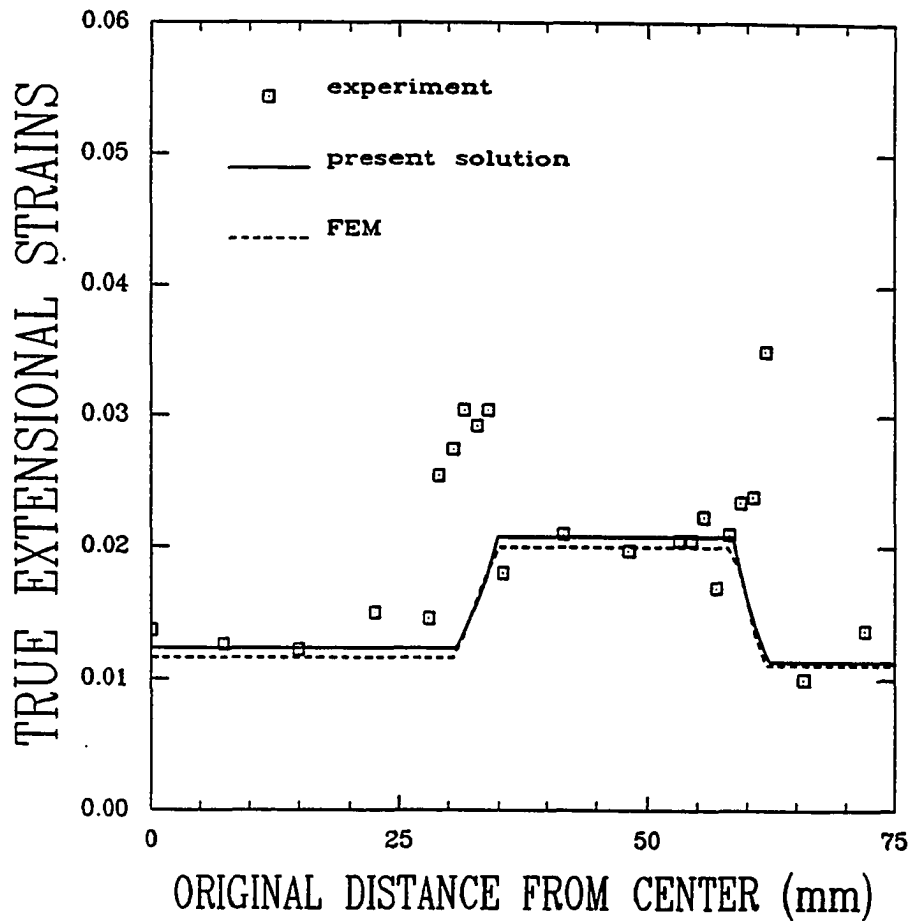


Figure 5.19: Deep drawing using flat bottom square punch. Comparison with FEM results and experimental measurements. (Punch travel is 15 mm,  $\mu=0.25$ ) Experiment and FEM are taken from Wang, et al., 1990, and Saran, et al., 1990b, respectively.

results of the current analysis in comparison with the experimental measurements and the results obtained by Saran. Deformation is plane-strain only for small punch travels. This is why results are compared at 15 mm of punch travel. Local peaks in the experimental measurements are due to bending effect at die and punch corner regions. The membrane solutions are not capable of determining these peaks.

In the current analysis, stresses and strains are calculated along the mid-surface of the sheet. Therefore, it is not capable of determining the peaks caused by bending at the locations of curvatures. An increment in the true strain on the outer and inner surfaces of the sheet is calculated at these locations. Further details can be found in Section 5.7.

## CHAPTER VI

### DEEP DRAWING AND REVERSE REDRAWING OF ROUND CUPS IN MULTI-ACTION ERC/NSM PRESS

A series of experiments were performed to evaluate the capabilities of the analysis program, SHEET\_FORM, and to investigate the effects of several process parameters on the quality of deep drawn cups. The process sequence in the deep drawing and reverse redrawing experiments is shown in Figure 6.1.

Two different aluminum alloys<sup>1</sup> were used in the experiments (Table 6.1).

**Table 6.1: Aluminum alloys which were used in the experiments.**

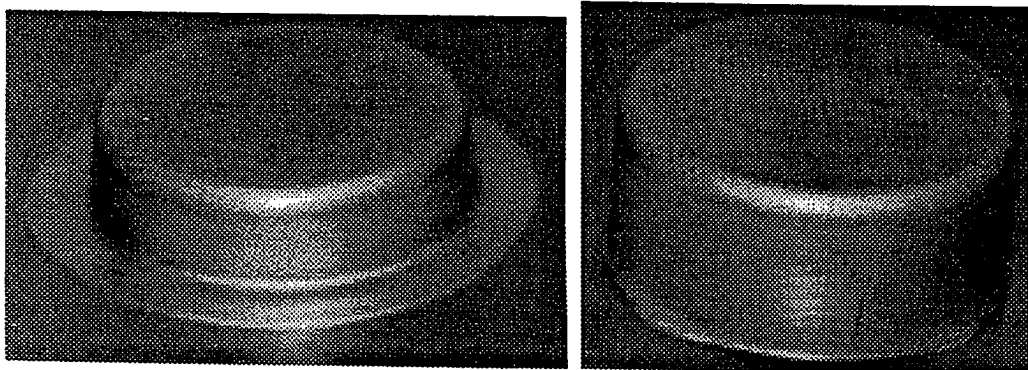
Material	Thickness
AA 3104-H19	0.012
AA 1100-O	0.020
AA 1100-O	0.032

---

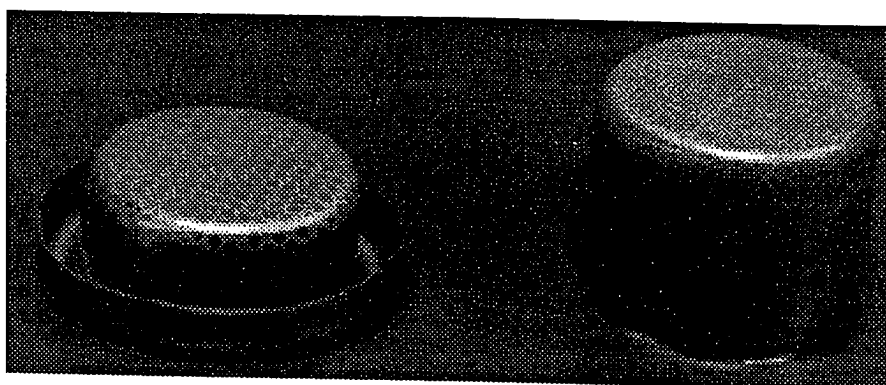
<sup>1</sup> All of the materials used in these experiments were donated by ALCAN Rolled Products Co.



a) initial blank, ( $D_b=3.32$  in,  $t=0.032$  in)



b) 1st stage: Deep drawing



c) reverse redrawing,

Figure 6.1: Deformed cups from the multi-stage forming experiments.

Three lubrication conditions were used in the experiments. These are;

- Water dilutable oil based lubricant<sup>2</sup> : This lubricant is commonly used for deep drawing of aluminum alloys, Al-coated steel, cold rolled steel, zinc coated steel (except 1.5 galv.) brass, and copper.
- Machine oil: This is a regular machine oil taken from the machine shop.
- Dry friction: Experiments were performed without lubrication. Before these experiments, workpiece, punch, and die surfaces were cleaned by acetone.

For strain measurement purposes, several workpieces were gridded. The initial diameter of the circular grids was 1.27 mm (0.05 in). After the deformation, the major and minor diameters of deformed grids were measured under a microscope and major and minor strains were calculated.

During the experiments, a constant blankholding pressure was used. The blankholding pressure in the first draw operation could be preset between 0 and 150 psi. In the reverse redrawing operation, the blankholding pressure would also be set between 0 and 150 psi.

### **6.1. Multi-Action ERC/NSM Press**

The ERC Multi-Action Servo press was designed and built at the ERC/NSM in 1989. The press was originally built to study precise forging of complex

---

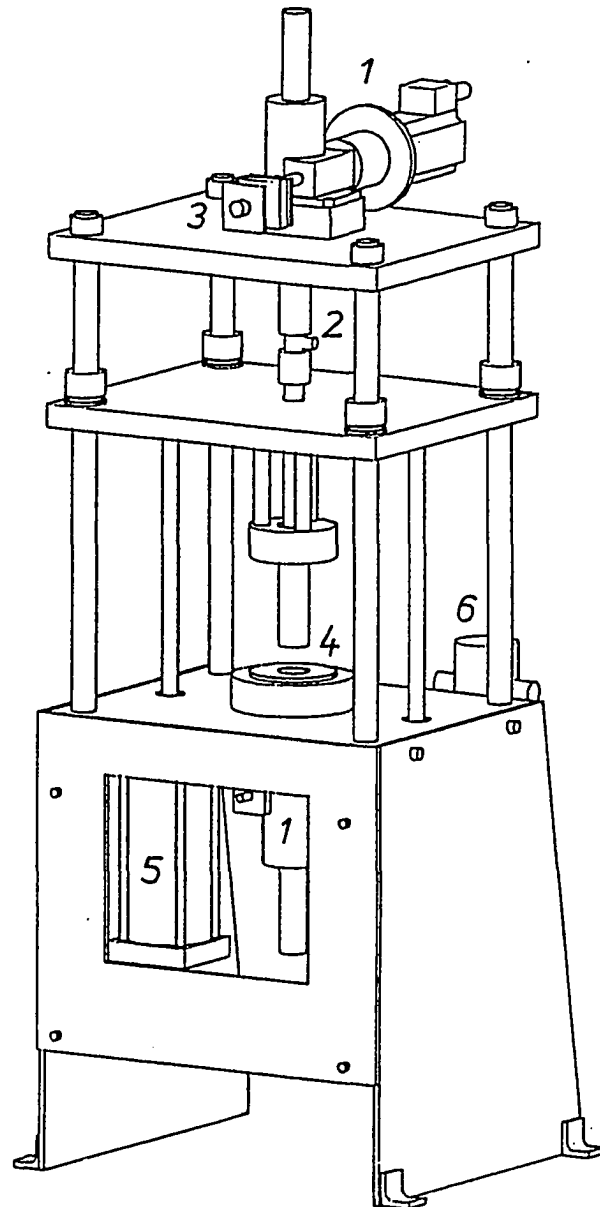
<sup>2</sup> Water dilutable oil based lubricant for deep drawing Aluminum Alloys was donated by Metal Lubricants Co. Product Number is DB-4251.

parts with physical modeling using plasticine. In the past two years, the press has been used extensively for this purpose. Recently, it has been modified to perform sheet metal forming. This research has focused on the effect of the blank holding forces on failure modes and drawing ratios in deep drawing.

A drawing of the press with deep drawing tooling can be seen in Figure 6.2. The press is 79.0 inches high with 18.0 inches of daylight and an effective die space of 14.0 inches x 14.0 inches. The press has two AC servo motors each coupled with ball screw jacks, which produce two of the three press actions. One motor is mounted on the top of the press and the other one is mounted on the bottom, producing opposing actions. Each screw has a maximum load capacity of 2.5 tons. The maximum screw speed is 1.25 inches/sec. The third action is a clamping plate which is moved up and down with two pneumatic cylinders and can produce approximately 3 tons of clamping force. Table 6.2 shows the current specifications of the press, [Pale, et al., 1989]. More details about the ERC/NSM press can be found in Appendix F (Section F.2).

An electro/pneumatic device is connected close to the cylinders and is used to control the clamping pressure. This valve provides pneumatic pressure output directly proportional to an analog voltage command signal of 1.0 to 5.0 volts. The response time of the pneumatic controller is .64 sec. The speed of the clamping plate is controllable by adjusting the exhaust ports of the air cylinders.

A personal computer is used to issue commands to control the press. This includes: the actuating of the clamping plate by controlling the pressure in the



- 1) Servomotor/Ball screw
- 2) Loadcell
- 3) Potentiometer
- 4) Deep draw die set
- 5) Pneumatic cylinders
- 6) Electro/Pneumatic controller

Figure 6.2: ERC/NSM Multi-Action servo press with deep draw tooling.



**Table 6.2: Specifications of ERC/NSM press.**

Number of punch actions	Two: opposing and independent
Maximum Punch Load	2.5 tons
Maximum Punch Velocity	1.25 in.sec (31.75 mm/sec)
Punch Velocity Profile	User specified / PC controlled
Punch Travel	5.5 in
Clamping	Air activated
Maximum Clamping Pressure	3.0 tons
Press Height	79.0 in (2007 mm)
Minimum Shut Height	8.0 in (203 mm)
Daylight	18.0 in (457 mm)
Effective Die Space	15x15 in <sup>2</sup> (381x381 mm <sup>2</sup> )

air cylinders, the independent control of the two servo motors and the monitoring of all limit and end of travel switches. "CONTROL" (written at the ERC, [Pale, et al., 1989]) is an interface program for the press from which one can either issue individual commands or execute a series of commands stored in an external command file. The source code for CONTROL is written in the C programming language.

The geometry of the tooling used in the first stage (deep drawing), and second stage (reverse redrawing) are shown in Figures 6.3 and 6.4. Detailed procedure to design these geometries are given in Appendix F (Section F.1).

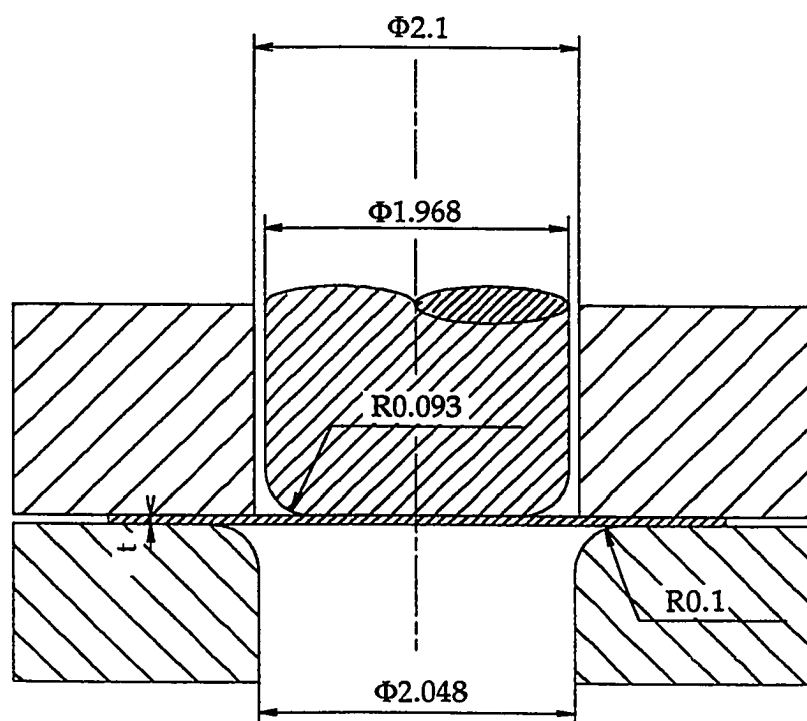


Figure 6.3: Geometry of the tooling used in the 1st stage (deep drawing) operation.

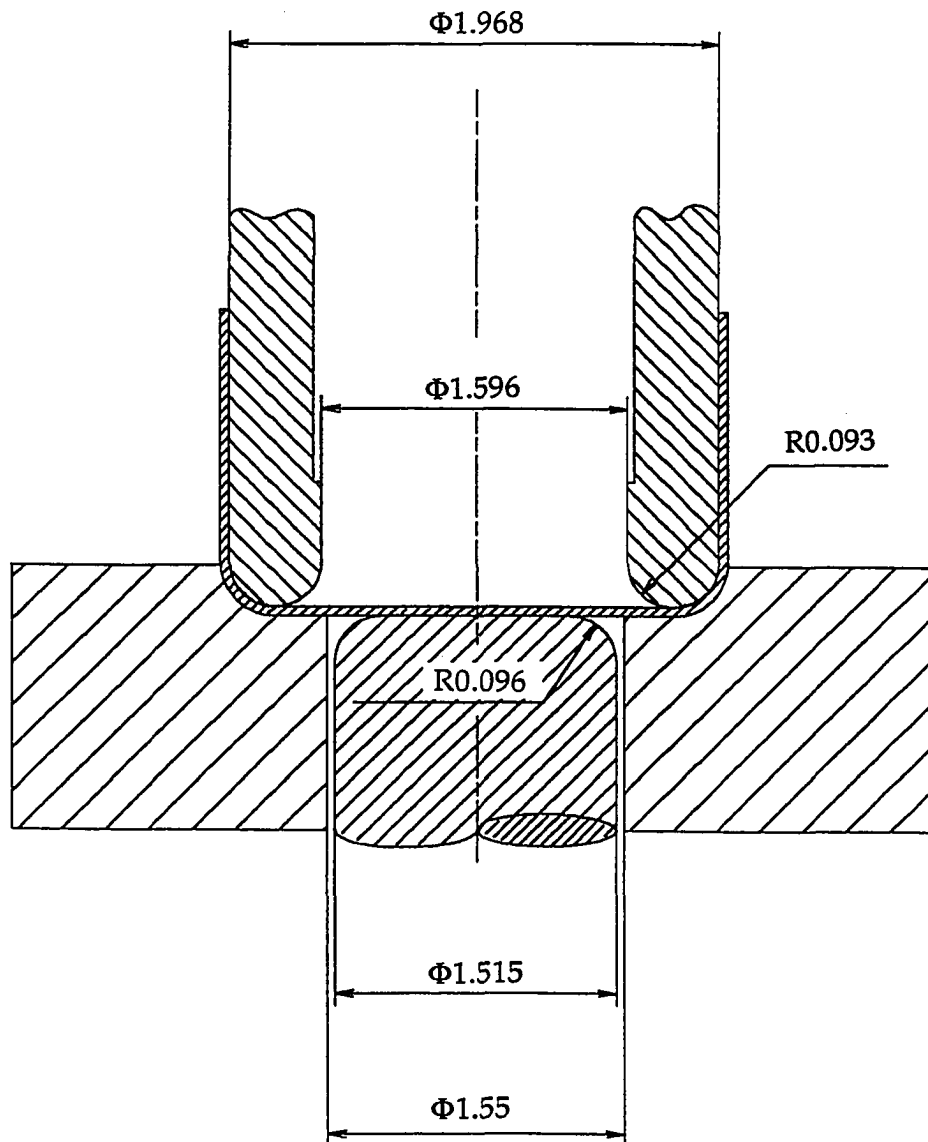


Figure 6.4: Geometry of the tooling used in the 2nd stage (reverse redrawing) operation.

## 6.2. Material Properties

In the simulations, material is modeled using the Holloman power law hardening equation

$$\bar{\sigma} = K\bar{\epsilon}^n \quad (6.1)$$

where  $\bar{\sigma}$  : true stress                      K : strength coefficient  
 $\bar{\epsilon}$  : true plastic strain              n : strain-hardening exponent

Tensile tests were performed at a local company, The Worthington Steel Co., based on the guide lines given in ASTM standards to determine the K, n, and R value, i.e. anisotropy factor. The designation number for the ASTM standards that was used in these tests are E8-89b (general tensile testing), E517-81 (for R-value), E646-78 (for K and n values).

It was not possible to determine the R-value for AA 3104-H19 based on the test results because of the small amount of thinning before fracture.

For AA 1100-O with a thickness of 0.032 in, the  $\bar{R}$  value was calculated at 15% elongation and is given in the following table;

**Table 6.3:  $\bar{R}$  values for AA 1100-O**

Angle	$t_0$	t at 15%	w at 15%	Final L	$r^{15}$
0	0.032	0.029	0.477	2.31	0.5831
45	0.032	0.030	0.466	2.30	1.1769
90	0.032	0.029	0.474	2.32	0.6150

The  $\bar{R}$  value is found to be 0.8955 for AA1100-O.

The  $n$  values are calculated based on the force/displacement curves obtained from tensile tests using the following procedure;

- Tensile tests were performed using specimens prepared in the rolling direction, normal to the rolling direction, and  $45^\circ$  to the rolling direction. Three tests were done in each direction. From the load/strain curves of each test, six data pairs  $(\sigma, \epsilon)$  were obtained between the yield stress and the ultimate tensile stress.

- The  $n$  value is calculated from the following equation

$$n = \frac{N \sum_{i=1}^N (\log \epsilon_i \log \sigma_i) - \left( \sum_{i=1}^N \log \epsilon_i \sum_{i=1}^N \log \sigma_i \right)}{N (\log \epsilon_i)^2 - \left( \sum_{i=1}^N \log \epsilon_i \right)^2} \quad (6.2)$$

- The  $K$  value is calculated as follows

$$b = \frac{\sum_{i=1}^N \log \sigma_i - n \sum_{i=1}^N \log \epsilon_i}{N} \quad (6.3)$$

$$K = 10^b \quad (6.4)$$

As a result, the following values were obtained;

**Table 6.4: K and n values for aluminum alloys**

Material	K (ksi)	n
AA 3104-H19	52.211	0.06547
AA 1100-O	23.437	0.2297

The ultimate tensile stress and yield stress for each material is determined as;

**Table 6.5: Yield and ultimate tensile strengths for aluminum alloys**

Material	YS (ksi)	UTS (ksi)
AA 3104-H19	37.13	41.73
AA 1100-O	8.55	13.65

### 6.3. Deep Drawing

The geometry used in the first stage deep drawing operation is shown in Figure 6.3. Three experiments were performed for each material and process condition, and the results plotted in this section show the mean value of these experiments. The variation from the mean value in the punch force plots changes from 0 to 0.05 kip, and in the radial and circumferential strain plots changes between 2-5%.

#### Aluminum Alloy AA1100-O

3.32 in diameter and 0.032 in thick AA 1100-O was formed in the 1st stage (deep drawing). The material parameters and process conditions are summarized in Table 6.6.

In these experiments, the blankholding force was set to a constant value of 2.15 kip, and the water dilutable oil based lubricant was used. Strain measurements were obtained at two punch stroke positions, 0.575 in and 0.94 in, by means of circular grid analysis technique. These measurements were

**Table 6.6: Material properties and process conditions for deep drawing of AA1100-O**

<u>Material Properties and Blank Dimensions</u>		
$\bar{R}$ (Anisotropy Factor)	=	0.8955
K (Strain-Hardening Coeff.)	=	23.437 Ksi
n (Strain-Hardening Exp.)	=	0.2297
Blank Diameter	=	3.32 in
Blank Thickness	=	0.032 in
<u>Process Conditions</u>		
Lubrication	=	oil based lube*
Blankholder Force	=	2.15 kip
Cup Height	=	0.575 in, 0.94 in

\* Water dilutable oil based lubricant. (DB-4251 by Metal Lubricants Co.)

then compared to the simulation results. Since a friction study was not conducted to determine the friction coefficient, two different friction conditions ( $\mu = 0.02$ , and  $0.09$ ) are selected (from the empirical range of values) and used in the simulations to determine the effect of friction on strain, and force predictions. Cup geometries predicted by FDM (SHEET\_FORM) at two punch travels are shown in Figure 6.5. Punch force measured during the experiment was compared with the predictions, using  $\mu = 0.02$ ,  $0.05$ , and  $0.09$ , as shown in Figure 6.6. A comparison of the radial strain measurements at punch travels of  $0.575$  in and  $0.94$  in are shown in Figures 6.7 and 6.8, respectively. From these results, it can be seen that the friction coefficient does not introduce a large difference in the strain predictions for

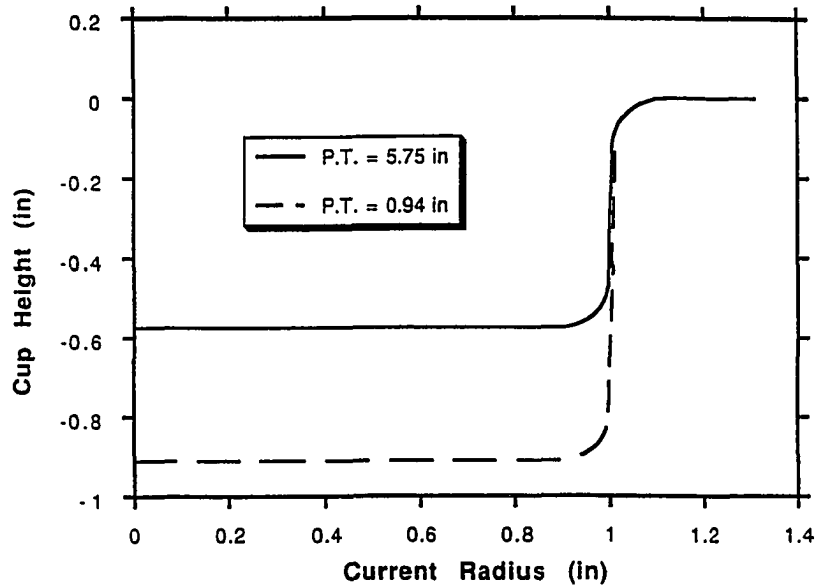


Figure 6.5: Calculated geometry of the cup at two different punch travels (0.575" and 0.94") during the first stage, deep drawing, operation.

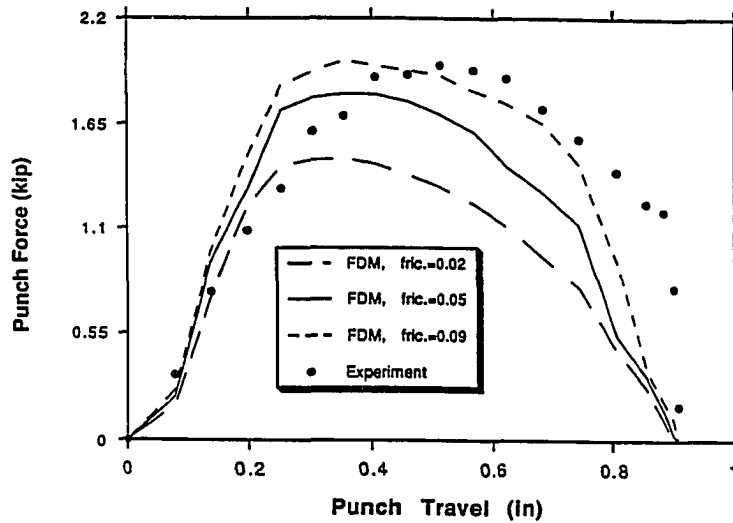


Figure 6.6: Punch force in the deep drawing of AA1100-O for different friction coefficients.



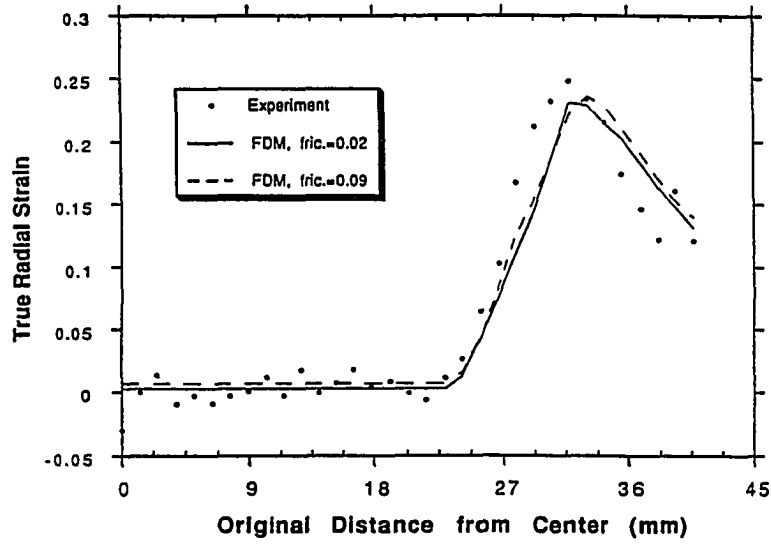


Figure 6.7: Radial strain distribution for deep drawing of AA1100-O at the punch travel of 0.575".

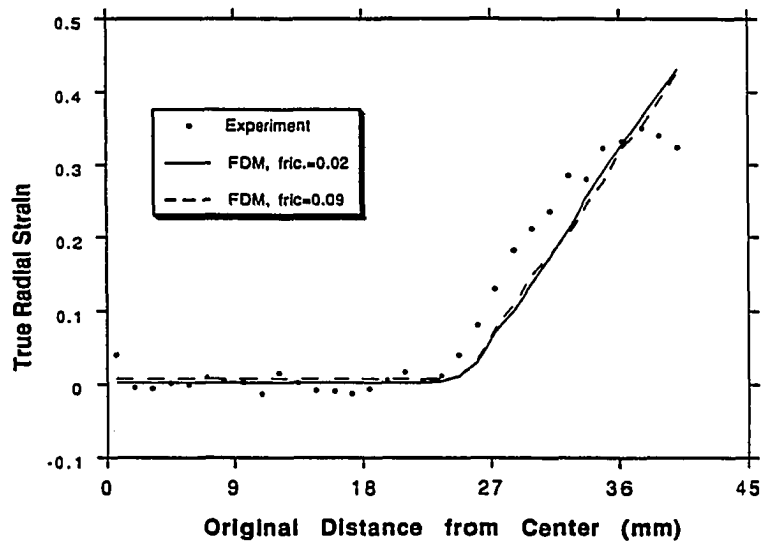


Figure 6.8: Radial strain distribution for deep drawing of AA1100-O at the punch travel of 0.94".

this geometry. However, the predicted punch force increases with increasing friction coefficient (Figure 6.6) since for the same value of BHF, if friction coefficient increases a bigger force (which is provided by the punch) is required to pull the sheet metal into the die cavity. As can be seen from Figure 6.6, the maximum punch force is predicted accurately using  $\mu=0.09$ . Therefore, in the later simulations,  $\mu=0.09$  was used as the friction coefficient to simulate the lubrication conditions for water dilutable oil based lubricant.

#### Aluminum Alloy AA3104-H19

Another deep drawing experiment was performed using 3.32 in diameter and 0.012 in thick AA3104-H19. The material parameters and process conditions are summarized in Table 6.7.

**Table 6.7: Material properties and process conditions for deep drawing of AA3104-H19**

<u>Material Properties and Blank Dimensions</u>		
$\bar{R}$ (Anisotropy Factor)	=	1.8
K (Strain-Hardening Coeff.)	=	52.211 Ksi
n (Strain-Hardening Exp.)	=	0.06547
Blank Diameter	=	3.32 in
Blank Thickness	=	0.012 in
<u>Process Conditions</u>		
Lubrication	=	oil based lube.
Blankholder Force	=	5.66 kip
Cup Height	=	0.875 in

In this experiment, a water dilutable oil based lubricant was used and the blankholding force was set to a constant value, 5.66 kip, throughout the process. The sheet metal blank was drawn to a punch stroke of 0.875 in. At this stage, the blank is fully drawn, i.e. there is no flange under the blankholder. Strain measurements were compared with FDM (SHEET\_FORM) predictions, using  $\mu = 0.09$ , in radial and circumferential directions in Figures 6.9 and 6.10, respectively.

The flange outer radii, which is explained in Figure 6.11, are predicted by the SHEET\_FORM at three punch travels, and these predictions are compared with experimental measurements in Figure 6.12. In these experiments, 3.32 in diameter and 0.012 in thick AA3104-H19 was used. The material parameters are similar to those of the previous experiments given in Table 6.7. Water dilutable oil based lubricant was used in these experiments and the friction conditions were approximated using 0.09 as the friction coefficient. Three sample cups, i.e. samples 1, 2, and 3, were drawn to the heights of 0.3 in, 0.7 in, and 0.9 in, respectively, under 3.13 kip blankholder force.

The maximum punch force predictions, using  $\mu = 0.09$ , with four different blankholder forces are compared with the experimental measurements in Figure 6.13. In these experiments, 0.012 in thick and 3.32 in diameter AA3104-H19 sheet metal blanks were fully drawn to the height of 0.9 in using the water dilutable oil based lubricant. As it is seen in Figure 6.13, the predicted punch forces were always less than the measured forces because the bending effects were neglected in the simulations. However, bending of the sheet over the die and the punch profiles contribute to the punch force.

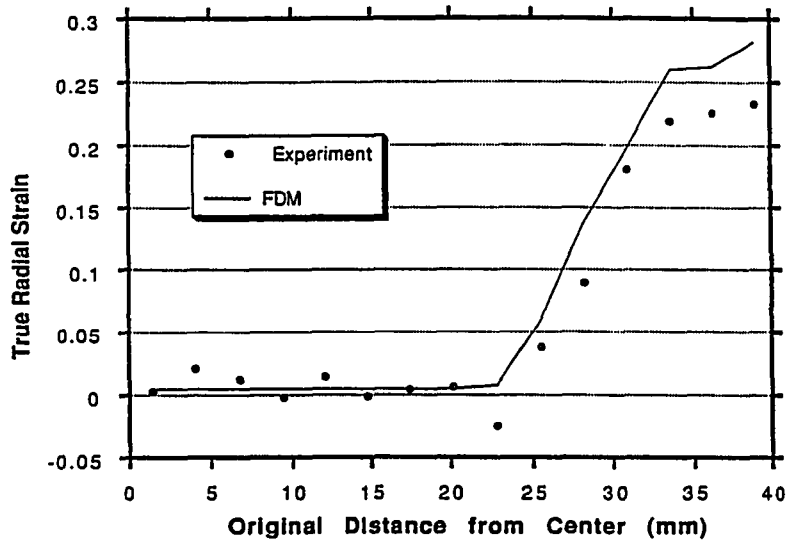


Figure 6.9: Radial strain distribution for deep drawing of AA3104-H19 at the punch travel of 0.875". ( $\mu=0.09$ )

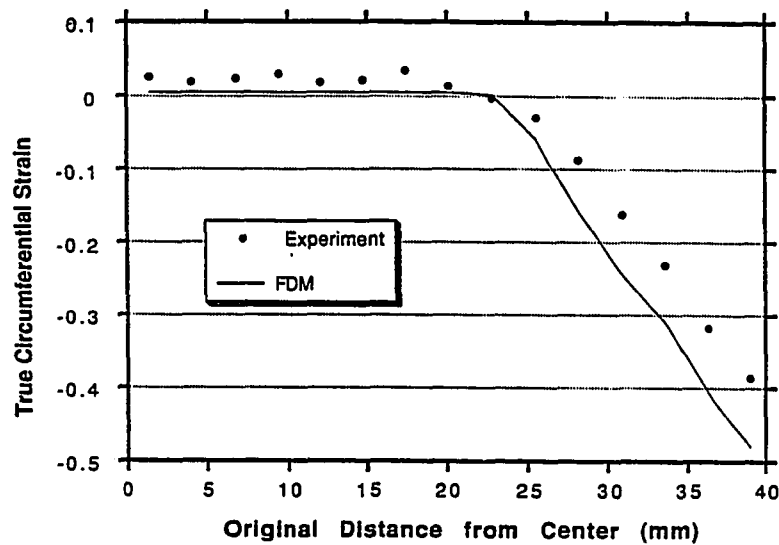


Figure 6.10: Circumferential strain distribution for deep drawing of AA3104-H19 at the punch travel of 0.94". ( $\mu=0.09$ )

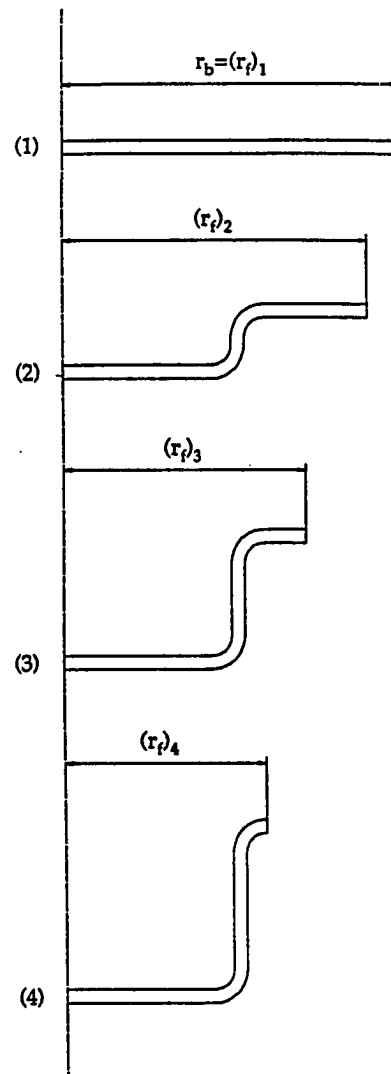


Figure 6.11: Draw-in during a deep drawing process.

$r_b$  = blank radius,  $r_b = (r_f)_1$

$r_f$  = flange outer radius

$r_f$  decreases with increasing punch travel and draw-in.

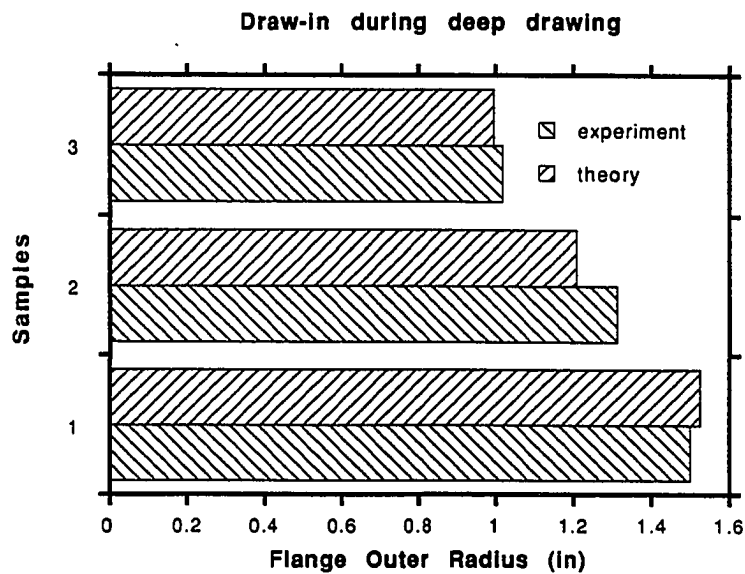


Figure 6.12: Comparison of the predicted outer flange radius,  $r_f$ , to measured flange radius at punch travels of (1) 0.3", (2) 0.7", (3) 1.0".

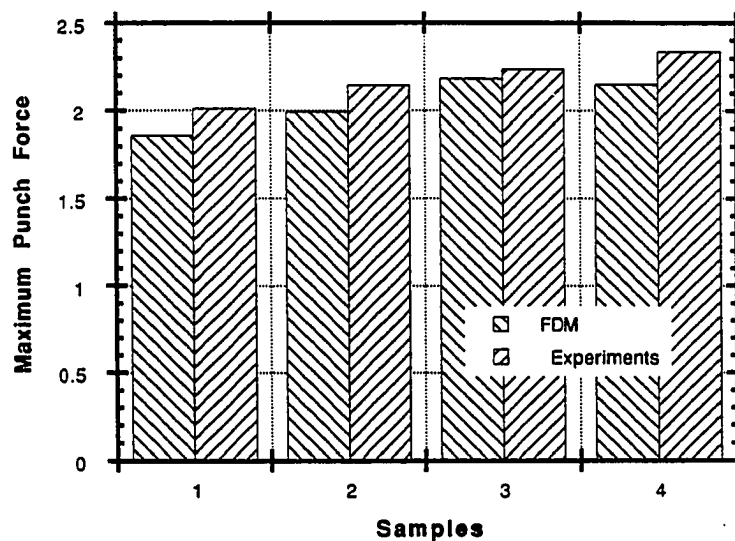


Figure 6.13: Comparison of experimentally measured maximum punch forces with predicted maximum punch forces for AA3104-H19. ( $\mu=0.09$ ) Following blankholder forces were used for corresponding samples; (1) 1.32 kip / (2) 1.88 kip / (3) 2.36 kip / (4) 2.79 kip.

#### 6.4. Reverse Redrawing

Several reverse redrawing experiments were performed following the first stage deep drawing. The geometry of the reverse redrawing operation is shown in Figure 6.4. First stage, deep drawing, and second stage, reverse redrawing, operations are performed continuously on the same tooling. The hollow punch that is used in the first stage becomes the die in the reverse redrawing operation, Figure F.12. The experimental results shown on the plots are the mean value of the three experiments. Variation from the mean value in the strain plots changes between 0 to 5%.

##### Aluminum Alloy AA3104-H19

The upper and lower punch forces were measured during the forming of 0.012 in thick AA 3104-H19 sheet metal blank, Figure 6.14. The first stage forming operation is performed between points A and B. Between these two points, the upper punch load initially increases and then decreases towards the end of the process. There is a delay between two processes and it is shown on the plot between points B and C. At point C, the lower blankholder starts moving upward and clamps the sheet metal against the upper punch. Due to this action, the upper punch load increases and reaches a constant value which is actually the lower blankholding force. At point D, the lower punch starts moving up and forms the sheet metal into the cavity of upper punch. The lower punch force increases in the beginning of the forming process and then decreases towards the end of the process. The lower punch load is transmitted to the upper punch through the sheet metal and increases the upper punch load as shown in Figure 6.14. Towards the end of the process,

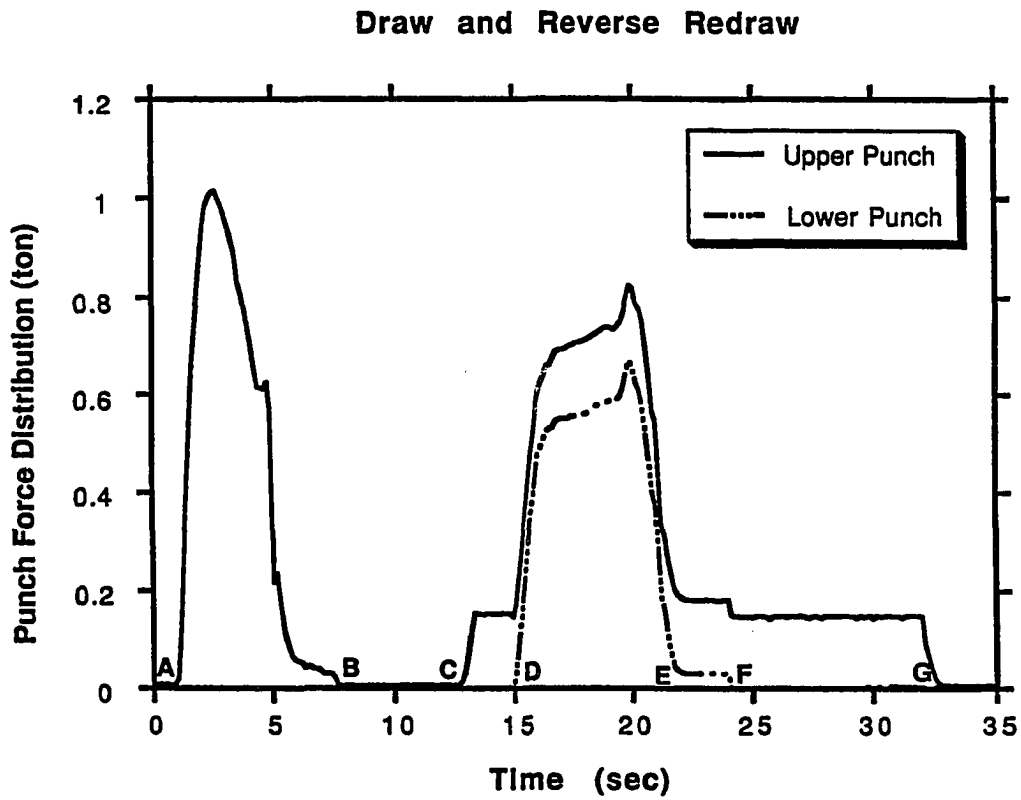


Figure 6.14: Measured upper and lower punch forces during the first stage (deep drawing, A-B) and second stage (reverse redrawing, D-E) forming operations.



there is a peak in the lower punch load. This is due to the thickness variations in the sheet metal that were created in the first stage forming operation. The edge of the cup that is formed in the first stage was thickened due to compressive stresses, and when this thicker part comes under the blankholder, it causes an increase in the blankholder force and consequently in the punch load because of flange upsetting. At point E, the reverse redrawing operation is completed but the lower punch stays inside the cavity of upper punch until point F. Due to the friction forces existing between the sheet metal and the inner surface of the upper punch, the lower punch load is not zero. It has a small constant value between points E and F. At point F, the lower punch retracts back to its original zero position and the lower punch force becomes zero. At this stage, the upper punch force is the lower blankholding force. At point G, the lower blankholder returns to its original position and the upper punch load becomes zero.

Another two stage forming operation was performed using 0.012 in thick and 3.32 in diameter AA 3104-H19 sheet metal blank. The material properties and process conditions are given in Table 6.8. The final diameter of the cup was 1.38 in, and its height was 1.31 in. The total punch travel was 1.5" and there was no metal over the die corner. Strain measurement are compared with FDM simulations in Figures 6.15 and 6.16 for the radial and circumferential directions, respectively.

**Table 6.8: Material properties and process conditions for deep drawing and reverse redrawing of AA3104-H19**

<u>Material Properties and Blank Dimensions</u>		
$\bar{R}$ (Anisotropy Factor)	=	1.8
K (Strain-Hardening Coeff.)	=	52.211 Ksi
n (Strain-Hardening Exp.)	=	0.06547
Blank Diameter	=	3.32 in
Blank Thickness	=	0.012 in
<u>Process Conditions</u>		
Deep drawing		
Lubrication	=	w.b. lube
Blankholder Force	=	5.66 kip
Cup Height	=	0.875 in
Reverse redrawing		
Lubrication	=	w. b. lube
Blankholder Force	=	0.353 kip
Cup Height	=	1.5 in

### Aluminum Alloy AA1100-O

A 3.32 in diameter and 0.032 in thick AA 1100-O sheet metal blank was used in the two stage forming operation. Material properties and process parameters are given in Table 6.9. The blank was formed to a cup of 1.968 in diameter and 0.94 in height in the first stage operation, Figure F.2c. The BHF during the first stage operation was 2.1 kip. This cup was then formed in the second stage operation, i.e. reverse redrawing, and its diameter was reduced to

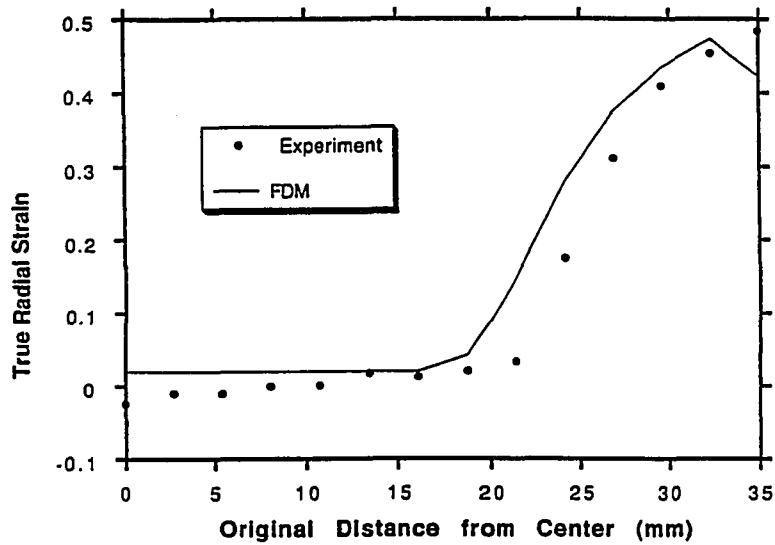


Figure 6.15: Radial strain distribution for reverse redrawing of AA3104-H19 at the punch travel of 1.5". ( $\mu=0.09$ )

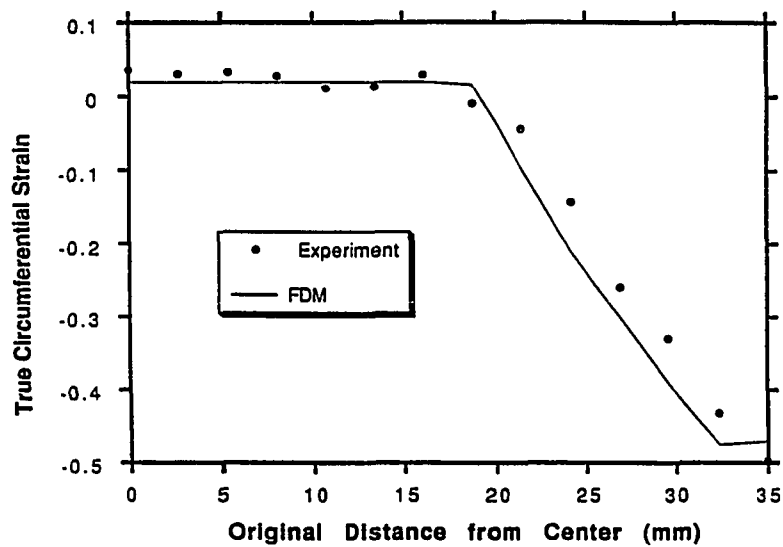


Figure 6.16: Circumferential strain distribution for reverse redrawing of AA3104-H19 at the punch travel of 1.5". ( $\mu=0.09$ )

**Table 6.9: Material properties and process conditions for deep drawing and reverse redrawing of AA1100-O**

<u>Material Properties and Blank Dimensions</u>		
$\bar{R}$ (Anisotropy Factor)	=	0.8955
K (Strain-Hardening Coeff.)	=	23.437 Ksi
n (Strain-Hardening Exp.)	=	0.2297
Blank Diameter	=	3.32 in
Blank Thickness	=	0.032 in
<u>Process Conditions</u>		
Deep drawing		
Lubrication	=	w. b. lube
Blankholder Force	=	2.1 kip
Cup Height	=	0.94 in
Reverse redrawing		
Lubrication	=	w. b. lube
Blankholder Force	=	0.353 kip
Cup Height	=	1.5 in

1.515 inches, Figure F.2e. The BHF in the second stage was 0.533 kip. The total punch travel in the reverse redrawing operation was 1.5 in. In the process simulations,  $\mu=0.09$  was used as friction coefficient. The deformed geometry at two different punch travels is shown in Figure 6.17. The punch force prediction for the reverse redrawing process is compared with the experimental measurement in Figure 6.18. It can be seen from this figure that there is a good match between the prediction and the measurement in the beginning of deformation. Towards the end of the process, there is a peak in the measured punch force distribution mainly because of the flange upsetting

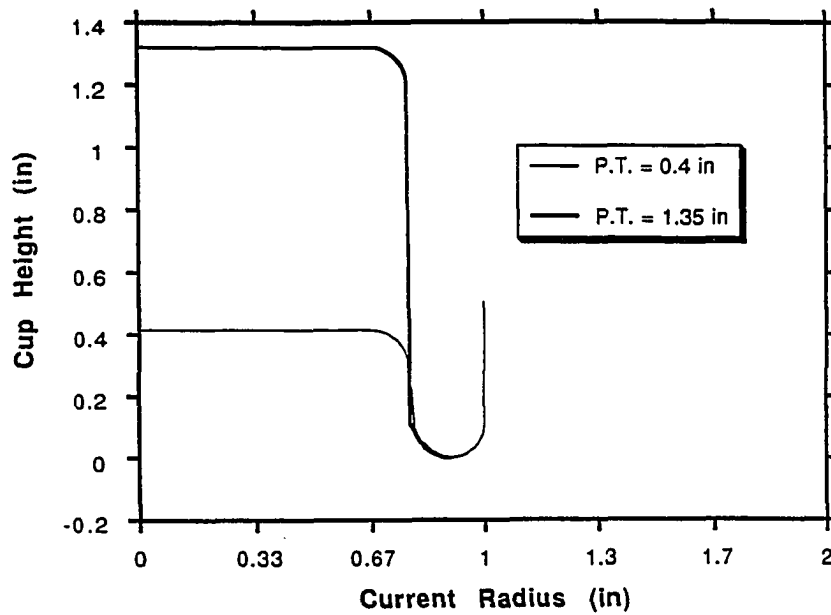


Figure 6.17: Deformed cup geometries at two different punch travels during the reverse redrawing operation.

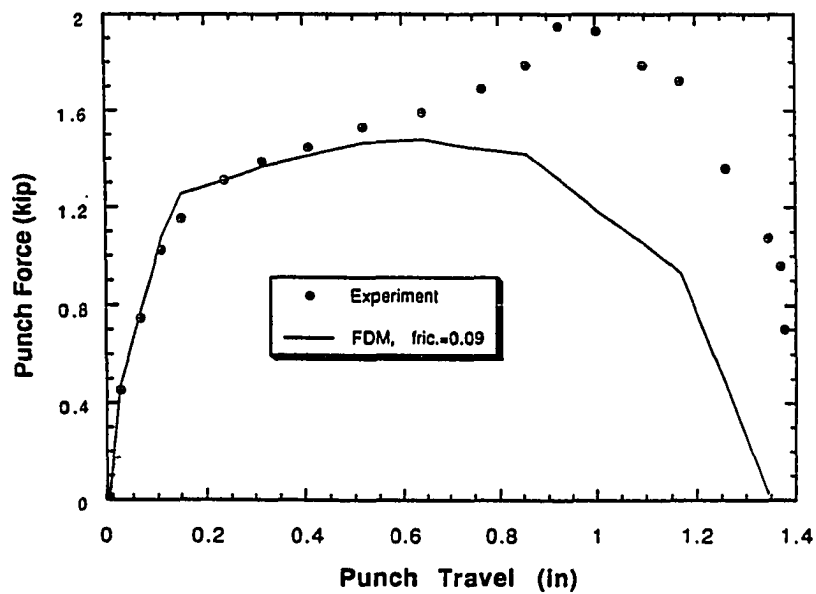


Figure 6.18: Punch force distribution for reverse redrawing of AA1100-O. ( $\mu=0.09$ )

effect near the edge of the stroke. Strains are measured after the process and compared with the FDM predictions in Figures 6.19 and 6.20 for radial and circumferential directions, respectively.

### 6.5. Failure Evaluation

The predominant failure modes in stamping of sheet metal parts (deep drawing and stretch forming) are wrinkling or tearing. Wrinkling may occur at the flange as well as in other areas of the drawn part. Wrinkling is generated by excessive compressive stresses that cause the sheet to buckle locally. Fracture occurs usually in the drawn material that is under excessive tensile stresses.

In forming round cups, wrinkling and/or tearing affect the limiting draw ratio (LDR), i.e. the ratio of the initial blank diameter to the diameter of the drawn cup. The magnitude and location of the tensile and compressive stresses can be influenced to some extent by the blank holder force (BHF). A high BHF can suppress the wrinkling but it may cause fracture in the sheet metal.

A fractured cup due to very high BHF during the first stage (deep drawing) forming operation is shown in Figure 6.21a. This experiment was performed with AA3104-H19 ( $D=3.32$  in,  $t=0.012$  in) using dry friction conditions. The punch diameter in the deep drawing experiment was 1.968 in. Therefore, the

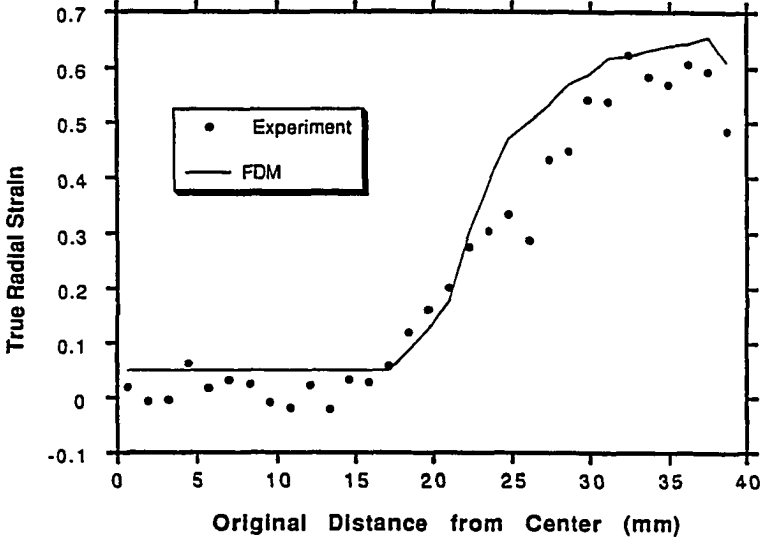


Figure 6.19: Radial strain distribution for reverse redrawing of AA1100-O at the punch travel of 1.5". ( $\mu=0.09$ )

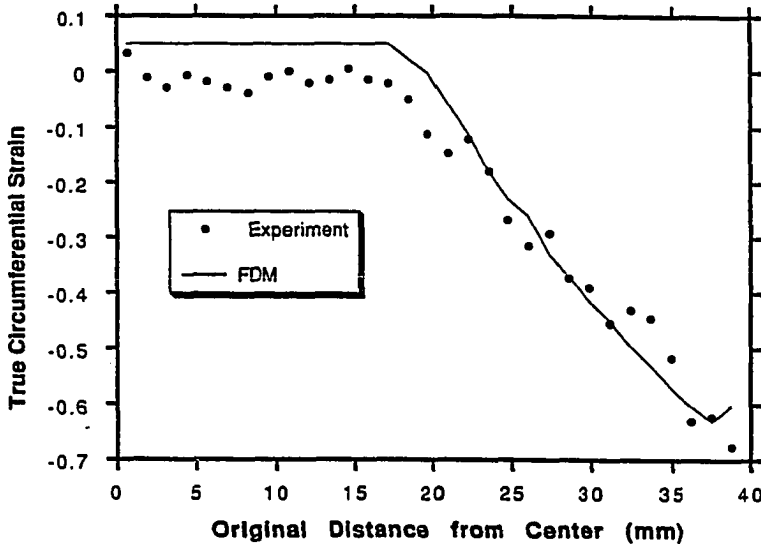
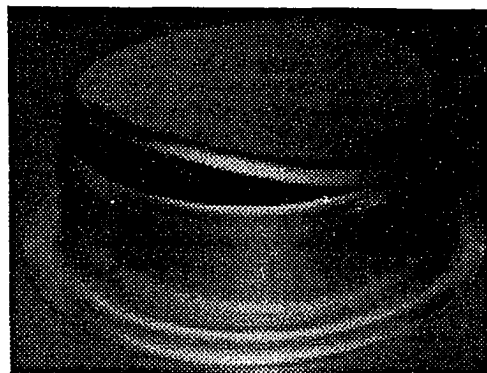
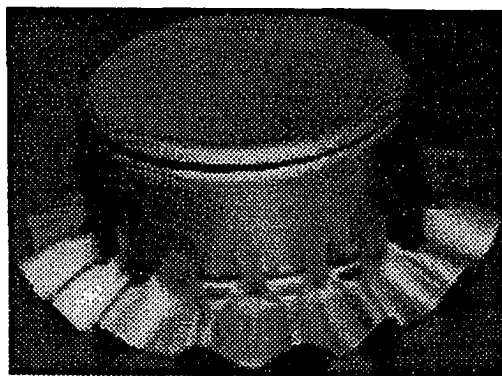


Figure 6.20: Circumferential strain distribution for reverse redrawing of AA1100-O at the punch travel of 1.5". ( $\mu=0.09$ )



a) AA3104-H19,  $D_b=3.32$  in,  $t=0.012$  in, BHF=1.5 kip



b) AA1100-O,  $D_b=4.0$  in,  $t=0.032$  in, BHF=0.0

Figure 6.21: Fracture and wrinkling in deep drawing of aluminum alloys.



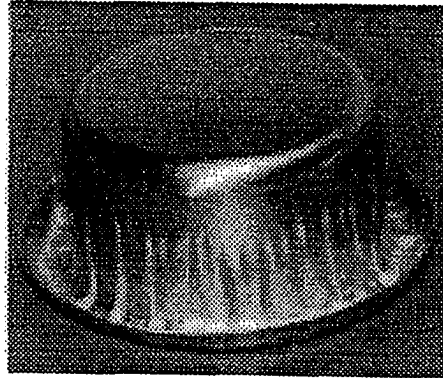
draw ratio in this experiment was 1.68 which is less than the maximum specified for this material, Table F.3. Thus, it was possible to suppress wrinkling completely using a high BHF (BHF=1.5 kip).

In the cup shown in Figure 6.21b, both fracture and wrinkling have occurred. This experiment was performed with AA1100-O (D=4.00 in, t=0.032 in) using water dilutable oil based lubricant under zero BHF. The draw ratio in this deep drawing operation was 2.033 which is higher than the maximum specified for this material, Table F.3. Since the draw ratio is very high it was not possible to prevent wrinkling and fracture using a constant BHF.

Wrinkling which occurred during the reverse redrawing operation is shown in Figure 6.22a. In this operation, a preformed blank (AA3104-H19, D=3.32 in, t=0.012 in) was formed in the second stage without using a BHF. Later, it was possible to suppress the wrinkling completely using a BHF of 0.353 kip, Figure 6.22b. A water dilutable oil based lubricant was used in these experiments.

#### **6.5.1. Failure Criteria**

A failure evaluation module built into SHEET\_FORM was used to predict fracture and wrinkling and the results are compared with experimental observations. The following failure criteria can be used to predict failure;



a) BHF=0.0



b) BHF=0.353 kip

Figure 6.22: Wrinkling in reverse redrawing of AA3104-H19.  
( $D_b=3.32$  in,  $t=0.012$  in)

Forming Limit Diagram (FLD):

Major and minor strains are plotted on a forming limit diagram to predict failure. Since it was not possible to find the actual FLD in the literature for the materials that are used in the experiments, the shape of the FLD is approximated by two lines in the negative and positive minor strain regions, together with  $FLD_0$  and a bandwidth around these lines. Initially, all the constants which are required to define the shape of the FLD are selected approximately. In this selection, since the FLD for AA1100-O was not readily available, the FLD's for other aluminum alloys, [ASM, 1988], are taken into consideration, Figure 6.23. Initial, guess, parameters to define the FLD diagram for AA1100-O are selected as follows;

Slope in the negative minor strain range : -1.4

Slope in the positive minor strain range : 0.5

Plane strain intercept ( $FLD_0$ )': 20

Bandwidth : 10

Later,  $FLD_0$  which is used in failure predictions during the simulation is calculated as follows;

$$FLD_0 = C_f \cdot (FLD_0)' \quad (6.5)$$

where  $C_f$  is a constant calculated from experiments. To determine  $C_f$ , several preliminary experiments with different blankholding forces were performed to cause fracture in the cup. Then  $C_f$  was calculated to predict fracture, using

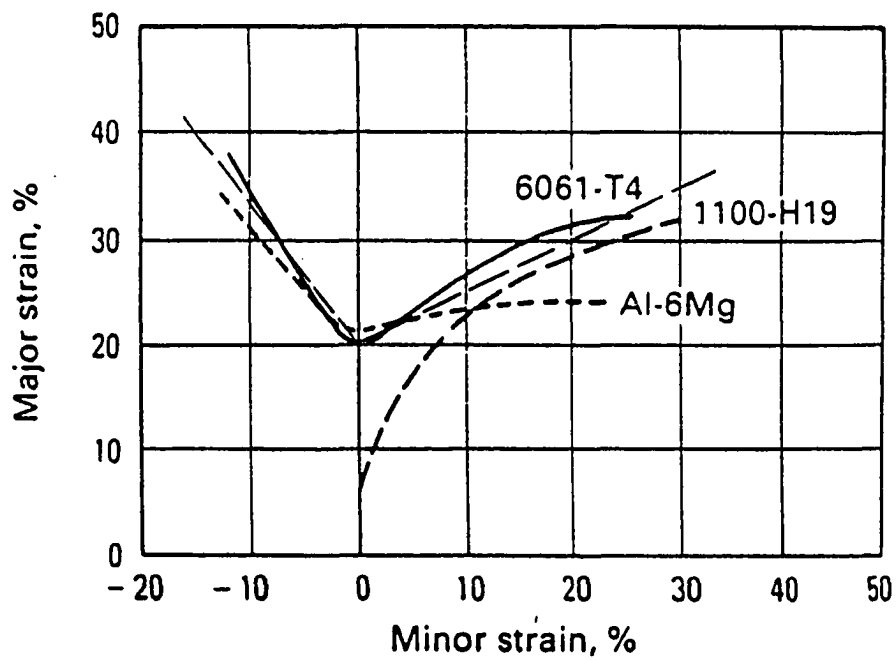


Figure 6.23: Initial, guess forming limit diagram for AA1100-O.

the FLD during the simulations, at the same punch travels measured in the preliminary experiments.

Stress Based Fracture Criterion (SBFC):

Based on the instability conditions in the flange and the wall areas, the Swift's power law equation, and the Hill's theory of plasticity, critical radial stresses can be found as, [Asthana, et al., 1991];

$$\text{in the flange area - } (\sigma_r)_{\text{critical}} = \sigma_0 n^n$$

$$\text{in the wall area - } (\sigma_r)_{\text{critical}} = \sigma_0 n^n S^{n+1}$$

$$\text{where } S = (1+R)/(1+2R)^{1/2}$$

$\sigma_0$  : tensile strength of the material

$n$  : strain hardening coefficient

$R$  : average anisotropy factor

If the radial stress exceeds these critical stresses at any point in the flange or wall area, failure is predicted to occur at that point.

Wrinkling Criterion (WC):

If the compressive stresses that occur in the flange area during the deformation exceeds the buckling resistance of the material, then wrinkling is predicted to occur.

$$\sigma_h \leq C_w \sigma_c \tag{6.6}$$

where  $\sigma_h$  : hoop stress in the flange area

$\sigma_c$  : critical buckling stress

$C_w$  : constant

$C_w$  is determined experimentally for each material. Several preliminary experiments were performed with different low blankholder forces to cause wrinkling, and  $C_w$  was calculated to predict wrinkling during the simulation at the same punch travels that wrinkling has occurred during the preliminary experiments.

The critical buckling stress for aluminum blanks having different thicknesses and diameters are given in Table 6.10.

**Table 6.10: Critical buckling stresses for aluminum alloys.  
Calculated based on material and geometry of the blanks.**

<u>t(in)</u>	<u>D(in)</u>	<u><math>\sigma_c</math>(psi)</u>
0.012	3.32	1346
0.020	3.32	3720
0.032	3.32	9574
0.012	4.00	504
0.020	4.00	1400
0.032	4.00	3584

### 6.5.2. Verification of the Failure Criteria with Experiments

During the experiments, cups were formed from different materials under different process conditions. "Failure heights", i.e. the cup height or punch stroke when failure occurs, were determined by conducting several experiments to determine the punch travel that will cause a crack and initiate fracture and actually measuring the cup height after the cup is removed from the press. "Wrinkling heights" were determined by forming the cups to different heights under the same blankholder load, and measuring the wave lengths of wrinkles. Each experiment to determine the punch travels at failure, for both wrinkling and fracture, was repeated three times to check the repeatability of the experiments. Thus, each experimentally measured data points shown on the plots in this section is the average of these three experiments.

#### AA3104-H19 - Dry friction

A series of experiments were performed using 3.32 in diameter and 0.012 in thick AA3104-H19 blanks under dry friction conditions. The blankholder pressure was kept constant during the experiments. Failure heights were determined corresponding to different levels of blankholder pressures. The forming process was simulated using SHEET\_FORM to predict failure theoretically. The friction coefficient was set to  $\mu=0.25$  based on suggested empirical values to simulate dry friction conditions.  $C_f$  of Equation 6.5 was

determined as 0.6 using 2.79 kip blankholder force, and  $C_w$  of Equation 6.6 was determined as 78 using 0.19 kip blankholder force. Material properties, process conditions, and required parameters to determine the failure criteria are given in Table 6.11.

**Table 6.11: Material properties, process conditions, and definition of failure criteria for deep drawing and reverse redrawing of AA3104-H19**

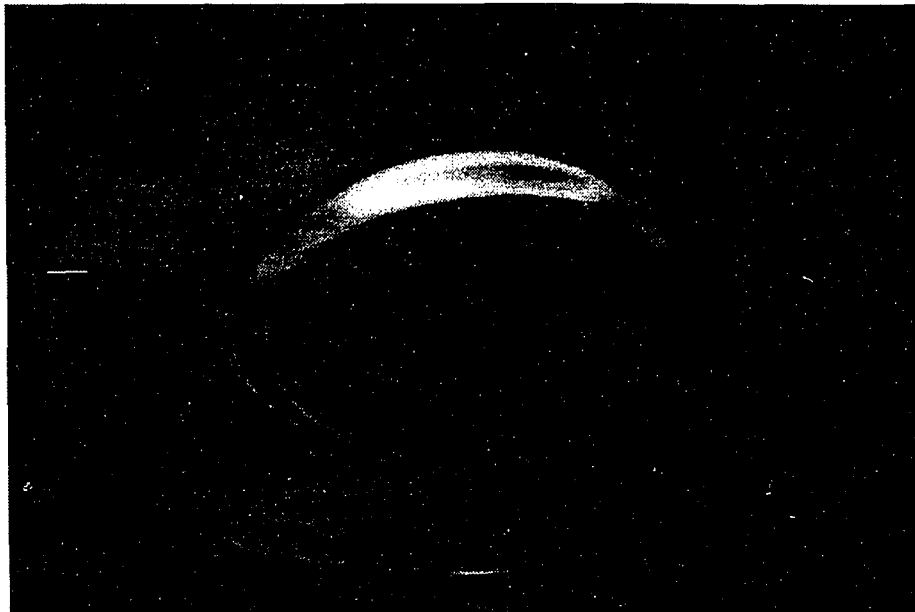
<u>Material Properties and Blank Dimensions</u>		
$\bar{R}$ (Anisotropy Factor)	=	1.8
K (Strain-Hardening Coeff.)	=	52.211 Ksi
n (Strain-Hardening Exp.)	=	0.06547
Blank Diameter	=	3.32 in
Blank Thickness	=	0.012 in
<u>Process Conditions</u>		
Lubrication	=	dry friction
Blankholder Force	=	0.19 - 2.79 kip
Cup Height	=	at failure
<u>Failure Criteria</u>		
FLD <sub>0</sub> '(initial plane strain interception)	=	20
$C_f$ (Correction factor of FLD <sub>0</sub> )	=	0.6
$\bar{\sigma}_c$ (Critical buckling stress)	=	1346 psi
$C_w$ (correction factor of $\bar{\sigma}_c$ )	=	78



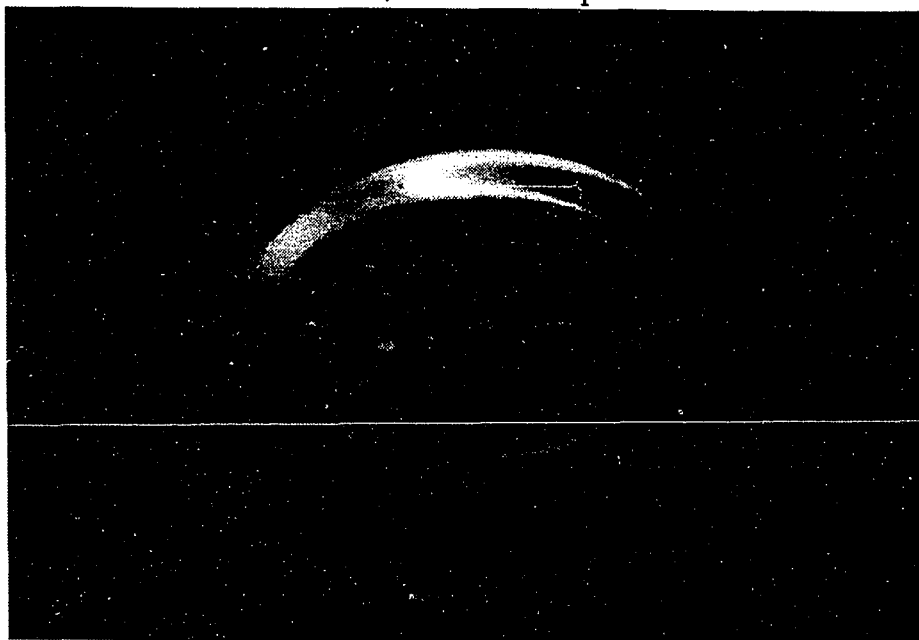
Two cups formed from AA 3104-H19 are shown in Figure 6.24. Both of the cups were drawn to a depth of 0.15 inches. The first cup (Figure 6.24a) was formed using a blank holder force of 0.25 kip. In this case, small wrinkles occurred at the flange area. In order to prevent these wrinkles from initiating BHF was increased to 0.55 kip and as it is seen in Figure 6.24b wrinkles disappeared.

Another defect which can be found in Figure 6.24 is the waviness in the flange area. This is due to small sheet thickness (0.012") compared to the large flange region. It was not possible to prevent this waviness by changing the BHF. However, it disappeared in the later stages of the deformation as the punch travel increased and the flange area was reduced.

Comparison of experimentally measured and theoretically predicted failure limits are shown in Figure 6.25. In this figure, the cup height at which failure, i.e. wrinkling or fracture, was determined is plotted against blankholder force. Since high BHF prevents the initiation of wrinkles, the wrinkling limit increases as the BHF increases until BHF reach around 1.32 kip. If the blankholder force increases further, then fracture occurs since it introduces excessive tensile stresses in the cup wall. The cup height that can be obtained without fracture at higher blankholder force decreases with increasing blankholder force. Two fracture criteria, i.e. the FLD and SBFC, were used to predict failure. The SBFC predicts a higher fracture limit. This is due to the determination of the critical stress in the wall region. The critical stress is determined under plane strain conditions, i.e.  $\epsilon_\theta = 0$ , in the wall region. This may not be true especially for non-annealed materials.



a) BHF=0.25 kip



b) BHF=0.55 kip.

Figure 6.24: Effect of BHF on wrinkling in deep drawing AA3104-H19. Blank diameter is 3.32", thickness is 0.012", cup diameter is 0.1968", cup depth is 0.15", dry friction.

## Wrinkling and Fracture Limits

Material : AA3104-H19

$t = 0.012$  In

Dry friction

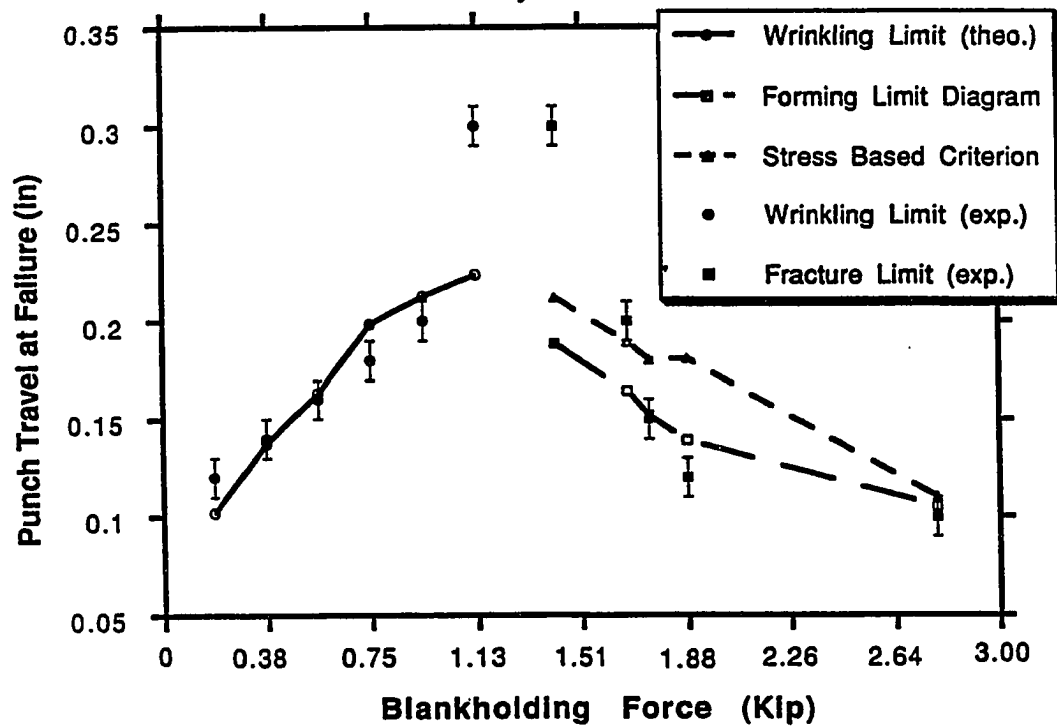


Figure 6.25: Fracture and wrinkling limits for deep drawing of AA3104-H19 under dry friction conditions. ( $\mu=0.25$ )

AA3104-H19 - Water Dilutable Oil Based Lubricant

Same experiments were repeated with 3.32 in diameter and 0.012 in thick AA3104-H19 blanks using water dilutable oil based lubricant. The lubrication conditions were simulated using  $\mu=0.09$  as a friction coefficient in the analysis program based on earlier experience. The experiments were repeated by changing the blankholder force between 0.19 kip and 2.83 kip, and fracture has never occurred.  $C_w$  of Equation 6.6 was determined as 45 using the experimental data at a 0.19 kip blankholder force. Material properties, process conditions, and required parameters to determine the failure criteria are given in Table 6.12.

**Table 6.12: Material properties, process conditions, and definition of failure criteria for deep drawing and reverse redrawing of AA3104-H19**

<u>Material Properties and Blank Dimensions</u>		
$\bar{R}$ (Anisotropy Factor)	=	1.8
K (Strain-Hardening Coeff.)	=	52.211 Ksi
n (Strain-Hardening Exp.)	=	0.06547
Blank Diameter	=	3.32 in
Blank Thickness	=	0.012 in
<u>Process Conditions</u>		
Lubrication	=	oil b. lube.
Blankholder Force	=	0.19 - 2.83 kip
Cup Height	=	at failure
<u>Failure Criteria</u>		
$\sigma_c$ (Critical buckling stress)	=	1346 psi
$C_w$ (correction factor of $\sigma_c$ )	=	45

Two cups which were formed from AA3104-H19 to a depth of 0.42 inches using water dilutable oil based lubricant are shown in Figure 6.26. The first cup (Figure 6.26a) was formed using a BHF of 0.75 kip. As it is seen in Figure 6.26a, small wrinkles has occurred in this cup. As the BHF was increased to 2.0 kip wrinkles disappeared (Figure 6.26b). Large waves has occurred in these experiments, too. However, as the deformation proceeded and the sheet was drawn-in to the die cavity the waviness disappeared (Figure 6.27).

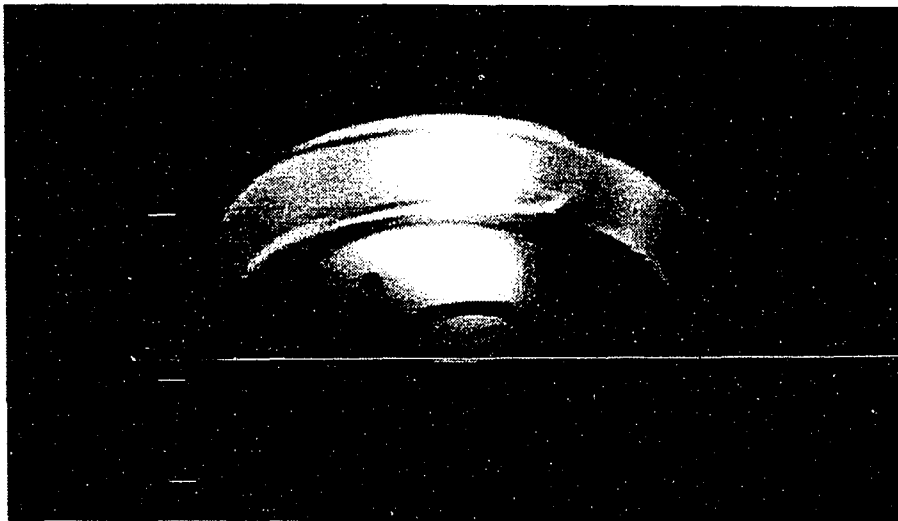
Both experimentally measured and theoretically predicted wrinkling limits are shown in Figure 6.28. The cup height or punch stroke position, at which wrinkling started, is increased by using the water dilutable oil based lubricant compared to the punch stroke position when wrinkling is observed in the experiments under dry friction conditions. This is due to the fact that lubrication provided better metal flow into the die cavity, and thus, caused a reduction in the compressive stresses in the flange region. Wrinkling was observed even with high blankholder forces but the number of wrinkles and their wave lengths were decreased with increasing force.

#### AA1100-O - Machine oil (sheet thickness is 0.020")

Another series of experiments were performed using 3.32 in diameter and 0.020 in thick AA1100-O blanks. In these experiments, a machine oil was used. Lubrication conditions were simulated by using  $\mu=0.11$ , based on suggested empirical values, as a friction coefficient in the analysis program. Fracture limit was predicted using FLD. A value for  $C_f$  in Equation 6.5 was determined as 0.7 using the experimental data obtained at a 2.1 kip blankholder force. A value for  $C_w$  in Equation 6.6 was determined as 0.81



a) BHF=0.75 kip



b) BHF=2.0 kip.

Figure 6.26: Effect of BHF on wrinkling in deep drawing AA3104-H19. Blank diameter is 3.32", thickness is 0.012", cup diameter is 0.1968", cup depth is 0.42", oil based lubricant.

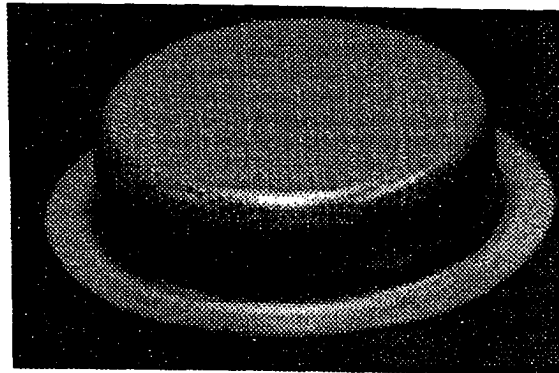
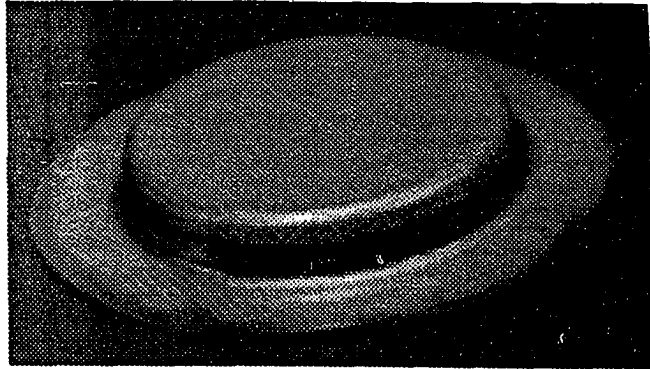


Figure 6.27: Deep drawing of AA 3104-H19 to the height of 0.42 inches and 0.75 inches using BHF of 2.0 kip. (Blank diameter is 3.32", thickness is 0.012", cup diameter is 0.1968", oil based lubricant.)





using the experimental data at a 0.28 kip blankholder force. Material properties, process conditions, and required parameters to determine the failure criteria are given in Table 6.13. Theoretically predicted failure limits are shown in Figure 6.29 compared with experimentally determined limits. Both wrinkling and fracture limits compare well with the experiments. The

**Table 6.13: Material properties, process conditions, and definition of failure criteria for deep drawing and reverse redrawing of AA1100-O**

<u>Material Properties and Blank Dimensions</u>		
$\bar{R}$ (Anisotropy Factor)	=	0.8955
K (Strain-Hardening Coeff.)	=	23.437 Ksi
n (Strain-Hardening Exp.)	=	0.2297
Blank Diameter	=	3.32 in
Blank Thickness	=	0.020 in
<u>Process Conditions</u>		
Lubrication	=	machine oil
Blankholder Force	=	0.28 - 2.1 kip
Cup Height	=	at failure
<u>Failure Criteria</u>		
FLD <sub>0</sub> ' (initial plane strain interception)	=	20
C <sub>f</sub> (Correction factor of FLD <sub>0</sub> )	=	0.7
σ <sub>c</sub> (Critical buckling stress)	=	9574 psi
C <sub>w</sub> (correction factor of σ <sub>c</sub> )	=	0.81

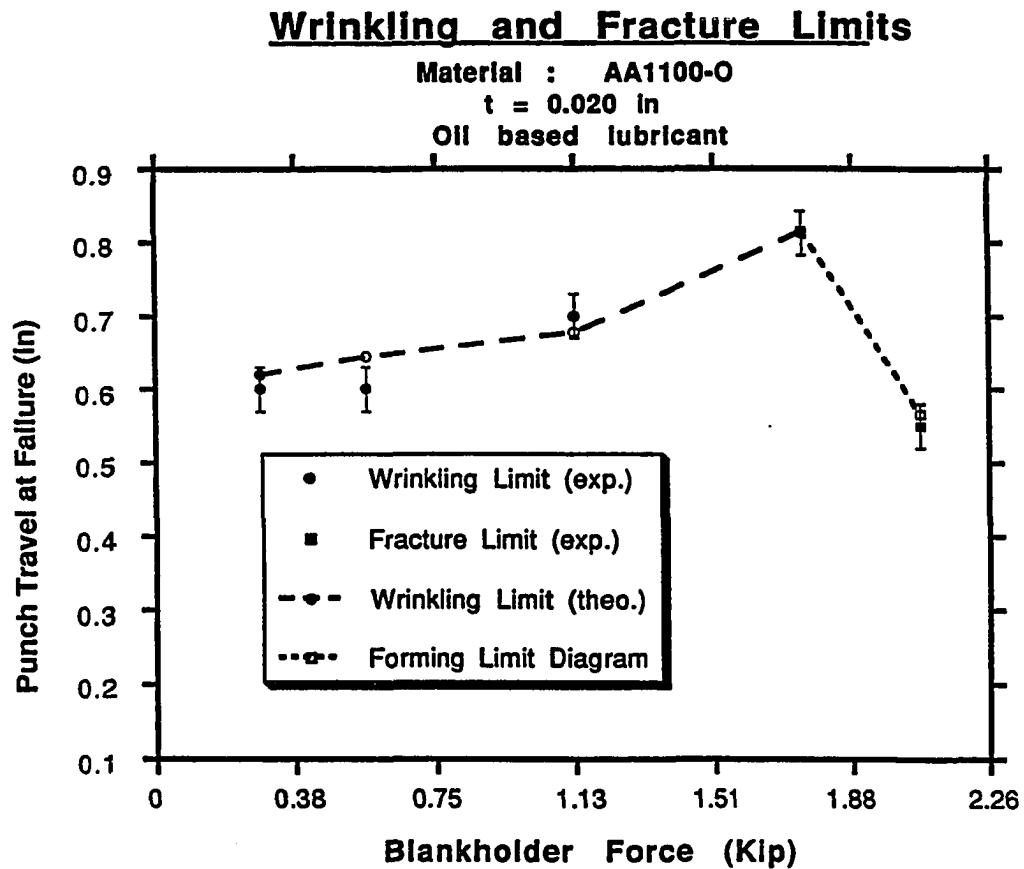


Figure 6.29: Wrinkling and fracture limits for deep drawing of 0.020" thick AA1100-O using machine oil. ( $\mu=0.11$ )

wrinkling limit did not vary much with increasing blankholder force, and it was not possible to obtain a fully drawn cup without failure. Fracture first occurs at .8125 in punch travel at 1.75 kip blankholder force. An increased blankholder force decreases the fracture height to 0.55 in at 2.1 kip. If the blankholder force is increased to 2.83 kip, fracture occurred at the same height.

AA1100-O - Machine oil (sheet thickness is 0.032")

Another set of experiments were performed using 3.32 in diameter and 0.032 in thick AA1100-O blanks, and a machine oil as the lubricant. The friction coefficient that was used in the simulations is 0.11, based on suggested empirical values. An FLD was used in the analysis to predict the fracture limit. The value for  $C_f$  in Equation 6.5 was determined as 0.75 using the experimental data at 2.83 kip blankholding force. Material properties, process conditions, and required parameters to determine the failure criteria are given in Table 6.14. The punch stroke positions at failure obtained in this case are shown in Figure 6.30. During the simulations, wrinkling was not predicted for the BHF range given in Figure 6.30. In the experiments, it was observed that the number of wrinkles and the wave lengths of wrinkles stayed about the same until the blankholder force of 1.7 kip was reached. Compared to the experiments with 0.020 inches thick AA 1100-O blanks (Figure 6.29), experiments with 0.032 inches thick AA 1100-O blanks (Figure 6.30) showed smaller overall cup heights at wrinkling. This may be an error in the experiments. Because, wrinkling is usually more severe with thinner materials. As the thickness of the material increases the BHF which is required to prevent wrinkling decreases.

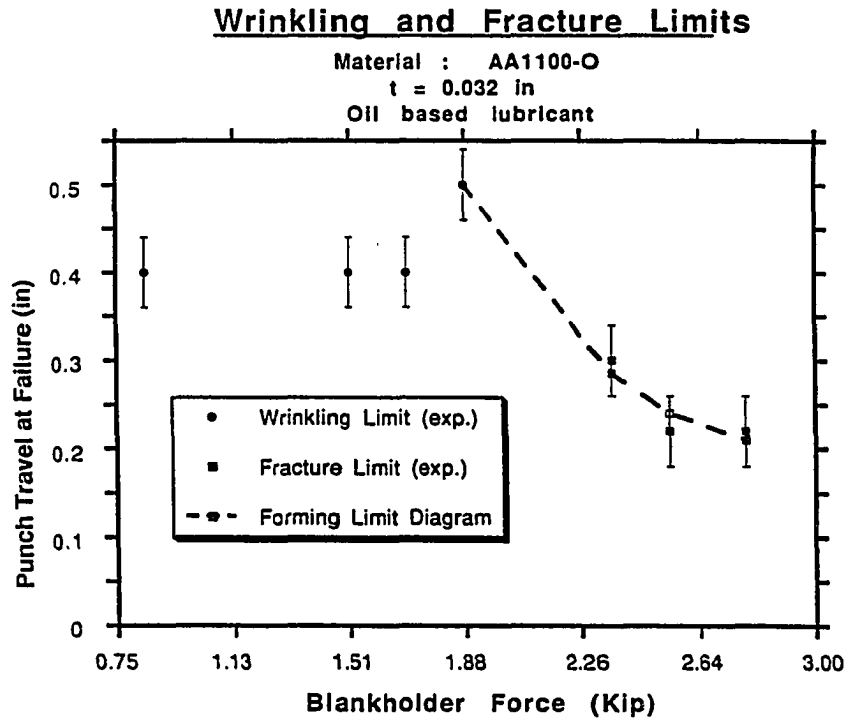


Figure 6.30: Wrinkling and fracture limits for deep drawing of 0.032" thick AA1100-O using machine oil. ( $\mu=0.11$ )

### Effect of Draw Ratio Upon Failure

The effect of draw ratio, i.e. the ratio of blank diameter to the punch diameter, on the fracture limit is studied in this section. Two experiments were performed using 0.012 in thick AA3104-H19 blanks. In these experiments, the

**Table 6.14: Material properties, process conditions, and definition of failure criteria for deep drawing and reverse redrawing of AA1100-O**

<u>Material Properties and Blank Dimensions</u>		
$\bar{R}$ (Anisotropy Factor)	=	0.8955
K (Strain-Hardening Coeff.)	=	23.437 Ksi
n (Strain-Hardening Exp.)	=	0.2297
Blank Diameter	=	3.32 in
Blank Thickness	=	0.032 in
<u>Process Conditions</u>		
Lubrication	=	machine oil
Blankholder Force	=	0.75 - 2.83 kip
Cup Height	=	at failure
<u>Failure Criteria</u>		
FLD <sub>0</sub> '(initial plane strain interception)	=	20
C <sub>f</sub> (Correction factor of FLD <sub>0</sub> )	=	0.75

blank diameters were 3.32 in and 4.00 in. These blank diameters correspond to 1.66 and 2.0 draw ratios, respectively. These blanks are formed using a

water dilutable oil based lubricant under a 1.7 kip blankholder force. The punch stroke positions at which failure occurs are shown in Figure 6.31. The blank with 3.32 original diameter was fully formed to the height of 0.875 in without any fracture. The second blank which has 4.00 in diameter has fractured at 0.65 in punch travel. Using this fracture point,  $C_f$  of Equation 6.5 was determined as 0.85. Fracture limits are determined theoretically by using both the FLD and SBFC, and the wrinkling criteria was turned off during these simulations. Material properties, process conditions, and required parameters for failure criteria are given in Table 6.15.

**Table 6.15: Material properties, process conditions, and definition of failure criteria for deep drawing and reverse redrawing of AA3104-H19**

<u>Material Properties and Blank Dimensions</u>		
$\bar{R}$ (Anisotropy Factor)	=	1.8
K (Strain-Hardening Coeff.)	=	52.211 Ksi
n (Strain-Hardening Exp.)	=	0.06547
Blank Diameter	=	3.32 in
Blank Thickness	=	0.012 in
<u>Process Conditions</u>		
Lubrication	=	w. b. lube.
Blankholder Force	=	1.7 kip
Cup Height	=	at failure
<u>Failure Criteria</u>		
FLD <sub>0</sub> '(initial plane strain interception)	=	20
$C_f$ (Correction factor of FLD <sub>0</sub> )	=	0.85

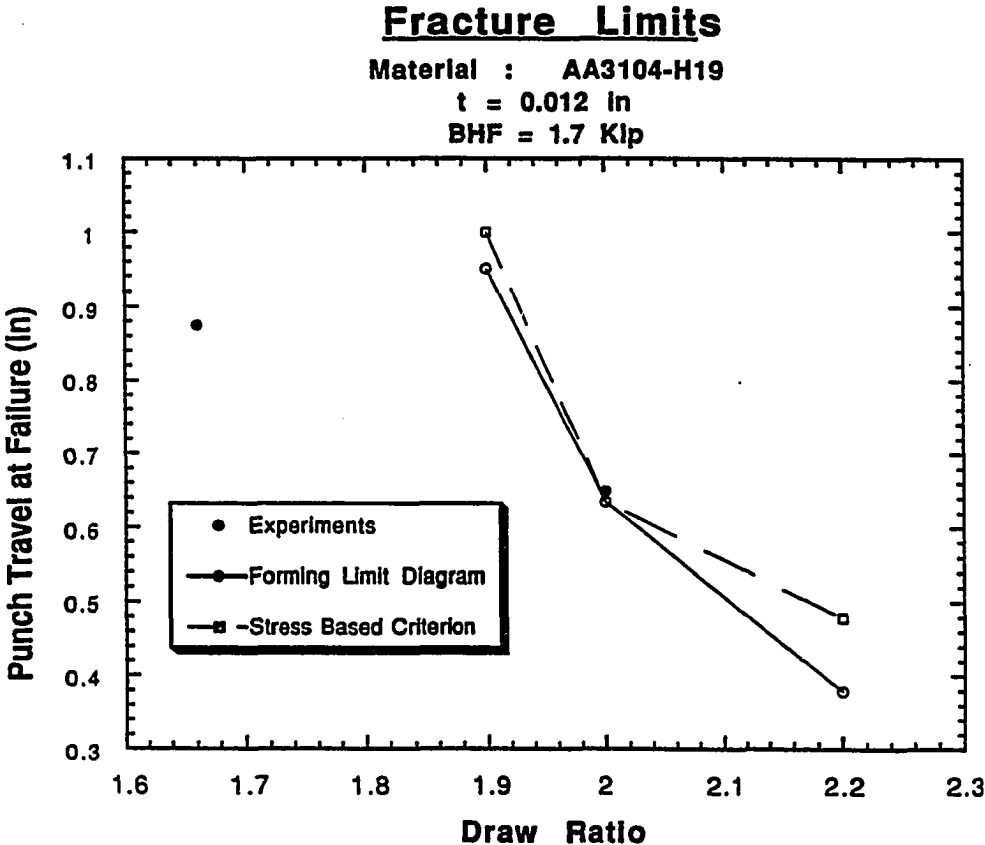


Figure 6.31: Effect of draw ratio on fracture limit. ( $\mu=0.09$ )

Theoretically determined FLD and SBFC limits are drawn with solid and dashed lines, respectively, in Figure 6.31. At the constant blankholder force level of 1.7 kip, as the draw ratio increases the cup height that can be obtained without fracture decreases. With small discrepancies both FLD and SBFC were able to determine this variation. In the following simulations, the draw ratio was kept constant at 2.2 and the blankholder pressure was set to different values to study the effect of blankholder pressure on the fracture limit at this draw ratio. Simulation results are shown in Figure 6.32. In this figure, the theoretically predicted wrinkling curve is shown too. As it can be seen from the figure, it is not possible to draw this cup completely using constant blankholder pressure. Fracture is predicted to occur even at lower blankholder pressures, and wrinkling is predicted to occur at high blankholder pressures. The blankholder pressure should be varied during the forming process to increase the draw height.



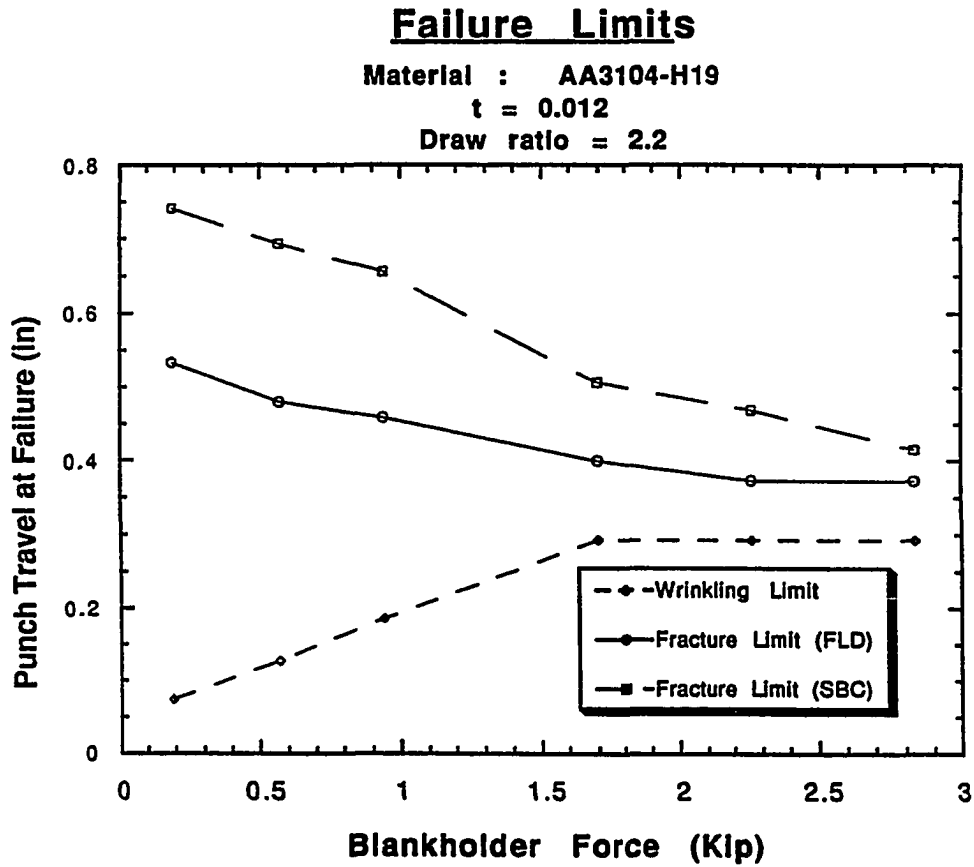


Figure 6.32: Predicted wrinkling and fracture limits for draw ratio of 2.2.  
 ( $\mu=0.09$ )

## CHAPTER VII

### DEEP DRAWING OF ROUND CUPS IN 160 TON DOUBLE ACTION HYDRAULIC MINSTER PRESS

#### 7.1. Specifications of the Minster Press

The MINSTER press was partially donated to ERC/NSM by Minster Machine Co., Minster, Ohio, and was installed at the ERC in early 1991. It belongs to the MINSTER/Tranemo DPA series which are designed for all types of metal-forming, from automated systems to manual operations. Its main dimensions and specifications are given in Table 7.1, and Figure 7.1.

#### Technical description

The frame of the press is of quality welded steel one-piece construction. The frame bed has extra heavy bolster support plates. The frame is designed for automatic feeding systems and has large upright openings for easy access. This rigid frame allows only minimum deflection which, in turn, gives longer die life.

**Table 7.1: Specifications of the 1-DPA-160-10 MINSTER/Tranemo Hydraulic Press.**

<b><u>Force</u></b>			
Nominal pressing force	160	[tonf]	
Die cushion force	100	[tonf]	
Ejector force	15	[tonf]	
<b><u>Stroke length</u></b>			
Slide stroke (A)*	500	[mm],	(19.7")
Die cushion stroke (B)	190	[mm],	(7.5")
Ejector stroke (C)	249	[mm],	(9.8")
<b><u>Dimensions</u></b>			
Press bolster right - left (D)	1000	[mm],	(39.4")
Press bolster front - back (E)	1000	[mm],	(39.4")
Press slide right - left (D)	1000	[mm],	(39.4")
Press slide front - back (F)	1000	[mm],	(39.4")
Cushion top plate right - left (G)	800	[mm],	(31.5")
Cushion top plate front - back (H)	800	[mm],	(31.5")
Maximum daylight (J)	800	[mm],	(31.5")
Minimum daylight (K)	292.1	[mm],	(11.5")
Width of opening in frame sides (Q)	749	[mm],	(29.5")
Height of opening (R)	800	[mm],	(31.5")
<b><u>Overall Dimensions</u></b>			
Total width left - right (L)	2800	[mm],	(110.2")
Total depth front - back (M)	2600	[mm],	(102.4")
Total height (N)	3900	[mm],	(153.5")
Height floor to top of bolster (P)	995	[mm],	(39.2")
<b><u>Weight</u></b>			
Total weight (approx.)	13,000	[Kg],	(28,700 [lb.])
<b><u>Speeds</u></b>			
Closing speed	365	[mms <sup>-1</sup> ]	(860"[min <sup>-1</sup> ])
Max. pressing speed at 98 tons	40	[mms <sup>-1</sup> ]	(100"[min <sup>-1</sup> ])
Max. pressing speed at full tonnage	30	[mms <sup>-1</sup> ]	(75"[min <sup>-1</sup> ])
Max. return speed	390	[mms <sup>-1</sup> ]	(920"[min <sup>-1</sup> ])
Max. return speed with engaged cushion	130	[mms <sup>-1</sup> ]	(310"[min <sup>-1</sup> ])
<b><u>Power</u></b>			
Motor power	30	[kW]	(40 [HP])

\* Capital letters between parentheses are used to illustrate the corresponding dimension in Figure 7.1.

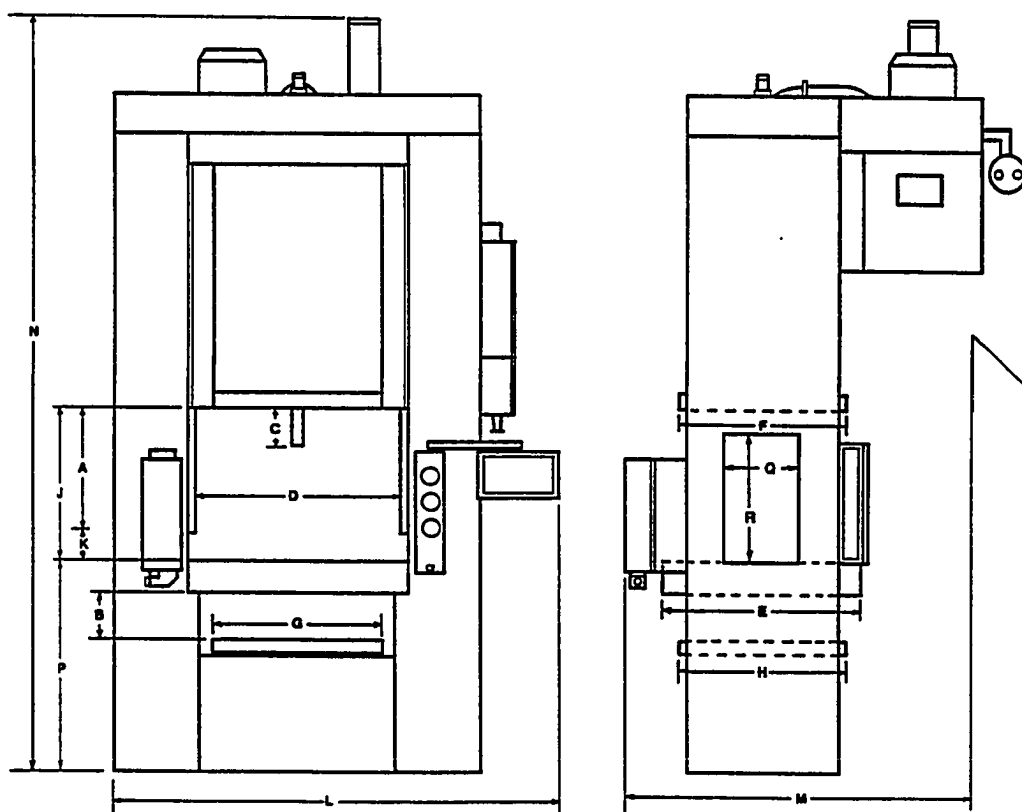


Figure 7.1: The 1-DPA-160-10 Minster/Tranemo hydraulic press, and overall dimensions. (L=2800 mm, M=2600 mm, N=3900 mm)

The slide is of welded steel and guided by eight adjustable (extra-long span), self-lubricating bronze gibs. The rigid slide is designed to accept the loading inherent in progressive tools and also when using several tools in one setup. The slide is furnished with 25.4 mm (1") T slots for die mounting.

The hydraulic system is mounted at the top of the press frame so as not to interfere with the working area of the press.

The slide has a built-in hydraulic ejector which can also be used as an upper die cushion cylinder or as a cylinder for controlling special tooling.

The die cushion is mounted within the press bed. Pressure and stroke length are adjustable within the stroke range by setting from control panel. The pressure from the cushion is transferred to the die by means of die cushion pins. The cushion top plate is mounted directly to the cylinder piston rod and guided by the steel pins. The cushion can also be operated separately without operating the main slide.

The press is equipped with an Allan Bradley PLC 5/15 Programmable Controller. The setup control units, along with "Manual", "Single-stroke", and "Continuos" operation controls are located in a swing-arm console with clear, easy-to-read visual displays of stroke lengths and pressures. The control system also includes a photo-electronic light curtain across the front of press for safety as well as ease of access to die area. The press control panel is mounted to the right hand side of the press frame above the swing-arm console.

The press is equipped with the following features.

- Complete hydraulic and electrical equipment with controls on movable console.
- Hydraulic die cushion, complete hardened cushion pins.
- Built-in machine lightning in both sides of frame.
- Automatic oil cooling (by water) system.
- Stroke counter and hour meter.
- Photo electric light curtain across the front of the press.
- Barrier guards on back and sides of press and access covers on die cushion top plate (front and back), electrically interlocked.

## 7.2. Material Properties and Process Conditions

### 7.2.1. Materials

To carry out deep drawing experiments five materials were available in our laboratory. These are: two different aluminum alloys<sup>1</sup> (AA), and three types of steel<sup>2</sup>. These materials and their thicknesses are shown in Table 7.2. Sheet metal blanks were cut into different diameters to study the effect of draw ratio on strains, forcés, and failure in deep drawing round cups.

---

<sup>1</sup> Aluminum alloys which are used in these experiments are obtained from the following companies;

AA1100-O : ALCAN Rolled Products Co.

AA2024-O : Grumman Aerospace Co.

<sup>2</sup> All types of steel which are used in these experiments are obtained from ARMCO Research and Technology, Carbon Steel Flat-Rolled Products, Middletown, Ohio.

**Table 7.2: Materials which are used in the experiments.**

Material	Thickness [mm]	[in]
AA 1100-O	0.8128	0.031
AA 2024-O	1.016, 1.6002	0.040, 0.063
High Strength Hot Dipped Galvanized Steel (HSG)	0.889	0.035
Interstitial Free Steel (IF)	0.8382	0.033
Univit Steel (UV)	0.7874	0.031

**Table 7.3: Material properties\***

Material	n	K [Nmm <sup>-1</sup> ]	R	$\epsilon_0$
AA 1100-O	0.2297	161.736	0.8955	0
AA 2024-O	0.134	266.15	0.73	0
High Strength Hot Dipped Galvanized Steel	0.143	603.83	1.40	0.000328
Interstitial Free Steel	0.263	622.38	1.95	0.000846
Univit Steel	0.254	525.19	1.45	0.008742

\* Material properties for different materials are obtained from the following sources;  
 AA1100-O; from tensile tests, [Ahmetoglu, et al., 1992b]  
 AA2024-O; from literature, [Nagpal, 1979]  
 All three types of steel; from the supplier

To carry out simulations using the finite difference method (FDM) based computer program, several material parameters, such as  $n$ ,  $K$ ,  $\epsilon_0$ , and  $R$ , are needed. Using FDM simulations, the necessary initial BHF to carry out the experiments were estimated. The material properties obtained are listed in Table 7.3.

### 7.2.2. Strain Measurements

A grid was etched on several blanks to measure the strains on deformed cups. There are two methods to produce circles on a surface:

- Photo printing
- Electrochemical etching

Photo printing is usually used for small components with low friction during the stamping operation, i.e. mainly stretching and no draw in.

Electrochemical etching produces a grid much more resistant to wear during deformation, since it is etched into the material. The depth varies from 0.0025 mm - 0.25 mm, and is not supposed to influence the sheet metal properties. Since this type of grid is more robust, electrochemical etching was chosen for our experiments. Circle diameters vary from 1.27 mm - 12.7 mm. The recommended size of the circles depends on the expected strain gradient and the sheet geometry. For geometry and strain distribution considered here, a 2.54 mm circle diameter would be accurate enough.



A 304.8 X 609.6 mm stensile was used to put circle grids on round sheet metal blanks (blank diameters vary from 254.0 mm to 330.2 mm). A sample blank of diameter 330.2 mm is shown in Figure 7.2.

To measure the circle diameters after deformation a traveling microscope which is located in the Material Science and Engineering Department was used. Major and minor strains were calculated from the measured diameters in two orthogonal directions, and later compared to the strain predictions by the FDM simulations.

### 7.2.3. Lubrication

Two types of friction conditions were used in the experiments. These are dry friction and lubricated<sup>3</sup>. Different lubricants were used for different blank materials. These lubricants are listed below;

- for aluminum alloys: product no. DB-4251
- for steel: product no. DB-4210N

Both lubricants are water based emulsified drawing compounds. DB-4251 is especially designed for use over aluminum surfaces. It contains neither pigmented nor extreme pressure additives. DA-4210 is a heavy duty, lightly pigmented, synthetic drawing compound for use in stretch drawing ferrous metals. The friction coefficients (for the simulations) are listed in Table 7.4.

---

<sup>3</sup> Lubricant for both aluminum and steel are obtained from Metal Lubricants Co.

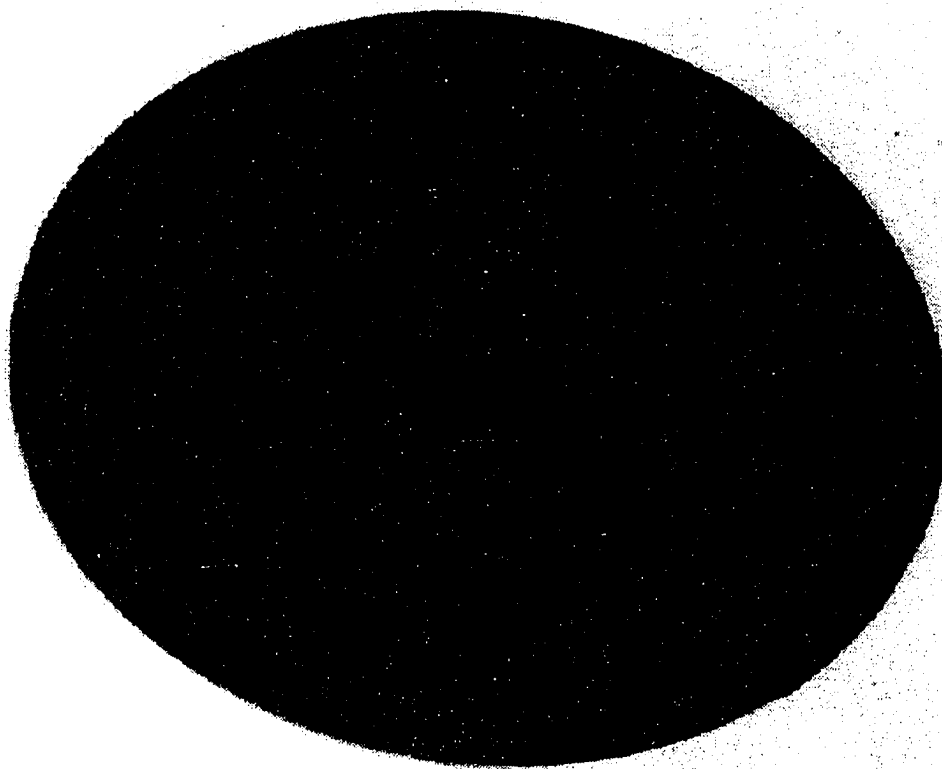


Figure 7.2: A sample round blank with circle grids etched on its surface for strain measurements.

Several simulations were conducted using different friction coefficients to simulate the deep drawing process under lubricated conditions. Predicted strains and punch forces were compared with the experiment results, and the best match is obtained using the friction coefficients given in Table 7.4.

**Table 7.4: Friction coefficients used in the simulations**

Friction condition	Friction coefficient
dry friction	0.25 <sup>*</sup>
DB-4251	0.13 <sup>**</sup>
DB-4210N	0.13

\* The friction coefficient for dry friction is based on suggested values from literature.

\*\* The friction coefficients for the two water base lubricants we used are derived from preliminary FDM simulations.

### 7.3. Deep Drawing of Round Cups

Deep drawing experiments were performed using the tool geometry shown in Figure 7.3, and strain and punch force measurements were compared with the simulation results. The effect of draw ratio, material, friction, and BHF on the strains and punch force have been studied. Strains were measured based on the circle grid analysis method. A sample round cup which was formed in the experiments is shown in Figure 7.4. Circle grids were scratched off at the edge of the blank due to high friction between the sheet metal and the blank holder surfaces. All of the circle grid measurements were

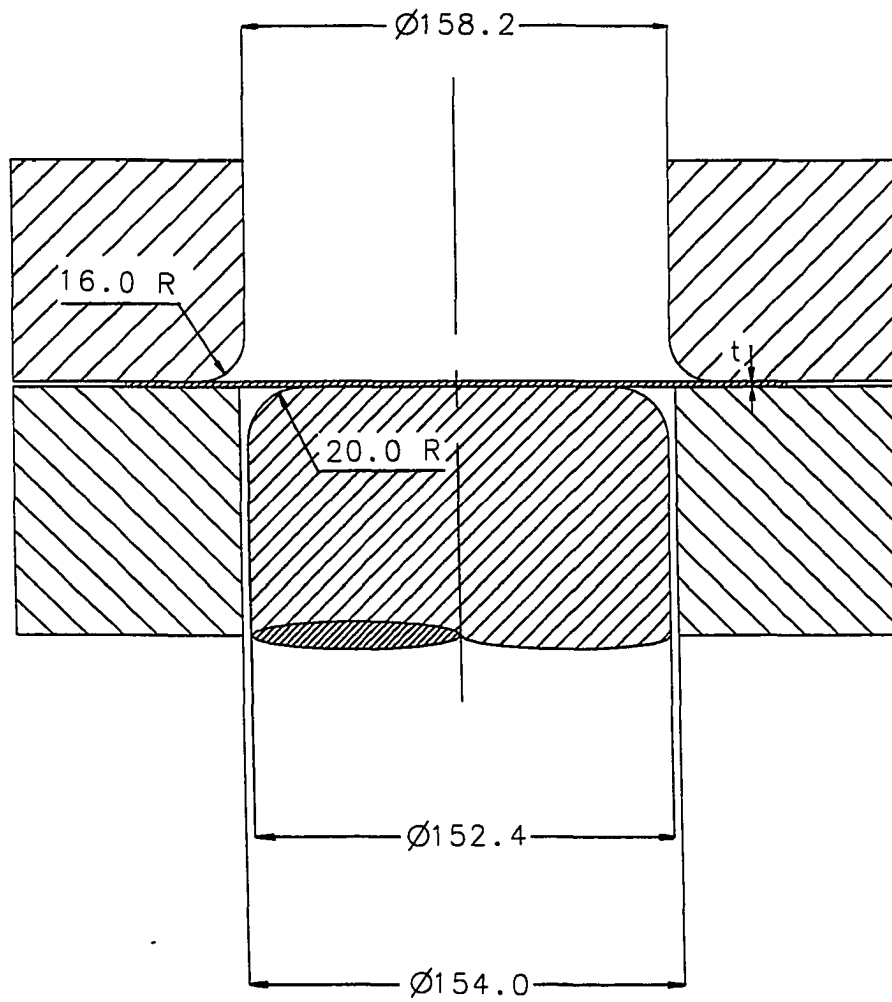


Figure 7.3: Tool geometry for deep drawing of round cups in Minster press.

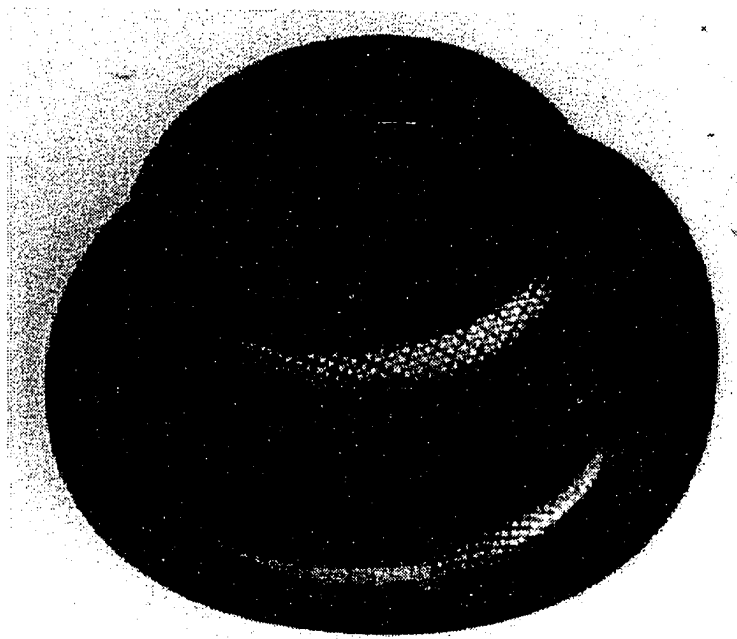


Figure 7.4: A sample cup formed in the experiments.

The experimental results shown on the plots are calculated based on the average of the three experiments. Punch force measurements were repeatable. The variation on the punch force measurements was within 1 tons. The variation from the mean value in the strain measurements was between 2 to 5%.

### Aluminum Alloy 1100-O

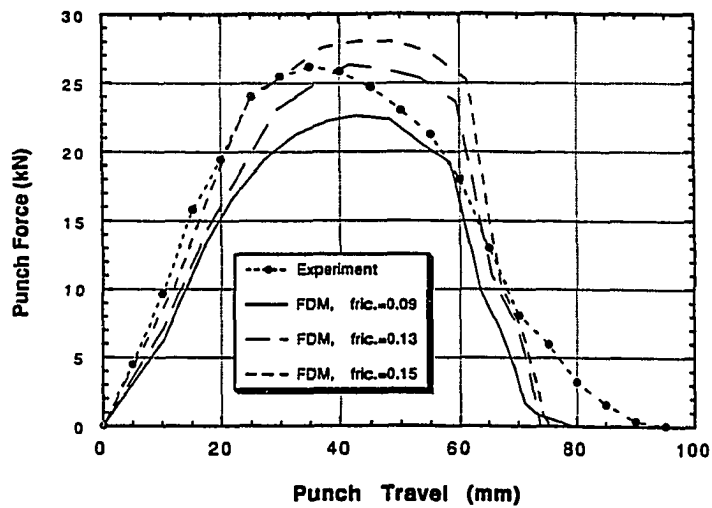
The first set of experiments was conducted using 0.81 mm thick Aluminum Alloy (AA) 1100-O. For clarity, a summary of the material and process conditions is given in Table 7.5. Two different blank diameters were used in the experiments. These are 254.0 mm and 266.7 mm corresponding to draw ratios of 1.667 and 1.75, respectively. Different constant BHF, given in Table 7.5, were used in these experiments.

**Table 7.5: Summary of material properties, and process conditions for deep drawing of AA 1100-O**

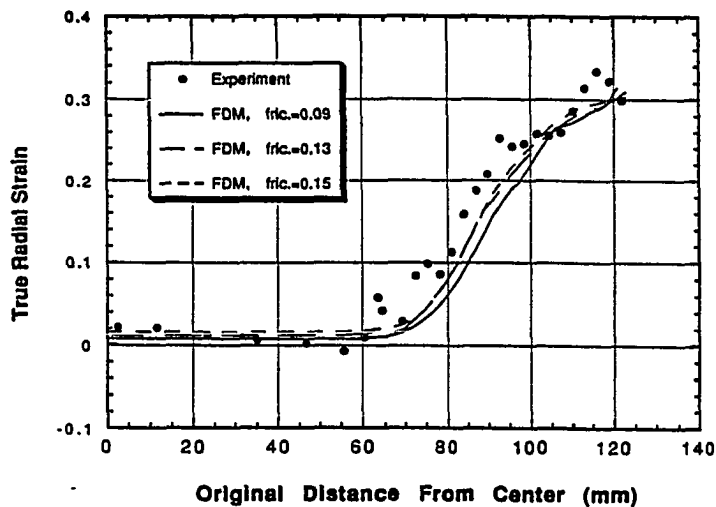
<u>Material properties and blank dimensions</u>	
r (anisotropy factor)	0.8955
K (strength coefficient)	161.736 [MPa]
n (strain hardening exponent)	0.2297
$\epsilon_0$ (pre strain)	0
Blank diameter	254.0, 266.7 [mm]
Blank thickness	0.8128 [mm]
<u>Process conditions</u>	
Lubrication	water base lubricant
Blank holder force	38.2, 54.0, 78.4 [kN]

An experiment was performed using 254.0 mm diameter blanks under 38.22 kN BHF. The cup was fully drawn to the height of 73.8 mm. The punch force versus punch travel diagram predicted by FDM simulations is shown in Figure 7.5a together with the measured punch force profile. Since no friction study had been conducted using the water based lubricant, the friction coefficient was not known a priori. Therefore, several friction coefficients were tried in the simulations. The best agreement was found for a friction coefficient of 0.13. The predicted punch load maximum, however, appears slightly later than the experimental determined one. Once the force starts declining, it can be seen that the FDM predicts a steeper drop than the experimentally obtained one. The most likely reason for this is the earing formation. The outer most parts of the ears are still under the blank holder while the mean flange diameter is on the die corner radius. This applies a force to the flange which results in an increased punch force. The FDM code does not take non-axisymmetry due to anisotropy into account, i.e., no earing is simulated. Thus as soon as the (mean) diameter has left the blankholder the punch load will drop sharply to zero. The predicted radial strain distribution matches the experimentally determined one quite well as shown in Figure 7.5b. As can be seen, a variation in friction coefficient does not alter the strain distribution very much.

Another experiment was performed under the same process conditions except with an increased BHF. The BHF was increased to 78.4 kN in this experiment. The predicted punch force profile shows a good match again



a) Punch force versus stroke diagram.



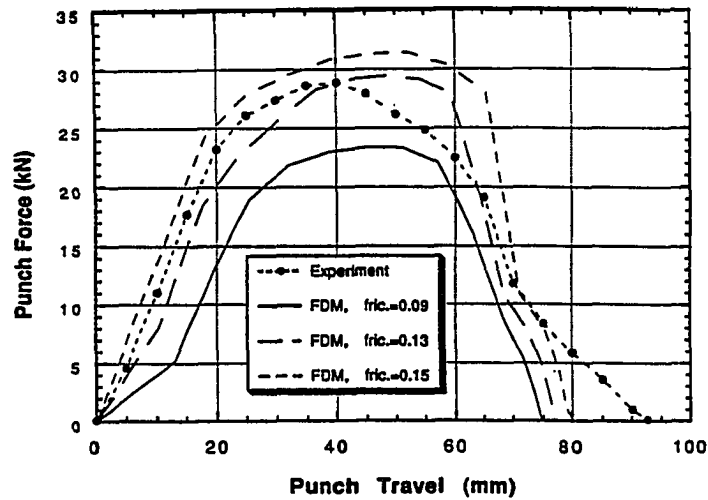
b) Radial strain distribution.

Figure 7.5: Comparison of FDM predictions with the measurements in deep drawing of AA1100-O. ( $D_p=254.0$  mm, BHF=38.22 kN, Punch Travel=73.8 mm, water based lubricant)

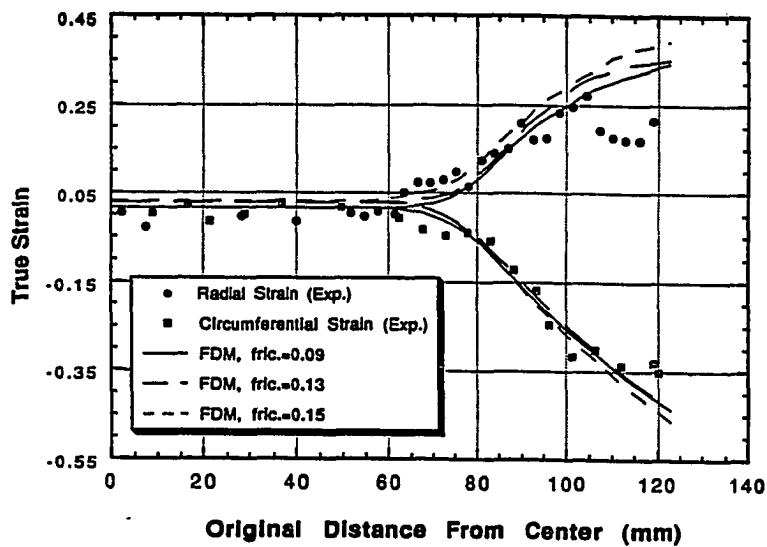


with the measured one as shown in Figure 7.6a. The best match again is found for a friction coefficient of 0.13. A slight shift of the load maximum can be seen in this plot, too. The radial and circumferential strain profiles show a good match except at the edge of the cup as shown in Figure 7.6b. In this region, the experimentally measured strains show a drop. The reason for this is that strain measurements were done in a section between the two ears. Since the BHF is applied only over the ears towards the end of the forming process, there is not much restraining force between the ears. Therefore, radial stresses and radial strains are lower in these regions. Again, it can be seen that a difference in friction coefficient does not make much of a difference in the finally predicted strain distribution. As can be expected, a higher punch load appears with increased blankholding force when comparing the previous two experiments.

Another experiments was performed using the same process conditions given in Table 7.5 except in this case a blank of 266.7 mm diameter was formed using a BHF of 54.0 kN. In this experiment, the cup was formed to a height of 84.9 mm. Punch force, and radial and circumferential strain distributions are shown in Figures 7.7a and b respectively. In the punch force versus stroke comparison, it looks like the best agreement occurs for a friction coefficient between 0.13 and 0.15. However, the friction coefficient does not have much effect on the resulting strain predictions.

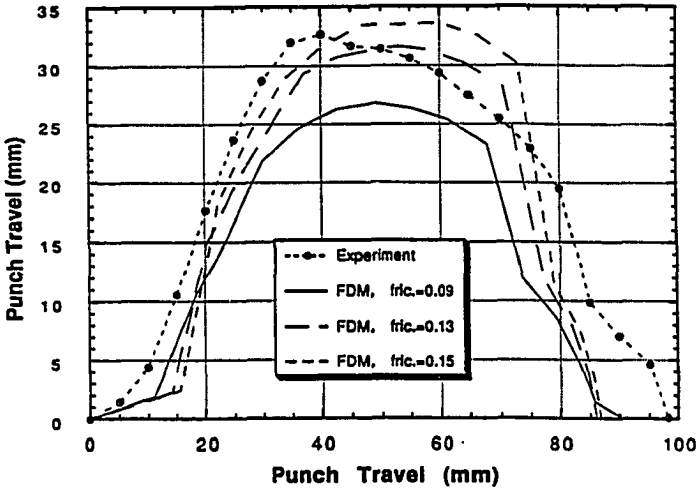


a) Punch force versus stroke diagram.

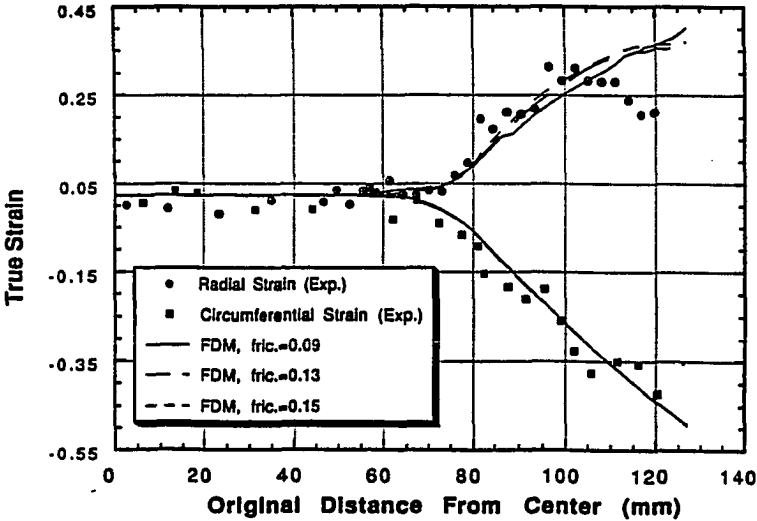


b) Radial and circumferential strain distributions.

Figure 7.6: Comparison of FDM predictions with the measurements in deep drawing of AA1100-O. ( $D_b=254.0$  mm, BHF=78.4 kN, Punch Travel=73.8 mm, water based lubricant)



a) Punch force versus stroke diagram.



b) Radial and circumferential strain distributions.

Figure 7.7: Comparison of FDM predictions with the measurements in deep drawing of AA1100-O. ( $D_p=266.7$  mm, BHF=54.0 kN, Punch Travel=84.9 mm, water based lubricant)

In the previous simulations, the best overall agreement was found for a friction coefficient of 0.13. This value was used in all of the subsequent simulations where the water base lubricant was used.

### Aluminum Alloy 2024-O

The second set of experiments were performed using AA 2024-O. A summary of the material properties, and process conditions are given in Table 7.6.

**Table 7.6: Summary of material properties, and process conditions for deep drawing of AA 2024-O.**

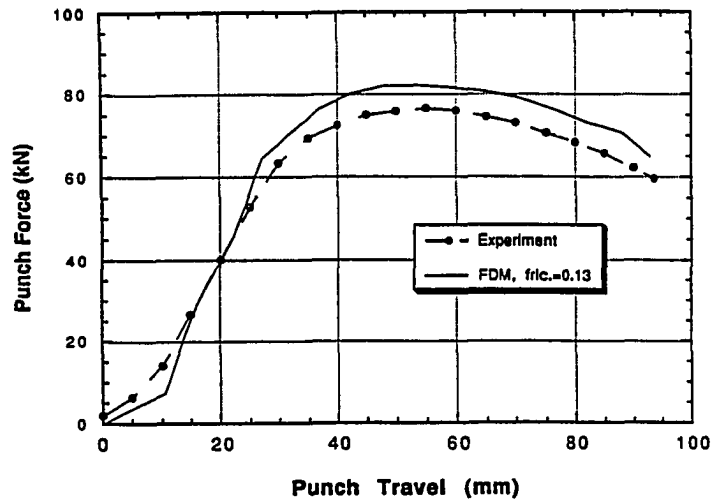
<u>Material properties and blank dimensions</u>	
r (anisotropy factor)	0.73
K (strength coefficient)	266.15 [MPa]
n (strain hardening exponent)	0.134
$\epsilon_0$ (pre strain)	0
Blank diameter	304.8 [mm]
Blank thickness	1.016, 1.60 [mm]
<u>Process conditions</u>	
Lubrication condition	water base lubricant
Blank holder force	60 [kN]

The water base lubricant was used in these experiments. Therefore, a friction coefficient of 0.13 was used in the simulations based on the previous results

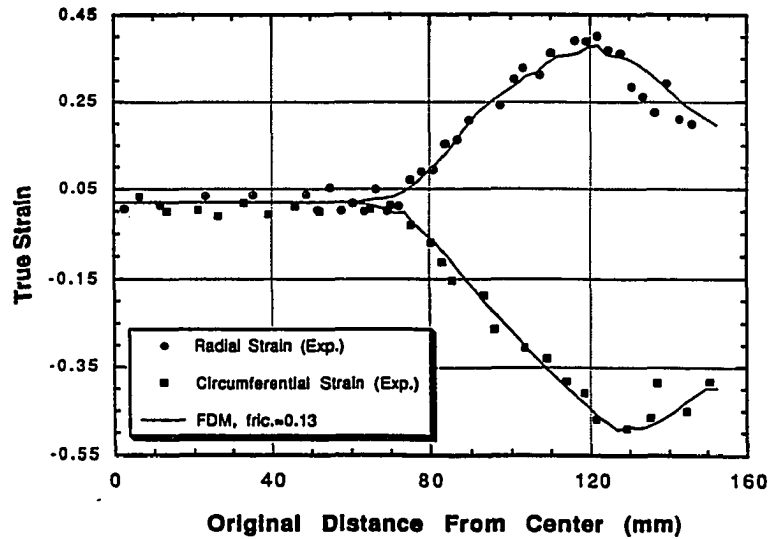
obtained during the deep drawing of AA 1100-O. In this section, two experiments are discussed. The only difference between these two experiments is the thickness of the blank.

An experiment was performed using a 1.016 mm thick and 304.8 mm diameter blank under a BHF of 60 kN. The punch load versus stroke profile is shown in Figure 7.8a. A good agreement between simulation and experiment can be seen except at the beginning of the punch travel where a slight irregularity shows for the FDM predictions. This is due to a too large initial step size. Since the FDM code automatically adjusts its step size if no convergence occurs, this problem could not be solved. The maximum punch force predicted by FDM simulations is also slightly higher than the measured one. However, a 6% difference is within acceptable limits. The predicted radial and circumferential strain distributions, shown in Figure 7.8b, are also in good agreement with the measured ones.

Another experiment was performed using 1.60 mm thick and 304.8 mm diameter blanks. The punch force and the strain distribution plots are shown in Figures 7.9a and b, respectively. Quite good agreement is obtained in both plots. The only slight mismatch shows for the radial and circumferential strains measured at the edge of the cup as shown in Figure 7.9b. This is due to the fact that the strains are measured along a line which is in between two ears. This is the direction where the restraining forces and radial strains are lower than average at that diameter.

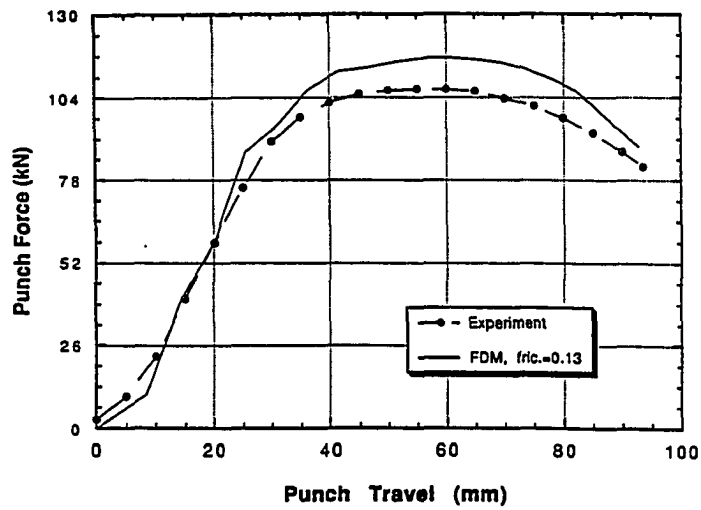


a) Punch force versus stroke diagram.

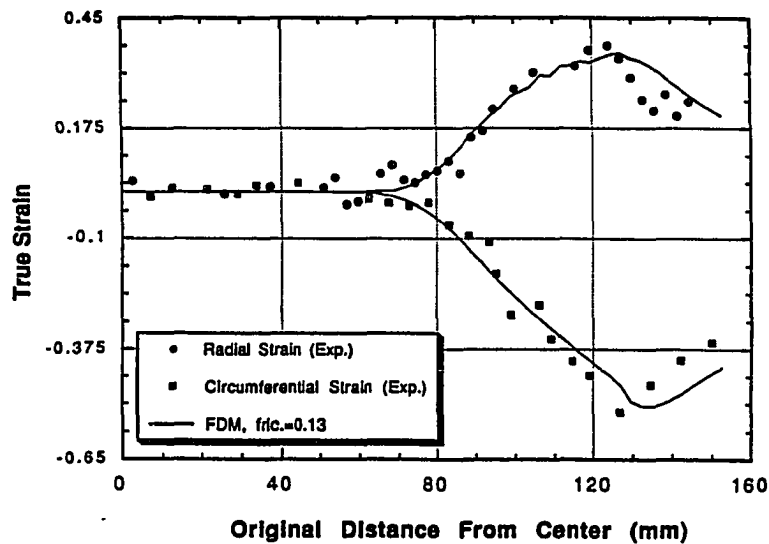


b) Radial and circumferential strain distributions.

Figure 7.8: Comparison of FDM predictions with the measurements in deep drawing of AA2024-O. ( $D_p=304.8$  mm,  $t=1.016$  mm, BHF=60.0 kN, Punch Travel=92.5 mm, water based lubricant)



a) Punch force versus stroke diagram.



b) Radial and circumferential strain distributions.

Figure 7.9: Comparison of FDM predictions with the measurements in deep drawing of AA2024-O. ( $D_p=304.8$  mm,  $t=1.6$  mm, BHF=60.0 kN, Punch Travel=92.5 mm, water based lubricant)

Finally, both punch load versus stroke profiles and radial strain distributions obtained in two experiments are plotted together in Figures 7.10 and 7.11, respectively. As expected, loads increase with increasing sheet thickness, and the radial strain distribution shows slightly lower strains for increasing sheet thickness.

### **High Strength Galvanized Steel.**

The third series of tests were carried out using high strength galvanized steel (HSG). The influence of blank holding force, draw ratio, and lubrication conditions are studied in this series of experiments. First, the individual experiments will be discussed, later comparisons between experiments with different process conditions will be made. A summary of the material properties, and process conditions are given in Table 7.7.

#### **Experiments using dry friction, and constant BHF:**

A 304.8 mm diameter blank was formed to the height of 60 mm using a BHF of 158.0 kN. In this case, the cup is not fully formed, and there is a flat flange left under the blankholder. In this experiment, no lubricant was used, and the die and blankholder surfaces were cleaned using alcohol to obtain dry friction conditions as much as possible. The punch force and radial and circumferential strain distributions measured in the experiments together



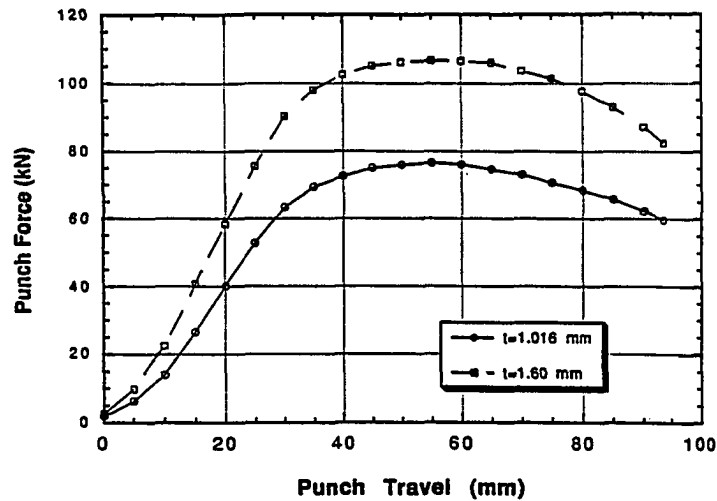


Figure 7.10: Comparison of measured punch force distributions for different thicknesses used in deep drawing of AA2024-O.

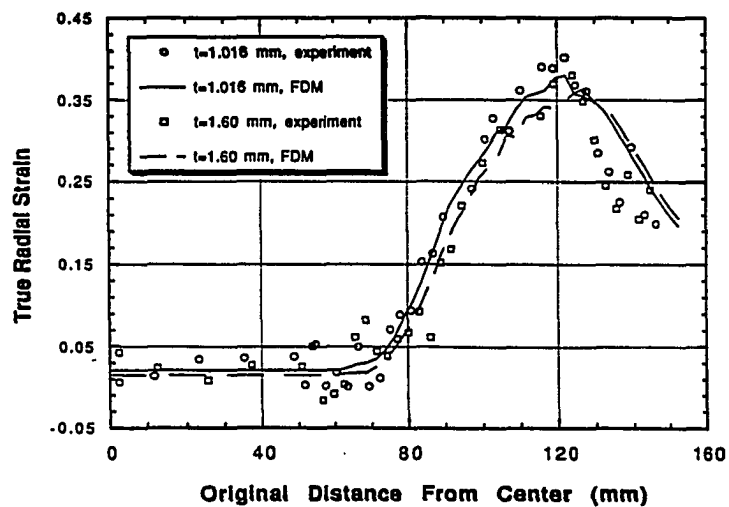


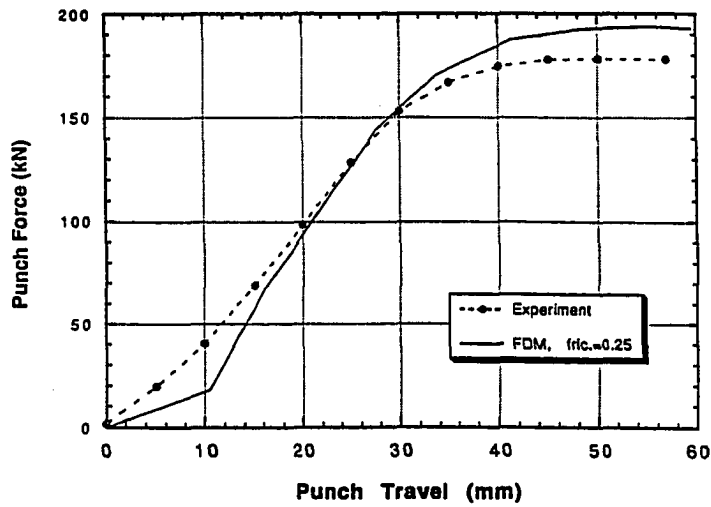
Figure 7.11: Comparison of radial and strain distributions for different thicknesses used in deep drawing of AA2024-O.

**Table 7.7: Summary of material properties, and process conditions for deep drawing of HSG steel.**

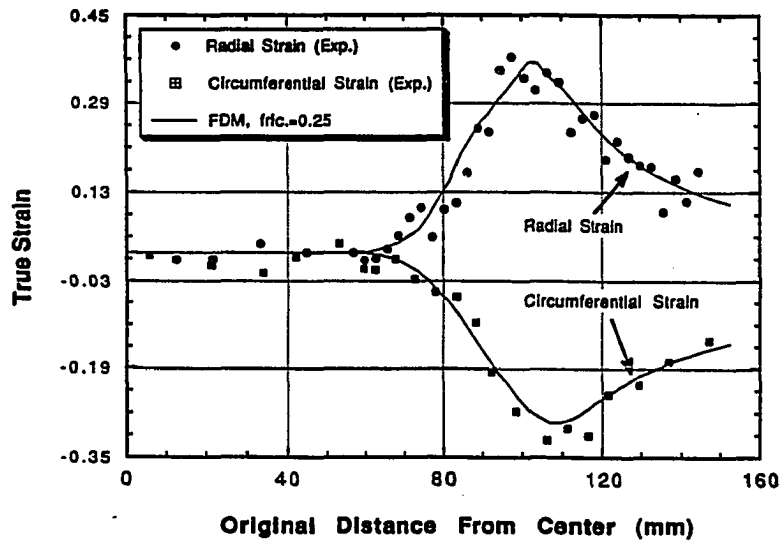
<u>Material properties and blank dimensions</u>	
r (anisotropy factor)	1.40
K (strength coefficient)	603.83 [MPa]
n (strain hardening exponent)	0.143
$\epsilon_0$ (pre strain)	0.000328
Blank diameter	254.0, 279.4, and 304.8 [mm]
Blank thickness	0.889 [mm]
<u>Process conditions</u>	
Lubrication condition	dry and water base lubricant
Blank holder force	85, 117, and 158 [kN]

with predicted ones are shown in Figures 7.12a and b, respectively. There are two discrepancy areas between predicted and measured punch force distributions as shown in Figure 7.12a. Firstly, there is the small irregularity at the beginning of the force profile predicted by the FDM simulation. Secondly, the FDM usually predicts a slightly higher maximum load than the experimentally determined one. However, these differences are relatively small.

In another experiment, a 254.0 mm diameter blank was formed to the height of 60 mm using a BHF of 158.0 kN under dry friction conditions. The punch force and radial and circumferential strain distributions are shown in Figures 7.13a and b, respectively. As can be seen from these plots, quite good agreement is obtained between the predicted and measured distributions.

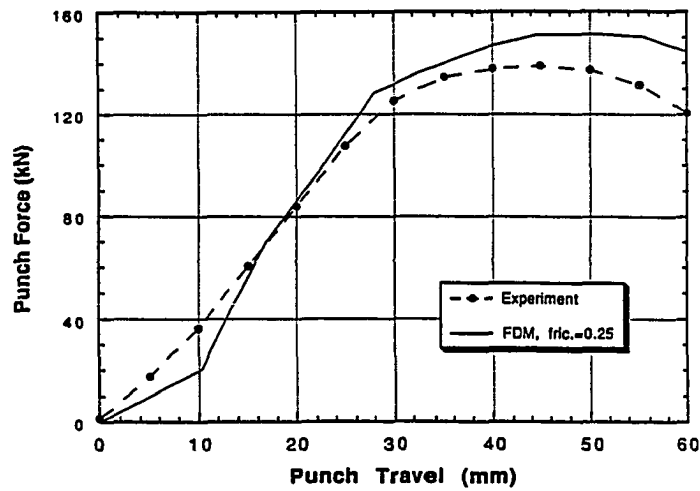


a) Punch force versus stroke diagram.

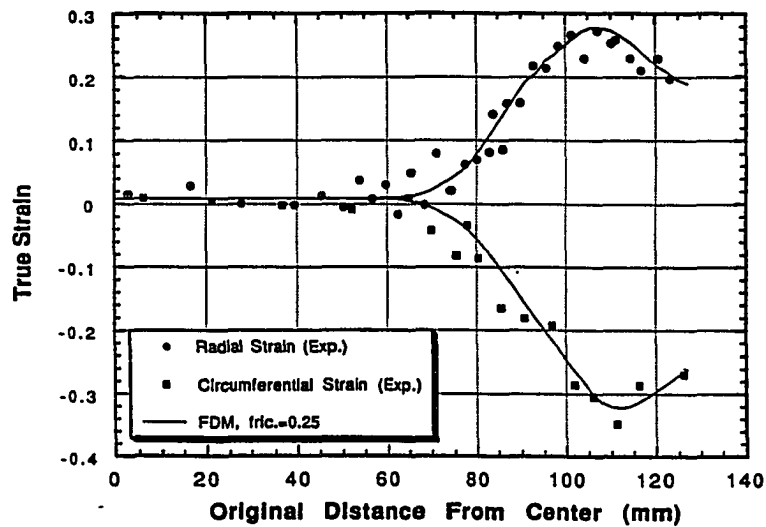


b) Radial and circumferential strain distributions.

Figure 7.12: Comparison of FDM predictions with the measurements in deep drawing of HSG steel. ( $D_b=304.8$  mm, BHF=158.0 kN, Punch Travel=60.0 mm, dry friction)



a) Punch force versus stroke diagram.



b) Radial and circumferential strain distributions.

Figure 7.13: Comparison of FDM predictions with the measurements in deep drawing of HSG steel. ( $D_p=254.0$  mm, BHF=158.0 kN, Punch Travel=60.0 mm, dry friction)

However, the same discrepancies explained in the previous paragraphs associated with the punch force distributions can also be seen in this experiment. The radial strain drops at the edge of the cup due to the flat flange left under the blankholder.

The effect of the initial blank diameter on the radial strain distribution is shown in Figure 7.14. In this figure, the radial strain distributions, both measured and predicted, shown in Figures 7.12b and 7.13b are plotted together. These experiments were performed using a BHF of 158.0 kN and dry friction conditions starting from the initial blank diameters of 304.8 mm and 254.0 mm. Since a larger flange results in a greater restraining force the radial strains increases with increasing initial blank diameter under the same BHF as shown in Figure 7.14.

The punch force versus punch travel profiles measured during the deep drawing of two cups from HSG steel are shown in Figure 7.15. Both experiments were performed using the BHF of 158.0 kN and dry friction conditions starting with different initial blank diameters (254.0 mm and 279.0 mm diameters). Both cups were fully formed without leaving a flat flange. As can be seen from Figure 7.15, the punch force increases with increasing blank diameter.

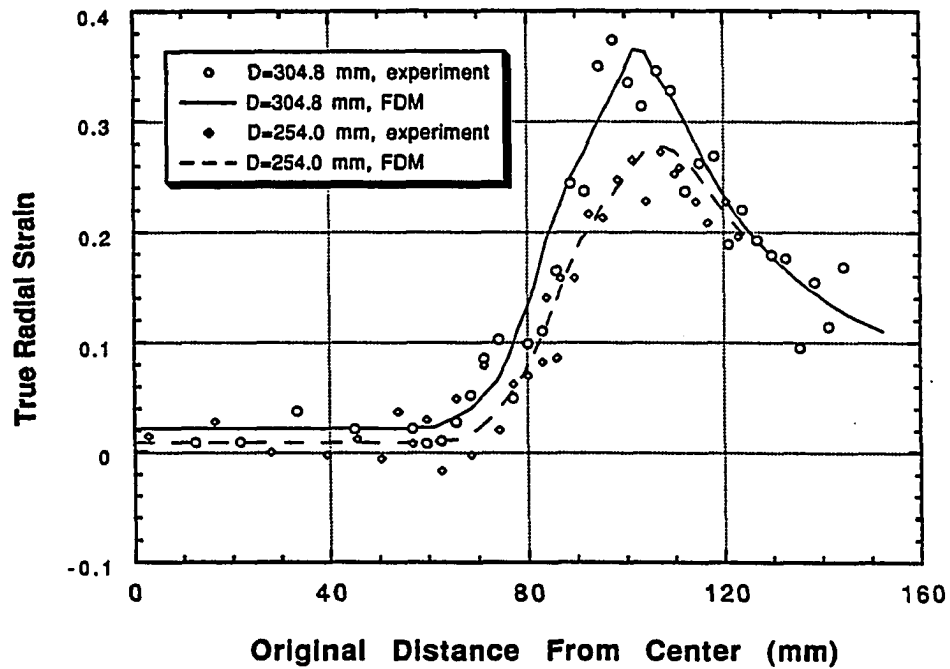


Figure 7.14: Comparison of radial strain distributions obtained using different initial blank diameters in deep drawing of HSG steel. (BHF=158.0 kN, Punch Travel=60.0 mm, dry friction)

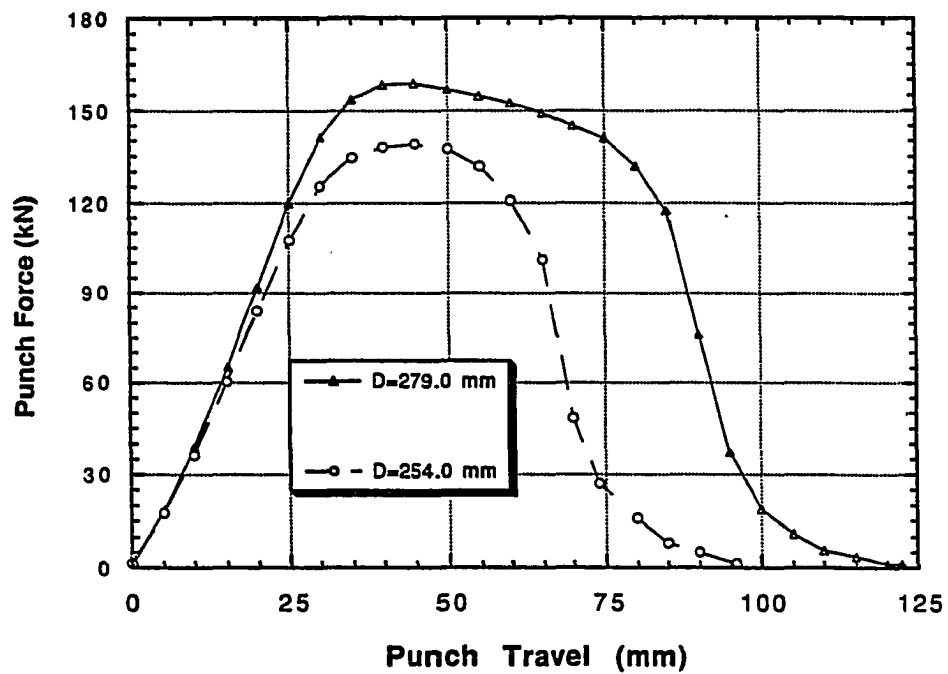


Figure 7.15: Comparison of punch force versus stroke diagrams for different initial blank diameters in deep drawing of HSG steel. (BHF=158.0 kN, dry friction)

### Experiments using water base lubricant, and constant BHF:

The next experiments were performed using a water base lubricant specifically developed for the deep drawing of steels.

Two cups were drawn to a height of 60.0 mm starting with two different blank diameters (304.8 mm and 254.0 mm) under a BHF of 117.0 kN. All the other process parameters are the same as the ones given in Table 7.7. The effect of the initial blank diameter on the punch force distribution can be seen in Figure 7.16 where experimentally measured punch force distributions corresponding to different diameter blanks are plotted together at a punch travel of 60 mm. The maximum punch load increases with increasing blank diameter. The increase in the maximum radial strain with increasing initial blank diameter is also seen in Figure 7.17. In this figure, radial strain distributions, both measured and predicted, are plotted together at a punch travel of 60 mm.

### Experiments using dry friction conditions, and variable BHF:

In this set of experiments, 304.8 mm diameter blanks were formed to the height of 93 mm under dry friction conditions. Punch travel was limited to 93 mm because a very small flat flange was left under the blankholder to have a restraining force and prevent puckering over the die corner radius. In these experiments, three different BHF variations were arbitrarily selected. These BHF variations are shown in Figures 7.18a, b, and c. The purpose of these



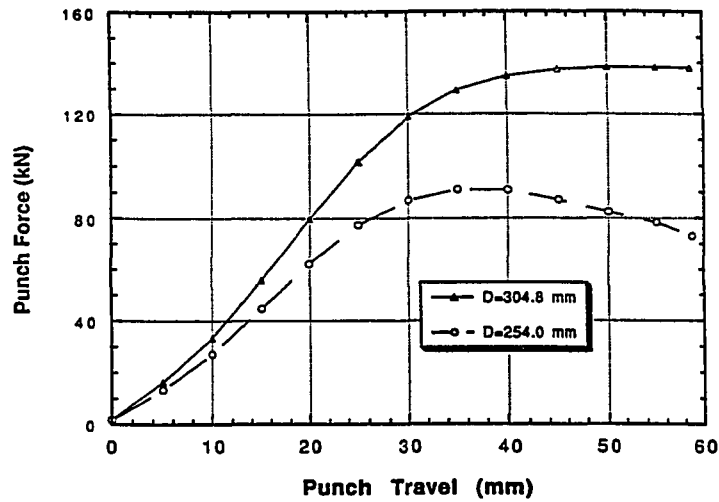


Figure 7.16: Comparison of punch force versus stroke diagrams for different initial blank diameters in deep drawing of HSG steel. (BHF=117.0 kN, water based lubricant)

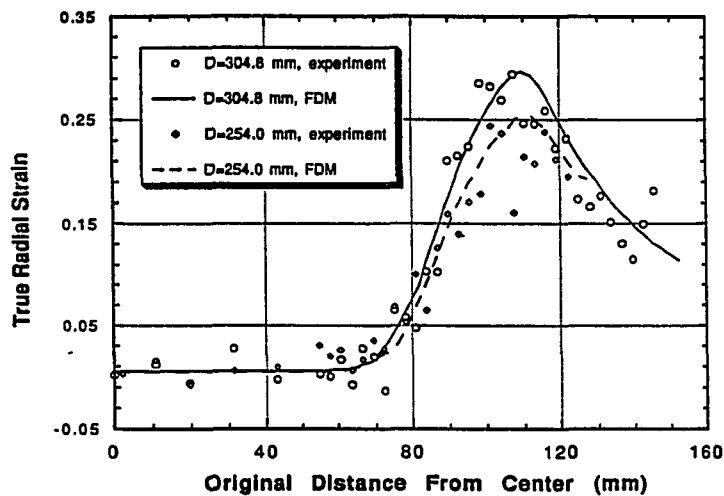
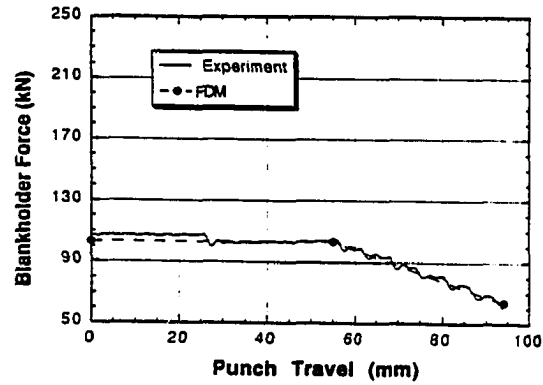
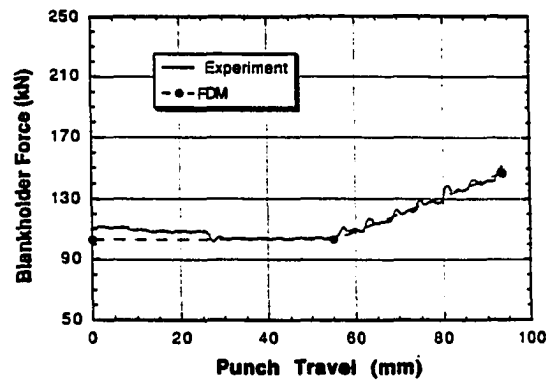


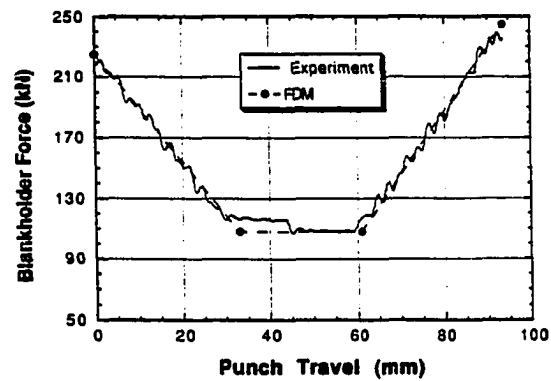
Figure 7.17: Comparison of radial strain distributions for different initial blank diameters in deep drawing of HSG steel.



a) BHF variation I



b) BHF variation II



c) BHF variation III

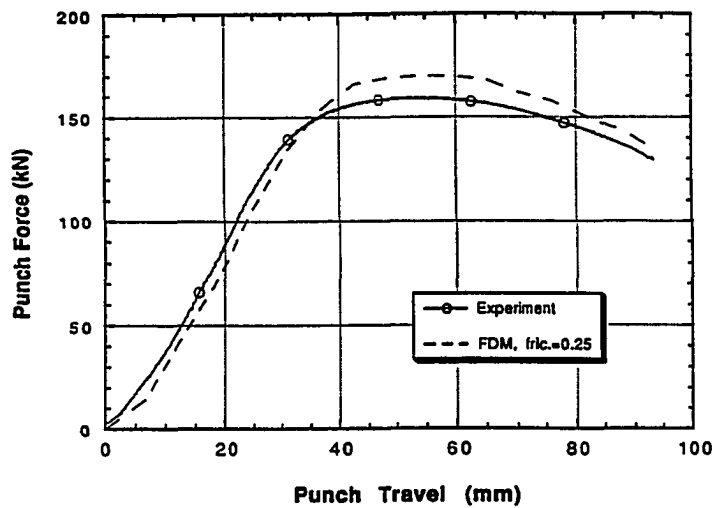
Figure 7.18: BHF variations used in the evaluation of SHEET\_FORM.

experiments is to study the effect of variable BHF on the punch force and the strain distributions. The results obtained from variable BHF experiments are compared with each other as well as with the results obtained from a constant BHF experiment.

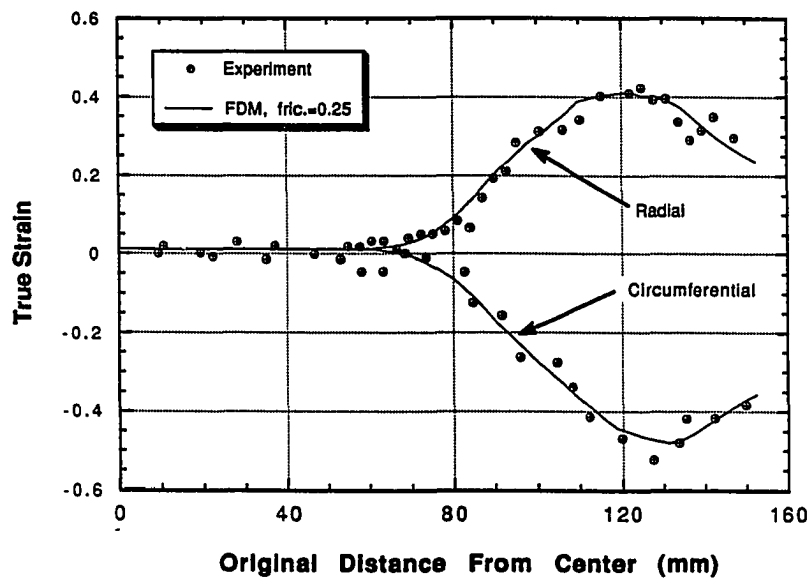
The first experiment was performed using a constant BHF of 85.0 kN. The punch force, and radial and circumferential strain distributions are shown in Figures 7.19a and b, respectively, at the punch travel of 93 mm. The second and third experiments were performed using the BHF Variations I and II which are shown in Figures 7.18 a and b, respectively.

The fourth experiment was performed using the BHF Variation-III which is shown in Figure 7.18c. The punch force and radial strain distributions are shown in Figures 7.20a and b, respectively, at the punch travel of 93 mm.

The effect of BHF variations on the punch force distribution is shown in Figure 7.21. In this figure, the measured punch force distributions corresponding to different blank holder force variations are plotted together. The blank holding force has a direct influence on the punch force. Thus, an increase in blank holding force results in an increase in punch force, and, similarly, a reduction in blank holding force results in a reduced punch force. This effect can be seen clearly in Figure 7.21 where punch force distributions differ greatly after a punch travel of 60 mm with changes in BHF distributions. Although there is a big jump at the beginning of BHF Variation-III, it does not cause a big difference in the punch force distribution

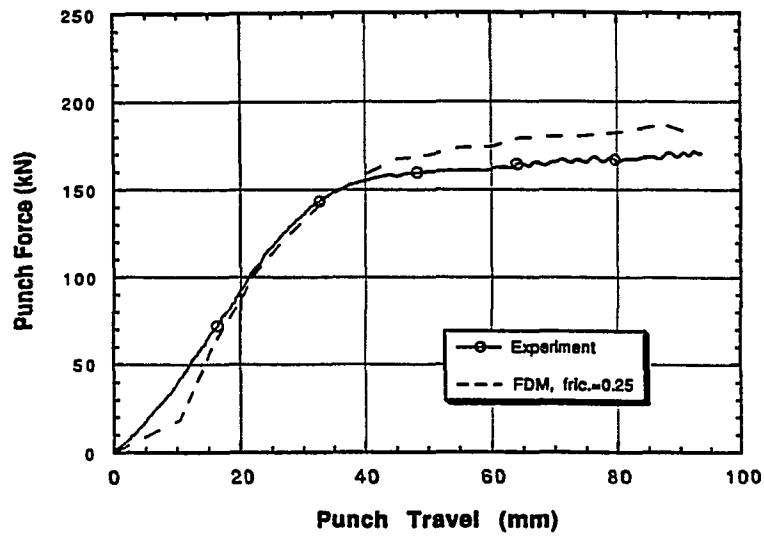


a) Punch force versus stroke diagram.

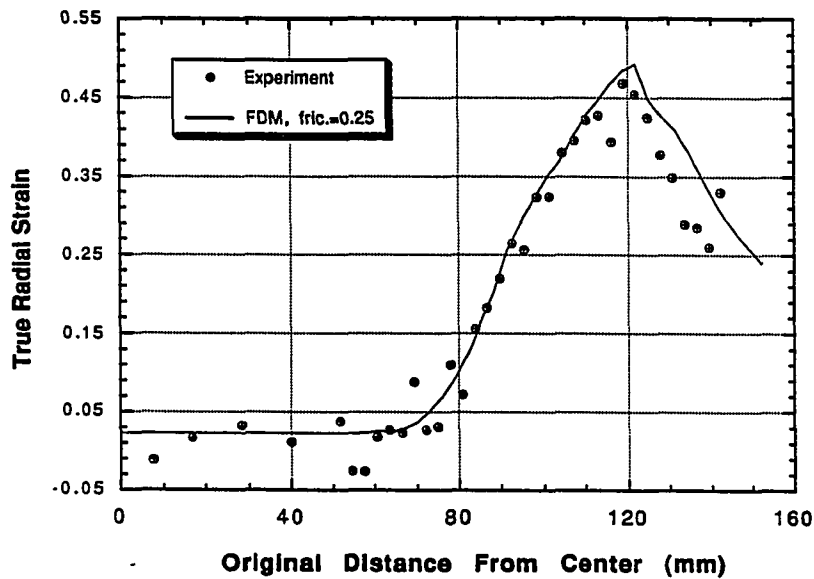


b) Radial and circumferential strain distributions.

Figure 7.19: Comparison of FDM predictions with measurements in deep drawing of HSG steel. ( $D_b=304.8$  mm, BHF=85.0 kN, Punch Travel=93.0 mm, dry friction)



a) Punch force versus stroke diagram.



b) Radial strain distribution.

Figure 7.20: Comparison of FDM predictions with measurements in deep drawing of HSG steel. ( $D_p=304.8$  mm, BHF=Variation-III, Punch Travel=93.0 mm, dry friction)

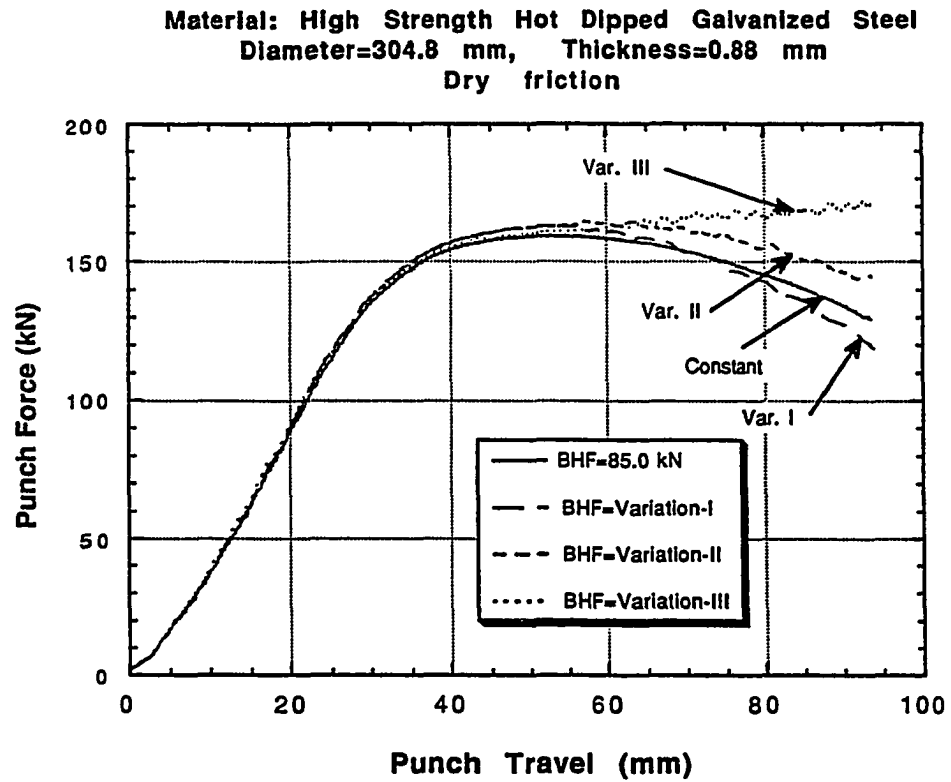


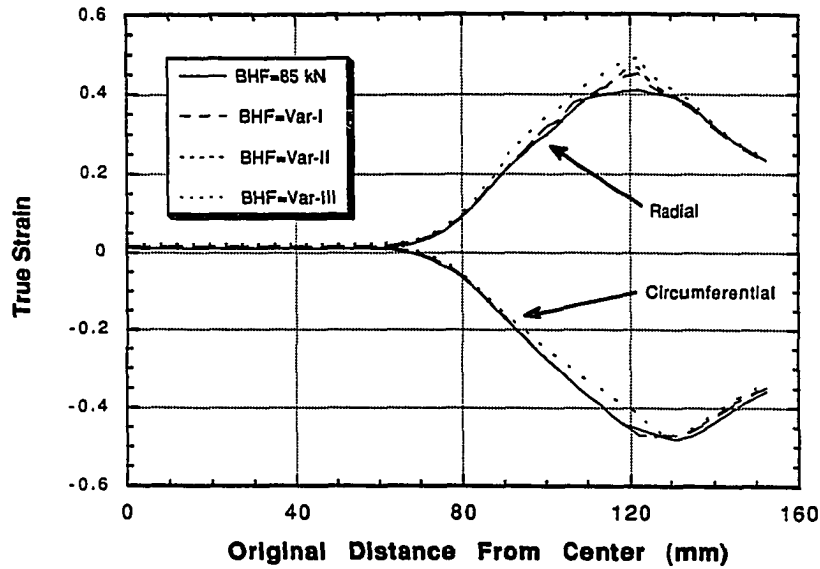
**Figure 7.21: Comparison of punch force versus stroke diagram for different BHF variations in deep drawing of HSG steel.**

at the beginning of the punch travel. Since BHF Variation-III has the largest increase towards the end of the punch stroke, it causes the highest punch force towards the end of the process.

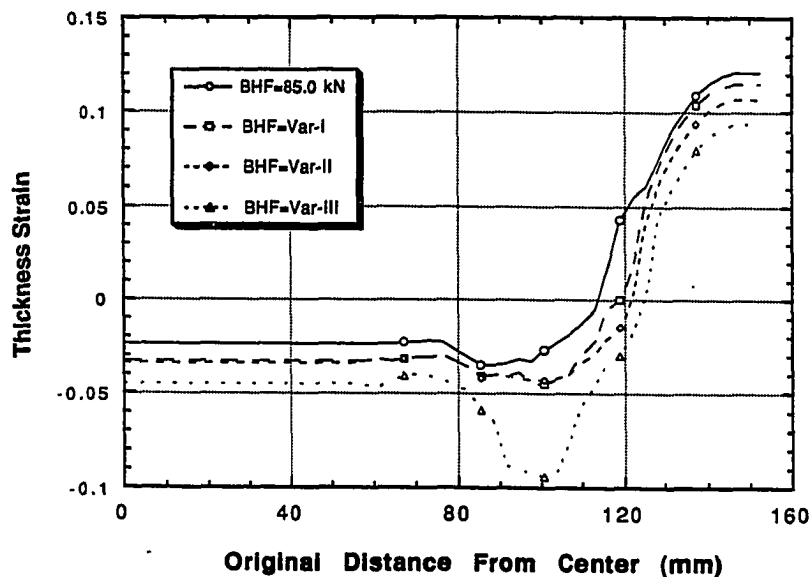
The effect of the BHF variations on the resulting strain distributions can be seen in Figure 7.22. As can be seen in Figure 7.22a, variations in the BHF does not significantly effect the maximum circumferential strain. However, The maximum radial strain changes greatly with changes in the BHF. An increase in the BHF towards the end of the process causes higher radial strain. Although the BHF Variation-I has a reduction towards the end of the process, it still causes a higher radial strain compared to the one obtained using a constant BHF of 85.0 kN since it is higher at the beginning of the process.

Thickness strain distributions obtained using different BHF variations are seen in Figure 7.22b. As it can be seen from this figure, thickness strain is also affected greatly by the changes in the BHF. The thickness strain at the flat bottom of the punch is affected by the BHF at the beginning of the punch travel. Later changes in the BHF does not effect the thickness strain at the flat bottom of the cup since the sheet metal is already wrapped around the punch nose. BHF Variation-III causes the highest thickness strain in this region since it has the highest value at the beginning of the process.

Since BHF Variations I and II have the same value until the punch travel of 60 mm, thickness strains obtained by these BHF variations are about the same at the flat bottom of the cup. However, due to variations in the BHF after the punch travel of 60 mm, the thickness strain distributions at the wall of the



a) Radial and circumferential strain distributions.



b) Thickness strain distribution.

Figure 7.22: Comparison of the resulting strain distributions using constant BHF=85.0 kN and the BHF variations shown in Figure 7.18. ( $D_p=304.8$  mm, Punch Travel=93.0 mm, dry friction)



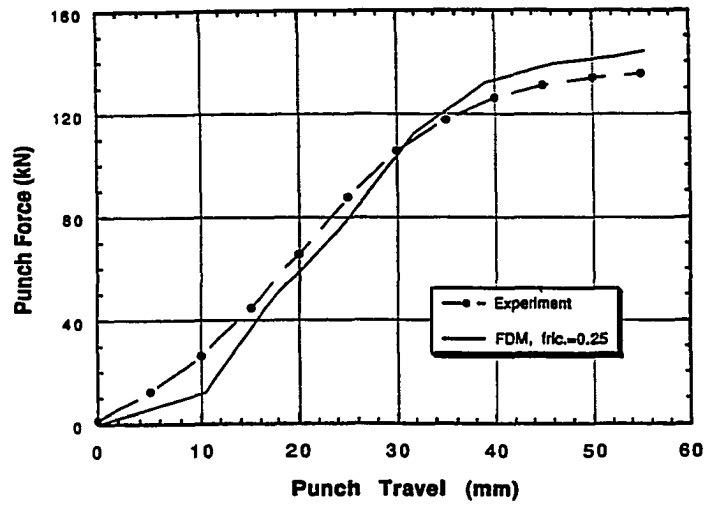
cup differs. An increase in the BHF towards the end of the process shows two effects on the thickness strain distributions:

- 1) It causes an increase in the thickness strain over the punch corner profile. This can be seen clearly in Figure 7.22b. An increase in BHF Variation-III towards the end of the process causes a peak in the thickness strain.
- 2) It causes less thickening at the flange due to flange upsetting. In Figure 7.22b, less thickening occurs by using BHF Variation-III since it has the highest peak at the end of the punch travel.

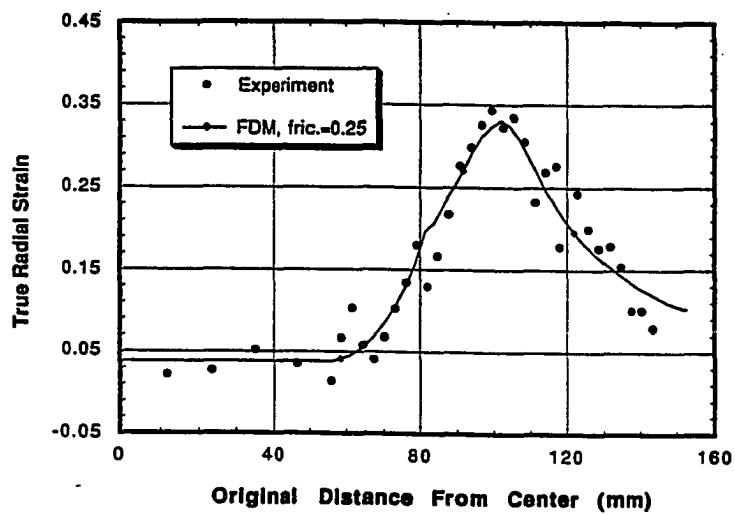
### **Univit Steel (UV)**

An experiment was performed using a 304.8 mm diameter blank and a BHF of 158.0 kN. A summary of the material properties, and process conditions is given in Table 7.8. The punch force and radial strain distributions are shown in Figures 7.23a and b at a punch travel of 55 mm.

In Figure 7.24, the influence of a different initial blank diameter on the resulting punch force distribution is shown where three measured punch force distributions corresponding to three different initial blank diameters are plotted. All the process conditions other than the initial blank diameters are the same in these three experiments and summarized in Table 7.8. As expected, the punch force increases with increasing draw ratios. Also, the punch force profile for the smallest blank diameter shows a drop off towards



a) Punch force versus stroke diagram.



b) Radial strain distribution.

Figure 7.23: Comparison of FDM predictions with measurements in deep drawing of UV steel. ( $D_p=304.8$  mm,  $BHF=158.0$ , Punch Travel=55.0 mm, dry friction)

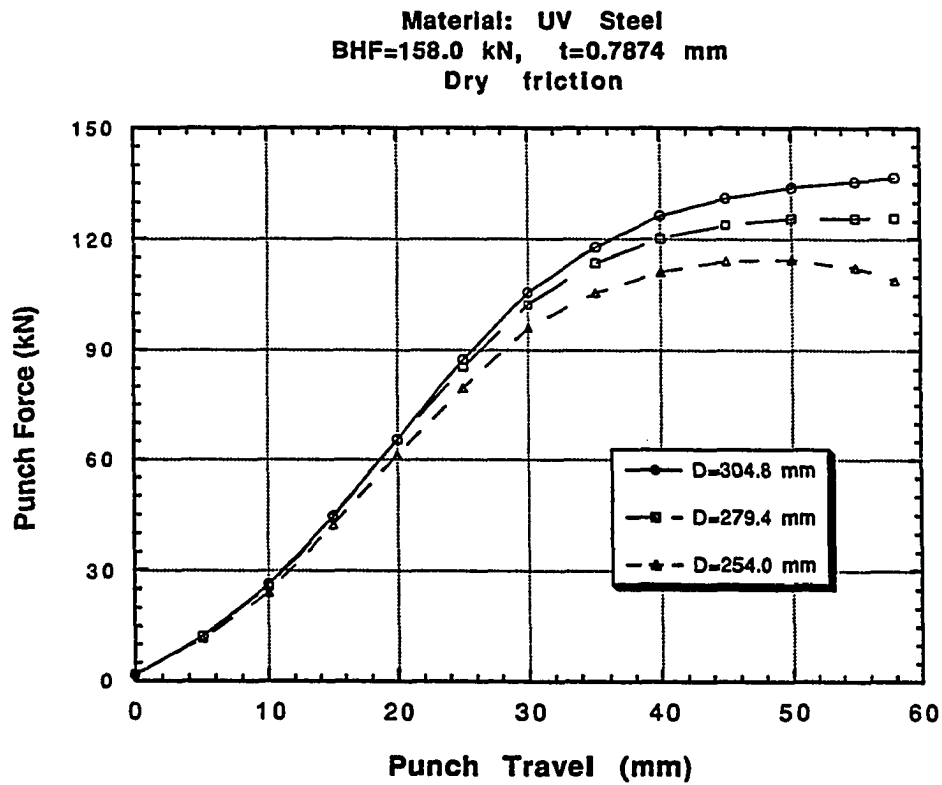


Figure 7.24: The effect of different draw ratios on the punch force versus stroke diagram in deep drawing of UV steel. (Punch travel is 55 mm)

the end of the stroke. This is also expected since with decreasing blank diameter the force maximum will shift towards the origin.

**Table 7.8: Summary of material properties, and process conditions for deep drawing of UV steel.**

<u>Material properties and blank dimensions</u>	
r (anisotropy factor)	1.45
K (strength coefficient)	525.19 [MPa]
n (strain hardening exponent)	0.254
$\epsilon_0$ (pre strain)	0.008742
Blank diameter	254.0, 279.4, and 304.8 [mm]
Blank thickness	0.7874 [mm]
<u>Process conditions</u>	
Lubrication condition	dry friction
Blank holder force	158 [kN]

### Interstitial Free Steel (IF)

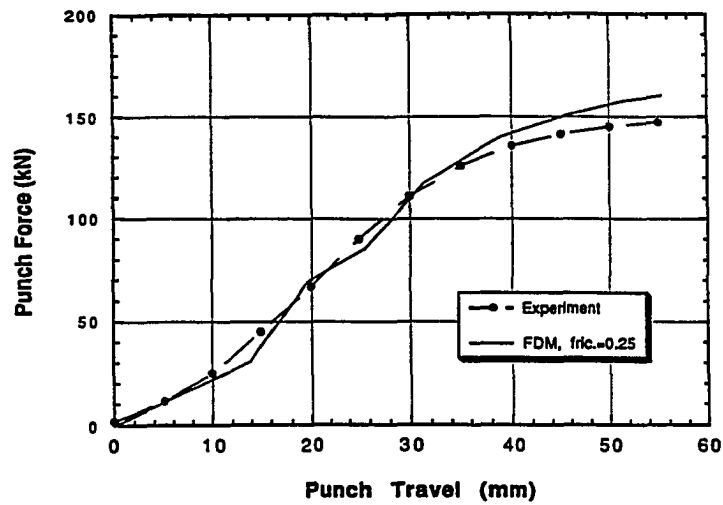
The last series of experiments to verify the FDM simulations was performed using IF steel. A summary of the material properties, and process conditions for this series of experiments is given in Table 7.9.

An experiment was performed using 304.8 mm diameter blanks and a BHF of 158.0 kN under dry friction conditions. The punch force and radial strain

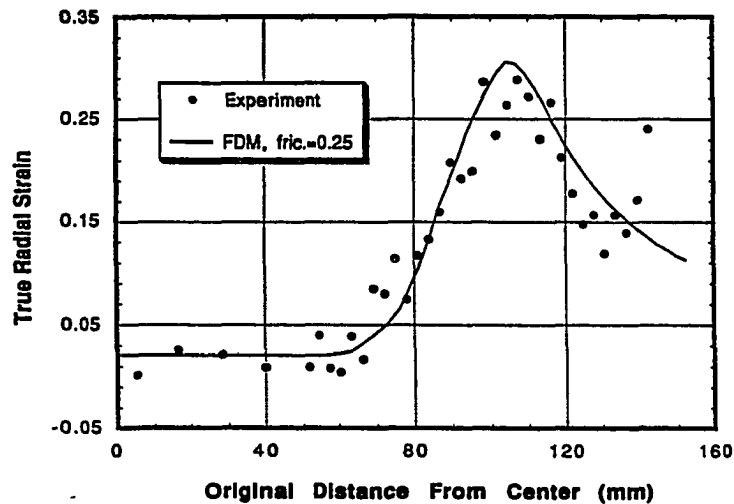
distributions are shown in Figures 7.25a and b. The punch load versus stroke simulation shows a good agreement with the measured curve (see Figure 7.25a). The predicted strain distribution also matches the measured one quite well (see Figure 7.25b). The slight scatter towards the end of the cup flange is caused by the fact that the grid is damaged due to very high friction between the blankholder and blank.

**Table 7.9: Summary of material properties, and process conditions for deep drawing of IF steel.**

<u>Material properties and blank dimensions</u>	
r (anisotropy factor)	1.95
K (strength coefficient)	622.38 [MPa]
n (strain hardening exponent)	0.263
$\epsilon_0$ (pre strain)	0.000846
Blank diameter	254.0, 279.4, and 304.8 [mm]
Blank thickness	0.7874 [mm]
<u>Process conditions</u>	
Lubrication condition	dry
Blank holder force	158 [kN]



a) Punch force versus stroke diagram.



b) Radial strain distribution.

Figure 7.25: Comparison of FDM predictions with measurements in deep drawing of UV steel. ( $D_b=304.8$  mm, BHF=158.0, Punch Travel=55.0 mm, dry friction)

Effect of material parameters on the punch force and radial strain distributions

Finally, a comparison is made between the punch forces and the strain distributions for deep drawing of different steels. For these experiments, all process conditions were kept the same except for slight differences in the sheet thicknesses for different materials.

For clarity, the properties and thicknesses of the different materials used in these experiments are listed again in Table 7.10.

**Table 7.10: Material properties.**

Material	n	K [MPa]	r	$\epsilon_0$	Thickness	
					[mm]	(in)
HS Galvanized Steel (HSG)	0.143	603.83	1.40	0.000328	0.889	0.035
Interstitial Free Steel (IF)	0.263	622.38	1.95	0.000846	0.8382	0.033
Univit Steel (UV)	0.254	525.19	1.45	0.008742	0.7874	0.031

If all process parameters except the material properties are kept the same, the punch load versus stroke profile will be mainly determined by the strain hardening exponent ( $n$ ) and the strength coefficient ( $K$ ). The  $r$  value also has a minor influence. The measured punch force versus stroke distributions for

three different steels are shown in Figure 7.26 at a punch travel of 55 mm. Since HSG steel has a high  $K$  value combined with a low  $n$ -value, this material is expected to show the highest punch force as shown in Figure 7.26. Additionally, HSG also has the largest thickness. IF steel has a slightly higher  $K$  value but also a considerably higher  $n$ -value. Mainly because of this high  $n$  value, the stresses will be lower at the beginning of the deformation, and thus the force resulting from these stresses will also be smaller. The lowest punch force versus stroke profile results for UV steel which combines a low  $K$  value with a high  $n$ -value. Also this material is the thinnest one of all.

Another interesting effect to be seen is that the steepness of the initial slope is mainly determined by the  $n$  value. If the  $n$ -value is lower, the slope is steeper. This effect of the  $n$ -value on the slope also results in a shift of the punch force maximum to the left for lower  $n$ -values as seen in Figure 7.26.

A high  $r$ -value decreases the punch load. This effect is not very clearly observed since the  $r$ -values do not differ much for the different materials. Even though differences are not that great, the material with the lowest  $r$ -value, UV steel, also has the lowest maximum punch load which agrees with the theoretical explanation.

The radial strain distributions for different steels are shown in Figure 7.27. In general, a higher punch load profile will also result in a higher radial strain distribution as can be seen in Figure 7.27. A high  $n$  value tends to further distribute strain localizations. This effect shows for both IF and UV steels



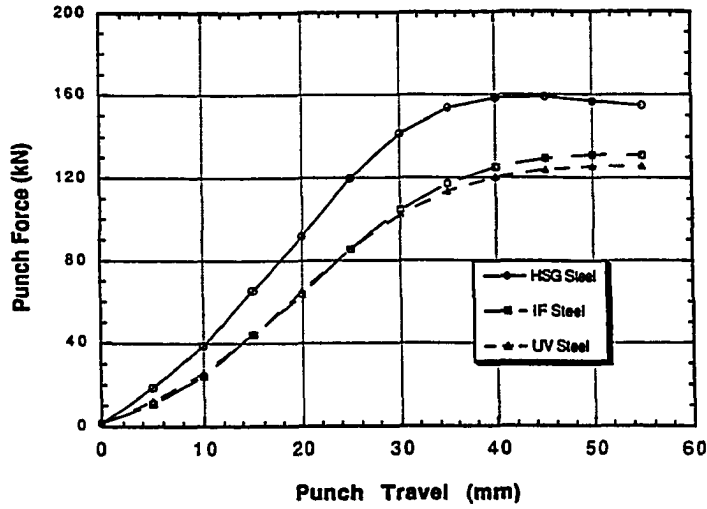


Figure 7.26: The effect of material parameters on the punch force versus stroke diagram. (BHF=158.0 kN,  $D_b=279.4$  mm, dry friction)

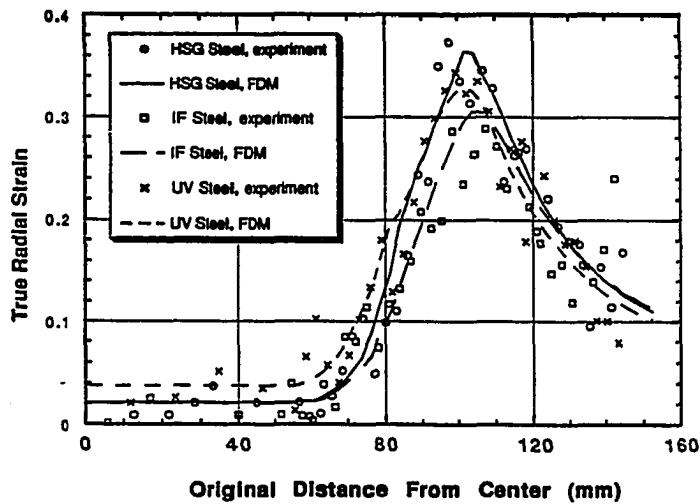


Figure 7.27: The effect of material parameters on the radial strain distribution. (Punch Travel=55 mm)

which have smooth strain maxima. HSG steel on the contrary has quite a sharp, i.e., localized, maximum which is due to the low  $n$  value.

#### **7.4. Effect of BHF on The Failure of Sheet Metal Products**

##### **7.4.1. Fracture**

A failure evaluation module is built into SHEET\_FORM. This module can be used to predict failure, i.e. wrinkling and fracture, based on the calculated stresses and strains during the process simulation. In this section, fracture predictions for the deep drawing of different materials and a comparison with the experimental results will be summarized.

Three different materials were used in these experiments. These materials are High Strength Galvanized Steel (HSG), Interstitial Free Steel (IF), and Univit Steel (UV). Three different initial blank diameters, i.e. 254.0 mm, 279.4 mm, and 304.8 mm, for each material were tested. The effect of the draw ratio and the material parameters on the cup height at fracture was studied.

The dry friction condition was chosen at the material-tool interface since this condition is easy to reproduce. To ensure dry friction conditions, the blank and tool surfaces were cleaned with a special cleaning solvent before each experiment.

To compare the effect of the material on the fracture, process conditions were kept constant, and only the blank material was changed throughout the experiments. For this purpose, a BHF which would cause fracture in all the blank materials and all the draw ratios had to be determined. Preliminary simulations were run to estimate the BHF necessary to fail the blank of the best formable material for the smallest draw ratio. Among the materials that we have, the best formable material was IF steel, and the smallest tested blank diameter was 254 mm. Preliminary simulations showed that this blank would fail under dry lubricated conditions for a blank holding force of 250 kN. To be on the safe side, a blank holding force of 270 kN was chosen for all experiments to be carried out.

As described in Section 6.6, the failure evaluation module of SHEET\_FORM consists of several different failure criteria. For the fracture predictions in this section, only the Forming Limit Diagrams (FLD) will be used. As described in Section 6.6.1, each material has a unique FLD for each thickness. These FLDs are usually determined experimentally, and many materials, the FLDs are available in the literature. Furthermore, formulas are available to calculate the plane-strain interception ( $FLD_0$ ) (Equation 7.1) [FLD User's Conference Notes, 1991].

$$FLD_0 = \frac{n}{0.21} (23.3 + 3.59t_0) \quad n \leq 0.21$$

$$FLD_0 = (23.3 + 3.59t_0) \quad n \geq 0.21$$
(7.1)

where  $n$  : strain hardening exponent  
 $t_0$  : initial thickness of the blank

In SHEET\_FORM, the FLD is approximated by four constants as explained in Section 6.6.1. These constants are;

- 1) plane-strain interception, ( $FLD_0$ )
- 2) slope of the line approximating the FLD in the negative minor strain region, ( $S_1$ )
- 3) slope of the line approximating the FLD in the positive minor strain region, ( $S_2$ )
- 4) band width separating the safe and fracture regions, (B)

The values of  $FLD_0$  for different materials are calculated from Equation 7.1, and the slopes are estimated from similar curves in the literature, [ASM; 1988]. The parameters used in the simulations to estimate FLDs for different materials are listed in Table 7.11.

**Table 7.11: Parameters to approximate Forming Limit Diagrams**

Material	$FLD_0$	$S_1$	$S_2$
HSG Steel	18.04	-1.35	0.5
UV steel	26.13	-1.2	0.5
IF steel	26.31	-1.25	0.5

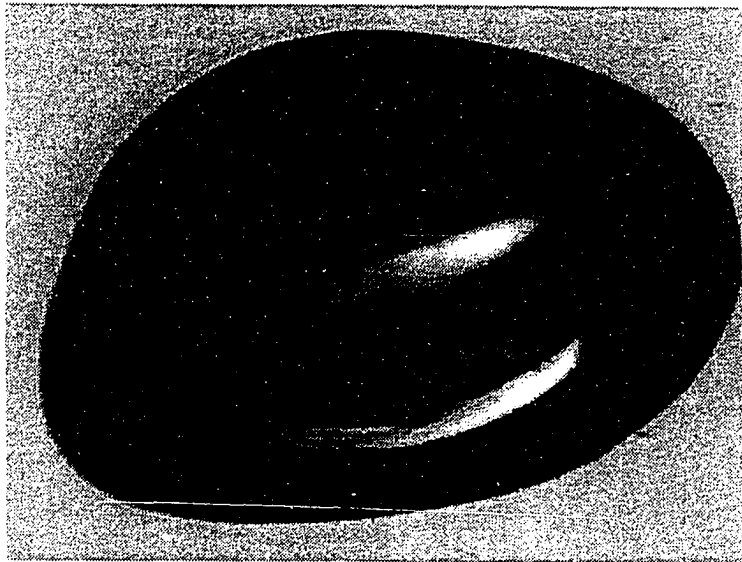
### High Strength Galvanized Steel

The first material tested was HSG steel. A list of the material properties, FLD parameters, and process conditions can be seen in Table 7.12.

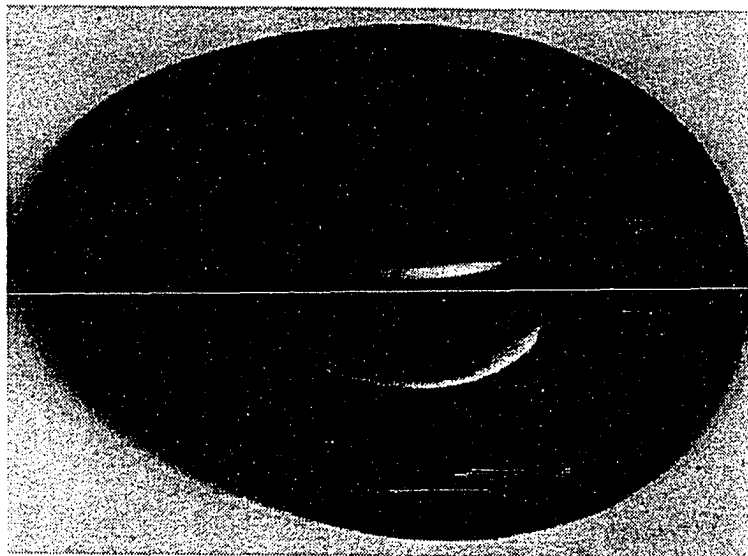
**Table 7.12: Summary of material properties, FLD parameters, and process conditions for deep drawing of HSG steel.**

<u>Material properties and blank dimensions</u>	
r (anisotropy factor)	1.40
K (strength coefficient)	603.83 [MPa]
n (strain hardening exponent)	0.143
$\epsilon_0$ (pre strain)	0.000328
Blank diameter	254.0, 304.8, and 355.6 [mm]
Blank thickness	0.889 [mm]
<u>FLD parameters</u>	
FLD <sub>0</sub>	18.04
S <sub>1</sub>	-1.35
S <sub>2</sub>	0.5
B	10
<u>Process conditions</u>	
Lubrication condition	dry friction
Blank holder force	270 [kN]

A picture of the fractured cups is shown in Figure 7.28. Both of the cups were formed using a constant BHF of 270 kN. As it is seen from the Figure 7.28,



a) Blank diameter is 254.0 mm.



b) Blank diameter is 355.6 mm.

Figure 7.28: Fracture in deep drawn cups from HSG steel.

increasing the draw ratio decreases the attainable cup height. The effect of draw ratio ( or reduction ratio, i.e., the ratio of the initial blank diameter to the cup diameter) on fracture (or tearing) in deep drawing of round cups is explained in Figure 7.29. For a certain reduction ratio, the attainable cup height is limited by either wrinkling or tearing depending on the value of the BHF. When the draw ratio is increased, the value of BHF which will cause tearing will decrease. This is due the fact that as the draw ratio increases the area of the flange where the BHF is applied increases which also increases the tension in the wall of the cup if the lubrication conditions and the BHF remain unchanged.

Failure predictions by SHEET\_FORM are listed in Table 7.13 together with the cup heights at fracture measured during the experiments. As can be seen

**Table 7.13: Predicted, and measured cup heights at fracture for HSG steel.**

Test No.	Blank Diameter		Measured Cup Height at Fracture		Predicted Cup Height at Fracture	
	(mm)	(in)	(mm)	(in)	(mm)	(in)
1	254.0	10	54	2.13	59.31	2.34
2	304.8	12	52	2.05	47.61	1.87
3	355.6	14	43	1.69	41.59	1.64

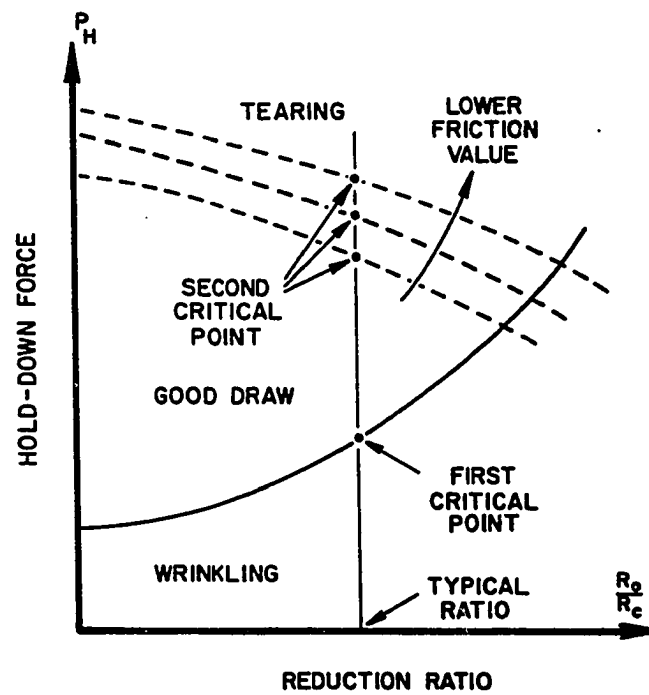


Figure 7.29: The respective domains of wrinkling and tearing in deep drawing of round cups, [Avitzur, 1983].



from Table 7.13, the FDM predictions agree well with experimentally obtained data. Especially when one takes into consideration that experimentally determined failure heights are always subject to some scatter. This is because the failure height is very sensitive to small variations in material parameters, e.g. thickness variations, inclusions or voids, etc.

The FLDs and strain plots for different draw ratios are shown in Figure 7.30. In Figure 7.30, each mark corresponds to the node for which failure is predicted. As can be seen, the strain state for which failure is predicted lies in the negative minor strain region. In Figure 7.30, the strain paths of the failed nodes are also displayed. One of the limitations of FLDs is that they are dependent on the strain path. By having the complex strain path which occurs in stamping operations with complex shapes, sometimes considerably larger strains than the ones predicted by the FLD can be obtained.

### Univit Steel

The next set of experiments were done using UV Steel. A list of the material parameters, FLD parameters, and process conditions is given in Table 7.14. The predicted cup heights at fracture are all very close to the experimentally determined ones (see Table 7.15). The FDM predictions can be seen from Figures 7.31a through 7.31c. The failed nodes again are situated in the left half of the FLD. The strain path has followed a slightly curved line and is almost the same as for HSG steel simulations.

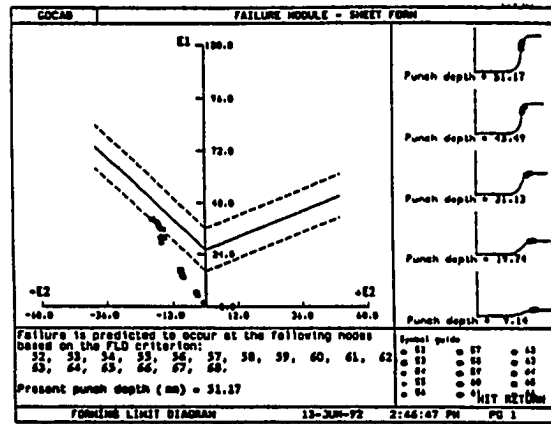


**Table 7.14: Summary of material properties, FLD parameters, and process conditions for deep drawing of UV steel.**

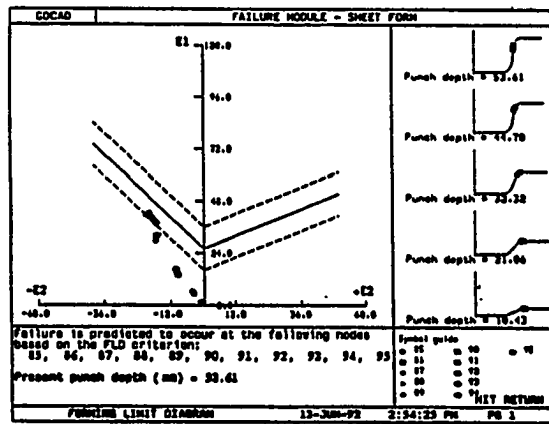
<u>Material properties and blank dimensions</u>	
r (anisotropy factor)	1.45
K (strength coefficient)	525.19 [MPa]
n (strain hardening exponent)	0.254
$\epsilon_0$ (pre strain)	0.008742
Blank diameter	254.0, 304.8, and 355.6 [mm]
Blank thickness	0.7874 [mm]
<u>FLD parameters</u>	
FLD <sub>0</sub>	26.13
S <sub>1</sub>	-1.2
S <sub>2</sub>	0.5
B	10
<u>Process conditions</u>	
Lubrication condition	dry friction
Blank holder force	270 [kN]

**Table 7.15: Predicted, and measured cup heights at fracture for UV steel.**

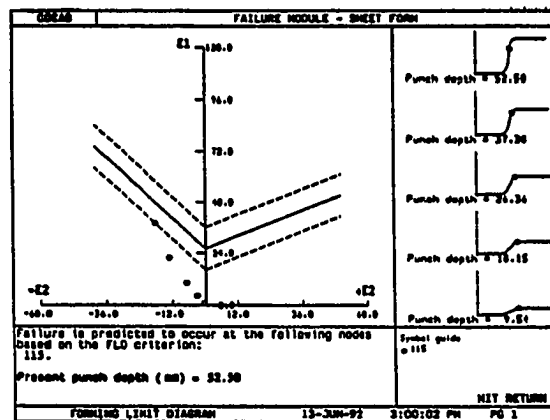
Test No.	Blank Diameter		Measured Cup Height at Fracture		Predicted Cup Height at Fracture	
	(mm)	(in)	(mm)	(in)	(mm)	(in)
1	254.0	10	51	2.01	51.17	2.01
2	304.8	12	53	2.07	53.61	2.11
3	355.6	14	49	1.93	52.50	2.07



a) Blank diameter is 254.0 mm.



b) Blank diameter is 304.8 mm.



c) Blank diameter is 355.6 mm.

Figure 7.31: Forming limit diagrams for deep drawing UV steel blank.

### Interstitial Free steel

The last material tested is IF steel. A list of the material parameters, FLD parameters, and process conditions is given in Table 7.16. The resulting failure predictions again show a very nice agreement with the experimentally obtained failure heights, see Table 7.17. As expected, the strain state for the failed nodes is situated in the left part of the FLD (see Figure 7.32a to 7.32c). Also for these tests, the strain path followed is along a line with a slight curvature.

Finally, a comparison among the cup heights at fracture obtained in the previous experiments for different materials will be made to show the influence of the material properties on the fracture. In the previous experiments, all the process conditions were kept the same, the same experiments were repeated with three different materials. The only parameter which could not be kept constant was the sheet thickness. This means a comparison is not based solely on material properties. The sheet thickness has an affect on the failure height since the failure height increases with increasing sheet thickness, [Kotthaus, 1955]. However, the differences in sheet thickness are small enough not to have too much influence in the obtained failure heights.

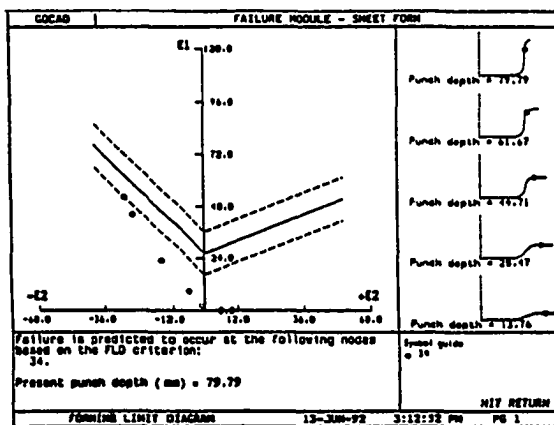
For clarity, the material parameters, FLD constants, and sheet thicknesses of the different materials are listed again in Table 7.18.

**Table 7.16: Summary of material properties, FLD parameters, and process conditions for deep drawing of IF steel.**

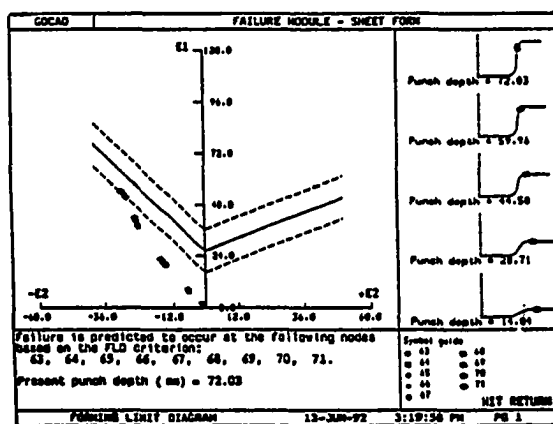
<u>Material properties and blank dimensions</u>	
r (anisotropy factor)	1.95
K (strength coefficient)	622.38 [MPa]
n (strain hardening exponent)	0.263
$\epsilon_0$ (pre strain)	0.000846
Blank diameter	254.0, 304.8, and 355.6 [mm]
Blank thickness	0.8382 [mm]
<u>FLD parameters</u>	
FLD <sub>0</sub>	26.31
S <sub>1</sub>	-1.25
S <sub>2</sub>	0.5
B	10
<u>Process conditions</u>	
Lubrication condition	dry friction
Blank holder force	270 [kN]

**Table 7.17: Predicted, and measured cup heights at fracture for IF steel.**

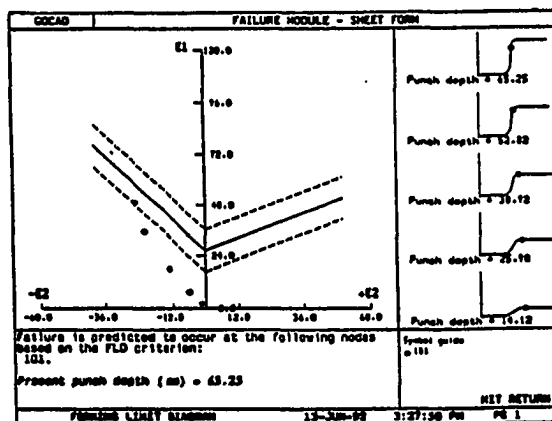
Test No.	Blank Diameter		Measured Cup Height at Fracture		Predicted Cup Height at Fracture	
	(mm)	(in)	(mm)	(in)	(mm)	(in)
1	254.0	10	79	3.11	79.79	3.14
2	304.8	12	68	2.68	72.03	2.84
3	355.6	14	62	2.44	65.25	2.57



a) Blank diameter is 254.0 mm.



b) Blank diameter is 304.8 mm.



c) Blank diameter is 355.6 mm.

Figure 7.32: Forming limit diagrams for deep drawing IF steel blank.

**Table 7.18: Material properties, FLD parameters, and sheet thicknesses for HSG, IF, and UV steel.**

	HSG Steel	IF Steel	UV Steel
n	0.143	0.263	0.254
K [MPa]	603.83	622.38	525.19
r	1.40	1.95	1.45
$\epsilon_0$	0.000328	0.000846	0.008742
Thickness			
[mm]	0.889	0.8382	0.7874
[in]	0.035	0.033	0.031
FLD <sub>0</sub>	16.0	26.31	26.13
S <sub>1</sub>	-1.35	-1.25	-1.2
S <sub>2</sub>	0.5	0.5	0.5
B	10	10	10

Both predicted and measured cup heights where fracture occurs in deep drawing HSG, UV, and IF steels are plotted in Figure 7.33. The material having the overall lowest fracture height is HSG steel. This is because HSG steel possesses a small n-value which means that not much stretching is possible. Additionally, the r value is not very high which also limits the fracture height. The fracture heights show a decrease with increasing draw ratio which is according to expectations.

The material yielding failure heights close to the ones found for HSG steel is UV steel. UV steel has a high n-value with a fairly high r-value which makes



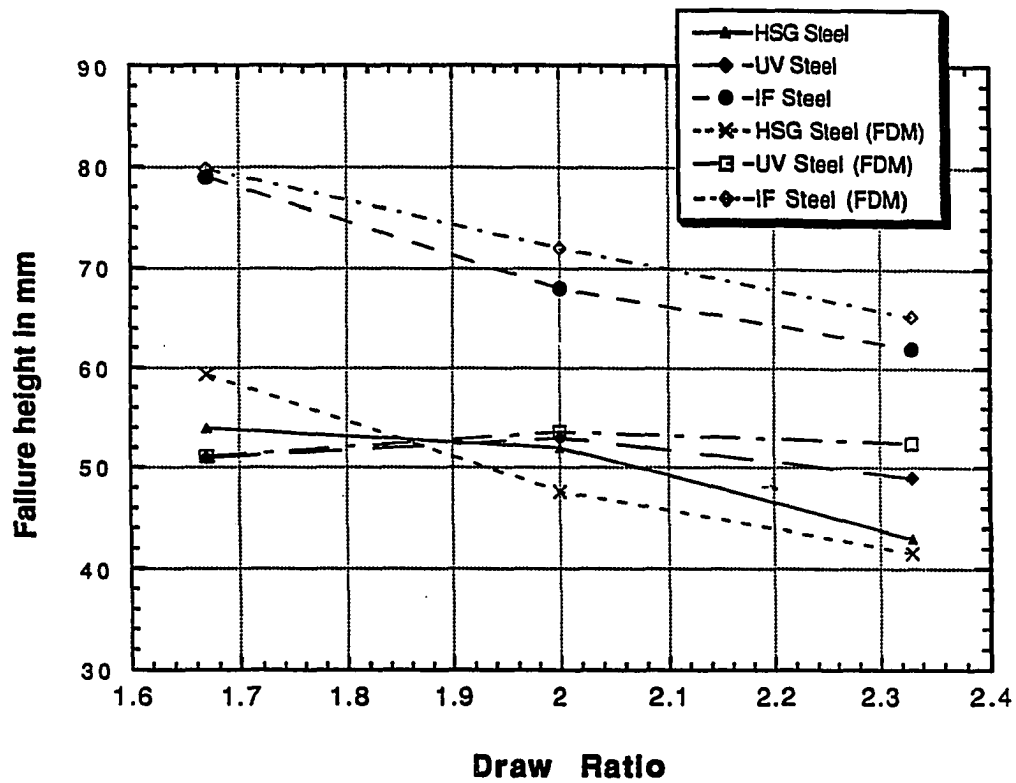


Figure 7.33: Comparison of failure heights for different draw ratios for different materials.

it very feasible for drawing operations which involve stretching. When looking at the fracture heights, one notices an increase in fracture heights for an increase in blank diameter from 254.0 mm to 304.8 mm. This is unusual since commonly the failure height decreases with increasing draw ratio. This is because the restraining force increases with an increasing flange surface area and the restraining force is usually the most important factor determining the deepest possible draw. The uncommon increase in failure height can be explained as follows. Stretching starts in the test carried out with a blank diameter of 254.0 mm (10") when the punch progressed about halfway which means not much flange was left, i.e. not much material was left to be stretched into the die cavity. On the contrary, for a stamping operation with a 304.5 mm (12") blank, quite a large flange is left when stretching starts. This means that less thickness strain will occur and thus the material can be stretched further. Since HSG steel does not possess a large  $n$ -value this effect does not show, and thus the failure heights of UV steel will be larger for greater draw ratios as can be seen from the experimental data.

When comparing fracture heights of UV and HSG steel, it can be seen that for small draw ratios, the failure heights are similar, but for increasing draw ratios UV steel shows larger fracture heights. This can be explained as follows. The test which is performed with a blank diameter of 254.0 mm (10") is almost pure deep drawing, i.e. almost no stretching is involved. Thus the maximum drawing depth will be determined mainly by the  $r$ -value. Therefore, it can be expected that the fracture height is roughly the same as the one found for HSG steel since the  $r$ -values of both materials do not differ

much. On the contrary, the deformation associated with larger draw ratios involve a considerable amount of stretching. Thus, the  $n$ -value will become more dominant in determining the maximum drawing depth. This can be explained as follows: Since the outer rim of the material thickens most, most of the BHF is applied at that region. Thus, the material closer to the die corner radius can be stretched relatively easily over the die corner radius into the die cavity. As explained before, the higher the  $n$ -value, the better the material can resist local thinning which results in an improved stretchability. This effect is indicated for the larger draw ratios of UV steel.

Related to this is the reason for the increase in failure height for a drawing operation applied to an initial blank diameter of 304.8 mm (12") when compared to one performed with an initial blank diameter of 254.0 mm (10").

The material yielding the highest failure heights of all is IF steel. This material possesses a high  $n$ -value combined with a high  $r$ -value which give it a superior drawability. The high  $n$ -value also distributes localized strains which clearly aids drawing when some stretching is involved. This is the reason why still a considerable failure height can be obtained for larger draw ratios. As expected, the line connecting the failure lines shows a steady decrease with increasing draw ratio.

### 7.4.2. Wrinkling

During the experiments, wrinkling/puckering occurred over the die corner radius for most materials tested under different process conditions. A wrinkled cup is shown in Figure 7.34. This phenomena was the most severe with Aluminum Alloy 1100-O. Thus, the next series of experiments concentrated on this material. For the material properties, and process conditions, see Table 7.19.

**Table 7.19: Summary of material properties, and process conditions for deep drawing of AA 1100-O**

<u>Material properties and blank dimensions</u>	
r (anisotropy factor)	0.8955
K (strength coefficient)	161.736 [MPa]
n (strain hardening exponent)	0.2297
$\epsilon_0$ (pre strain)	0
Blank diameter	254.0 [mm]
Blank thickness	0.8128 [mm]
<u>Process conditions</u>	
Lubrication condition	water base lubricant *
Blank holder force	6.4 kN, 113.7 kN

- \* Lubrication was put on both sides of the sheet but not on the area where the punch would come into contact with the blank. A water base lubricant (product no. DB-4251) was used. All blanks were cleaned with a special cleaning solvent before the experiments.

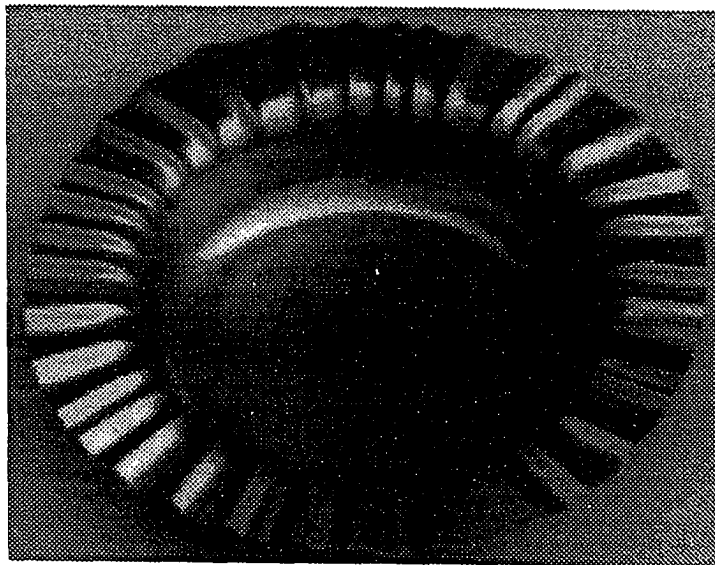


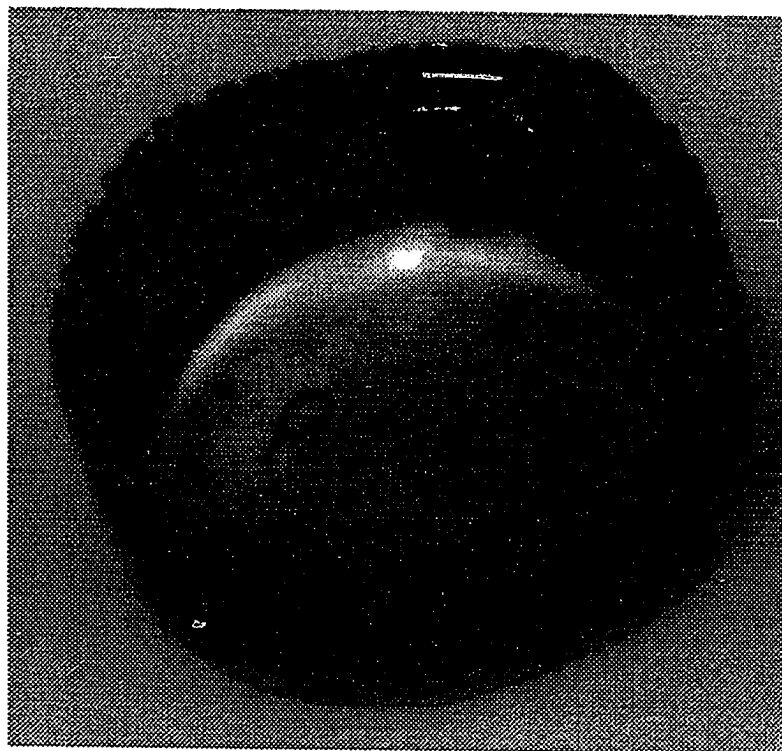
Figure 7.34: Wrinkling in deep drawing AA1100-O. Blank diameter is 279.4 mm, thickness 0.8128 mm, and BHF is 6.4 kN..

The drawing of cups using a large die corner radius often causes problems. The reason is that the sheet material drawn over the die corner is only semi-supported, i.e. there is no means to apply a load perpendicular to that specific part of the cup. Thus when tangential compressive stresses are applied to the sheet, it will easily start wrinkling. With decreasing blank thickness, it will become more severe, since the moment of inertia decreases. This wrinkling phenomena is often called puckering when it occurs over the die corner.

Since puckers appear close to the blank edge, they are impossible to remove. Investigations by Beisswanger, 1947, have shown that puckers formed in the early stages of the draw in thick sheet can be reduced during continuing deformation, but puckers in thin sheets always tend to grow.

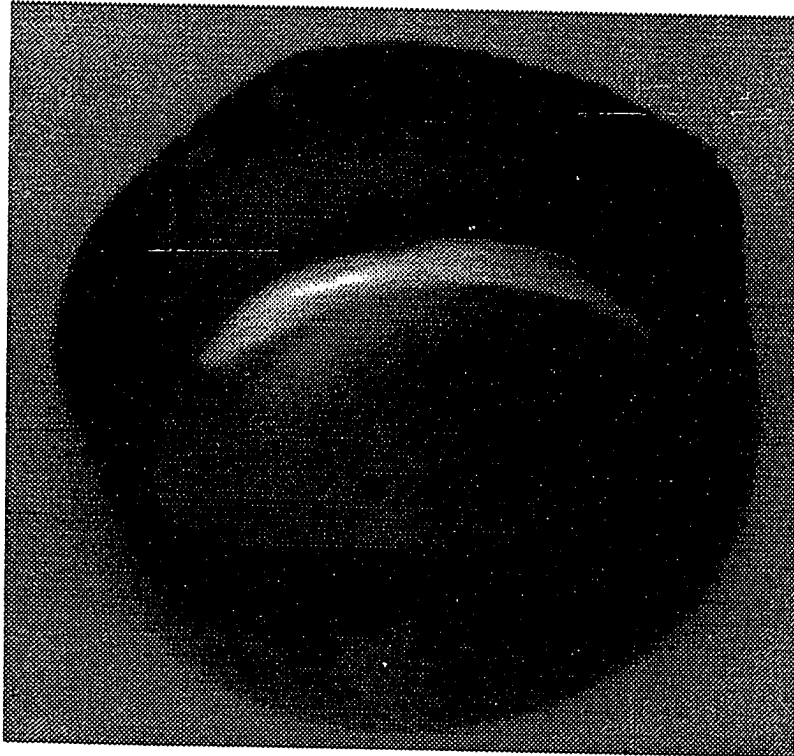
A cup was formed from an AA1100-O blank having a diameter of 254.0 mm using a BHF of 6.4 kN. In this case, severe wrinkling has occurred (Figure 7.35a) These wrinkles were due to two reasons: 1) low BHF was not enough to create enough pressure to prevent the initiation of the wrinkles in the flange region, 2) large die corner radius caused extensive tangential stresses over the die corner where the sheet metal was not constrained and was free to wrinkle. When the BHF was increased, initiation of the wrinkles at the flange region was prevented. However, puckering over the die corner still occurred (Figure 7.35b).

All recommended actions to eliminate puckering are based on the elimination of the tangential compressive stress. Lange presents 3 different ways to avoid puckering when drawing conical shapes, [Lange, 1985]. These



a) BHF is 6.4 kN.

Figure 7.35: Wrinkling in deep drawing of AA1100-O. Blank diameter is 254.0 mm, thickness is 0.8128.



b) BHF is 113.7 kN.

Figure 7.35: Continued.



recommendations can also be applied, in some modified form, to our geometry. The recommendations are:

1) Increase the blank holding pressure. This increases the restraining force applied to the material and the radial stress in the material. According to the flow criterion, tangential stresses are reduced and puckering is less likely to occur.

2) Increase the initial blank diameter  $d_0$ . The reason is the same as the one mentioned under recommendation 1. It causes an increase in the radial stress over the die corner radius, and, hence a decrease in the tangential compressive stress in that region. The larger the blank diameter, the larger the resulting radial stress is. When drawing conical shapes, it is even possible to increase the radial stress so much that the tangential stress changes sign and becomes tensile near the punch, see Figure 7.36.

3) Use of drawbeads. Since drawbeads increase the restraining force, the risk of puckering is reduced as explained under recommendation 1. An additional benefit is that the material also is cold worked when it passes through a drawbead. This restrains the material which makes it harder for wrinkling or puckering to start.

These recommendations cannot readily be transferred to our problem which is caused by the large die corner radius. The specific problems encountered during experiments were:

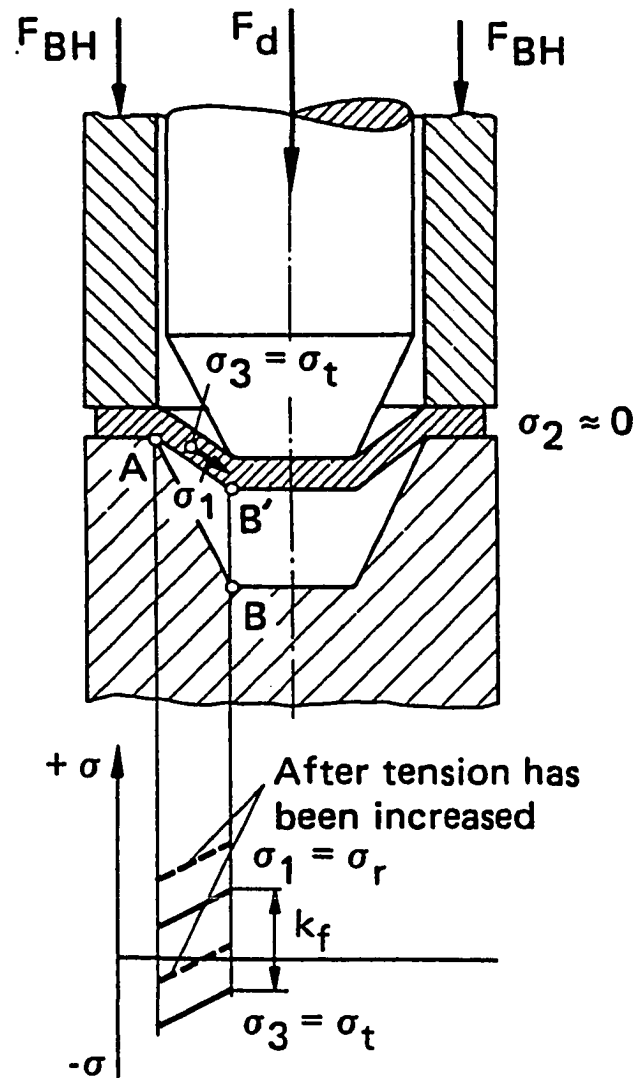


Figure 7.36: Schematic diagram of deep drawing conical shapes, and the corresponding stress distribution, [Lange, 1985].

1) The material, AA 1100-O, used in the experiments possessed a fairly large  $\Delta r$  value which resulted in large ears. When getting close to the final stage of the drawing process, the flange only consisted of 4 ears since the valleys already had passed over the starting point of the die corner. Thus, the BHF is applied to the ears only since those are the only parts constrained between the die and blankholder. When this situation appeared, puckers easily formed at the unsupported valleys. This problem could not be solved by increasing the BHF.

2) The other problem was that puckering had already started when there was still some flange left all around the die corner radius. From tests conducted, it was found that the puckers start occurring simultaneously with the onset of earing. Puckering was more severe with increasing blank holding force. The reason for this is that due to earing an uneven restraining force distribution acts on the flange. As can be seen, the restraining force will increase at the cross sections with ears. The higher the BHF the more uneven the restraining force distribution is. Thus, puckers will show up more severely.

Finally, an investigation of the BHF variation on the initiation of wrinkling was carried out. For this set of experiments, punch travel was set to 65 mm. Two different BHF variations were used (Figure 7.37). In both variations, initial BHF was 80 kN. In the first variation, BHF was increased to 200 kN at 40 mm punch travel. In the second variation, BHF was reduced to 10 kN at 40 mm punch travel. The results of the first and the second experiments are shown in Figures 7.38a and Figure 7.38b, respectively. In both of the

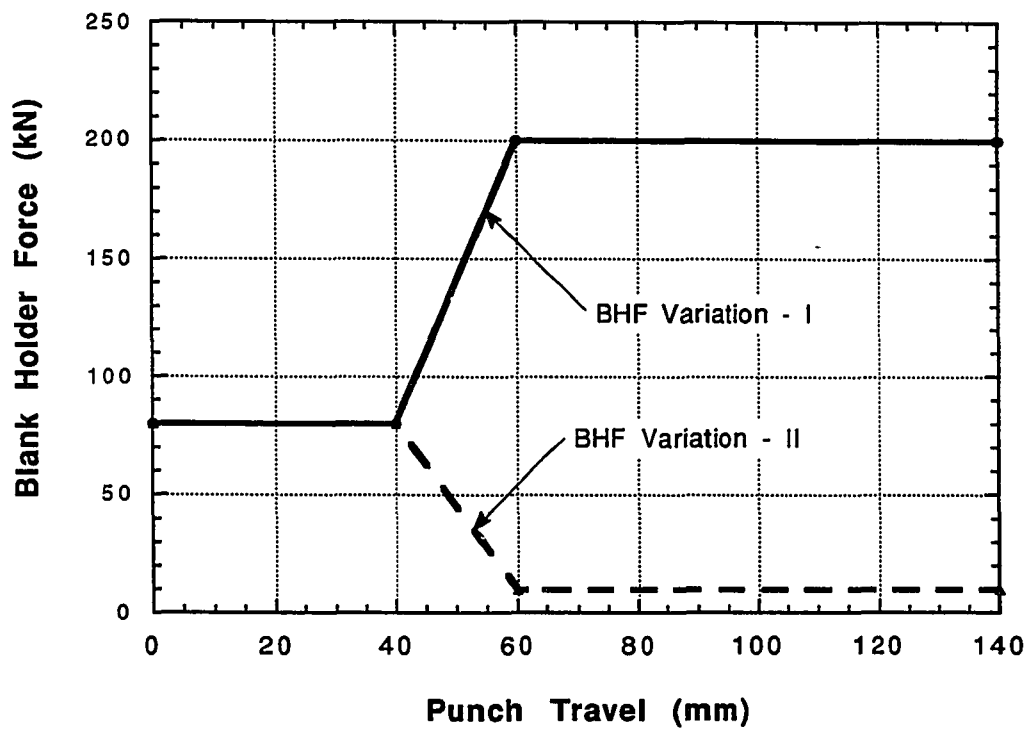


Figure 7.37: BHF variations used in the experiments to study the wrinkling.



- a) Effect of an increase in the BHF towards the end of the process as shown in Figure 7.37.

Figure 7.38: Effect of BHF variation on wrinkling.



a) Effect of a decrease in the BHF towards the end of the process as shown in Figure 7.37.

Figure 7.38: Continued.

experiments, initial BHF of 80 tons was enough to prevent the initiation of wrinkles at the flange region in the beginning of the process. In the first experiments, since the BHF was increased towards the end of the deformation and ears started to grow, a large portion of BHF was applied on the ears and the material between ears was relatively less constrained, therefore, wrinkles has occurred in the valleys. In the second experiment, BHF was reduced towards the end of the deformation and material was allowed to flow into the die cavity easily all around the periphery of the cup. Therefore, wrinkling (or puckering) was prevented.

#### **7.5. Optimum BHF to Improve The Drawability**

During the deep drawing of axisymmetric cups, the important failure modes are wrinkling and fracture. The most commonly used method to prevent wrinkling is the application of blank holding forces (BHF) at the periphery of the cup. The value of the BHF is an important factor to eliminate wrinkling, and in the mean time, not to cause fracture. If the BHF is low, wrinkling may occur. On the other hand, if it is too high, fracture will occur. If a constant BHF is used, then the BHF should be kept within a certain operating range to obtain the desired depth, as shown in Figure 3.12.

Considering the fact that different modes of failure becomes important at different punch travels during the deformation, the BHF does not have to be kept constant throughout the deformation. Wrinkling is important at the

beginning of the deformation due to the large compressive stresses in the flange of the cup. However, as the deformation progresses radial stresses buildup in the wall of the cup and fracture may occur due to an excessive amount of stretching. Therefore, the BHF should be varied during the forming process instead of being kept constant.

There are several methods suggested in the literature to identify the variation of the BHF during the forming process. Three of these methods are programmed into SHEET\_FORM. In this section, these methods will be explained.

#### **7.5.1. Punch Force Control Method**

In deep drawing, the main reason for applying the BHF is to control the metal flow and prevent wrinkling. The punch force control method comes from the idea that the BHF should be as high as possible to prevent wrinkling without causing fracture in the sheet metal. One method to predict fracture in the sheet metal is to monitor the punch force since it is related to the forces in the sheet metal. The procedure for the punch force control method is explained below.

In deep drawing, deformation is obtained by the application of a punch force at the bottom of the cup. This force is carried to the wall and the flange of the cup in the form of radial stress, Figure 7.39. Considering the free body



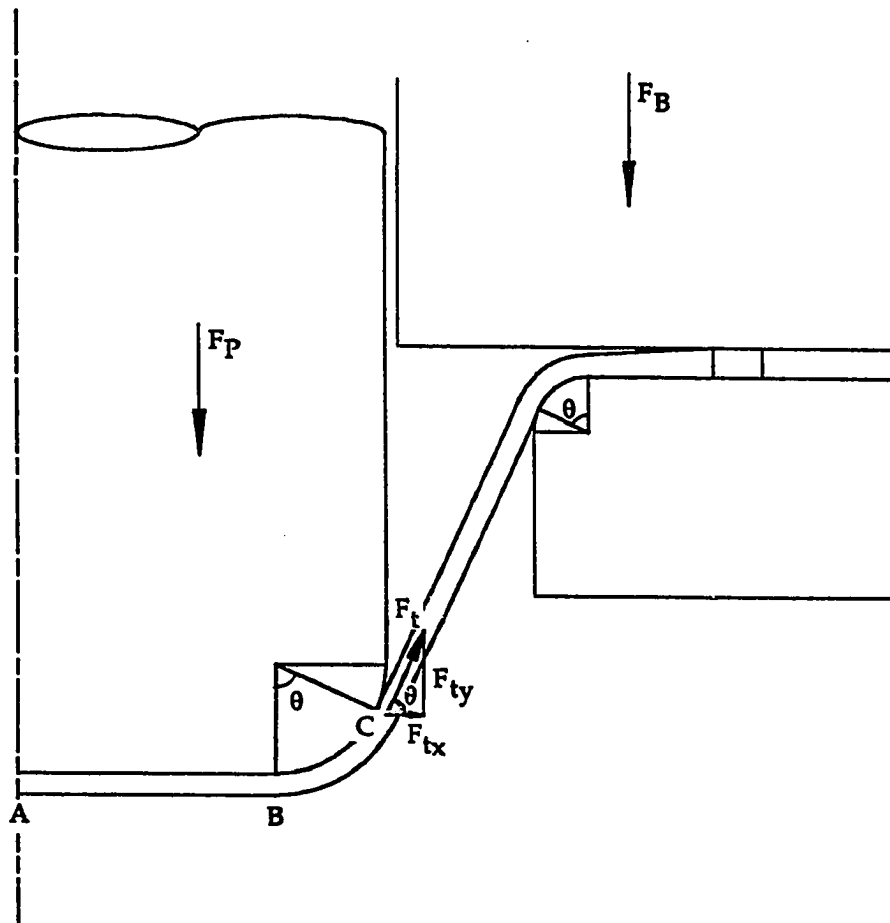


**Figure 7.39:** Forces acting on the sheet metal during a deep drawing operation.

diagram of the cup between the points A and C, Figure 7.39, the punch force,  $F_p$ , should be in equilibrium with the vertical component of the tangential force,  $F_{ty}$ , at the punch nose.

$$F_p = F_t \sin \theta \quad (7.2)$$

The tangential force should not be so high as to cause fracture or necking in the sheet metal. The maximum value of the tangential force,  $F_t$ , can be calculated from the necking conditions.

$$F_t = A\sigma_c \quad (7.3)$$

The critical stress can be calculated as

$$\sigma_c = K(n + \epsilon_0)^n \quad (7.4)$$

Combining equations 7.2, 7.3 and 7.4 gives

$$F_p = AK(n + \epsilon_0)^n \sin \theta \quad (7.5)$$

where

- A: normal area of the sheet at point C
- $F_t$ : tangential force at point C
- $\theta$ : separation angle of the sheet at the punch nose
- K: strength coefficient
- n: strain hardening exponent
- $\epsilon_0$ : initial strain

During the process simulation, the starting value for the BHF is defined by the user. At each step of the simulation, the punch force is calculated and compared to the value calculated from Equation 7.5. In the beginning of the deformation when there is not much metal flow, the punch force is low

compared to the value calculated from Equation 7.5. To increase the punch force, the BHF should be increased to a high level. This will cause an extensive amount of stretching and fracture at the punch nose in the very early stages of the deformation. Therefore, the punch force control scheme starts after a certain amount of deformation or when the punch force reaches the value calculated from Equation 7.5. By adjusting the BHF, the punch force computed during the simulation is kept close to the optimum punch force calculated from Equation 7.5. Several iterations with an adjusted value of the BHF are required to obtain the desired tolerances.

Punch force control method is illustrated using High Strength Hot Dipped Galvanized Steel and the geometry shown in Figure 7.2. The cup geometry, process, and material parameters are given in Table 7.20.

**Table 7.20: Summary of material properties, and process conditions for deep drawing of HSG steel.**

<u>Material properties and blank dimensions</u>	
r (anisotropy factor)	1.40
K (strength coefficient)	603.83 [MPa]
n (strain hardening exponent)	0.143
$e_0$ (pre strain)	0.000328
Blank diameter	330.2 [mm]
Blank thickness	0.889 [mm]
<u>Process conditions</u>	
Lubrication condition	dry
Initial blank holder force	200 kN, 400 kN

A blank of 330.2 mm diameter and 0.889 mm thick was used in the simulations. Two different starting value of the BHF were used. The predicted BHFs are shown in Figure 7.40. As can be seen in Figure 7.40, the BHF initially stays constant until the critical punch force calculated from the Equation 7.5 is reached, and it is lowered initially to reduce the punch force and prevent fracture. Towards the end of the deformation, as the flange area decreases, the punch force drops, and at this point the BHF can be increased. After the sheet metal leaves the blank holder area, there is no need for the BHF, and it stays constant, as shown in Figure 7.40.

Punch force distributions resulted from the BHF variations starting from 200 kN, and 400 kN are shown in Figures 7.41 and 7.42, respectively together with the optimum punch force distribution calculated from Equation 7.5. Punch force distributions obtained by using constant BHFs of 200 kN and 400 kN in the simulations are also shown in these figures. As shown, fracture was predicted in each case using constant BHFs. However, during the simulations using both BHF variations shown in Figure 7.40, fracture was not predicted.

Starting from two different values, almost the same variations are predicted. The punch force distributions resulting from both BHF variations shown in Figure 7.39 are plotted in Figure 7.43.

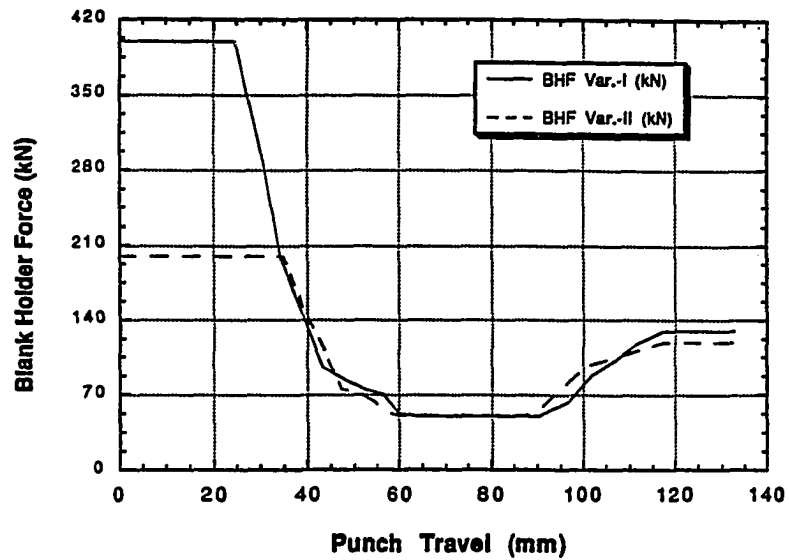


Figure 7.40: BHF variation predicted based on punch force control method.

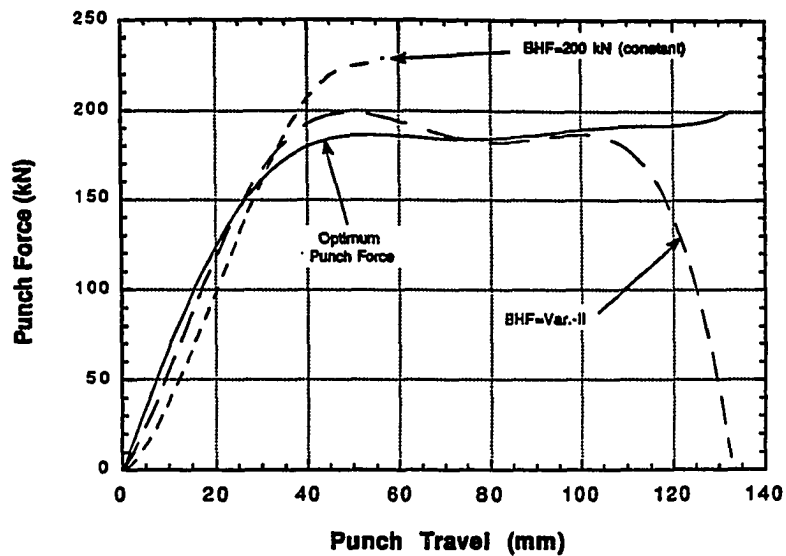


Figure 7.41: Punch force profile using constant 200kN, and variable BHF based on punch force control method together with the optimum punch force distribution calculated from the Equation 7.5.

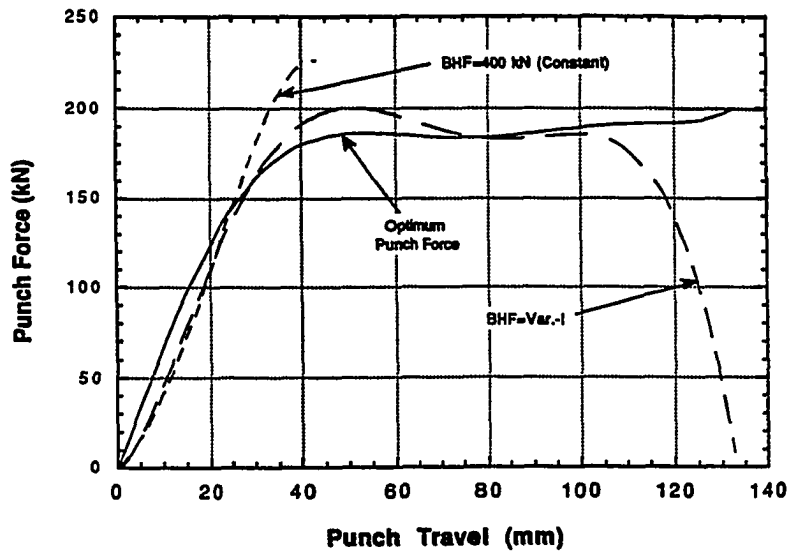


Figure 7.42: Punch force distributions using constant 400 kN, and variable BHF based on punch force control method together with the optimum punch force distribution calculated from Equation 7.5.

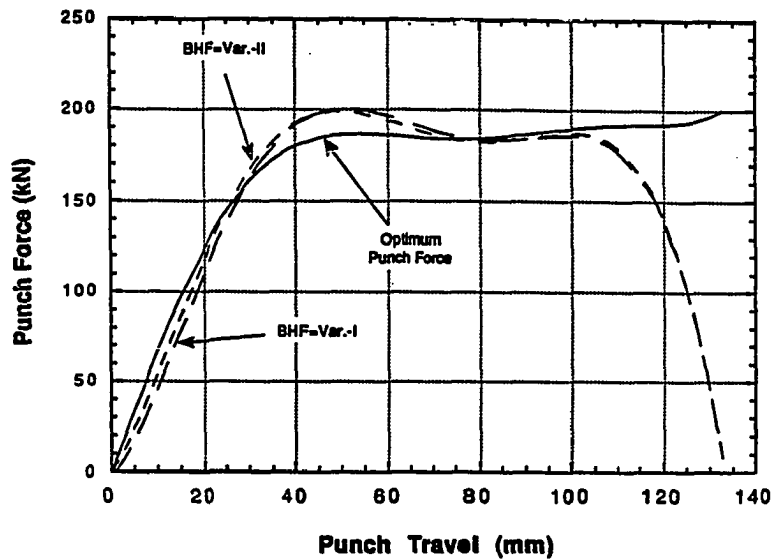


Figure 7.43: Punch force distributions using the BHF variations shown in Figure 7.40 together with the optimum punch force distribution calculated from the Equation 7.5.

### 7.5.2. Radial Stress Control Method

Instead of comparing the punch force with an optimum value, the maximum radial stress computed during the process simulation can be directly compared to a critical value. This critical value can also be obtained from the critical stress from the necking conditions (Equation 7.4).

If the maximum radial stress exceeds this critical stress, necking will start and will result in fracture. On the other hand, if the radial stress is too low which means a low BHF, it will result in wrinkling. Therefore, the BHF is varied during the process simulation to keep the maximum radial stress close to the critical value within a tolerance. An iteration is performed on BHF at each step during the simulation to predict the optimum BHF variation.

Two BHF force variations are predicted starting from the initial values of 200 kN and 400 kN, Figure 7.44. The radial stress control method is activated when the radial stress reaches the critical value. BHF is initially reduced and later increased towards the end of the deformation. This increase towards the end of the deformation may not be necessary for most of the materials because wrinkling will not be important since the flange area is reduced considerably at that stage.

The maximum radial stress distributions resulting from the BHF variations shown in Figure 7.44 are plotted in Figures 7.45 and 7.46 together with the

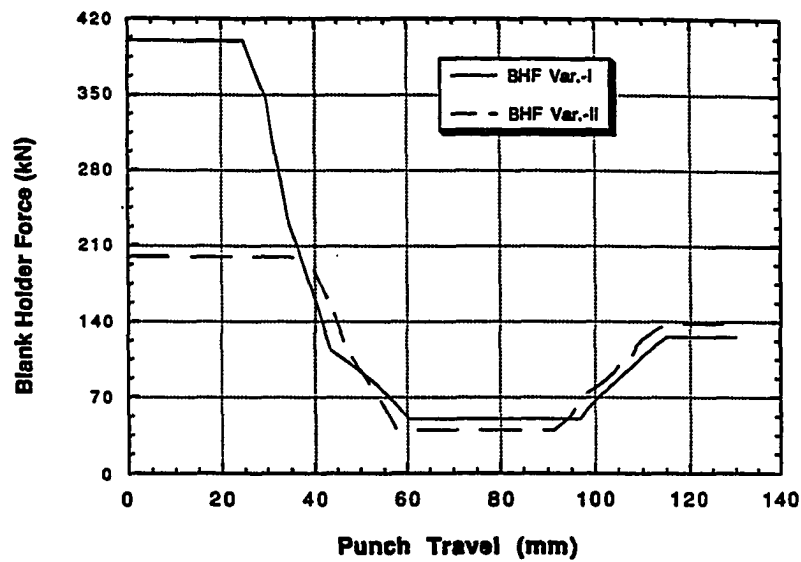


Figure 7.44: BHF variations predicted based on radial stress control method.

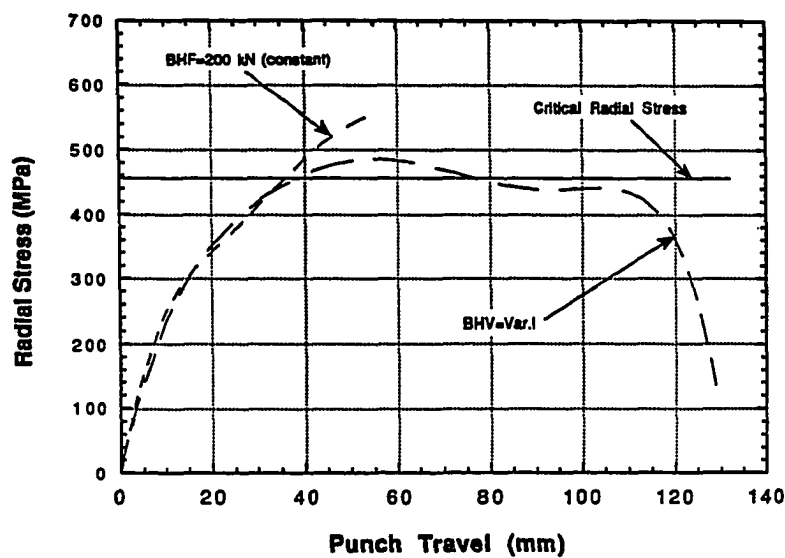


Figure 7.45: Maximum radial stress vs. punch travel using constant 200 kN, and variable BHF based on radial stress control method together with the critical radial stress calculated from the Equation 7.4.



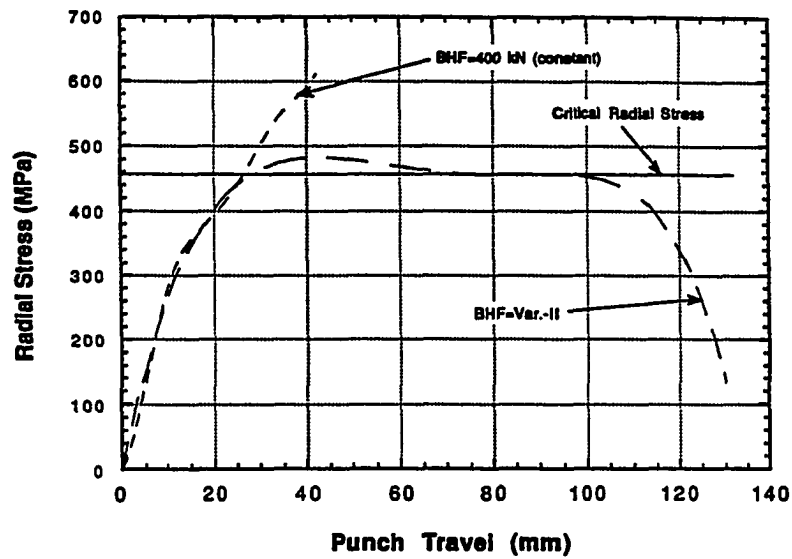


Figure 7.46: Maximum radial stress vs. punch travel using constant 400 kN, and variable BHF based on radial stress control method together with the critical radial stress calculated from the Equation 7.4.

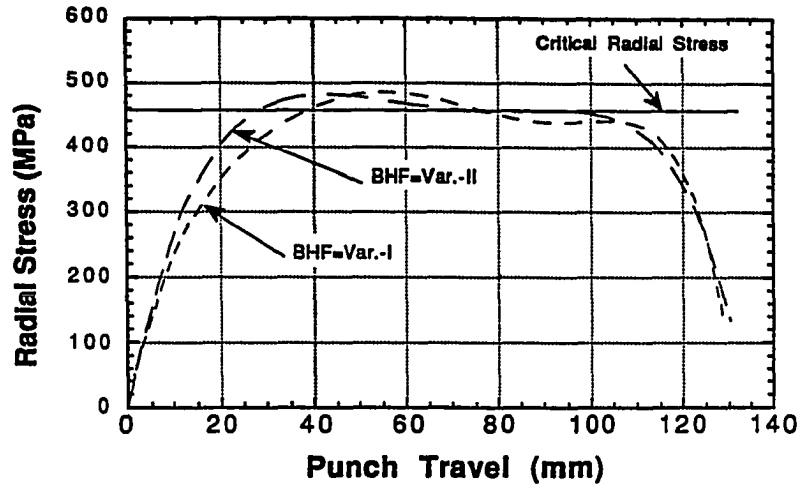


Figure 7.47: Maximum radial stress distributions using the BHF variations shown in Figure 7.44 together with the critical radial stress calculated from the Equation 7.4.

results of constant BHF. As can be seen in Figures 7.45 and 7.46, in both cases, fracture was predicted using constant BHFs.

Both maximum radial stress distributions resulting from two BHF variations given in Figure 7.44 are plotted in Figure 7.47. As can be seen in the figure, the difference in the initial value of the BHFs does not affect the resulting distribution very much.

### **7.5.3. Thickness Strain Control Method**

Thickness strain and thickness strain gradient computed during the process simulation can be used to predict fracture. If the thickness strain is more than a predefined limit, then the BHF can be modified to reduce it.

BHF variations starting from 200 kN and 400 kN initial values are shown in Figure 7.48. In these simulations, a limit of 10% thickness strain was used. The BHF was reduced in the beginning of the deformation and stayed constant until the end of the deformation.

Maximum thickness strain distributions for both BHF variations given in Figure 7.47 are given in Figures 7.49 and 7.50. As can be seen in Figure 7.50, the maximum thickness strain has reached 25% and fracture was predicted at this point. However, by varying the BHF it was possible to keep the maximum thickness strain around 10% and complete the deformation.

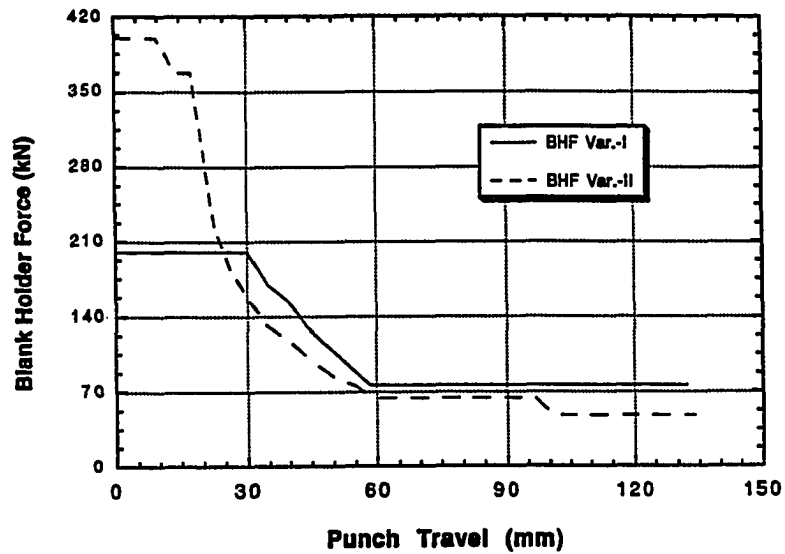


Figure 7.48: BHF variations predicted based on maximum thickness strain control method.

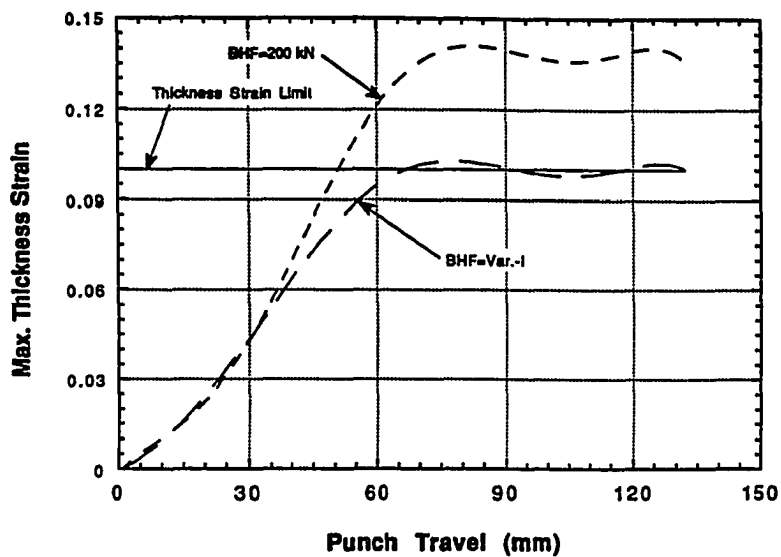


Figure 7.49: Maximum thickness strain vs. punch travel using constant 200 kN, and variable BHF based on thickness strain control method together with the maximum desirable thickness strain.

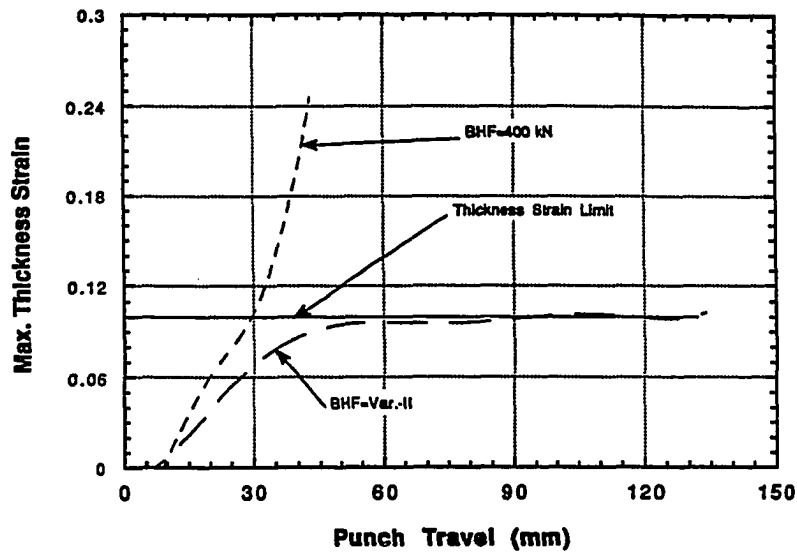


Figure 7.50: Maximum thickness strain vs. punch travel using constant 400 kN, and variable BHF based on thickness strain control method together with the maximum desirable thickness strain.

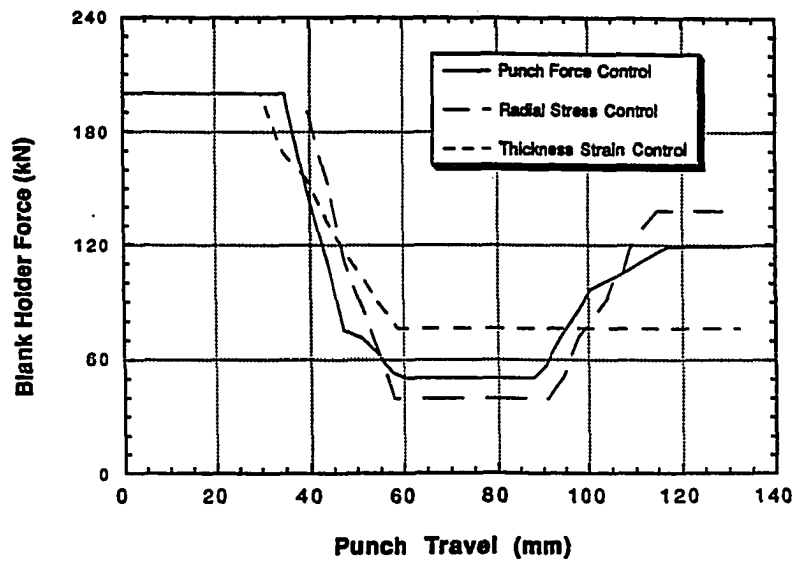


Figure 7.51: BHF variation predictions based on punch force, maximum radial stress, and maximum thickness strain control methods with an initial BHF of 200 kN.

Failure criterion was turned off during the simulation using the constant BHF of 200 kN. In this case, the maximum thickness strain reached 14%. By varying the BHF, it was possible to reduce the maximum thickness strain to 10% as shown in Figure 7.49.

BHF variations predicted using the three methods explained before are shown in Figures 7.51 and 7.52 for the starting value of 200 kN and 400 kN, respectively. All three methods yielded similar variations. In the BHF variation obtained by maximum thickness strain method, an increase is not predicted because this method does not try to approach an optimum thickness strain trajectory; rather it tries to keep the thickness strain lower than a certain value.

#### **7.5.4. Experiments and Comparison with Simulation Results**

In the previous experiments, blank diameters were all less than 304.8 mm. For this section, the blank diameter was increased, and the effect of BHF on the quality of the cup was studied. The BHF variations were first estimated by using SHEET\_FORM, and later will be modified to improve the cup quality. Several comparisons with the constant BHF can be made.

The geometry of the tooling is the same as the one shown in Figure 7.3. Dry friction conditions and three different steel blanks of 330.2 and 355.6 mm diameter were used in the experiments. It was not possible to completely form the blank with 355.6 mm diameter without fracture. However, using a

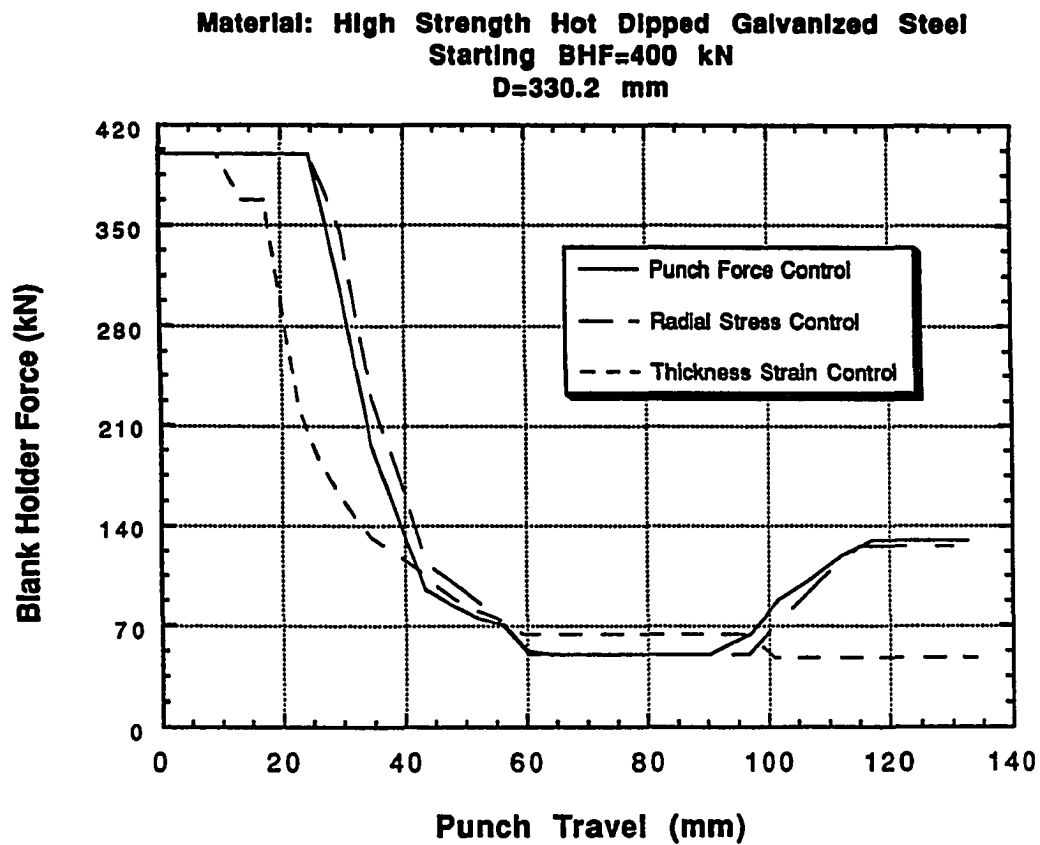


Figure 7.52: BHF variation predictions based on punch force, maximum radial stress, and maximum thickness strain control methods with an initial BHF of 400 kN.

variable BHF it was possible to increase the attainable cup height. These experiments are summarized in the following paragraphs.

High Strength Hot Dipped Galvanized Steel:

Material properties, and process conditions used in these experiments are the same as the ones given in Table 7.7 except for the blank diameter, and the BHF. The blank diameters used were 330.2 and 355.6 mm.

Several experiments were done using a constant BHF and a blank of 330.2 mm in diameter. The results of these experiments are given in Table 7.21:

**Table 7.21: Results of constant BHF experiments.**

BHF (tons)	Result
15	fracture at 28.5 mm punch travel
10	fracture at 73.0 mm punch travel
7	severe wrinkling

Based on Table 7.21, the following conclusions were drawn:

- (1) Using a constant BHF of 15 tons, the cup fractured at a punch travel of 28.5 mm.

- (2) Using a constant BHF of 10 tons, the cup fractured at a punch travel of 73.0 mm. The BHF and the punch force distribution measured during this experiment is shown in Figure 7.53. As can be seen in this figure, the punch force is still increasing close to the position where the fracture occurred. If the BHF were reduced close to a 70 mm punch travel to decrease the punch force, it would be possible to fully form this cup. There was also some minor wrinkling which probably occurred during the initial stages of the deformation.
- (3) Using a constant BHF of 7 tons, severe wrinkling occurred and the deformation was not completed.

Based on these results it was apparent that it would not be possible to form 330.2 mm diameter blanks into 152.4 mm cup using a constant BHF under the current process conditions. The BHF should be varied to prevent wrinkling and, at the same time, avoid fracture.

Possible BHF variations were estimated based on simulation and three control methods explained in Section 7.7.1 through 7.7.3. The results are shown in Figure 7.54. The initial BHF was defined as 15 tons in these simulations. The punch force and radial stress control methods predicted similar variations for the BHF. In the beginning of the deformation, the BHF is kept constant until a critical punch force or radial stress is reached. Later, the BHF is reduced where the maximum punch force occurs. Towards the end of the deformation, since the flange area is reduced and the punch force starts decreasing, BHF can be increased without exceeding the critical punch



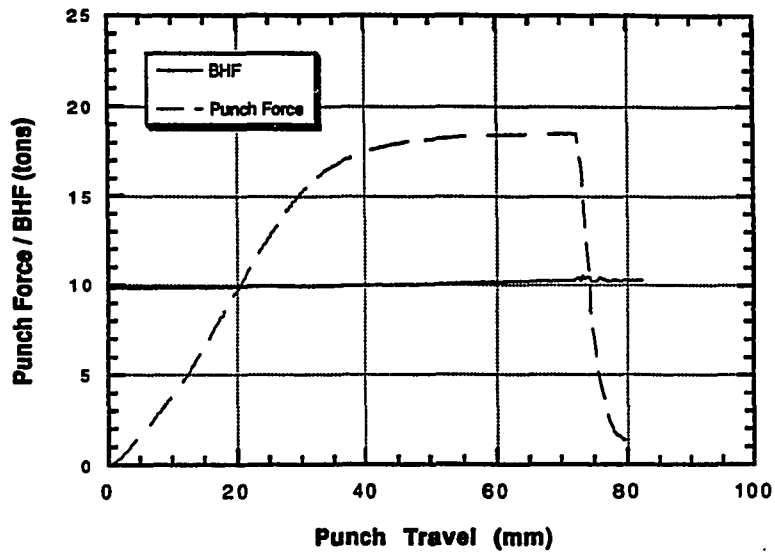


Figure 7.53: Punch force and BHF distributions measured during the deep drawing of HSG steel. (Blank diameter is 13 inches)

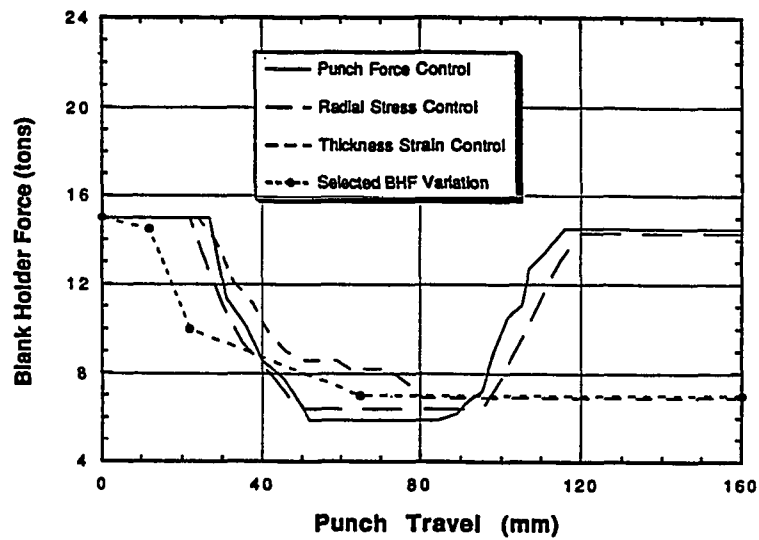


Figure 7.54: Estimated BHF variations for deep drawing of high strength steel.

force or radial stress. This increase in the BHF may be necessary in deep drawing of conical cups or non-symmetric cups to increase the restraining forces and prevent wrinkling or puckering towards the end of the process. In deep drawing of cylindrical cups as in our case, an increase in the BHF with increasing ram stroke is not necessary. Once the sheet metal leaves the blank holder contact region, there is no control on the BHF, and this is represented as the constant region at the end of the BHF profile, Figure 7.54.

The BHF profile as a function of punch travel predicted by thickness strain control method is also shown in Figure 7.54. Based on this method, the BHF is reduced to prevent excessive thinning during the deformation.

Based on the simulation results and the previous experiments using constant BHFs, Table 7.21, a BHF variation was selected and it is shown in Figure 7.54. Dots shown on the profile are used to enter the variation into the Minster press control system. An experiment was performed using this predicted BHF variation and the cup was successfully formed to a height of 159 mm. Blank holder and punch force distributions measured during the experiment are shown in Figure 7.55 together with simulation results.

Experiments were also conducted using a blank of 355.6 mm in diameter. But, it was not possible to draw this blank completely due to severe wrinkling and fracture in the early stages of deformation.

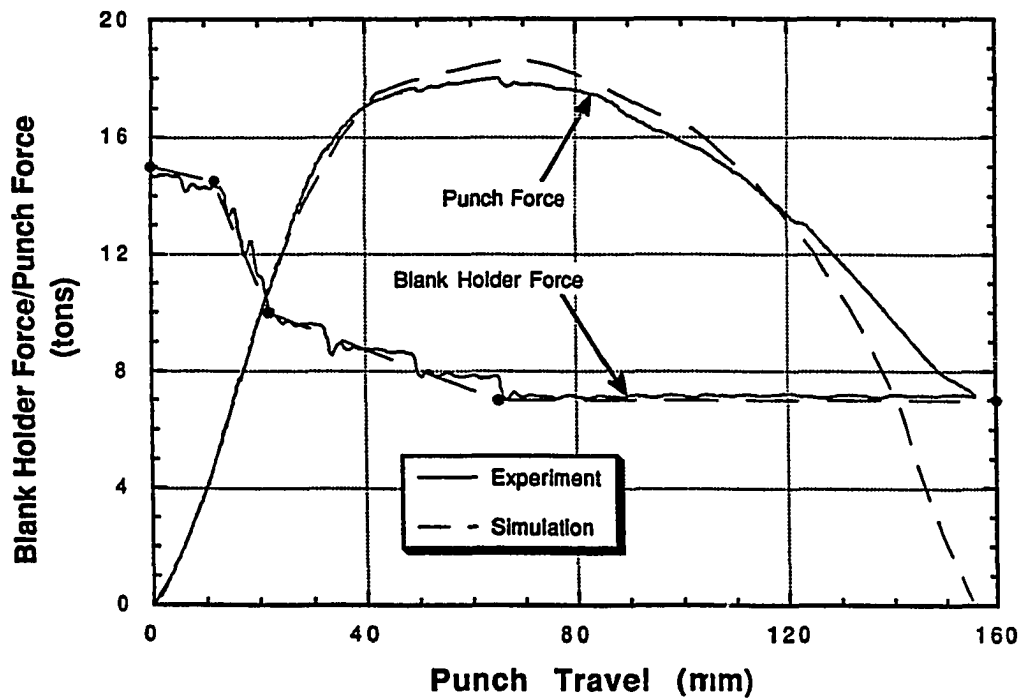


Figure 7.55: Punch force and BHF distributions measured during the deep drawing of HSG steel together with the predicted ones. (Blank diameter is 13 inches)

Univit Steel:

Process conditions, and material properties used in these experiments are the same as the ones given in Table 7.9 except for the blank diameter and the BHF. Blanks 330.2 and 335.6 mm in diameter were used in the experiments together with the variable and constant BHFs described in the following paragraphs.

Using a constant BHF of 151 kN and a 330.2 mm diameter blank, fracture occurred at 38 mm punch travel.

An experiment using the BHF variation shown in Figure 7.56 and a 330.2 mm diameter blank was performed. The punch force distribution measured during this experiment is also shown in Figure 7.56. Reduction in the BHF after the punch travel of 35 mm was not enough to reduce the punch force, and fracture occurred at a punch travel of 43 mm. This BHF was modified in the second experiment. In this experiment, the BHF was sharply reduced after the punch travel of 20 mm as shown in Figure 7.57. Using the BHF variation shown in Figure 7.57, it was possible to increase the cup height; however, fracture occurred at a punch travel of 87 mm. By further reducing the BHF after 70 mm punch travel, it would be possible to fully form the cup.

Using a constant BHF of 80 kN and a 330.2 mm diameter blank, both wrinkling and fracture occurred during the early stages of the deformation. It

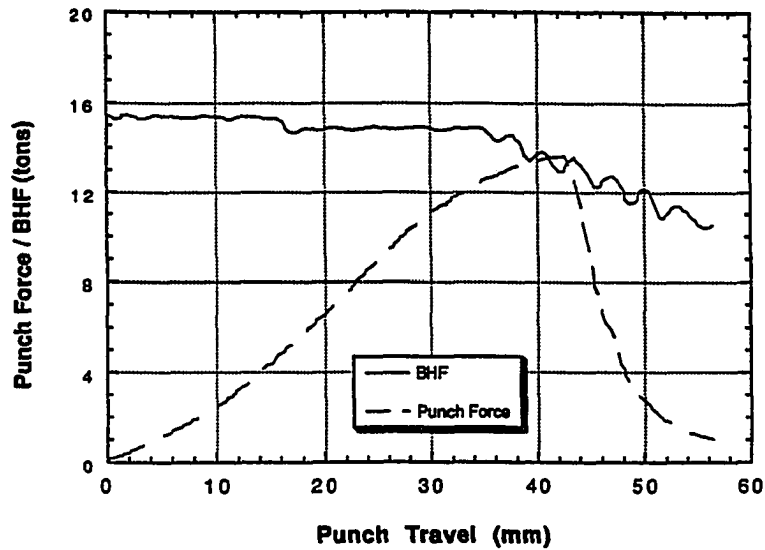


Figure 7.56: Punch force and BHF distributions measured during the deep drawing of UV steel. (Blank diameter is 13 inches)

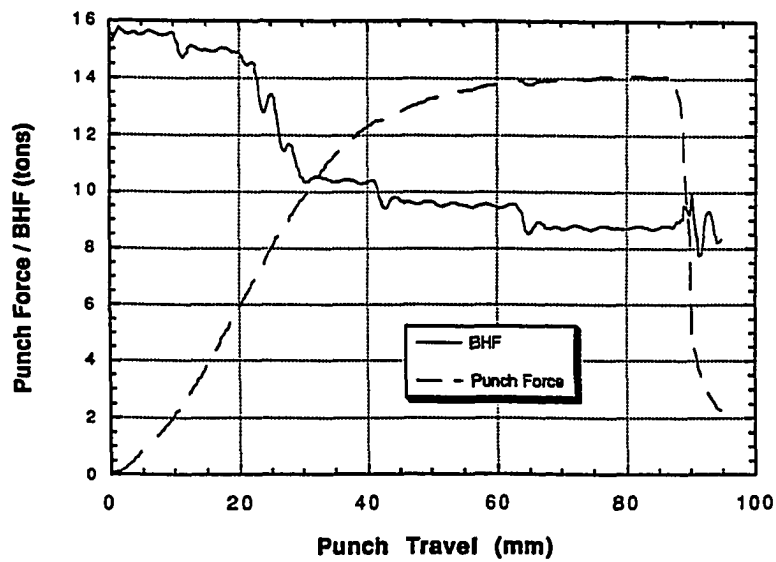


Figure 7.57: Punch force and BHF distributions measured during the deep drawing of UV steel. (Blank diameter is 13 inches)

was not possible to form a 355.6 mm diameter blank due to severe wrinkling and fracture during the early stages of the deformation.

#### Interstitial Free Steel:

Process conditions, material properties, and the tool geometry is the same as the ones given in Table 7.10. However, different BHF's were used together with 330.2 and 355.6 mm diameter blanks.

The first experiment was conducted using a constant BHF of 151 kN, and a 330.2 mm diameter blank. Fracture occurred at 58 mm punch travel.

The second experiment was conducted using the BHF variation shown in Figure 7.58. The punch force measured during the experiment is also shown in Figure 7.58. The cup was fully formed without fracture and wrinkling. The third experiment was conducted using a 330.2 mm diameter blank but this time with a constant BHF of 70 kN. Results of this experiment are shown in Figure 7.59. The cup was again fully formed without fracture but, there were some minor wrinkling. The punch force was slightly lower than the one obtained in the second experiment, as shown in Figure 7.58.

Another experiment was conducted using a constant BHF of 100 kN. Results from this experiment are shown in Figure 7.60. This time fracture occurred at a punch travel of 76 mm.

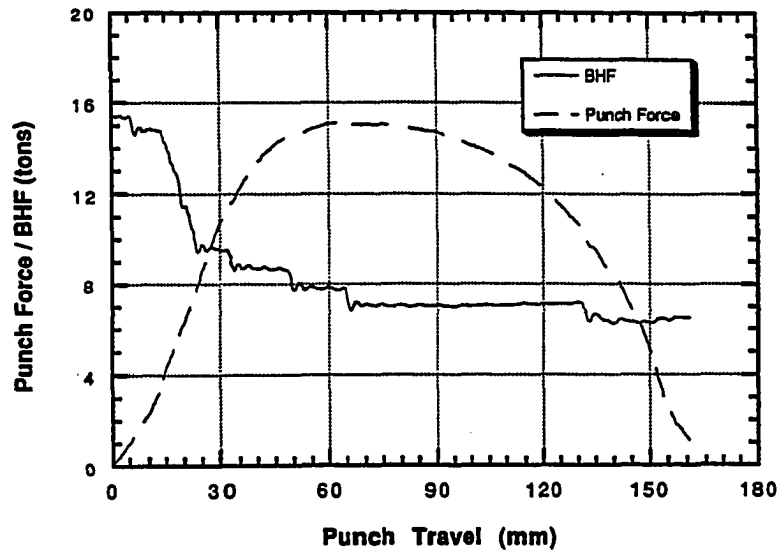


Figure 7.58: Punch force and BHF distributions measured during the deep drawing of IF steel. (Blank diameter is 13 inches)

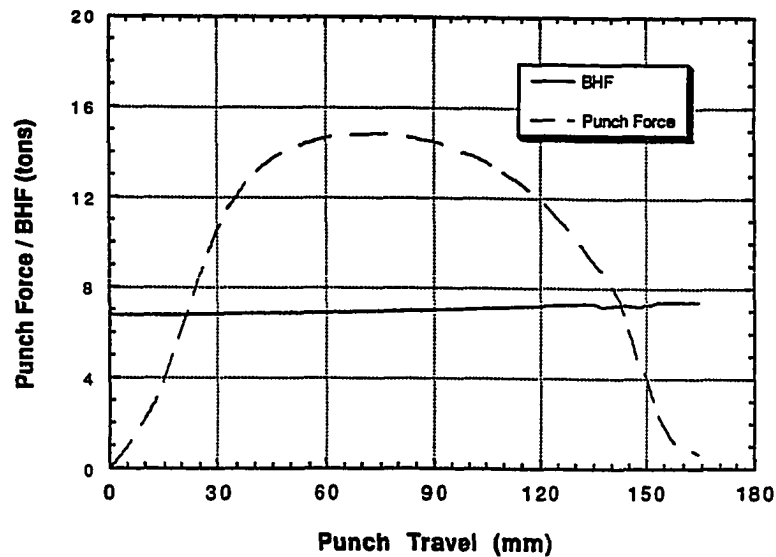


Figure 7.59: Punch force and BHF distributions measured during the deep drawing of IF steel. (Blank diameter is 13 inches)

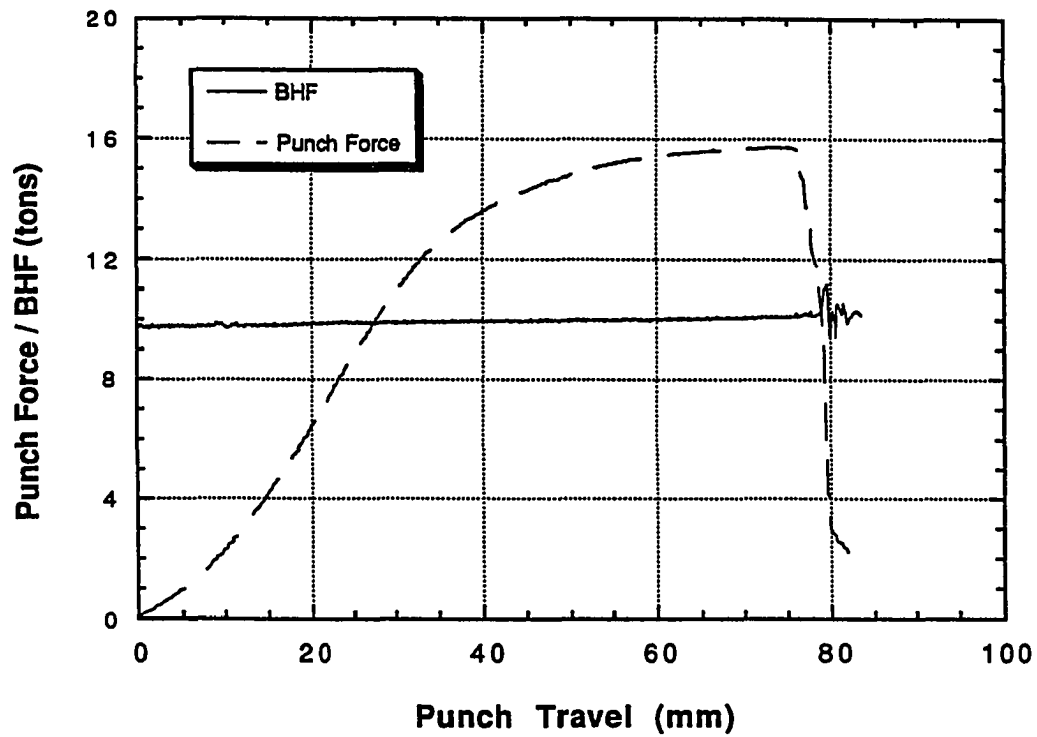


Figure 7.60: Punch force and BHF distributions measured during the deep drawing of IF steel. (Blank diameter is 13 inches)



Several experiments were conducted using a 355.6 mm diameter blank. None of the cups were fully formed due to fracture, but some improvement in the attainable cup height was obtained. Using the BHF variation shown in Figure 7.61, the cup was fractured at a punch travel of 97 mm. In this variation, the BHF was sharply reduced to 40 kN at 65 mm punch travel. In the second variation, the BHF was reduced to 30 kN at 65 mm punch travel as shown in Figure 7.62. The punch force distribution obtained in the second experiment is also shown in Figure 7.62. In this case, fracture occurred at a punch travel of 110 mm.

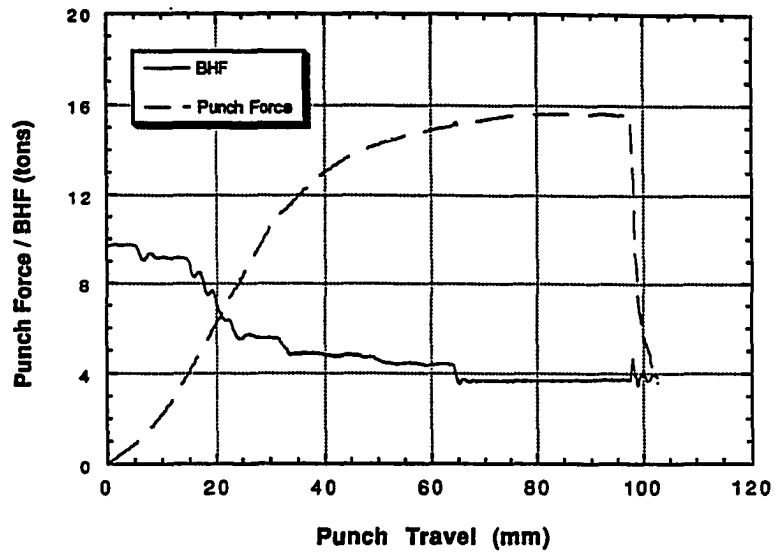


Figure 7.61: Punch force and BHF distributions measured during the deep drawing of IF steel. (Blank diameter is 14 inches)

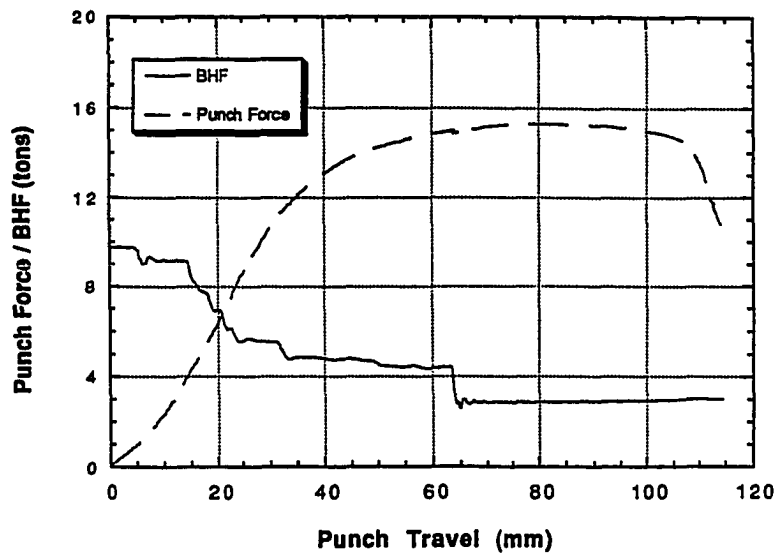


Figure 7.62: Punch force and BHF distributions measured during the deep drawing of IF steel. (Blank diameter is 14 inches)

## CHAPTER VIII

### SUMMARY AND CONCLUSIONS

#### 8.1. Analysis of Deep Drawing and Redrawing

The analysis of stretch forming and deep drawing of axisymmetric and plane-strain geometries using the finite difference based computer program, SHEET\_FORM, has been completed. Details of the formulation can be seen in Chapter V. Predicted major and minor strain, and punch force distributions have been compared with the experimental measurements and Finite Element solutions. Analysis of direct and reverse redrawing of axisymmetric and plane-strain sections with different draw ratios have also been completed. Details of the redrawing formulation can be seen in Appendix E. In the analysis of the deep drawing process, a constant or variable blankholder force as a function of punch travel can be used (Section 5.8). Predicted strain and force distributions agree well with the experiments within engineering accuracy.

## 8.2. Failure Evaluation

One of the major tasks in process simulation is to predict the formation of defects at the design stage, and to modify the part design and/or the process conditions accordingly. This task is undertaken by means of several failure criteria built into the analysis module, SHEET\_FORM. Details of the Failure Evaluation Module are given in Section 6.6. Based on the prediction of stresses and strains under certain process conditions, such as lubricant, material, and BHF, a failure evaluation is performed to predict if failure, i.e., wrinkling and/or tearing, would occur during the actual forming process. Attainable cup heights using constant or variable BHF's as a function of punch travel were calculated and compared with the cup heights at fracture measured during the experiments.

## 8.3. BHF Control in Sheet Metal Forming

During the deep drawing of sheet metal products, wrinkling and fracture may become dominant mode of failure at different punch travels. Therefore, the BHF needs to be adjusted as a function of punch travel rather than being kept constant. SHEET\_FORM has been modified so that the BHF can either be kept constant or varied as a function of the punch stroke during the process simulation. The BHF profile can either be pre-determined and input by the user, or it can be optimized based on several criteria, such as punch force, thickness strain, wrinkling, etc. Details of predicting the optimum BHF

distribution to improve the drawability can be found in Section 7.7. BHF variations were predicted using SHEET\_FORM for three different types of steel blanks. These predictions were later modified and tried out in the experiments. An increase in the attainable cup height was observed when an adjusted BHF was used during the experiments.

#### **8.4. Deep Drawing Experiments**

Several experiments were conducted to verify the results of SHEET\_FORM for the analysis of deep drawing, and redrawing of round cups. Deep drawing experiments were conducted in the 160 ton double-action hydraulic Minster press, and 5 ton triple-action ERC/NSM press. Punch and blankholder forces were measured during the forming process, and the circle grid analysis technique was used to measure the strains. Measured punch forces and strain distributions were compared with the simulation results. Experiments were conducted using both constant and variable BHF as a function of punch travel, and the effect of the BHF on the quality of deep drawn products were studied. Experimental studies are explained in Chapters VI and VII.

#### **8.5. Future Work**

In practice, die design for sheet metal forming processes are usually based on trial-and-error. In general, a sheet metal forming die is quite complex, and it

requires several trial-and-error stages to come up with the final die design. Therefore, this method is time consuming and costly. Any technique which will help die designers to reduce the number of trial-and-error stages will result in a considerable amount of time and money savings. One method is to supply die designers with a robust and easy to use simulation program which will predict failure so that a die design can be fine tuned before the dies are manufactured. Such a simulation program should consist of a simulation module with failure prediction capabilities, and it should be easy to use. SHEET\_FORM has all of these capabilities, and it can be used in such a design environment. However, further modifications should be done to SHEET\_FORM to improve its capabilities:

- 1- A user interface should be developed to present the results from a designers point of view and to make suggestions to improve the design based on simulation results.

- 2- Axisymmetric and plane-strain geometries are not very widely used in the sheet metal forming industry. However, in complex shaped sheet metal parts, there are usually sections close to axisymmetric and plane-strain geometries. Approximate, 2-D, formulations may be used to evaluate these sections without going through a full 3-D analysis of the complex geometry. The application of SHEET\_FORM to analyze complex geometries should be verified, the formulation should be improved, if necessary, and guidelines should be developed.

- 3- The knowledge-based and the analysis modules should be combined to simulate the conventional, trial-and-error, die design method. The hybrid expert system for process planning in progressive die design for the

manufacture of axisymmetric and rectangular sheet metal parts would probably be the first of its kind. The interface with the feature extraction module and the analysis module will make the expert system more efficient and flexible than conventional rule-based expert systems in other areas of manufacturing which utilize only empirical formulas and other rules of thumb for reasoning. The idea of interfacing analysis modules with the inference engine of the expert system is relatively new and is being tried out in engineering design-oriented applications on an experimental basis.

Another feature of the SHEET\_FORM which would be very useful for process designers for sheet metal parts is the prediction of the optimum BHF variation. With a constant BHF, the attainable cup height is limited by either wrinkle or fracture. There is no need to keep the BHF constant throughout the forming process. The BHF can be varied as a function of punch travel to obtain deeper cups and to increase the limiting drawing ratio. The BHF predictions by SHEET\_FORM can be used as an initial estimate and later can be fine tuned by the designers to find the optimum BHF variation. The BHF prediction module should be further improved and it should be extended to more complex geometries such as rectangular cups.

## **8.6. Summary of Research Contributions**

The current study has the following contributions from a practical as well as an academic standpoint:

1) The development of finite-difference method based analysis module for simulating processes such as deep drawing, redrawing, and stretch forming is a difficult and challenging task. The proposed models would satisfy equilibrium, plasticity and compatibility equations at every stage of the process and would be free from empirical justifications. The techniques employed by the current research and its results, being academically fundamental and comparable to recent progress, would likely become an important addition to the expanding realm of literature on process modeling of sheet metal forming.

2) Several experiments were conducted as part of this research. These experiments are reverse redrawing using a cylindrical punch in the Multi Action ERC press, and deep drawing using cylindrical punch in Minster press. The findings from these experiments will be an important contribution to the literature of sheet metal forming.

3) Several criteria have been developed and applied to predict wrinkling and/or tearing during the deep drawing of sheet metal products. This method of predicting failure in the sheet metal during the design stage using the simulation module will help die designers to reduce the number of trial-and-error stages.

4) Real time control of the BHF is an important aspect of sheet metal forming. It is possible to increase the attainable cup height by controlling the BHF. Combined with analytical methods to predict wrinkling and fracture,



methods developed in this study would estimate the BHF variation as a function of the punch travel in order to increase the limiting drawing ratio.

## LIST OF REFERENCES

Adachi, M., and Inoue, K., Funayama, T., 1983, "Integrated CAD System for Progressive Dies", *FUJITSU Sci. Tech. J.*, vol. 19/2, pp. 133-148.

Ahmetoglu, M. A., Kinzel, G. L., and Altan, T., 1990, "Sheet Metal Forming Processes: State of The Technology and Analysis", Report No. ERC/NSM-S-90-46, The Ohio State University, Columbus, Ohio.

Ahmetoglu, M.A., Kinzel, G.L., and Altan, T., 1992a, "Improvement of Part Quality in Stamping by Controlling Blank Holder Force and Pressure (A State of The Art Review)", Report No. ERC/NSM-S-92-12, The Ohio State University, Columbus, Ohio.

Ahmetoglu, M.A., Sweeney, K.E., Brandelstein, J., Kinzel, G.L., and Altan, T., 1992b, "Deep Drawing and Reverse Redrawing of Aluminum Alloy Cups", Report No. ERC/NSM-S-92-49, The Ohio State University, Columbus, Ohio.

Ahmetoglu, M.A., Coremans, A.L.P, Kinzel, G.L., and Altan, T., 1992c, "Deep Drawing of Round Cups Using Variable Blank Holder Force (BHF)", Report No. ERC/NSM-S-92-50, The Ohio State University, Columbus, Ohio.

Aita, S., El Khaldi, F., Fontaine, L., Tamada, T., and Tamura, E., 1992, "Numerical simulations of a Stretch Drawn Autobody: Part I - Assesment of Simulation Methodology and Modelling of Stamping Components", SAE Paper No. 920639.

ASM, 1988, Forming and Forging, Metals Handbook, 9th Edition, Editors S.L. Semiatin et.al., vol. 14.

Asthana, A., Ahmetoglu, M. A., Kinzel, G. L., and Altan, T., 1991, "Evaluation of Failure Estimation and Prediction Techniques in Sheet Metal Forming", Report No. ERC/NSM-S-91-27, The Ohio State University, Columbus, Ohio.

Avitzur, B., 1983, Handbook of Metal Forming Processes, John Wiley & Sons, Pennsylvania.

Behrens, A. W., 1986, "Simulation of Deep-Drawing Processes with Special regard to Circular and rectangular Cups", Advanced Technology of Plasticity, vol. I, pp. 665-670.

Beisswanger, H., 1947, Deep Drawing of Thin Sheets with Special Tools (in German), Dr.-Ing. Thesis, Technische Hochschule Stuttgart.

Brazier, W., 1987, "New Methods for Improving the Sheet Metal Stamping Process", *Metal Stamping*, August, pp. 3-13.

Brekelmans, W.A.M., and Hoogenboom, S.M., 1986, "Stationary Sheet Bending and Straightening", Advanced technology of Plasticity, vol. I, pp. 171-176.

Chakrabarty, J., 1970, "A Theory of Stretch Forming Over Hemispherical Punch Heads", *Int. J. of Mech. Sci.*, vol. 12, pp. 315-325.

Cherek, H., and Neumann, C.P, 1991, "Draw Cushions in Hydraulic and Mechanical Presses" (in German), Proceedings of The Conference on "Draw Systems for Single Action Presses for Sheet Forming", ed. K. Siegert, Technical University of Stuttgart, July, 1991, pp. 135-147.

Doege, E., 1987, "Stamping Technology in Manufacturing of Autobody Panels" (in German), HFF Report, Ed. E Doege, Technical University Hannover, Germany, no. 11, p.3.

Doege, E., and Sommer, N., 1987, "Blank-holder Pressure and Blank-Holder Layout in Deep Drawing of Thin Sheet Metal", Advanced Technology of Plasticity, vol. II, pp. 1305-1314.

Duncan, J.L., and Altan, T., 1980, "New Directions in Sheet Metal Forming", *Annals of CIRP*, vol. 29, no. 1, pp. 153-158.

Duncan, J.L., and Sowerby, R., 1981, "Computer Aids in Sheet Metal Engineering", *Annals of CIRP*, vol. 30/2, pp. 541-546.

Duncan, J. L., and Sowerby, R., Chu, E., 1985, "The Development of Sheet Metal Modeling", Proc. of 12th Annual Automotive Materials Symp., Computer Modeling of the Sheet Metal forming Process, TMS-AIME, April 28-30.

Duncan, J. L., and Sowerby, R., 1987, "Review of Practical Modelling Methods for Sheet Metal Forming", Advanced Technology of Plasticity, vol. I, pp. 615-624.

Eary, D. F., Reed, E. A., 1974, Techniques of Pressworking Sheet Metal: An Engineering Approach to Die Design, 2nd Edition, Prentice-Hall Inc., Englewood Cliffs, N. J.

Eshel, G., Barash, M., and Chang, T.C., 1985, "A Rule Based System for Automatic Generation of Deep Drawing Process Outlines", Computer-Aided Intelligent Process Planning, ASME Winter Annual Meeting, Miami-Beach, Florida, November.

FLD User's Conference Notes, 1991, General Meeting No. 3, April 4, 1991

Frey, W. H., and Wenner, M. L., 1987, "Development and Applications of a One-Dimensional Finite Element Code for Sheet Metal Forming Analysis", *GMR Research Report*, GMR-5982.

Furubayasi, T., Ujihara, S., and Sakamoto, T., 1988, "Simulation of Forming Severity on Autobody Panels Using a CAD System - Analysis of Drawbead and Its Control", Proc. of 15th IDDRG, Dearborn, Michigan, May, 1988, pp. 243-250.

Gerdeen, J. C., 1984, "Development of a Computer Program "AXIFORM" for The Analysis of Forming of Axisymmetric Sheet Metal Parts", Proc. NAMRC-XII, Houghton, Michigan, pp. 209-213.

Germain, Y., Chung, K., Wagoner, R. H., and Lee, J. K., 1987, "Sheet Forming Analysis (Report for 07/01/86-06/30/87)", Report No. ERC/NSM-87-09, The Ohio State University, Columbus, Ohio.

Hardt, D., Boyce, M. C., and Fenn, R.P., 1990, "Real-Time Control of Binder Force During Stamping", Proc. of 16th IDDRG, May, 1990, pp. 17-27.

Herderich, M.R., 1990, "Experimental Determination of The Blank holder Forces Needed for Stretch Draw Die Design", SAE paper no. 900281.

Higashi, M., Mori, T., Taniguchi, H., and Yoshimi, J., 1985, "Geometric Modeling for Efficient Evaluation of Press Forming Severity", Computer Modeling of Sheet Metal Forming Processes, 12th Automotive Materials Symposium, Ed. N. M. Wang, and S. C. Tang, Ann Arbor, MI, pp. 21-35

Hill, R., 1948, "A Theory of The Yielding and Plastic Flow of Anisotropic Metals", Proc. Roy. Soc. London Ser. A, vol. 193, pp. 281-297.

Hill, R., 1950, The Mathematical Theory of Plasticity, Oxford University Press.

Hill, R., 1979, "Theoretical Plasticity of Textured Aggregates", Math. Proc. Camb. Phil. Soc., vol.85, pp. 179-191.

Hishida, Y., Ujihara, S., Furubayashi, T., Hirose, Y., and Kojima, M., 1990a, "Part-I: Development of Blank Holding Force Control Forming Method", Proc. of 4th Symp. of Japan Soc. for Technology of Plasticity, Tokyo, May, 1990, pp. 49-52.

Hishida, Y., Ujihara, S., Furubayashi, T., Hirose, Y., and Kojima, M., 1990b, "Part-II: Body Wrinkling Suppression Through Blank Holding Force Control", Proc. of 4th Symp. of Japan Soc. for Technology of Plasticity, Tokyo, May, 1990, pp. 45-48.

Hoffmann, H., 1991, "Comparative studies with Hydraulic and Pneumatic Draw Cushions" (in German), Proc. of The Conference on "Draw Systems for Single Action Presses for Sheet Metal Forming, Ed. K. Siegert, Technical University of Stuttgart, July, 1991, p.1.

Holzner, M., and Mannl, V., 1987, "Mechanics of Drawing With Rubber Pads", Advanced Technology of Plasticity, vol. II, pp. 1151-1157.

Hora, P., and Vu, T. C., Wollrab, P. M., Reissner, J., 1986, "Simulation of the Forming Process for Irregularly Shaped Autobody Panels", Advanced Technology of Plasticity, vol. I, pp. 633-640.

Hosford, W. F., and Caddell, R. M., 1983, Metal Forming: Mechanics and Metallurgy, Prentice-Hall Inc., Englewood Cliffs, N. J.

Ishigaki, H., Okamoto, I., Nakagawa, N., and Arima, K., 1984, "Analysis of Growing and Disappearing Behavior of Surface Deflection in Press Forming Large-Sized Autobody Panels", *JSAE Review*, July, pp. 30-39.

Kaftanoglu, B., and Alexander, J. M., 1970, "On Quasistatic Axisymmetric Stretch Forming", *Int. J. of Mech. Sci.*, vol. 12, pp. 1065-1084.

Kaftanoglu, B., and Tekkaya, A. E., 1981, "Complete Numerical Solution of the Axisymmetric Deep Drawing Problem", *ASME J. of Eng. Materials and Technology*, vol. 103, pp. 326-332.

Karima, M., and Richardson, J., 1987, "A Knowledge-Based System Framework for Computer-Aided Technologies in Metal Forming", *J. of Mechanical Working Technology*, vol. 15, pp. 253-273.

Karima, M., 1989, "On the Micro and Macro Perspectives of Stamping Engineering", *J. Mater. Shaping Technology*, v. 7, pp. 213-227.

Karima, M., and Donatelli, V., 1989, "Understanding Blank holder Effect on Formability of Sheet Metal Stamping", SAE Annual Congress and Expo., pp.1-10.

Kim, D. W., and Kim, N. S., 1984, "A Study on the Pure Stretch Forming", Advanced Technology of Plasticity, vol. I, pp. 753-758.

Kobayashi, S., Kim, J. H., and Oh, S. I., 1978, "Analysis of stretching of Sheet Metals with Hemispherical Punch", *Int. J. of Mach. Tool Des. Res.*, vol. 18, pp. 209-226.

Kobayashi, S., Oh, S. I., Altan, T., 1989, Metal Forming and The Finite Element Method, Oxford University Press, New York.

Kotthaus, H., 1955, "An Investigation of the Transportability of Test Results from Models to Full-Scale Tooling for Deep Drawing of Round Cylindrical Components" (in German), *Doctoral Dissertation*, Technische Hochschule Stuttgart.

Lange, K., 1985, Handbook of Metal Forming, McGraw-Hill, New York

Majlessi, S. A., and Lee, D., 1987, "Analysis of Multi-Stage Sheet Metal Forming Processes", 15<sup>th</sup> NAMRC Proceedings, Bethlehem, PA, pp. 330-334.

Makinouchi, A., Nakamachi, E., and Nakagawa, T., 1991, "Development of CAE System for Auto-body Panel Forming Die Design by Using 2-D and 3-D FEM", *Anal. of the CIRP*, v. 40, pp. 307-310.

Manabe, K., and Nishimura, H., 1987, "An Improvement in Deep Drawability of Steel/Plastic Laminated Sheet by Control of Blank Holding Force", Advanced Technology of Plasticity, vol. II, pp. 1297-1304.

Marcal, P.V., and King, I.P., 1967, "Elastic-Plastic Analysis of Two-Dimensional Stress Systems by The Finite Element Method", *Int. J. Mech. Sci.*, v. 9, pp. 143-155.

Murakami, H., Shirai, K., Yamada, O., and Isoda, K., 1980, "A CAD System for Progressive Dies", Proc. 21st Machine Tool Design and Research Conference, pp. 587-591.

Nakamachi, E., 1988, "A Finite Element Simulation of the Sheet Metal Forming Process", *Int. J. for Num. Meth. in Eng.*, vol. 25, pp. 283-292.

Nagpal, V., Shabel, B.S., Thomas, J.F., and Gegel, H.L., 1978, "Formability Models for 2024-O Aluminum Alloy Sheet Material", Proc. of 9th NAMRC, pp. 172-179.

Okamoto, I., and Takahashi, A., Sugiura, H., Hiramatsu, T., Yamada, N., Mori, T., 1988, "Computer Aided Design and Evaluation Systems for Stamping Dies in Toyota", SAE paper no. 880524, *Advances and Trends in Automotive Sheet Steel Stamping*, SAE, Warrendale, Pennsylvania, February, pp. 79-89.

Pale, J. A., Shivpuri, R., and Altan, T., 1989, "Development of Equipment and Capabilities for Investigation of the Multi-Action Forming of Complex Parts", Report No. ERC/NSM-B-89-28, The Ohio State University, Columbus, Ohio.

Patrishkoff, D., 1991, "Design for Manufacturability", SME Seminar on "Practical Sheet Metal Part Design", Dearborn, Michigan, April, 1991.

Pool, G.A., 1990, "Overview of The Die Fabrication Process for Sheet Metal Parts", SME Seminar on "Practical Sheet Metal Part Design", Troy, Michigan, May, 1990.

Redecop, D., and Nguyen, V., 1986, "Simulation of Sheet Metal Forming Process Using FEM", 5th Canadian CAD/CAM and Robotics Conference, Toronto, Ontario, Canada.

Reissner, J., and Ehrismann, J., 1987, "Computer-Aided Deep-Drawing of Two-Part Cans", *Annals of CIRP*, vol. 36, NO. 1, pp. 199-202.

Sachs, G., 1934, "New Researches on The Drawability of Cylindrical Shells", Proc. Institute of Automobile Engineers, v. 29, pp. 588-595.

Saran, M. J., and Wagoner, R. H., 1990a, "A New Method for Stable FEM Simulation of Draw and Reverse Draw Forming Processes", Report No. ERC/NSM-S-90-12, The Ohio State University, Columbus, Ohio.



Saran, M. J., Keum, Y. K., and Wagoner, R. H., 1990b, "Section Analysis Approach for Numerical Simulation of Irregular Stampings with 2-Side Draw-in", Report No. ERC/NSM-S-90-26, The Ohio State University, Columbus, Ohio.

Saran, M. J., Schedin, E., Samuelsson, A., Malender, A., and Gustafsson, C., 1990c, "Numerical and Experimental Investigations of Deep Drawing of Metal Sheets", *J. of Eng. for Ind.*, vol. 112, pp. 272-277.

Schneider, F., 1987, "Control of Force Stroke Curve in Forming-illustrated in the Draw Station of a Large Transfer Press" (in German), HFF Bericht, Nr. 11, (Ed. E. Doege), Technical University Hannover, pp. 99-113.

Sevenler, K., Raghupathi, P.S., Altan, T., and Miller, R.A., 1986, "Knowledge-Based Approach to Forming Sequence Design for Cold Forging", Knowledge-Based Expert Systems for Manufacturing, ASME Winter Annual Meeting, Anaheim, California, December, pp. 299-310.

Sfiligoj, M., 1983, "Sheet Metal System Built", AMM, November, pp. 10

Siegert, K., 1991, Foreword to "Proceedings of the Conference on: Draw Systems for Single Action Presses for Sheet Metal forming ", Technical University of Stuttgart, July, 1991.

Siegert, K., and Klamser, 1991, "Four-Pont Hydraulic Draw System for Single Acting Mechanical Presses" (in German), Proc. of the Conference on "Draw Systems for Single Action Presses for Sheet Metal Forming", Technical University Stuttgart, July, 1991, p. 41.

Siegert, K., Klamser, M., and Straube, O., 1990, "Detection of Failures in Deep Drawing" (in German), *Zeitschrift fur Fertigungstechnik*, v. 815, Nr. 8, p. 416.

Siekirk, J.F., 1988, "A Systems Approach to Sheet Metal Forming Process Control", Proc. of The IDDRG, pp. 1-7.

Sitaraman, S. K., and Kinzel, G. L., and Altan, T., 1988a, "Finite-Difference Method for Rigid-Plastic Analysis of Sheet Metal Stretching", ASME Winter Annual Meeting, Computer-Aided Design and Manufacture of Dies and Molds, Chicago, Il., Nov. 28-Dec. 2.

Sitaraman, S. K., and Kinzel, G. L., and Altan, T., 1988b, "A Computer Aided Design System for Process Squence in Axisymmetric Sheet Metal Forming", Conference Proc., Near Net Shape Manufacturing, ASM Int., Columbus, OH, Nov. 8-10.

Sitaraman, S. K., 1989a, "A Hybrid Computer-Aided Engineering System to Process Sequence Design in Axisymmetric Sheet Metal Forming", Ph. D. Dissertation, Ohio State University.

Sitaraman, S. K., Kinzel, G. L., and Altan, T., 1989b, "Process Sequence Design for Multi-Stage Forming of Axisymmetric Sheet Metal Parts", Report No. ERC/NSM-S-89-49, The Ohio State University, Columbus, Ohio.

Sommer, N., 1986, "Blank Holder Force and Design of Blank holders in Deep Drawing" (in German), Doctoral Dissertation, Technical University of Hannover.

Swift, H.W., 1939, "Drawing Tests for Sheet Metal", Proc. Institute of Automobile Engineers, v. 34, pp. 361-367.

Takahashi, A., Okamoto, I., Hiramatsu, T., and Yamada, N., 1985, "Evaluation Methods of Press Forming Severity in CAD Applications", Computer Modeling of Sheet Metal Forming Process, 12th Automative Materials Symposium, Ed. N M. Wang and S. C. Tang, Ann Arbor, Michigan, April, pp. 37-50.

Takahashi, A., and Okamoto, I., 1988, "Computer Aided Engineering in Body Stamping", *Annals. of the CIRP*, vol. 37/2, pp. 569-577.

Tisza, M., 1987, "A CAD/CAM System for Deep-Drawing Processes", Advanced Technology of Plasticity, vol. I, pp. 145-152.

TMEH, 1984, Forming, Tool and Manufacturing Engineers Handbook, 4th Edition, Editors C. Wick, J.T. Benedict, and R.F. Veilleux, vol. II.

Vemuri, K.R., Hoang-Vu, K., and Raghupathi, P.S., 1986, "A Computer Aided Design System for Axisymmetric Deep Drawing Process", NAMRC XIV, Proc. North American Manufacturing Research Conference, pp. 365-371.

Wagoner, R. H., 1980, "Measurement and Analysis of Plane Strain Work Hardening", *Metall. Trans.*, vol. IIA, pp.165-175.

Waller, J. A., 1978, Press Tools and Presswork, The Graphic Group, Great Britain.

Wang, C., and Wagoner, R. H., 1990, "Finite Element Analysis and Experimental Investigation of Square Punch Stretching and Draw-in Process", Report No. ERC/NSM-S-90-05, The Ohio State University, Columbus, Ohio.

Wang, N. M., 1982a, "A Rigid-Plastic Rate-Sensitive Finite Element Procedure for SheetMetal Forming Calculations. Part-I: In-Plane Deformation", *GMR Research Report*, GMR-407

Wang, N. M., 1982b, "A Rigid-Plastic Rate-Sensitive Finite Element Procedure for SheetMetal Forming Calculations. Part-II: Out-of-Plane Deformation", *GMR Research Report*, MA-231.

Wenner, M. L., 1979, "Deep Draw of Sheet Metal in Plane Strain, With Application to a Bumper Facebar", *GMR Research Report*, MA-164.

Wenner, M. L., 1981, "On Work Hardening and Springback in Plane Strain Draw Forming", *GMR Research Report*, GMR-3645.

Wifi, A.S., 1982, "Finite Element Correction Matrices in Metal Forming Analysis (with application to hydrostatic bulging of a circular sheet)", *Int. J. Mech. Sci.*, v. 24, pp. 393-406.

Woo, D. M., 1964, "Analysis of the Cup Drawing Process", *J. of Mec. Eng. Sci.*, vol. 6, pp. 116-131.

Woo, D. M., 1965, "The Stretch Forming Test", *The Engineer*, London, vol. 220, pp. 876-880.

Woo, D. M., 1968, "On The Complete Solution of The Deep Drawing Problem", *Int. J. Mech. Sci.*, Vol. 10, pp.83-94.

Yamada, Y., Yoshimura, N., and Sakurai, T., 1968, "Plastic Stress-Strain Matrix and Its Application for The Solution of Elastic-Plastic Problems by Finite Element Method", *Int. J. Mech. Sci.*, v. 10, pp. 343-354.

Yoshida, K., Hayashi, Y., 1979, "Developments in Research into Sheet Metal Forming Processes in Japan-Part 2", *Sheet Metal Industries*, March, 1979, pp. 261-270.

Yossifon, S., Messerly, D., Kropp, E., Shivpuri, R., and Altan, T., 1990, "A Servo Motor Driven Multi-Action Press for Sheet Metal Forming", Report No. ERC/NSM-S-B-90-27, The Ohio State University, Columbus, Ohio.

Yossifon, S., Sweeney, K.E., Ahmetoglu, M.A., and Altan, T., 1992, "On the Acceptable Blank Holder Force Range in Deep Drawing Process", *J. of Mat. Process. Tech.*, v. 33, pp. 175-194.

Zienkiewicz, O.C., Valliappan, S., and King, I.P., 1969, "Elasto-Plastic Solutions of Engineering Problems ('Initial Stress' Finite Element Approach)", *Int. J. Num. Meth. Eng.*, v. 1, pp. 75-100.

## **APPENDIX A**

### **PLASTICITY EQUATIONS BASED ON HILL'S OLD THEORY**

## PLASTICITY EQUATIONS BASED ON HILL'S OLD THEORY

The following section provide a detailed outline for obtaining the plasticity equations for anisotropic materials using Hill's 'old' yield function, [Wang, 1982a; Germain, 1987].

The yield function,  $f$ , is given as [Hill, 1950]

$$f = F(\sigma_2 - \sigma_3)^2 + G(\sigma_1 - \sigma_3)^2 + H(\sigma_1 - \sigma_2)^2 \quad (\text{A.1})$$

where  $\sigma_1$ ,  $\sigma_2$ , and  $\sigma_3$  are the principal stresses and  $F$ ,  $G$ , and  $H$  are constants.

Assuming normal anisotropy in the  $x_3$  direction and planar isotropy in the  $x_1$ - $x_2$  plane,  $\sigma_1$  and  $\sigma_2$  can be interchanged in Equation A.1 and can be written as

$$f = F(\sigma_1 - \sigma_3)^2 + G(\sigma_2 - \sigma_3)^2 + H(\sigma_2 - \sigma_1)^2 \quad (\text{A.2})$$

Comparing Equation A.2 with A.1 and substituting  $\sigma_1 = \bar{\sigma}$ ,  $\sigma_2 = 0$ , and  $\sigma_3 = 0$  for a uniaxial loading, it can be seen that

$$F = G = \alpha \quad (\text{A.3})$$

and

$$f = \alpha(\sigma_1 - \sigma_3)^2 + \alpha(\sigma_2 - \sigma_3)^2 + H(\sigma_2 - \sigma_1)^2 = (\alpha + H)\bar{\sigma}^2 \quad (\text{A.4})$$

where  $\alpha$  is an arbitrary constant and  $\bar{\sigma}$  is the equivalent stress.

The flow rule is written as

$$d\varepsilon_{ij}^p = d\lambda \frac{\partial f}{\partial \sigma_{ij}} \quad (\text{A.5})$$

where  $d\varepsilon_{ij}^p$  is the strain tensor. Under large plastic deformation, the elastic strain component can be neglected and therefore  $d\varepsilon_{ij} = d\varepsilon_{ij}^p$ . Using Equation A.5, the constitutive equations between principal stresses and strains can be derived as

$$\frac{d\varepsilon_1}{\alpha(\sigma_1 - \sigma_3) + H(\sigma_1 - \sigma_2)} = \frac{d\varepsilon_2}{\alpha(\sigma_2 - \sigma_3) + H(\sigma_2 - \sigma_1)} = \frac{d\varepsilon_3}{\alpha(2\sigma_3 - \sigma_1 - \sigma_2)} = 2d\lambda \quad (\text{A.6})$$

Since normal anisotropy factor  $R$  is defined to be  $d\varepsilon_2^p / d\varepsilon_3^p$  under uniaxial normal loading in  $x_1$  direction, from Equation A.6, it can be shown that

$$\frac{d\varepsilon_2}{d\varepsilon_3} = \frac{H}{\alpha} = R \quad (\text{A.7})$$

Equation A.6 can be rewritten using the above relation as

$$\frac{d\varepsilon_1}{(1+R)\sigma_1 - R\sigma_2 - \sigma_3} = \frac{d\varepsilon_2}{(1+R)\sigma_2 - R\sigma_1 - \sigma_3} = \frac{d\varepsilon_3}{(2\sigma_3 - \sigma_1 - \sigma_2)} = 2\alpha d\lambda \quad (\text{A.8})$$

The equation for equivalent plastic work can be written as

$$\bar{\sigma}d\bar{\varepsilon} = \sigma_1 d\varepsilon_1 = \sigma_1 d\varepsilon_1 + \sigma_2 d\varepsilon_2 + \sigma_3 d\varepsilon_3 \quad (\text{A.9})$$

Using volume constancy relation  $d\varepsilon_1 + d\varepsilon_2 + d\varepsilon_3 = 0$  and using Equation A.8 an expression for  $d\lambda$  can be derived as

$$d\lambda = \frac{d\bar{\varepsilon}}{2\alpha(1+R)\bar{\sigma}} \quad (\text{A.10})$$

and  $\bar{\sigma}$  can be shown to be

$$\bar{\sigma} = \left\{ \frac{1}{1+R} [(\sigma_2 - \sigma_3)^2 + (\sigma_1 - \sigma_3)^2 + (\sigma_1 - \sigma_2)^2 + ] \right\}^{0.5} \quad (\text{A.11})$$

The inverse normality equations between principal strain increments and principal stresses can be derived from the above equations as

$$\begin{aligned} d\varepsilon_1 &= \frac{d\bar{\varepsilon}}{(1+R)\bar{\sigma}} [(1+R)\sigma_1 - R\sigma_2 - \sigma_3] \\ d\varepsilon_2 &= \frac{d\bar{\varepsilon}}{(1+R)\bar{\sigma}} [(1+R)\sigma_2 - R\sigma_1 - \sigma_3] \\ d\varepsilon_3 &= \frac{d\bar{\varepsilon}}{(1+R)\bar{\sigma}} [2\sigma_3 - \sigma_1 - \sigma_2] \end{aligned} \quad (\text{A.12})$$

From Equation A.12, it is obvious that

$$\begin{aligned} \sigma_2 - \sigma_1 &= \frac{(1+R)\bar{\sigma}}{(1+2R)d\bar{\varepsilon}} [d\varepsilon_2 - d\varepsilon_1] \\ \sigma_3 - \sigma_2 &= \frac{(1+R)\bar{\sigma}}{(1+2R)d\bar{\varepsilon}} [Rd\varepsilon_3 - d\varepsilon_2] \\ \sigma_3 - \sigma_1 &= \frac{(1+R)\bar{\sigma}}{(1+2R)d\bar{\varepsilon}} [Rd\varepsilon_3 - d\varepsilon_1] \end{aligned} \quad (\text{A.13})$$



Using Equations A.9 and A13 and eliminating all stress terms, a relation between the equivalent strain and principal strains can be established as

$$d\bar{\epsilon}^2 = \left( \frac{1+R}{1+2R} \right) (d\epsilon_1^2 + d\epsilon_2^2 + R d\epsilon_3^2) \quad (\text{A.14})$$

In axisymmetric formulation,  $d\epsilon_1 = d\epsilon_r$ ,  $d\epsilon_2 = d\epsilon_\theta$ ,  $d\epsilon_3 = d\epsilon_t$ , and  $\sigma_1 = \sigma_r$ ,  $\sigma_2 = \sigma_\theta$ ,  $\sigma_3 = \sigma_t$ . Hence

$$\begin{aligned} \sigma_\theta - \sigma_r &= \frac{(1+R)\bar{\sigma}}{(1+2R)d\bar{\epsilon}} [2d\epsilon_\theta + d\epsilon_t] \\ \sigma_t - \sigma_r &= \frac{(1+R)\bar{\sigma}}{(1+2R)d\bar{\epsilon}} [d\epsilon_\theta + (1+R)d\epsilon_t] \\ d\bar{\epsilon}^2 &= \left( \frac{1+R}{1+2R} \right) (2d\epsilon_\theta^2 + (1+R)d\epsilon_t^2 + 2d\epsilon_\theta d\epsilon_t) \end{aligned} \quad (\text{A.15})$$

In plane-strain formulation, assuming zero deformation in  $x_2$  direction,  $d\epsilon_1 = d\epsilon_w$ ,  $d\epsilon_2 = 0$ ,  $d\epsilon_3 = d\epsilon_t$ , and  $\sigma_1 = \sigma_w$ ,  $\sigma_2 = \sigma_1$ ,  $\sigma_3 = \sigma_t$ . Hence

$$\begin{aligned} \sigma_1 - \sigma_w &= \frac{(1+R)\bar{\sigma}}{(1+2R)d\bar{\epsilon}} [d\epsilon_t] \\ \sigma_t - \sigma_w &= \frac{(1+R)\bar{\sigma}}{(1+2R)d\bar{\epsilon}} [(1+R)d\epsilon_t] \\ d\bar{\epsilon}^2 &= \left( \frac{1+R}{1+2R} \right) [(1+R)d\epsilon_t^2] \end{aligned} \quad (\text{A.16})$$

## **APPENDIX B**

### **EQUILIBRIUM EQUATIONS FOR GENERAL PUNCH PROFILES**

## EQUILIBRIUM EQUATIONS FOR GENERAL PUNCH PROFILES

The following sections present a detailed outline for deriving the equilibrium equations for the workpiece undergoing deformation over a curved profile.

### B.1. Axisymmetric Geometries

Referring to Figure 5.1 for an axisymmetric geometry, the force balance equation along the radial direction is

$$\begin{aligned}
 & -\left(\sigma_1 - \frac{\delta\sigma_1}{2}\right)\left(r' - \frac{\delta r'}{2}\right)\delta\theta\left(t - \frac{\delta t}{2}\right)\cos\left(\alpha - \frac{\delta\alpha}{2}\right) + \\
 & \left(\sigma_1 + \frac{\delta\sigma_1}{2}\right)\left(r' + \frac{\delta r'}{2}\right)\delta\theta\left(t + \frac{\delta t}{2}\right)\cos\left(\alpha + \frac{\delta\alpha}{2}\right) + \\
 & \mu r \delta\theta \rho_1 \delta\alpha \sin\alpha - \mu r \delta\theta \rho_1 \delta\alpha \cos\alpha - 2\sigma_2 \rho_1' \delta\alpha t \sin\frac{\delta\theta}{2} = 0
 \end{aligned} \tag{B.1}$$

where  $\mu$  is the friction coefficient

Similarly, in the vertical direction, the force equilibrium equation can be written as

$$\begin{aligned}
 & \left(\sigma_1 - \frac{\delta\sigma_1}{2}\right)\left(r' - \frac{\delta r'}{2}\right)\delta\theta\left(t - \frac{\delta t}{2}\right)\sin\left(\alpha - \frac{\delta\alpha}{2}\right) - \\
 & \left(\sigma_1 + \frac{\delta\sigma_1}{2}\right)\left(r' + \frac{\delta r'}{2}\right)\delta\theta\left(t + \frac{\delta t}{2}\right)\sin\left(\alpha + \frac{\delta\alpha}{2}\right) + \\
 & \mu r \delta\theta \rho_1 \delta\alpha \cos\alpha + \mu r \delta\theta \rho_1 \delta\alpha \sin\alpha = 0
 \end{aligned} \tag{B.2}$$

For a small element,  $d\theta$  and  $d\alpha$  are small, and therefore, in the limiting case, Equations B.1 and B.2 can be rewritten as

$$\frac{1}{r'} \frac{d}{dr'} (\sigma_1 t r') + \left[ \rho_1 p \frac{r}{r'} (\tan \alpha - \mu) - \sigma_1 t \tan \alpha - \sigma_2 \frac{\rho'_1 t}{r' \cos \theta} \right] \frac{d\theta}{dr'} = 0 \quad (\text{B.3})$$

$$\frac{1}{r'} \frac{d}{d\alpha} (\sigma_1 t r') + \left[ \sigma_1 t \cot \alpha - \rho_1 p \frac{r}{r'} (\cot \alpha + \mu) \right] \frac{d\theta}{dr'} = 0 \quad (\text{B.4})$$

From the above two equations, an expression for pressure,  $p$ , can be obtained

$$p = \frac{t}{\rho_1 r} [\sigma_1 r + \sigma_2 \rho_1 \sin \alpha] \quad (\text{B.5})$$

and eliminating  $p$  from Equation B.3 using Equation B.5, a general purpose equilibrium equation in terms of principal stresses and geometric parameters for elements over the punch or die rounding radius can be derived as

$$\frac{1}{r'} (\sigma_1 t) \frac{dr'}{d\alpha} + \frac{d}{d\alpha} (\sigma_1 t) = \frac{\sigma_2 \rho'_1 t}{r'} (\cos \alpha + \mu \sin \alpha) + \sigma_1 \mu t \quad (\text{B.6})$$

In polar coordinates  $\sigma_1 = \sigma_r$  and  $\sigma_2 = \sigma_\theta$ . Therefore, Equation B.6 can be rewritten as

$$\frac{1}{r'} (\sigma_1 t) \frac{dr'}{d\alpha} + \frac{d}{d\alpha} (\sigma_1 t) = \frac{\sigma_\theta \rho'_1 t}{r'} (\cos \alpha + \mu \sin \alpha) + \sigma_r \mu t \quad (\text{B.7})$$

For an axisymmetric geometry

$$\frac{dr'}{d\alpha} = \rho'_1 \cos \alpha \quad (\text{B.8})$$

Therefore, the equilibrium equation for elements over the punch profile of a flat bottomed cylindrical punch, Figure B.1, can be written in finite difference form as

$$(\sigma_r t)_{i+1} = (\sigma_r t)_i + \int_{\phi_i}^{\phi_{i+1}} \frac{\rho'_1}{r'} [\sigma_\theta t (\cos \phi + \mu \sin \phi) - \sigma_r t \cos \phi] d\phi + \int_{\phi_i}^{\phi_{i+1}} \sigma_r \mu t d\phi \quad (\text{B.9})$$

where  $\phi = \pi - \alpha$

$$r' = r_c + \rho'_1 \sin \phi = r_c + \left( \rho_1 + \frac{t}{2} \right) \sin \phi$$

and similarly for a hemispherical punch where  $r_c = 0$ , it can be shown that

$$(\sigma_r t)_{i+1} = (\sigma_r t)_i + \int_{\phi_i}^{\phi_{i+1}} [\sigma_\theta t (\cot \phi + \mu) - \sigma_r t \cot \phi] d\phi + \int_{\phi_i}^{\phi_{i+1}} \sigma_r \mu t d\phi \quad (\text{B.10})$$

## B.2. Plane-Strain Geometries

A simple force balance can be written in tangential and radial directions to determine the equilibrium equations over a curved surface. Figure 5.2 shows the forces acting on an element.

Force balance in tangential direction;

$$-(\sigma_1 - \frac{\delta \sigma_1}{2})(t - \frac{\delta t}{2}) \text{Cos}(\frac{\delta \theta}{2}) + (\sigma_1 + \frac{\delta \sigma_1}{2})(t + \frac{\delta t}{2}) \text{Cos}(\frac{\delta \theta}{2}) - \mu P \rho \delta \theta = 0 \quad (\text{B.11})$$

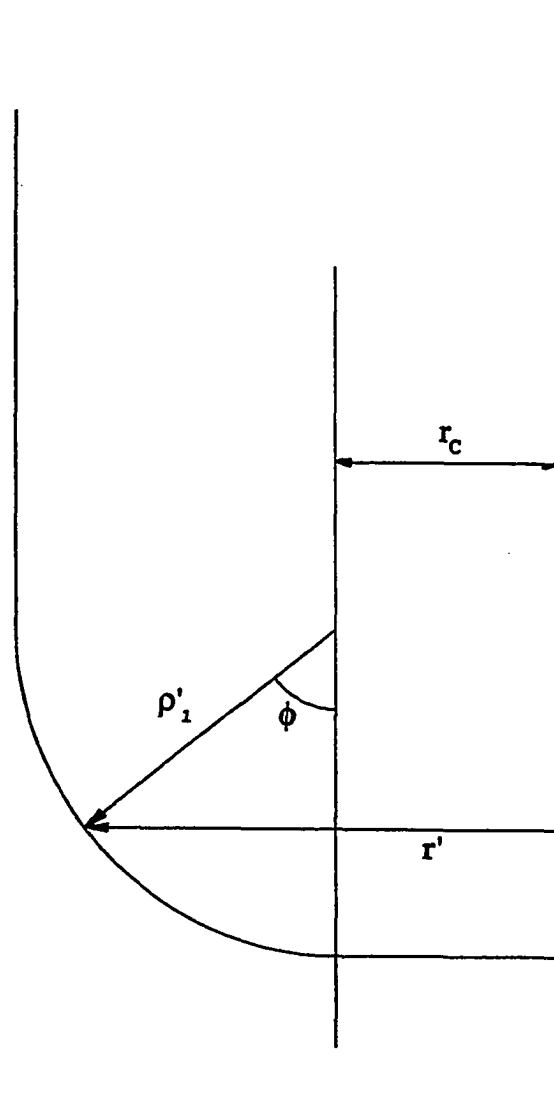


Figure B.1: Flat bottomed punch geometry.

Force balance in radial direction;

$$-(\sigma_1 - \frac{\delta\sigma_1}{2})(t - \frac{\delta t}{2})\sin(\frac{\delta\theta}{2}) - (\sigma_1 + \frac{\delta\sigma_1}{2})(t + \frac{\delta t}{2})\sin(\frac{\delta\theta}{2}) + P\rho\delta\theta = 0 \quad (\text{B.12})$$

For small element  $\delta\theta$  will be small, and therefore, in the limiting case, Equations B.11 and B.12 can be written, respectively, as

$$d(\sigma_1 t) - \mu P\rho\delta\theta = 0 \quad (\text{B.13})$$

$$\sigma_1 t = P\rho \quad (\text{B.14})$$

Combining these two equations will determine the equilibrium equation over the punch and die profile. That is

$$\frac{d(\sigma_1 t)}{d\theta} = \mu(\sigma_1 t) \quad (\text{B.15})$$

This equation can easily be integrated between nodes  $i$  and  $i+1$ ;

$$(\sigma_1 t)_{i+1} = (\sigma_1 t)_i \exp[\mu(\theta_{i+1} - \theta_i)] \quad (\text{B.16})$$

By adjusting the sign of the quantity in brackets, this expression can be used in any region where there is relative motion between sheet and tool.

## **APPENDIX C**

### **DESCRIPTION OF THE ANALYSIS MODULE**



## DESCRIPTION OF THE ANALYSIS MODULE

### C.1. Analysis of Deep Drawing

The deep drawing analysis used in SHEET\_FORM is based on Woo's approach, [Woo, 1964; Woo, 1968]. Any cup drawing process can be divided into two major stages: embossing stage and the drawing stage. In the initial embossing stage, the punch bottom shape is merely impressed on the flat blank, therefore, the punch load required is small. In the drawing stage, the flange is compressed, the material is bent over the die radius and then unbent and straightened to form the wall of the cup.

During the deep drawing process, the workpiece can be divided into six distinct zones, as seen in Figure 5.3,

- Zone 1: Radial drawing of the flange between the die and the blankholder with frictional resistance present at the interface,
- Zone 2: Radial drawing of sheet not in contact with the blankholder,
- Zone 3: Radial drawing and bending over the die corner radius,
- Zone 4: Unbending and straightening to form the wall of the cup,
- Zone 5: Bending, sliding, and stretching over the punch profile,
- Zone 6: Biaxial tensile stretching of sheet over the bottom surface of the punch.

At any stage, the punch force required to draw the sheet can be determined from the knowledge of stresses in the sheet at the beginning of Zone 4,

because this zone serves as a link for transmitting the punch force to the flange compression. For the analysis of axisymmetric and plane-strain geometries the number and the boundaries of each zone are the same. Equilibrium equations for general punch profile in axisymmetric and plane-strain geometries are derived in Appendix B. An overview of equations governing mechanics of metal forming employed in SHEET\_FORM is provided in Appendix D for plane-strain geometries. Similar equations for axisymmetric geometries can be found elsewhere, [Sitaraman, 1989a].

## **C.2. Analysis of Redrawing**

Redrawing is used when the desired shape of the finished cup cannot be obtained in one draw station. This happens typically when the draw ratio of the finished geometry exceed the formable limiting drawing ratio for the material under optimum process conditions or when the cup has two or more step-like parts of different dimensions. Redrawing is the drawing of an already-drawn cup to obtain desired final cup dimensions.

When the direction of redrawing is in the same direction as the original drawing, then it is known as direct redrawing, Figure 5.4, and when the direction of redrawing is in the opposite direction to the previous draw, then it is called reverse redrawing, Figure 5.5.

The analysis of redrawing is similar to drawing except that the starting material is work-hardened if no annealing was done before redrawing, and that more zones need to be considered for analysis.

### C.2.1. Direct redrawing

Woo's analysis of drawing has been extended to redrawing by Reissner and Ehrismann, [Reissner, et al., 1987]. Their analysis was able to predict the thickness variation along the length of the cup and the punch load displacement variation. Although, they have determined the onset of bottom cracking and flange wrinkling, a detailed description of all stress and strain distributions which is essential in identifying the locations close to limiting strain conditions is not available from their work. Referring to Figure 5.4, the workpiece can be divided into eight distinct zones:

- Zone 1: Vertical displacement of the first-drawn cup,
- Zone 2: Radial drawing and bending over the blankholder corner radius,
- Zone 3: Radial drawing of the flange between the die and the blankholder with frictional resistance present at the interface,
- Zone 4: Radial drawing of sheet not in contact with the blankholder,
- Zone 5: Radial drawing and bending over the die corner radius,
- Zone 6: Unbending and straightening to form the wall of the cup,
- Zone 7: Bending, sliding, and stretching over the punch profile,
- Zone 8: Biaxial tensile stretching of sheet over the bottom surface of the punch.

An overview of equations governing the mechanics of metal forming is given in Appendix E.

### **C.2.2. Reverse Redrawing**

The analysis of reverse redrawing is similar to direct redrawing. As before, the workpiece can be divided into eight zones, Figure 5.5, as;

- Zone 1: Vertical displacement of the first-drawn cup,
- Zone 2: Radial drawing and bending over the die outer corner radius,
- Zone 3: Radial drawing of the flange between the die and the blankholder with frictional resistance present at the interface,
- Zone 4: Radial drawing of sheet not in contact with the blankholder,
- Zone 5: Radial drawing and bending over the die corner radius,
- Zone 6: Unbending and straightening to form the wall of the cup,
- Zone 7: Bending, sliding, and stretching over the punch profile,
- Zone 8: Biaxial tensile stretching of sheet over the bottom surface of the punch.

An overview of equations governing mechanics of metal forming is given in Appendix E. The reverse redrawing differs from direct redrawing in one significant aspect. In reverse redrawing, the deep drawn cup wall undergoes two bendings in the same direction, while in direct redrawing the second bending is in the opposite direction to the first.

### **C.3. Analysis of Stretch Forming**

For the analysis of stretch forming over a hemispherical punch as shown in Figure C.1, the sheet can be divided into following four sections;

- Zone 1: Punch contact zone,
- Zone 2: Unsupported zone,
- Zone 3: Stretching and bending over the die corner,
- Zone 4: Stretching of the flange.

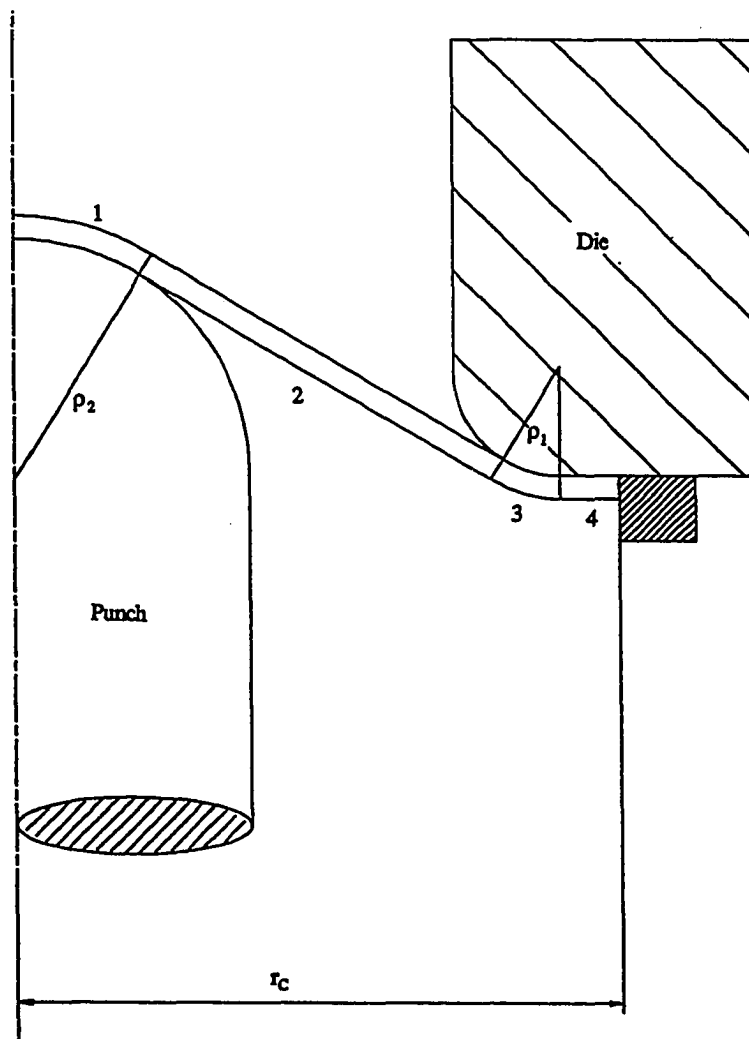


Figure C.1: General geometry and different zones in stretch forming operation.

## **APPENDIX D**

### **EQUILIBRIUM AND VOLUME CONSTANCY EQUATIONS FOR PLANE-STRAIN GEOMETRIES**

**EQUILIBRIUM AND VOLUME CONSTANCY EQUATIONS  
FOR PLANE-STRAIN GEOMETRIES**

In the following formulation,  $\sigma_1$ , and  $\sigma_3$  represents extensional and thickness stresses respectively.

Zone-1: Edge of the flange which is under the pressure of the blankholder.

Volume constancy equation;

$$(W_i - W_{i+1})t_0 = (w_i - w_{i+1})t_b \quad (D.1)$$

where  $W$ : initial distance from the center

$w$ : distance from the center after the deformation

$t_0$ : original sheet thickness

$t_b$ : constant sheet thickness under the blankholder

Equilibrium equation:

$$\frac{d\sigma_1}{dr} = \frac{2\mu\sigma_3}{t_b} \quad (D.2)$$

In finite difference form;

$$(\sigma_1)_{i+1} = (\sigma_1)_i + \frac{\mu_b}{t_b} [(\sigma_3)_i + (\sigma_3)_{i+1}] (w_{i+1} - w_i) \quad (D.3)$$

**Zone-2:** Part of the flange which is not in contact with the blankholder.

Volume constancy equation;

$$(W_i - W_{i+1})t_0 = (w_i - w_{i+1})\left(\frac{t_i + t_{i+1}}{2}\right) \quad (\text{D.4})$$

Equilibrium equation;

$$d(\sigma_1 t) = 0 \quad (\text{D.5})$$

In finite-difference form;

$$(\sigma_1 t)_{i+1} = (\sigma_1 t)_i \quad (\text{D.6})$$

**Zone-3:** Die corner region.

Volume constancy equation;

$$(W_i - W_{i+1})t_0 = \left(\rho_d + \frac{t_i + t_{i+1}}{2}\right)\left(\frac{t_i + t_{i+1}}{2}\right)(\theta_i - \theta_{i+1}) \quad (\text{D.7})$$

where  $\rho_d$ : die corner radius

Equilibrium equation;

$$\frac{d(\sigma_1 t)}{d\theta} = \mu_d \sigma_1 t \quad (\text{D.8})$$

In finite difference form;

$$(\sigma_1 t)_{i+1} = (\sigma_1 t)_i \exp[\mu_d(\theta_{i+1} - \theta_i)] \quad (\text{D.9})$$



Zone-4: Unsupported region.

Volume constancy equation;

$$(W_i - W_{i+1})t_0 = \left( \frac{w_i - w_{i+1}}{\cos\theta_i} \right) \left( \frac{t_i + t_{i+1}}{2} \right) \quad (\text{D.10})$$

Equilibrium equation;

$$(\sigma_1 t)_{i+1} = (\sigma_1 t)_i \quad (\text{D.11})$$

Zone-5: Over the punch profile.

Volume constancy equation;

$$(W_i - W_{i+1})t_0 = \left( \rho_p + \frac{t_i + t_{i+1}}{2} \right) \left( \frac{t_i + t_{i+1}}{2} \right) (\theta_i - \theta_{i+1}) \quad (\text{D.12})$$

where  $\rho_p$ : punch corner radius

Equilibrium equation;

$$(\sigma_1 t)_{i+1} = (\sigma_1 t)_i \exp[\mu_p (\theta_{i+1} - \theta_i)] \quad (\text{D.13})$$

Zone-6: Flat bottom of the punch.

Volume constancy equation;

$$(W_i - W_{i+1})t_0 = (w_i - w_{i+1})\left(\frac{t_i + t_{i+1}}{2}\right) \quad (\text{D.14})$$

Equilibrium equation;

$$(\sigma_1 t)_{i+1} = (\sigma_1 t)_i \quad (\text{D.15})$$

## **APPENDIX E**

### **ANALYSIS OF REDRAWING**

## ANALYSIS OF REDRAWING

Following section describes briefly the analysis procedure which is used for redrawing processes.

### E.1. Direct Redrawing

Zone 1 (Figure C.2): Material in this zone undergoes a vertical displacement with almost no straining. Therefore, all strains and stresses are equal to zero in this zone.

Zone 2 (Figure C.2): The analysis for this zone is similar to the analysis for punch corner region in a simple deep drawing operation except the frictional force which acts in the opposite direction. The volume constancy equation for axisymmetric geometries can be written as

$$(\bar{r}_i^2 - \bar{r}_{i+1}^2)t_0 = 2\rho'_{Dl}{}^2 \left[ \frac{r_{Dl}}{\rho'_{Dl}} (\phi_i - \phi_{i+1}) - (\cos \phi_i - \cos \phi_{i+1}) \right] \frac{t_i + t_{i+1}}{2} \quad (E.1)$$

and the equilibrium equation, based on Appendix B, can be written as

$$(\sigma_r t)_{i+1} = (\sigma_r t)_i + \int_{\phi_i}^{\phi_{i+1}} \frac{\rho'_1}{r'} [\sigma_\theta t (\cos \phi - \mu \sin \phi) - \sigma_r t \cos \phi] d\phi - \int_{\phi_i}^{\phi_{i+1}} \sigma_r \mu t d\phi \quad (E.2)$$

where  $r' = r_{Dl} + \rho'_{Dl} \sin \phi = r_{Dl} + \left( \rho_{Dl} + \frac{t}{2} \right) \sin \phi$

For plane-strain geometries, volume constancy equation can be written as

$$(W_i - W_{i+1})t_0 = \left( \rho_{DI} + \frac{t_i + t_{i+1}}{2} \right) \left( \frac{t_i + t_{i+1}}{2} \right) (\theta_i - \theta_{i+1}) \quad (E.3)$$

Equilibrium equation, based on Appendix B, can be written as

$$(\sigma_1 t)_{i+1} = (\sigma_1 t)_i \exp[\mu_d (\theta_i - \theta_{i+1})] \quad (E.4)$$

**Zone 3 - 8** (Figure C.2): The analysis for zones 3 through 8 is similar to the analysis for zones 1 through 6 in a simple deep drawing operation, Figure C.1.

## E.2. Reverse Redrawing

**Zone 1** (Figure C.3): Material in this zone undergoes a vertical displacement with almost no straining. Therefore, all strains and stresses are equal to zero in this zone.

**Zone 2** (Figure C.3): As before, the analysis procedure is similar to the analysis procedure for punch contact region in a simple deep drawing operation. In this case, however, the frictional force has the same direction as in the deep draw operation. The volume constancy and equilibrium equations are

$$(\bar{r}_i^2 - \bar{r}_{i+1}^2)t_0 = 2\rho'_{DI} \left[ \frac{r_{DI}}{\rho'_{DI}} (\phi_{i+1} - \phi_i) + (\cos \phi_i - \cos \phi_{i+1}) \right] \frac{t_i + t_{i+1}}{2} \quad (E.5)$$

$$\begin{aligned}
 (\sigma_r t)_{i+1} = (\sigma_r t)_i + \int_{\phi_i}^{\phi_{i+1}} \frac{\rho_1'}{r'} [\sigma_\theta t (\cos \phi - \mu \sin \phi) - \sigma_r t \cos \phi] d\phi - \\
 \int_{\phi_i}^{\phi_{i+1}} \sigma_r \mu t d\phi
 \end{aligned} \tag{E.6}$$

For plane-strain geometries, volume constancy equation can be written as

$$(W_i - W_{i+1})t_0 = \left( \rho_{D1} + \frac{t_i + t_{i+1}}{2} \right) \left( \frac{t_i + t_{i+1}}{2} \right) (\theta_i - \theta_{i+1}) \tag{E.7}$$

Based on Appendix B, equilibrium equation can be written as

$$(\sigma_1 t)_{i+1} = (\sigma_1 t)_i \exp[\mu_d (\theta_i - \theta_{i+1})] \tag{E.8}$$

**Zone 3 - 8** (Figure C.3): The analysis for zones 3 through 8 is similar to the analysis for zones 1 through 6 in a simple deep drawing operation, Figure C.1.

**APPENDIX F**

**TOOL DESIGN FOR MULTI-STEP DEEP DRAWING EXPERIMENTS  
IN ERC/NSM PRESS**

**TOOL DESIGN FOR MULTI-STAGE DEEP DRAWING EXPERIMENTS  
IN ERC/NSM PRESS**

**F.1. Die Design for Multi-Stage Deep Drawing Process**

The maximum drawing ratio, i.e., the ratio of blank diameter to the cup diameter, that can be obtained in one drawing operation is limited due to formability considerations. For Aluminum alloy (AA) 1100-O, depending on the thickness of the sheet metal, this ratio is suggested to be between 1.72 and 1.87, [Lange, 1985]. If the desired geometry of the cup requires a bigger drawing ratio, then, forming process should include one or more intermediate stages.

The final cup geometry which will be formed in the experiments was selected as shown in Figure F.1. Using the symbols, shown in Figure F.1, the blank diameter,  $D_b$ , for this geometry is calculated to be 3.32 inches, based on Equation F.1, [Lange, 1985];

$$D_b = \sqrt{D^2 + 4D(H_1 + 0.57R_p) - 0.56R_p^2} \quad (F.1)$$

In this case, the drawing ratio is 2.22 which is not possible to form in one operation and at least one preform has to be made before forming the final cup geometry. The preform is obtained in deep drawing operation. At this stage, flat sheet metal blank of proper diameter is formed into an intermediate geometry. The second step may be a direct or reverse redrawing operation, and in this stage, intermediate geometry is further deformed and the desired cup geometry is obtained. In the current experiments, the second



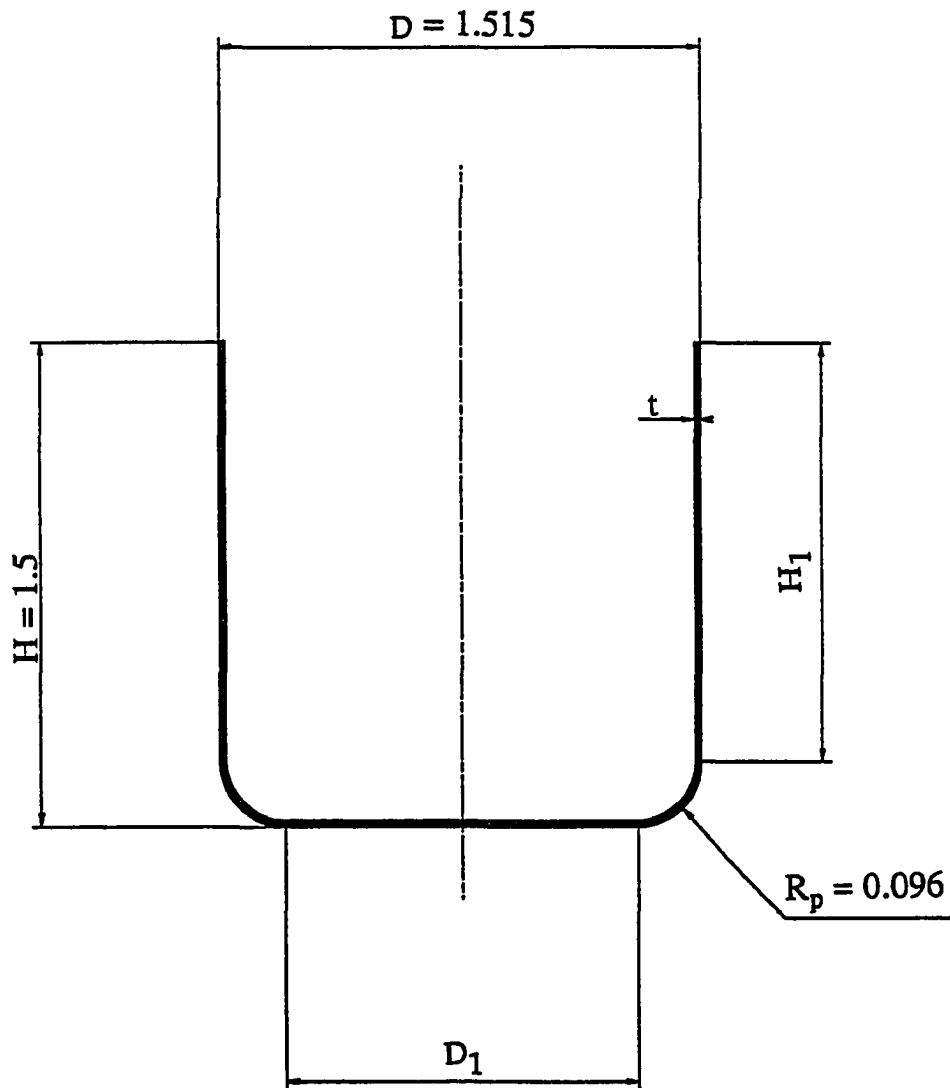


Figure F.1: Final cup geometry, (all the dimensions are given in inches).

stage is performed as a reverse redrawing operation and the process sequence is shown in Figure F.2. Design of the process sequence and the proper tooling for the forming operations at each stage is explained in the following sections.

### **F.1.1. Process Sequence Design**

Starting from the desired final cup shape, a design procedure is followed to determine the intermediate cup geometry and the initial blank diameter. The procedure is explained below. In this section, all the parameters for formability and design considerations are selected from die design handbooks based on the following assumptions:

- material is AA 1100-O
- blank thickness varies between 0.012 and 0.032 inches

#### Reverse Redraw (2nd Stage)

In this section, the selection of the dimensions for reverse redrawing punch and die, the diameter of the intermediate cup geometry, and the calculation of the initial blank diameter are explained. All the design parameters used in this section together with their finally selected values are shown in Figure F.2.

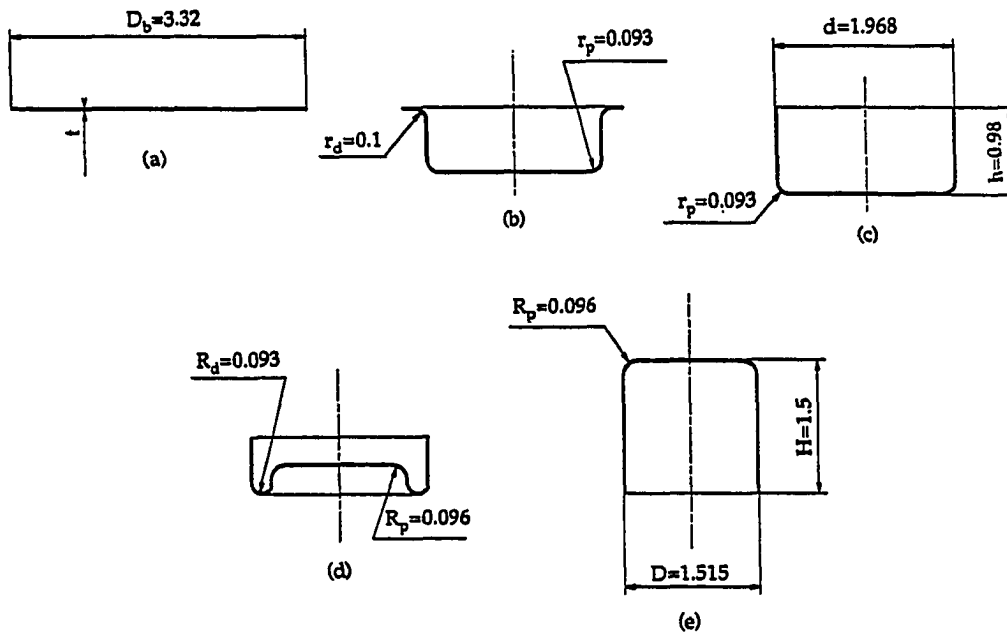


Figure F.2: Process sequence for the experiments (all the dimensions are given in inches).

Thickness,  $t$ , varies between 0.012 and 0.032 inches.

- initial blank
- deformation during the deep drawing (1st stage)
- intermediate cup geometry after the 1st stage
- deformation during the reverse redrawing (2nd stage)
- final cup geometry after the 2nd stage

Select the punch profile radius ,  $R_p$  :

Punch profile radius is recommended to be (4 to 8) times the thickness,  $t$ , for aluminum alloys, [ASM, 1988]. In the current design,  $R_p$  is selected to be 0.096 in. It is possible to increase  $R_p$  for the subsequent experiments. For the material thicknesses we have, the ratio of profile radii,  $R_p=0.096$ " to sheet thicknesses are shown in Table F.1.

**Table F.1:  $R_p/t$  ratios used in the experiments**

$t$	$R_p/t$
0.012	8
0.020	4.8
0.032	3

For the thicker material,  $R_p/t$  ratio is less than recommended. In this case, friction effects will be high at the punch corner profile. Bending effects will be significant, too. This way we will be able to test the simple bending correction that is used to determine the outer surface strains in SHEET\_FORM.

*Die profile radius,  $R_d$  :*

Die profile radius is recommended to be (5 to 10) times the sheet thickness, [Lange, 1985].  $R_d$  is selected to be 0.1 in, but because of the design considerations it was reduced later to 0.093 inches.

*Clearance ,  $C$ , between punch and die:*

It is recommended that  $C$  be at least;  $C = t + 0.10t$

where  $t$  : sheet metal thickness

Material thickening in the edge of the cup during the first draw should be taken into consideration in calculating the clearance at the redrawing stages.

*Draw ratio:*

Maximum reduction in the diameter at a redrawing operation is suggested to be 20%, [ASM, 1988]. Based on this recommendation, we have selected the cup diameter,  $d$ , in the first draw as 1.968 in (50 mm). In this case, the reduction in the cup diameter is 22% and the draw ratio, i.e., the ratio of initial diameter to the final diameter of the cup is 1.29.

Lange has suggested the following draw ratios for aluminum, [Lange, 1985];

for  $t = 0.012$       Draw ratio = 1.26 - 1.29

for  $t = 0.032$       Draw ratio = 1.28 - 1.32

The draw ratio 1.29 is within formability limits according to these recommendations.

*Calculation of Blank Diameter:*

For the round cups shown in Figure F.1, the blank diameter,  $D_b$ , can be calculated from the Equation F.1. Based on this equation, the required blank diameter is found to be 3.32", Figure F.2.

Deep Draw (1st Stage)

In this section, the selection of punch and die geometries that will be used in the first draw operation, shown in Figure F.2, is explained.

*Select the punch profile radius,  $r_p$  :*

Based on the recommendations given in the previous section, punch profile radius,  $r_p$ , for the first draw operation is selected to be 0.093 in. It is possible to increase it. Since the hollow punch of the 1st stage will be used as the die in the second stage  $r_p = R_d$ , where  $R_d$  is the profile radius of the second stage die.

*Select the die profile radius,  $r_d$  :*

Based on the recommendations given in the previous section,  $r_d$  is selected to be 0.1". It is possible to increase  $r_d$ .

*Clearance,  $c$ , between punch and die :*

Based on the recommendations given in the previous section, the clearance is selected as 0.040 in. This value corresponds to the maximum sheet thickness that will be used in the experiments plus 12% of that thickness.

*Draw Ratio :*

The diameter of the cup that will be drawn in the first draw operation was determined in the previous section as 1.968 in (50 mm). The initial blank diameter was also determined as 3.32 in. In this section, we will check if it is possible to form this cup.

The maximum reduction in the diameter at the first draw operation is suggested to be 40%, [ASM, 1985]. With the above determined dimensions, the reduction in the diameter is found to be 42%.

The draw ratio, i.e., the ratio of initial blank diameter to the cup diameter is 1.71. This draw ratio is compared with the recommended values given in Table F.2.

**Table F.2: Recommended draw ratios, [Lange, 1985].**

t	$t/D_b$	max. draw ratio
0.012	0.004	1.72 - 1.82
0.032	0.01	1.82 - 1.87

where t : thickness of the blank  
 $D_b$  : initial blank diameter

Based on these recommendations, it is concluded that it is possible to draw this cup.

*Calculation of cup height, h:*

Since both the initial blank diameter,  $D_b$ , and intermediate cup diameter,  $d$ , are known, the cup height which will be obtained in the 1st stage is found to be 0.98 inches from Equation F.1.

Selected design parameters together with the recommended values in the literature are summarized in Table F.3, using the symbols shown in Figure F.2. Based on the selected design parameters, tool geometries for the first stage, i.e. deep drawing, and the second stage, i.e. reverse redrawing, operations are shown in Figures 6.3 and 6.4 respectively.

### **F.1.2. Tool Design**

Based on the process sequence and the geometries determined above, a set of tools is designed and manufactured to perform the desired operations. Principles and design specifications are explained below.



**Table F.3: Design Parameters used in Multi-Stage Tool Design for Aluminum Alloys**

	Suggested	Reference	Selected (Fig. F.2)
Punch profile radius 1st stage, $r_p$ 2nd stage, $R_p$	$(4 \div 8) t$	[ASM, 1988]	0.093" 0.096"
Die Profile radius 1st stage, $r_d$ 2nd stage, $R_d$	$(5 \div 10) t$	[Lange, 1985]	0.100" 0.093"
Maximum reduction in the cup diameter 1st stage 2nd stage	40% 20%	[ASM, 1988]	42% 22%
Clearance between punch and die, (1st and 2nd stages)	$1.1 t$	[ASM, 1988]	0.040"
Draw ratio in the 1st stage $t = 0.012 \quad t/D_b = 0.004$ $t = 0.032 \quad t/D_b = 0.010$	$1.72 \div 1.82$ $1.82 \div 1.87$	[Lange, 1985]	1.71 1.71
Draw ratio in the 2nd stage $t = 0.012$ $t = 0.032$	$1.26 \div 1.29$ $1.28 \div 1.32$	[Lange, 1985]	1.29 1.29

### Principles of Deep Drawing Tooling

The first stage (deep drawing) operation can be performed in a single-action press with die cushion or in a double-action press. The second draw operation, i.e. either direct or reverse redrawing can be performed in a

double-action press with die cushion or triple-action press. If these actions do not exist in the press they have to be built in the tooling.

The deep drawing operation performed in a double action press is illustrated in Figure 3.2a. In this operation, the die is stationary, the blankholder ring is attached to the outer slide, and the punch is attached to the inner slide. Inner and outer slides can be actuated by means of hydraulic or air cylinders. In hydraulic presses, it is possible to preset the blank holder pressure and its variation as a function of punch travel. An illustration of deep drawing performed in a single action press with die cushion is illustrated in Figure F.3. In this case, punch is stationary which is placed on the lower plate and blankholding ring is placed on the cushion rings. The blankholding pressure is controlled by controlling the cushion pressure. Since the ram pushes against the die cushion ram, the load will increase considerably.

Principles of deep drawing and subsequent reverse redrawing operation is shown in Figure F.4. The sheet metal blank which is clamped between the first stage, i.e. deep draw, die and blankholder is drawn into the die cavity using a hollow first stage punch, Figure F.4. The first stage punch becomes the die in the second stage, i.e. reverse redraw, operation. The preformed sheet metal cup is clamped between the die and the blankholder for the reverse redraw operation close to the corner area. The greater the draw ratio, i.e. the ratio of first draw punch diameter to the reverse redraw punch diameter, the thicker the die wall and the greater the contact surface between the sheet metal and the blankholder. The blankholder and die curvatures should be the same at the contact area to increase the contact surface. In the

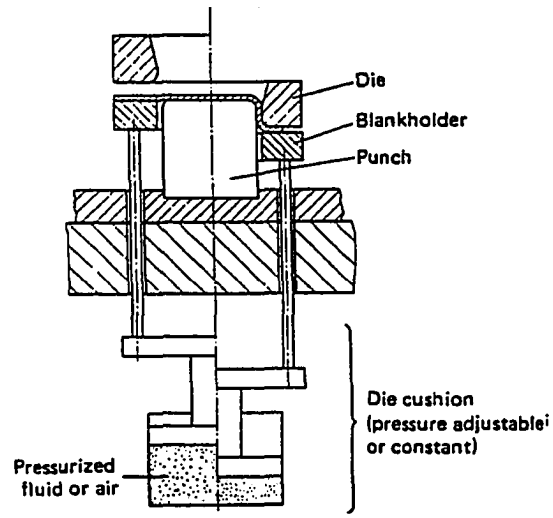


Figure F.3: Tool arrangement for deep drawing, [Lange, 1985].

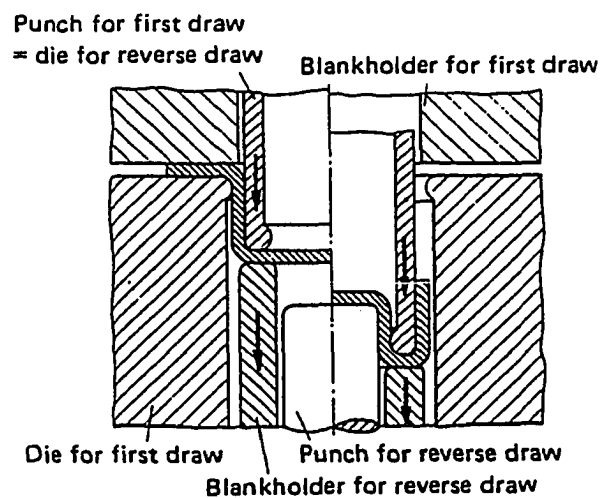


Figure F.4: Principles of draw and reverse redraw operations, [Lange, 1985].

reverse redraw operation, either the die and the blankholder both move down to form the metal around the stationary punch, Figure F.4, or the die and the blankholder both stay stationary and the punch moves up to draw the sheet metal into the die cavity.

### Load Requirements

For the process sequence shown in Figure F.2, blankholder and punch forces are estimated as follows:

Punch force required in the first draw operation can be calculated from the following equation, [Lange, 1985];

$$F_d = \pi d_m t \left[ 1.1 \frac{\sigma}{\eta_F} \left( \ln \frac{D_b}{d} - 0.25 \right) \right] \quad (F.2)$$

where

- $F_d$  : maximum draw force
- $d_m$  : mean cup wall diameter
- $t$  : initial sheet thickness
- $\sigma$  : flow stress,  $\sigma \cong 1.3 * S_u$  where  $S_u$  is the ultimate tensile strength
- $\eta_F$  : efficiency of the operation, (0.5 ÷ 0.7)
- $D_b$  : initial blank diameter
- $d$  : punch diameter

Maximum punch forces required to form the sheet metal, Al 1100-O, in the first draw operation with different thicknesses,  $t$ , are calculated from Equation F.2 and they are shown in the following table;

**Table F.4: Maximum punch forces required in the first stage (deep drawing)**

t(in)	F <sub>d</sub> (lb)
0.012	665
0.032	1793

The blankholder pressure,  $p_{NA}$ , which is required in the first draw operation can be estimated based on Equation 4.1.

Then, the blankholder force,  $F_b$ , can be calculated from;

$$F_b = p_{NA} \frac{\pi}{4} (D_b^2 - D^2) \quad (F.3)$$

where  $D_b$ : blank diameter  
 $D$  : punch diameter

For the first drawing operation in our experiments, blankholding pressure is estimated to be 43 psi for thickness 0.012 in, and 26.4 psi for thickness 0.032 in.

Punch force required in the reverse redrawing operation can be calculated from the Equation F.4, using the symbols shown in Figure F.5, [Lange, 1985];

$$F_d = \pi d_m t \left[ e^{\mu\pi/2} \left( 1.1\sigma_m \ln \frac{d_2}{d_m} + \frac{2\mu F_n}{\pi d_2 t} \right) + \sigma_m \frac{t}{2R_{d1}} \left( \frac{d - R_{d1}}{d_m} \right) + \sigma_m \frac{t}{2R_{d2}} \right] \quad (F.4)$$

- where
- $F_d$  : maximum punch force
  - $d_m$  : mean cup wall diameter,  $d_m = D + t$
  - $D$  : punch diameter
  - $t$  : sheet thickness
  - $\sigma_m$  : mean flow stress
  - $d_2$  :  $d + s_0$
  - $d$  : die outer diameter
  - $F_n$  : blankholder force
  - $\mu$  : friction coefficient at the sheet-die interface
  - $R_{d1}$  : die outer profile radius
  - $R_{d2}$  : die inner profile radius

Based on this equation, the required punch forces in the reverse redrawing operation with different sheet thicknesses are found to be;

**Table F.5: Maximum punch forces required in the second stage (reverse redrawing)**

t(in)	$F_d$ (lb)
0.012	440
0.032	1615

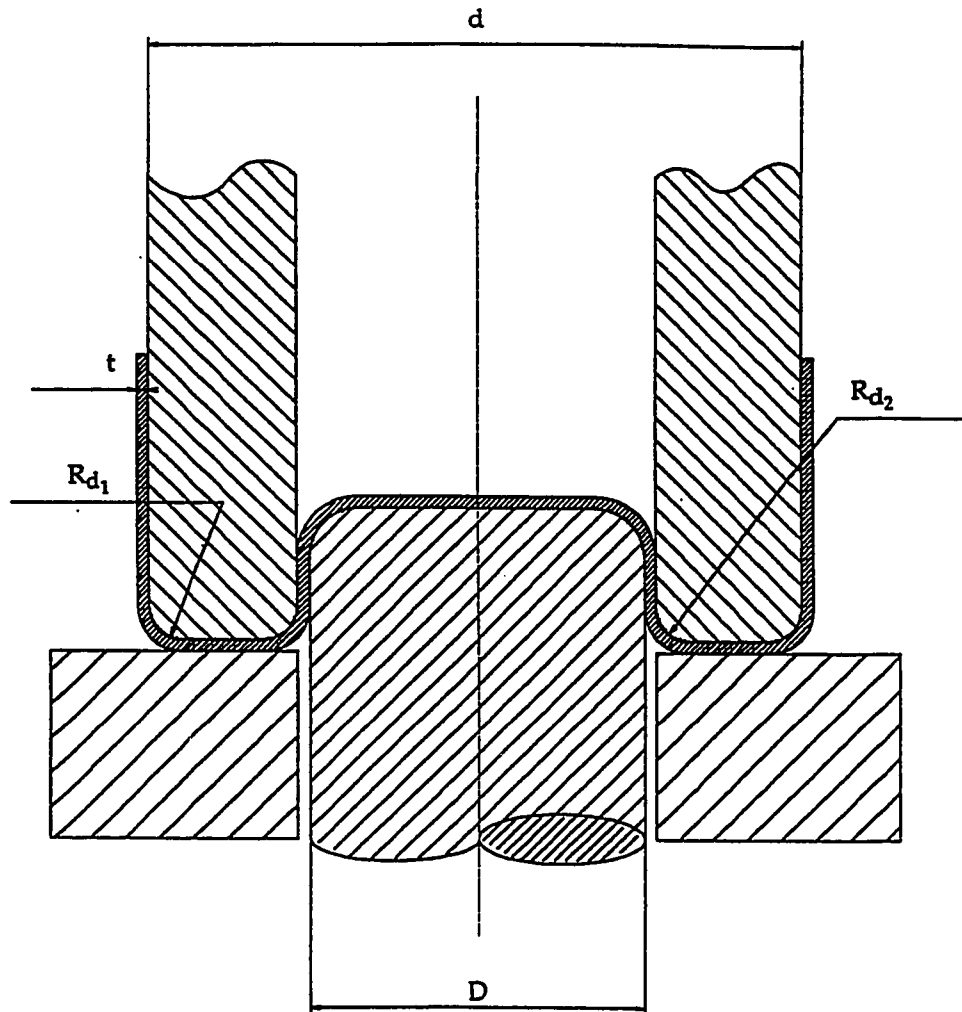


Figure F.5: Geometry of a reverse redrawing tooling.

All the forces calculated for different stages of the forming process are within the capabilities of the ERC/NSM press whose capabilities are explained in Section 6.2.

### Final Design

Experiments are done in the multi action press which was designed and built at the ERC/NSM, [Pale, et al., 1989]. A sketch of the press is shown in Figure F.2. Also, specifications of the press are given in Table F.2. Based on these overall dimensions and the desired process sequence, necessary tooling is designed and built to carry out draw and reverse redrawing operations. Assembly drawing of the tooling is shown in Figure F.6.

In Figure F.6, the clamp plate, (12), and the base plate, (20), are parts of the press. They are used as upper and lower plates of a die set and other parts of the tooling are attached to them. Spacers, (1) and (3), are used as guides for upper punch, (11), and connecting plates for the first stage blankholder plate, (4), respectively. The first stage punch, (11), is designed to be hollow in order to use it as the die in the second stage. An air piston, (13), is used to eject the workpiece out of the hollow punch after the reverse redrawing operation.

For the first stage draw operation, shown in Figure F.2b, the workpiece, (10), is located on the die, (5), Figure F.7. A circular step, 0.010 in deep, is machined on the die to center the workpiece. The first stage die, (5), is sitting on the



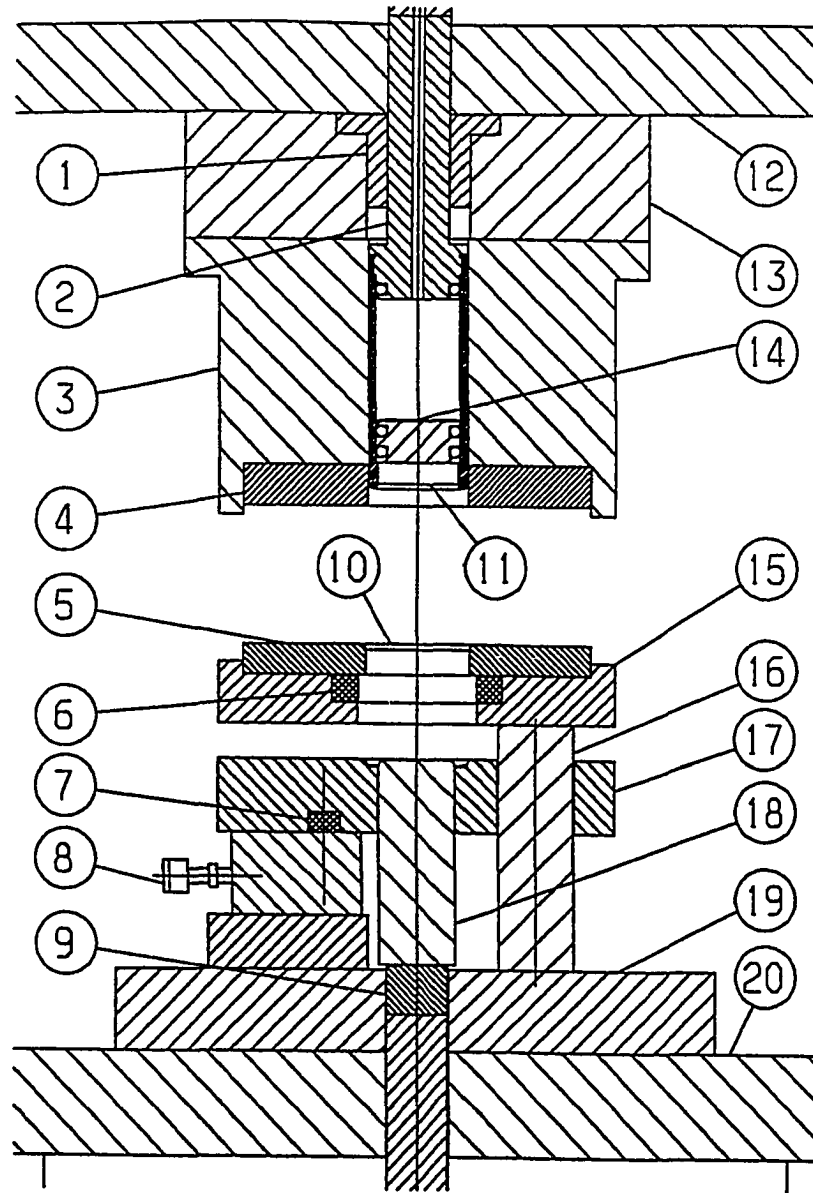


Figure F.6: Assembly drawing of the tooling used in the experiments.

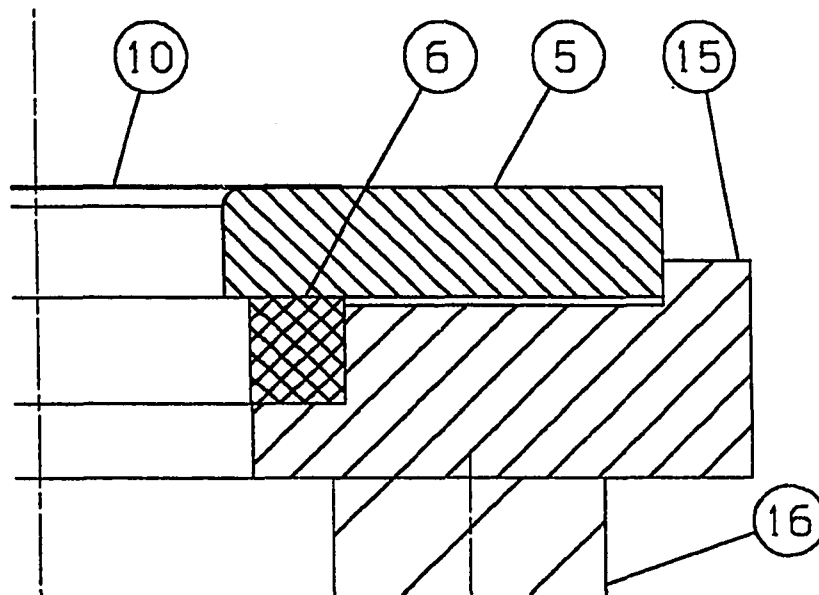


Figure F.7: First stage die assembly, and the positioning of the hollow loadcell for the blankholder force measurements.

hollow blankholder load cell<sup>1</sup>, (6), Figure F.7. The holder, (15) locates both die, (5) and the hollow load cell, (6), and it is connected to the base plate, (20) by means of a spacer, (16). The purpose of the spacer, (16) is to create enough space for the second stage blankholder, (17), and the hydraulic cylinders, (8).

In the second stage, the preformed sheet metal cup, Figure F.2c, is further deformed in a reverse redrawing operation, Figure F.2d, into a smaller diameter cup, Figure F.2e. During this operation, there was no means of obtaining blankholder action on the press. Therefore, a blankholder action is built in the tooling by means of three hydraulic cylinders, (8). Blankholder is not directly in touch with the hydraulic cylinders. Connection is supplied by means of three load cells, (7), located between them, Figure F.8. The reverse redrawing punch, (18), is connected to the lower servomotor via an inline loadcell, (9), to measure the punch load during the reverse redrawing operation. Same kind of arrangement exist between the hollow punch, (11), and the upper servomotor to measure the punch load during the first draw operation.

All the parts that are not in contact with the workpiece during the forming process are made of AA 6061-T6 or AISI 1020. Upper blankholder, (4), upper die, (5), upper and lower punches, (11) and (18) respectively, are made of Ph 15-5 (stainless steel), and they are heat treated after they machined to increase their hardness to 40 R<sub>c</sub>.

---

<sup>1</sup> All the loadcells, (6),(7), and (9), shown in Figure 6.12, were custom manufactured and donated to ERC/NSM by Helm Instrument Co., Inc.

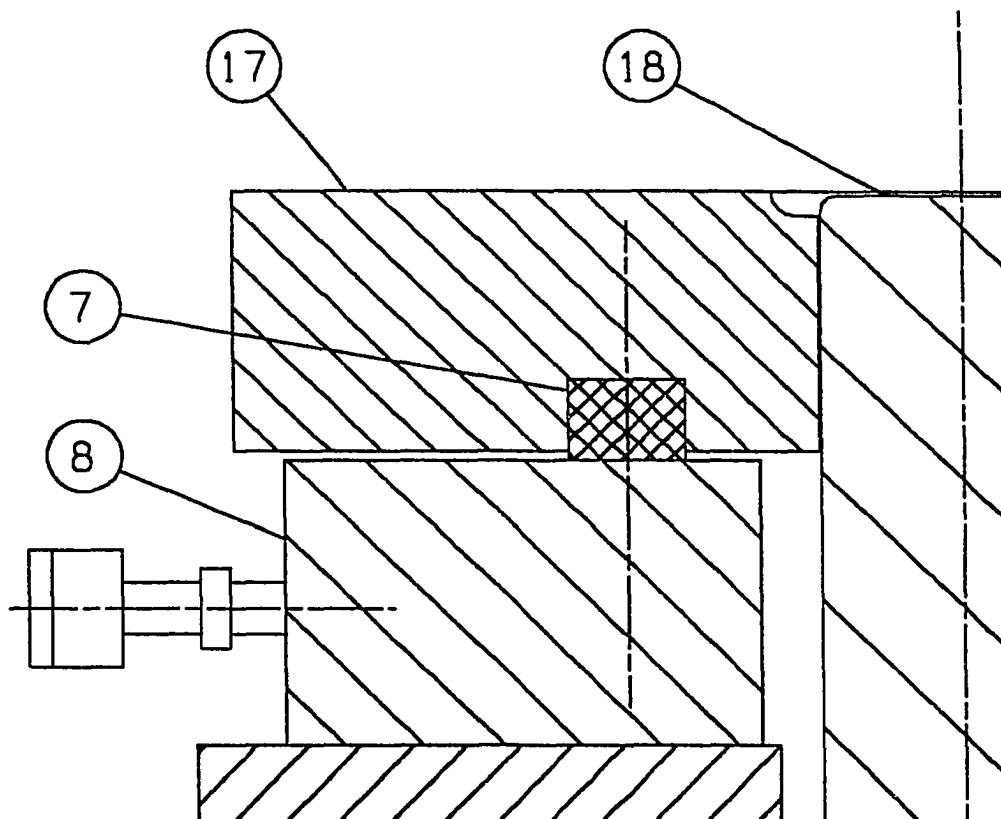


Figure F.8: Second stage blankholder assembly, and the positioning of the "button" loadcell for blankholder force measurements.

### F.2.3. Operation Sequence

In this section, the operation sequence to carry out the forming process is explained. All the part numbers referred to in this section are shown in Figure F.6.

Figure F.9 shows the upper and lower die assemblies in their open position. This is the upper most position of the clamp plate, (12), and the hollow punch, (11). The lower punch, (18), is also at its lowest position and the hydraulic cylinders, (8), are not extended out of their cases. At this position, workpiece, (10), is located on top of the die, (5).

Both the upper blankholder, (4), actuated by air cylinders and the hollow punch, (11), connected to the upper servomotor comes down to clamp the workpiece between the die, (5), and the blankholder, (5), Figure F.10. At this position, the hollow punch, (11), may contact the workpiece, (10), but it does not start forming it. Readings obtained from the hollow loadcell, (6), should be equal to the blankholding force at this time.

The hollow punch, (11), actuated by the upper servomotor, moves down to force the workpiece, (10), into the die cavity. Figure F.11 shows the hollow punch at the bottom dead center position. At this point, the first stage drawing operation is completed and the cup is fully formed, and left the first stage die, Figure F.2c. During this process, the punch force increases first and then decreases to zero when the sheet metal leaves the die. Since the punch

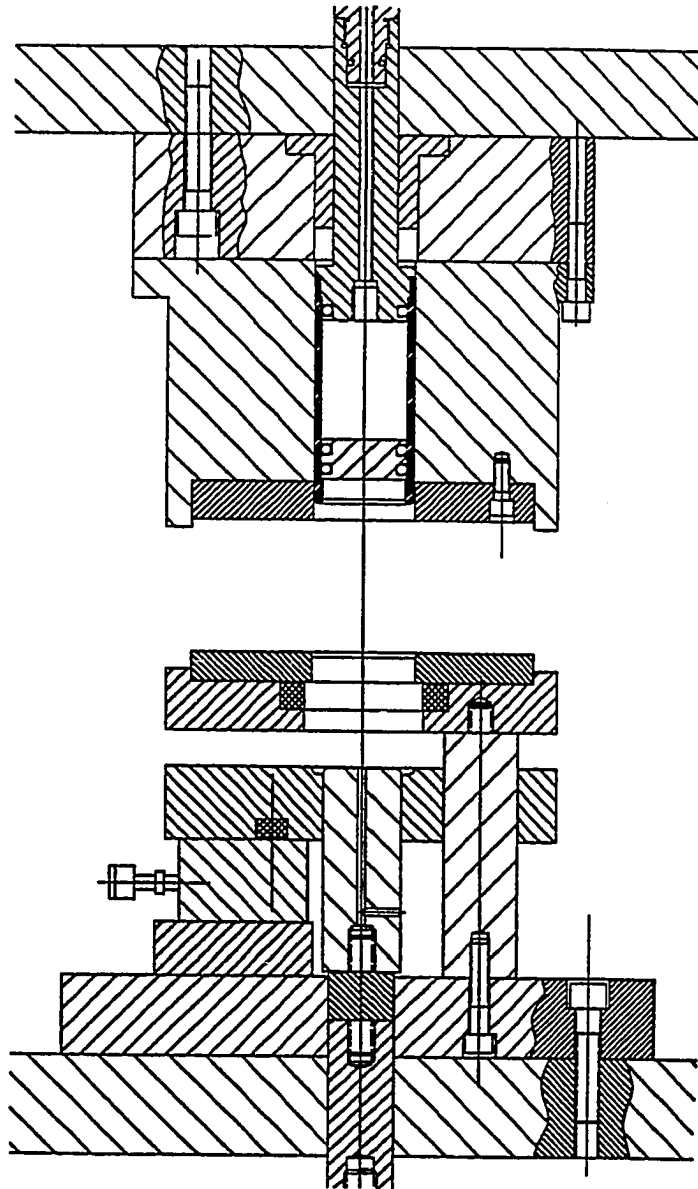


Figure F.9: Open position of the dies.

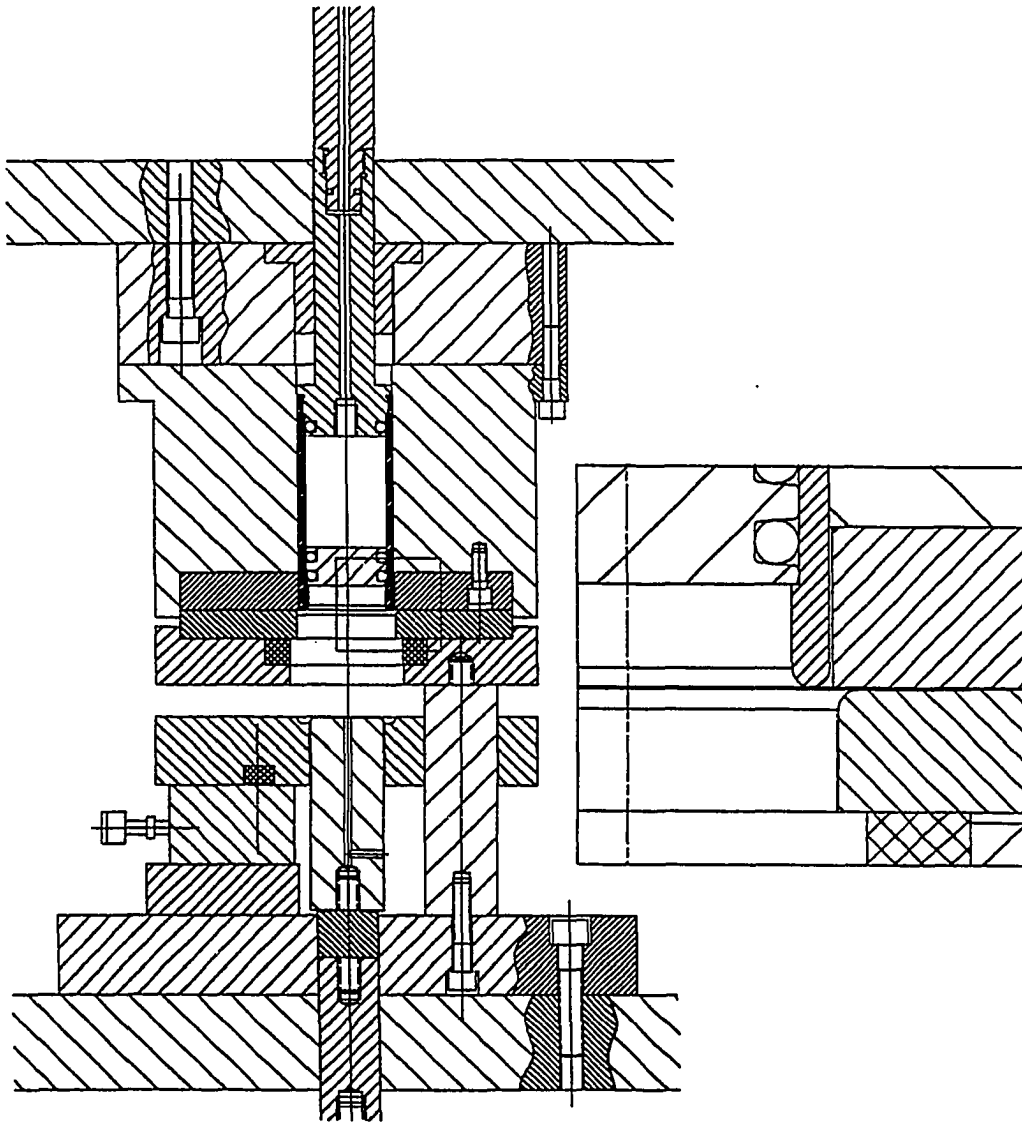


Figure F.10: Clamp position of the dies.

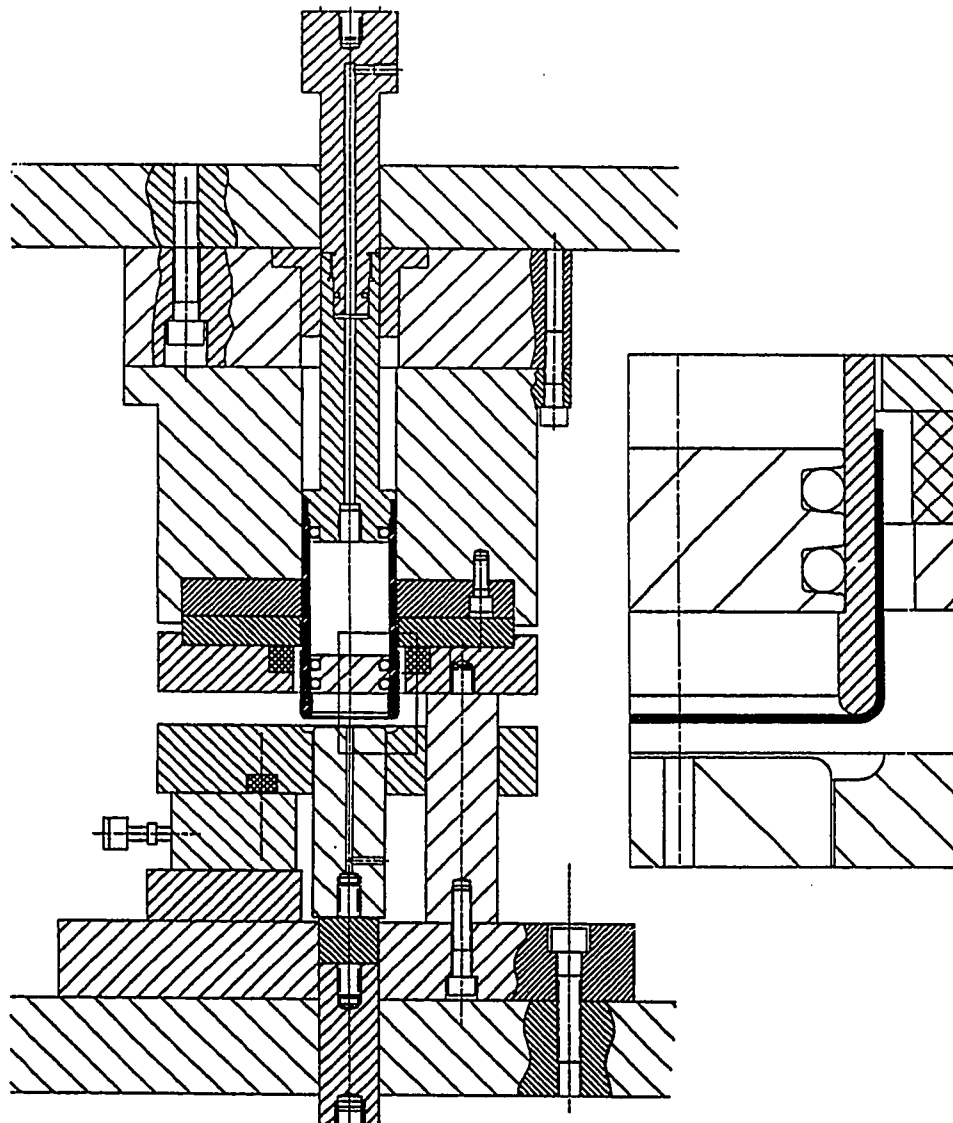


Figure F.11: Position of the tooling after the first stage, deep draw, operation.



force is transmitted to the die via the sheet metal, readings from the hollow load cell include the punch force in addition to the blankholding force.

In the next step, the lower blankholder, (17), is raised by extending the hydraulic cylinders, out of their cases, (8), Figure F.12. The lower punch, (18), is also raised to touch the sheet metal. The sheet metal cup is still wrapped around the hollow punch, (11), which is used as die in the reverse redrawing process. At this point, the blankholding force is measured from the point load cells, (7), located on top of hydraulic cylinders.

In the last stage of the forming operation, the lower punch moves up to form the cup to its final shape, Figure F.13. During this process, the lower punch load is measured from the inline load cell, (9). Once the operation is completed the upper and lower die assemblies return to their open positions, Figure F.9. At this time, the sheet metal cup is still inside the hollow punch, (11). It is ejected out by means of the air piston, (14), located inside the hollow punch, (11).

## **F.2. Features of The ERC/NSM Press**

To perform the multi-stage deep drawing operation explained above, some modifications or additions were required to the press whose details are given in Section 6.2. These additions are the hydraulic unit to provide the blank holder action during the reverse redrawing, the pneumatic ejector to eject the

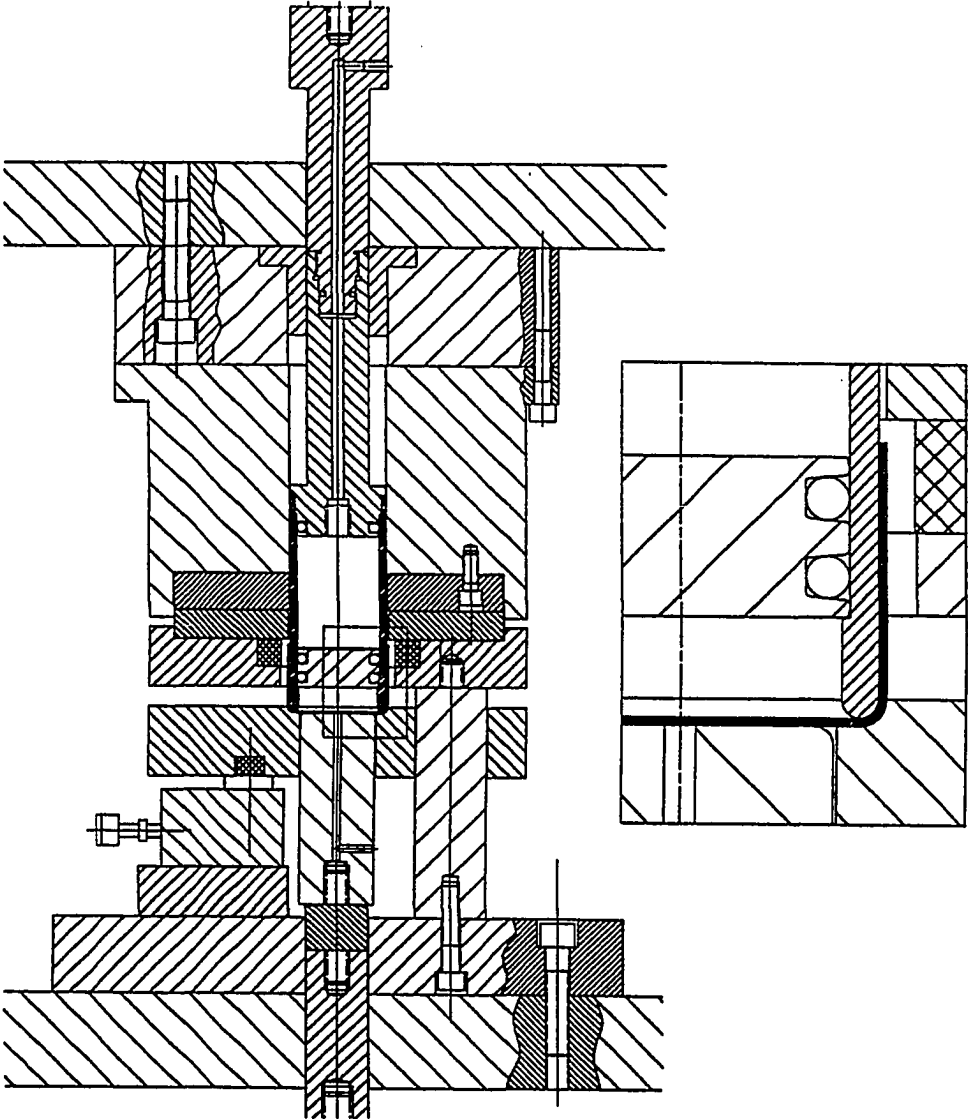


Figure F.12: Clamp position before the reverse redrawing operation.

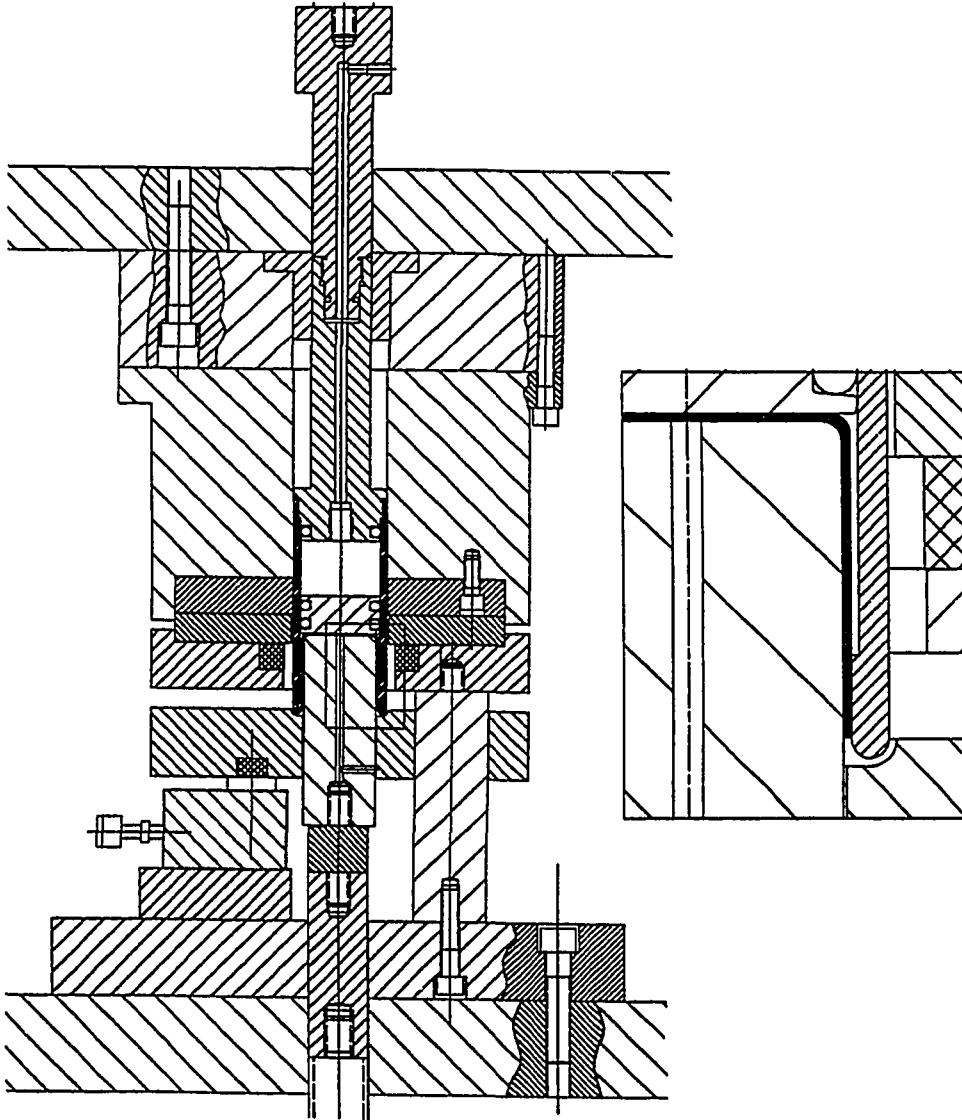


Figure F.13: Position of the tooling after the reverse redrawing operation.

part after the reverse redrawing is completed, and loadcells to measure the punch and blank holder forces. These modifications will be explained in the following sections. In addition, clamping system and servomotors are explained in more detail in the following sections.

### **F.2.1. Servo Motors**

The specifications of the electric servo motors can be seen in Table F.6. The system is made up of servo motor, resolver, driver, and indexer board. The motors are rated at 1.74 horsepower and 2400 RPM, resulting in 127.5 in-lbs torque. They are brushless, 3 phase wye wound, 4 pole pair, AC synchronous type. [Pale, et al., 1989]

Each motor is coupled to a 2.5 ton ball screw jack, each with a nominal 5.5" travel and maximum speed of 1.25 in./sec.. Originally, these jacks were equipped with high lead screws, which permitted speeds up to 5.0 in./sec. at 1800 RPM. They needed only 6 motor revolutions for 1.0 inch of travel. The amount of torque to raise a 1.0 lb load was .0404 in-lbs. The maximum force each screw could take was 3000 lb at 121.2 in-lb. For applications involving higher punch forces, these screws were not sufficient. The new, normal lead screws, have 24 motor revolutions per 1.0 inch of screw travel. The amount of torque to raise a 1.0 lb load is now .0102 in-lb. With the available motor torque of 127 in-lb, the screw jacks can easily produce 2.5 tons force.

**Table F.6: Specifications of electro servomotors**

Continuous Stall Torque	42.5 lb-in 4.80 H-m
Peak Torque	127.50 lb-in 14.40 N-m
Rated Power	1.74 Hp 1,300.00 Watts
Rated Speed	2,600 rpm 43.33 rps
Rated Motor Stall Current	6.0 A
AC Input Power	1.00 A rms
Single Phase 120 VAC	4.71 A rms
Three Phase 240 VAC	19.14 oz-in sq.
Rotor Inertia	350.0 x 10.6 Kg sq. 41,141 rd/sec sq.
Acceleration at Peak Torque	32,768 step/rev
Maximum Resolution	14.70 lbs
Motor Weight	6.67 kg

### F.2.2. Pneumatic Clamping System

The pneumatic circuit consists of two pneumatic cylinders (5.0" diameter and 10" stroke) driven by a four port/two directional solenoid air valve with integrated piston speed exhaust control, a filter-regulator-lubricator unit, an exhaust muffler, and a electro/pneumatic relay-converter valve to control the pressure in the cylinders. The diagram of the pneumatic circuit can be seen in Figure F.14.

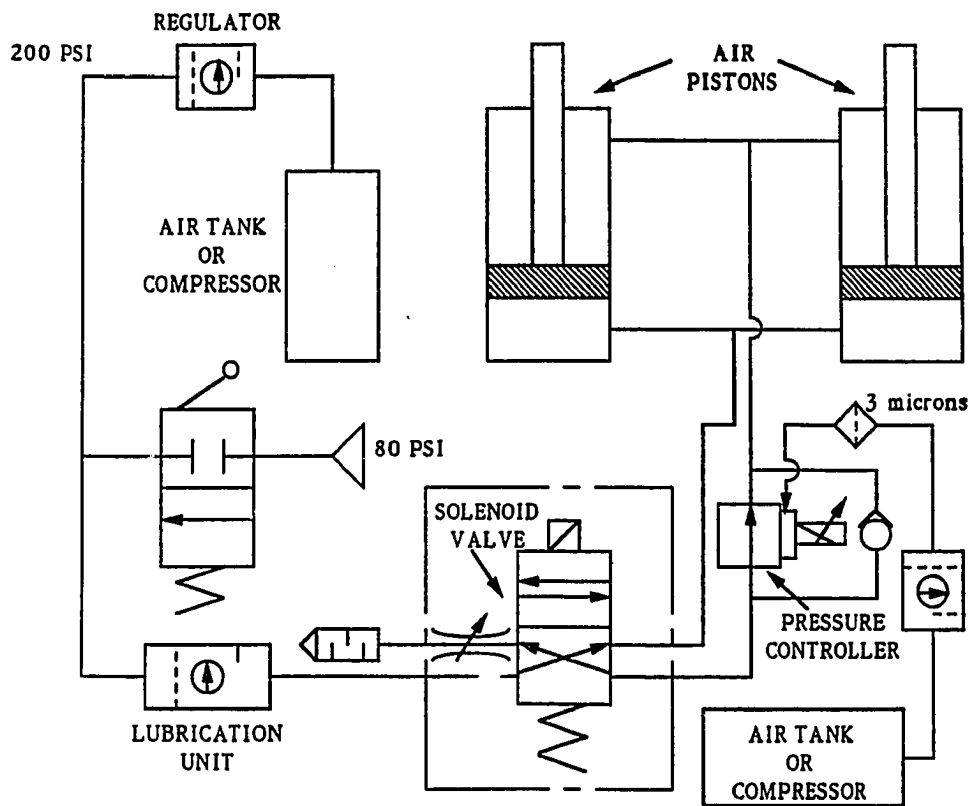


Figure F.14: Pneumatic circuit of ERC/NSM press , [Yossifon, et al., 1990].

The air cylinders are rated at 200 psi. They can produce approximately 4 tons of clamping force (with the weight of the plate included). The other components in the circuit are rated at 150 psi, which limits the maximum clamping force to approximately 3 tons. For pressures lower than 80 psi (170 tons clamping force), the shop air can be used. For greater pressures, another source of compressed air must be used, [Yossifon, et al., 1990].

### **F.2.3. Hydraulic Unit for 2nd Stage BHF**

The blank holding pressure for the reverse redrawing operation is provided by means of an external hydraulic power supply. The unit is a Double A CircuitPak, (model number T3V-10-M-P1A/JFF01/GF20-F3-B1-059) which has a 1 GPM fixed delivery pump powered by a 1-1/2 horsepower motor (1800 RPM). It can produce up to 2000 psi. The system is equipped with a 4-way, 2 position, spring offset, solenoid directional valve. These and the remaining specifications of the system can be seen in Table F.7.

The unit is attached to three, single-acting hydraulic cylinder rams from Dayton Electric Mfg. Co. (model 6Z782). These were designed into the tooling to produce the blankholding force during the reverse redrawing. A drawing of the hydraulic circuit can be seen in Figure F.15. The hydraulic cylinders (detail 8 in Figure F.6) are evenly spaced and act on the bottom surface of the blank holding ring (detail 17 in Figure F.6). The tooling does not require that they have significant travel, just that they are able to produce correct and

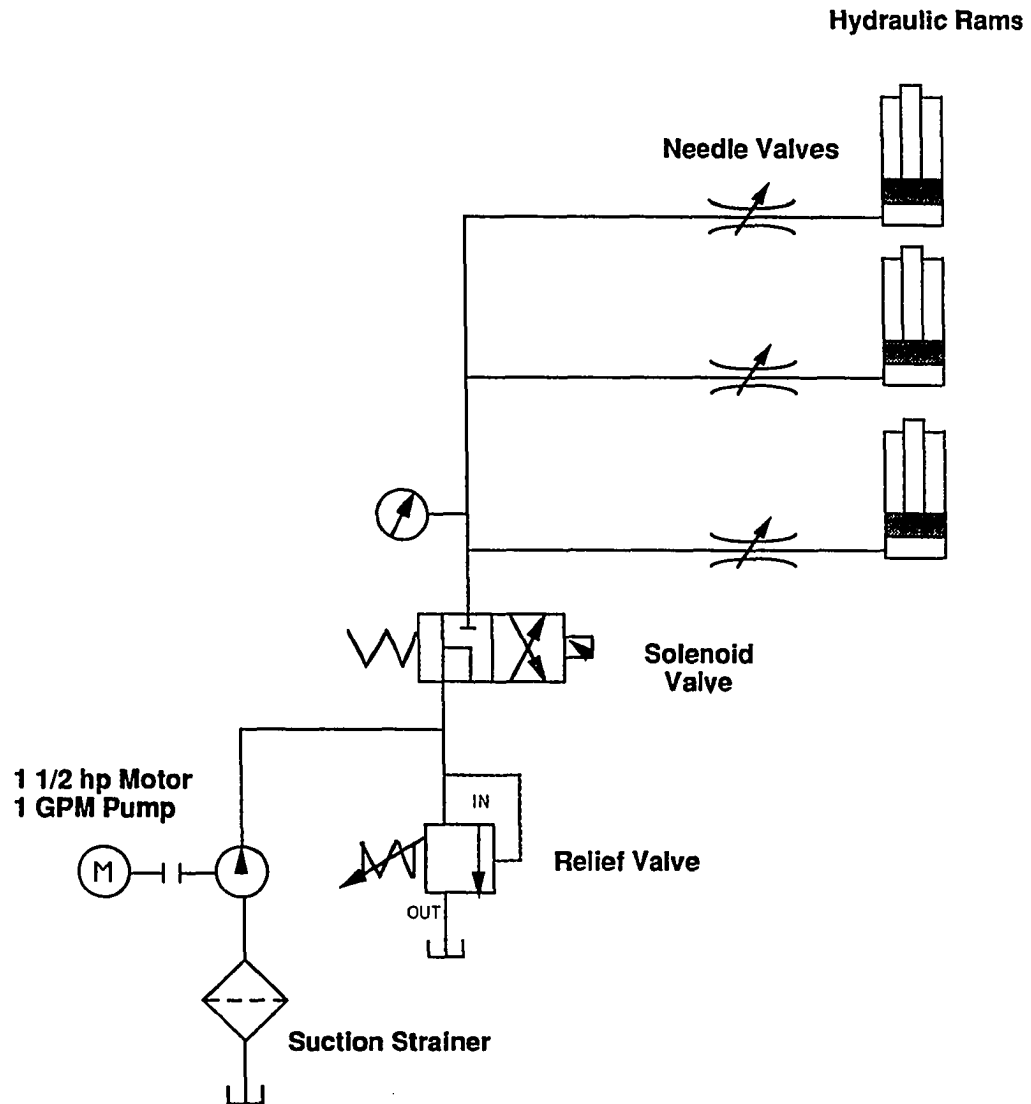


Figure F.15: Hydraulic circuit for the blankholder action in reverse redrawing operation on ERC/NSM press.



evenly distributed forces. The rams can produce up to 5 tons force each, with a stroke of 5/8 of an inch. Their cylinder rod diameter is 1.0 inch.

**Table F.7: CircuitPak Hydraulic Power Unit (Model Number T3V-10-M-P1A/JFF01/GF-F3-B1-059)**

- 1 GPM Fixed Delivery Pump
- 1-1/2 H.P., 230/460/3, 1725 RPM, TE Motor
- Relief Valve
- 2000 PSI Gauge with Snubber
- 10 Micron Return Line Filter
- 4-Way, 2 Position, Spring Offset, Solenoid Directional Valve
- 3 Gallon Reservoir with Sight Gauge, Thermometer, Filler Breather, 100 Mesh Suction Strainer, and Drain

#### **F.2.4. Pneumatic Ejector System**

As seen in the layout of the draw-redraw tooling in Figure F.6, there is a need for an ejector to knock out the finished part after the reverse redrawing. This is performed by means of a pneumatically actuated plunger (detail 14 in Figure F.6) in the upper punch assembly. This plunger will move down from

the applied air pressure when a palm valve is pushed, knocking out the part. The pneumatic circuit used with this plunger can be seen in Figure F.16.

### **F.2.5. Loadcells**

Helm Instruments has provided loadcells to be used on the reverse draw tooling for the ERC 5 ton press. There are 6 loadcells. These loadcells are shown in Figure F.17.

- A) one on each punch (2),
- B) one on each hydraulic ram (3), and
- C) a ring loadcell for the first draw blankholder (1).

Each of the punch loadcells (A) will have 5 ton maximum capacity, with an overload rating of 6.1 tons. They will have threaded ends that are screwed in-line between the ball screw and the punch.

The hydraulic ram loadcells (B) have a 0.5 ton capacity with a 0.61 ton overload rating. They have an outside diameter of .615 inches and rest on the rams' 1.0 inch diameter cylinders.

The ring loadcell (C) for measuring the blankholder forces during the first draw has a normal capacity of 1.0 ton. It has a overload capacity of 12.2 tons. More of this 12.2 tons can be used if the loadcell is calibrated for a larger range.

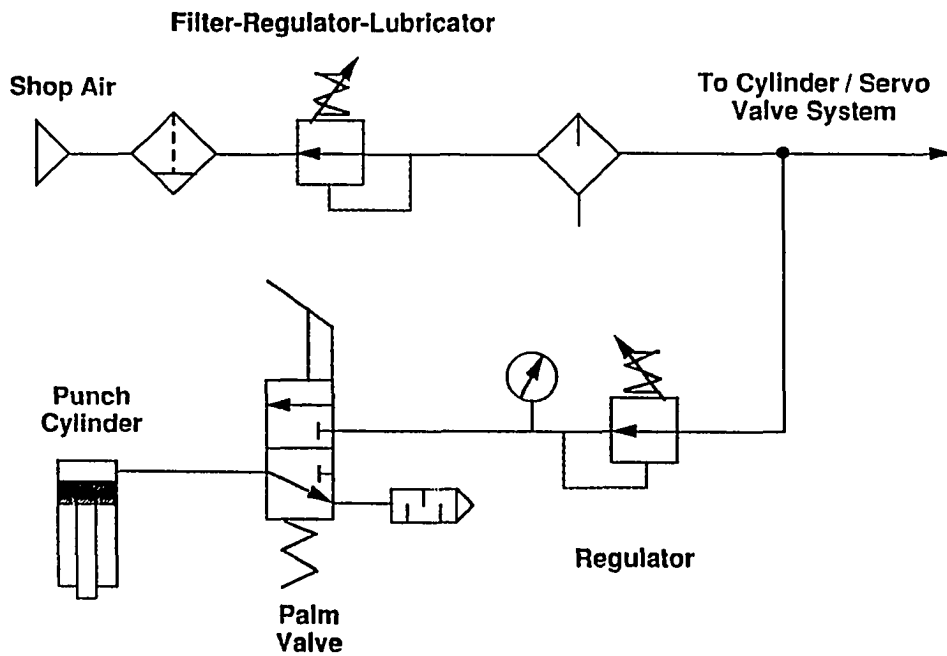


Figure F.16: Pneumatic circuit for the ejector on the draw/reverse redraw tooling.

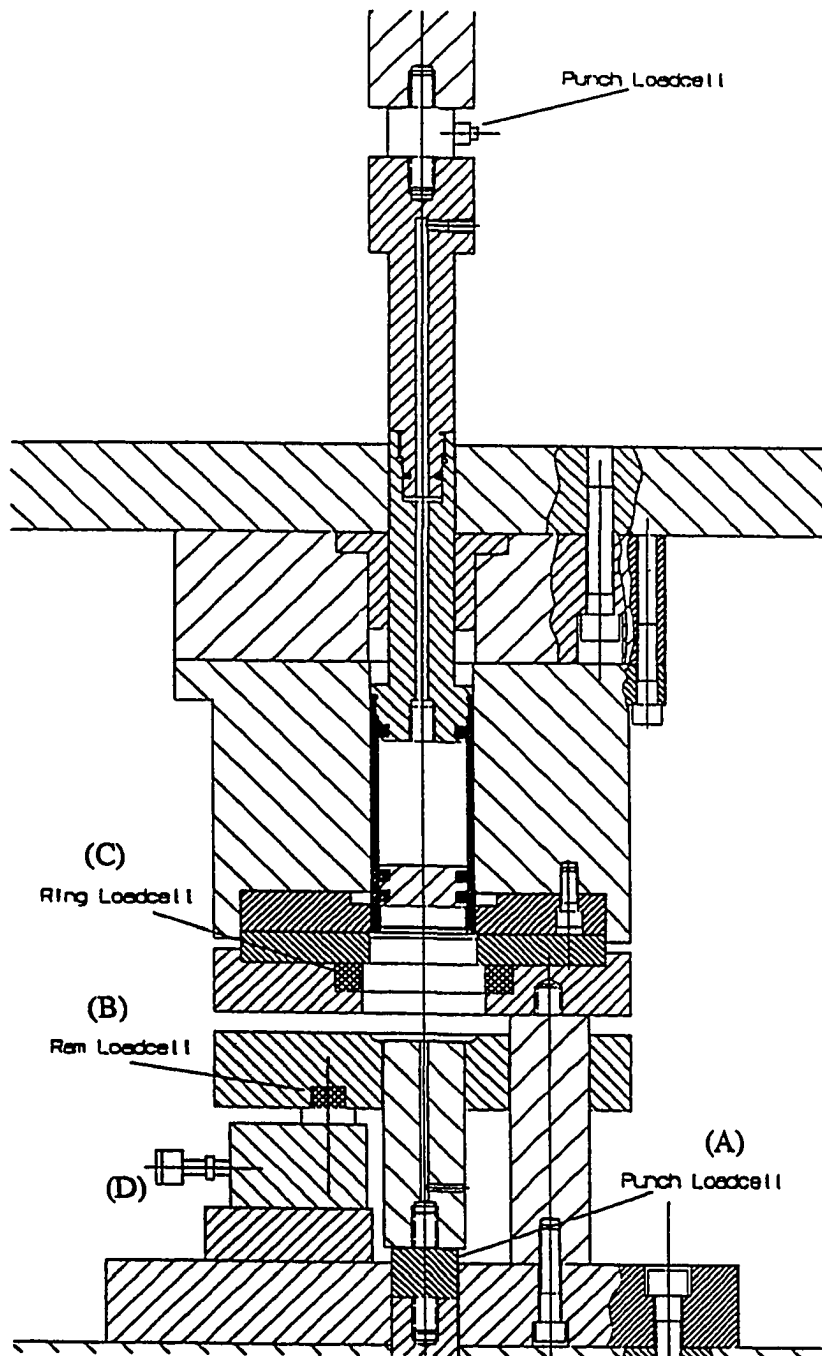


Figure F.17: Draw/reverse redraw tooling with loadcells in place.

The ring is 3.375 inches outer diameter and 2.375 inches inner diameter. The height of the ring is .625 inches.

#### **F.2.6. Position Measurements**

Since the desired output from our experiments is a relationship between the punch force and punch displacement, some way of measuring the punch travel was needed. Knowing the position commands of the motors and their timing, a fairly accurate knowledge of the punch position can be predicted. However, as the forming loads increase, the punch position becomes less and less predictable. There is a limited position reporting ability from the Compumotor PC-23 Indexer. An accurate absolute position report can be easily obtained while the motor is stationary, but not while the motor is moving. This uncertainty leads to the need for some external position transducer.

There are a number of ways to get a position signal during the operation of the motor. These include adding an LVDT to the punches, a rotary encoder to the motor, or a rotary potentiometer to the output shaft of the screw. The latter was done because it was the simplest and most straight forward method, while still providing a high resolution and reasonably accurate position signal. This method is also not affected by a change of tooling. Also, the potentiometers provide us with an analog voltage signal, which we can read in conjunction with the loadcell readings.

### F.3. Data Acquisition System

A data acquisition system is used to collect signals of punch and blankholding forces, punch and slide displacements, and air and hydraulic cylinder pressures during the sheet metal forming experiments on the 5 Ton ERC/NSM press.

The system, which runs on a Macintosh IIfx, was manufactured by Strawberry Tree Inc. The system is made up of a data acquisition card and a software package. The card (ACM2-12-16) has 16 analog input channels, 16 digital I/O channels, and a counter/timer. It has a 12-bit resolution and can collect at speeds up to 10,000 samples per second.

The software, Workbench, is an icon based or object oriented programming package for data acquisition, control, and data display. It can collect data, display it on the screen in a graph form in real time and write it to the disk. It can also perform numerical calculations on the data as it collects it.

Also included in the data acquisition system is a general purpose terminal panel for 8 analog inputs, 8 digital I/O lines and 2 analog outputs. The entire system is enclosed in a portable and securable cabinet. This allows it to be transferred easily between different labs at the ERC. The Macintosh IIfx comes with a 80 MB hard disk drive with 4 MB RAM. It has 8 NuBus expansion slots.

**APPENDIX G**

**TOOL DESIGN FOR DEEP DRAWING EXPERIMENTS  
IN MINSTER PRESS**

## TOOL DESIGN FOR DEEP DRAWING EXPERIMENTS IN MINSTER PRESS

### G.2. Die Design for Deep Drawing Experiments

A set of tooling is designed and built with assistance from Superior Tool and Die Co. of Columbus, Ohio, a member company of ERC/NSM. This die set is used for deep drawing of round cups in 160 Ton Minster press located in ERC/NSM laboratories. Wide variety of materials, e.g. aluminum, low carbon steel, stainless steel, etc., having thicknesses varying from 0.81 mm (0.032") to 1.63 mm (0.064"), are intended to be used in the experiments. Therefore, during the design of tooling, design parameters are selected for the most critical material assuming the remaining materials will be formed without any difficulty using the same tooling. In the following section, die design is explained step by step using the parameters shown in Figure G.1. The procedure outlined in this section can be used as a general guideline to design dies for axisymmetric forming operations.

#### G.2.1. Selection of The Design Parameters, (R.5)

*Select the diameter ,  $d$ , for round cup:*

Because of the limitations due to die cushion pin positions and force requirements for different materials the largest diameter of a cup that can be



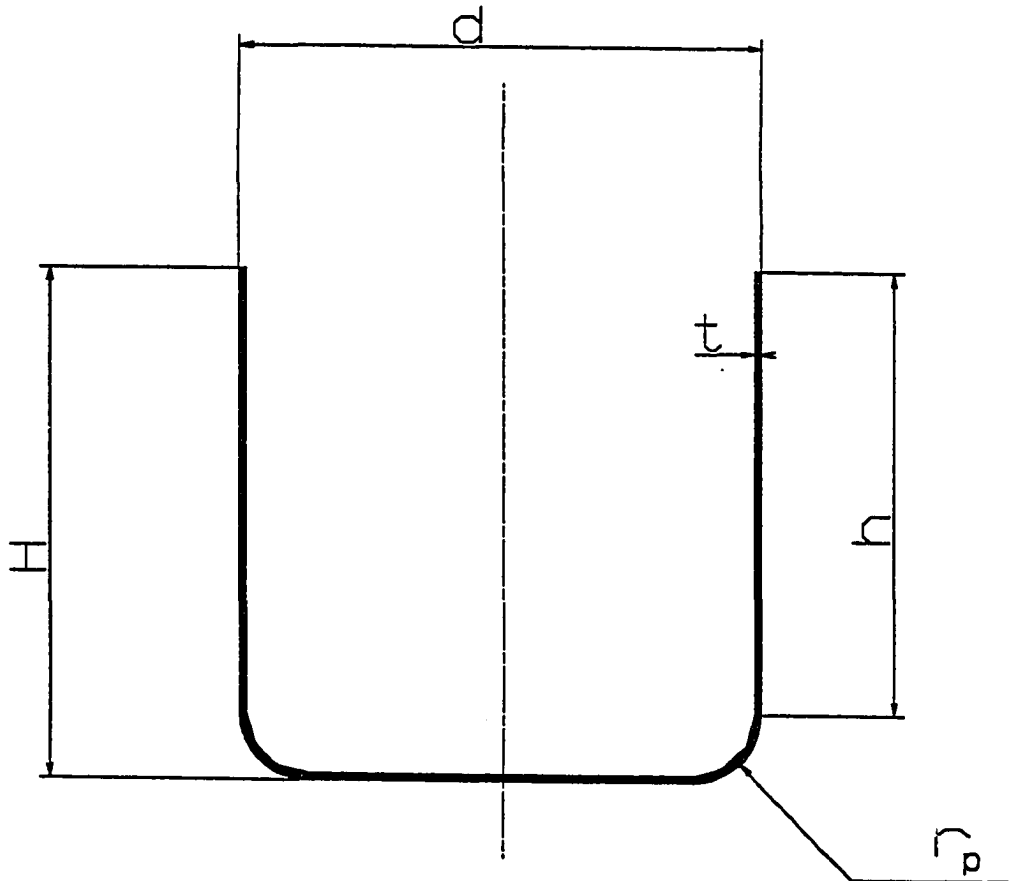


Figure G.1: Axisymmetric cup geometry.

formed in this press is found to be 152.4 mm (6"). Therefore, the diameter of the cup,  $d$ , is selected to be 152.4 mm (6").

Select the profile radius of the punch,  $r_p$ , and die,  $r_d$ :

For stainless steel, die profile radius,  $r_p$ , is critical, and for aluminum, punch corner radius,  $r_d$ , is more critical. Therefore, punch and die profile radii should be selected accordingly.

Recommended values for punch and die profile radii which are obtained from literature are given in Table G.1.

We have selected the punch profile radius as  $r_p=20.1$  mm (0.79"), and the die corner radius as  $r_d=16.0$  mm (0.63").

**Table G.1: Recommendations for punch and die profile radii**

Material	Reference	Die, $r_d$	Punch, $r_p$
Aluminum	[ASTE, 1955]	$(4 \div 6) t$	$(4 \div 10) t$
Aluminum	[Lange, 1985]	$(5 \div 10) t$	$(8 \div 10) t$
Stainless steel	[ASM, 1988]	10t	5t
Aluminum	[ASM, 1988]		$(4 \div 8) t$

For the thickest material which might be used in our experiments,  $t=2.54$  mm (0.1"), we obtained the following ratios;

$$\frac{r_d}{t} = \frac{0.63}{.1} = 6.3$$

$$\frac{r_p}{t} = \frac{0.79}{.1} = 7.9$$

For thinner materials, these ratios will increase and the deformation will be easier. On the other hand, if the thickness is reduced too much puckering may occur over the die corner radius.

*Clearance, c, between punch and die:*

It is recommended that the clearance should be  $c=t+0.10t$  per side for aluminum, and  $c=t+0.35t$  per side for stainless steel, [ASM, 1988]. We have selected 2.92 mm (0.115) clearance per side. This clearance corresponds to

$$t+0.15t \quad \text{for } t=2.54 \text{ mm (0.100")}$$

$$t+2.83t \quad \text{for } t=0.76 \text{ mm (0.030")}$$

*Draw ratio, DR :*

Draw ratio in a deep drawing operation is defined as the ratio of initial blank diameter to the final cup diameter. Since we have selected the final cup diameter as  $d=152.4$  mm (6"), the initial blank diameter should be calculated based on recommended reductions in the blank diameter. It is recommended that maximum reduction that can be obtained in a deep drawing operation is 40% for aluminum, and 40-60% for stainless steel, [ASM, 1988]. Based on these recommendations we have selected 50% reduction in the blank

diameter. This reduction corresponds to the initial blank diameter of  $D=304.8$  mm (12"), and the draw ratio of  $DR=D/d=2$ .

This ratio is bigger than the recommended value for aluminum. For thick aluminum sheet metal, it is possible to complete the draw operation successfully, but for thin metal wrinkling and/or fracture will occur. For thin metals, it would be possible to complete the draw operation by using variable blankholding force.

Using the current tools, it is possible to increase the blank diameter up to 355.6 mm (14") which will increase the draw ratio to  $DR=2.33$ . Punch travel will not be a limiting factor to increase the draw ratio and, thus, the required stroke of the punch.

*Calculation of the cup height, H:*

Since the initial blank diameter, final cup diameter, and punch profile radius are known, the final height of the cup can be calculated, using the symbols shown in Figure G.1, based on Equation G.1, [Lange, 1985].

$$D = \sqrt{d^2 + 4d(h + 0.57r_p) - 0.56r_p^2} \quad (G.1)$$

From this equation, the final cup height is calculated as;

$$H=120.27 \text{ mm (4.735")} \quad \text{for } DR=2$$

$$H=174.50 \text{ mm (6.87")} \quad \text{for } DR=2.33$$

Design parameters which are used in the die design (Figure G.1) are listed in Table G.2 together with suggested values taken from literature.

**Table G.2: Design Parameters Used in The Deep Drawing Tool Design**

	Suggestion	Reference	Selection
Punch profile radius, $r_p$ Aluminum Steel	$(4 \div 8) t$ 5t	[ASM, 1988]	20.07 mm (0.79")
Die corner radius, $r_d$ Aluminum Steel	$(5 \div 10) t$ 10t	[Lange, 1985] [ASM, 1988]	16.00 mm (0.63")
Clearance between punch and die, c Aluminum Steel	1.10t 1.35t	[ASM, 1988]	2.92 mm (0.115")
Reduction in diameter Aluminum Steel	40% 40-60%	[ASM, 1988]	50-57%

### G.2.2. Tool Design

Based on the design parameters selected above, a set of tooling is designed and manufactured<sup>1</sup> to perform desired operations. Principles and design specifications are explained below.

#### Principles

Deep drawing operation using a blankholder can be performed in a single action press with die cushion or a double action press having a separate slide

<sup>1</sup> Tooling is manufactured by Superior Tool and Die, Co., Columbus, Ohio, an affiliate Member of ERC/NSM..

for a blankholder. A single action hydraulic press with die cushion, i.e. 160 ton Minster press whose specifications are given in Section G.1, is used in the experiments. Principle of cup forming operation in a single action press is shown in Figure F.1. In this tool arrangement, punch is stationary and placed on the lower plate, blankholding ring is placed on the cushion pins, and die is attached to the ram. During the deformation, slide moves down and forms the sheet metal around the stationary punch. The blankholder is indirectly driven by the ram of the press, and blankholding pressure is produced by hydraulic or pneumatic cushion cylinders and can be controlled during the deformation by controlling the cushion pressure. Since the slide constantly pushes against the blankholder, this increases the load on the ram. The maximum load available on the ram should be more than the total of blankholding load and the drawing load.

### Load Requirements

Maximum punch and blankholding forces required to form the cup shown in Figure G.1 whose specifications are given in Table G.2 are calculated based on stainless steel.

Maximum punch force required to form 304.8 mm (12.0") diameter and 2.54 mm (0.100") thick stainless steel blank is estimated, based on Equation F.2, as  $F_d=95.35$  tons, and required blankholding force is estimated, based on Equation F.3, as  $F_b=12.52$  tons. In total, maximum slide force required to form this cup is 107.87 tons which is available in Minster press.

If the draw ratio is increased to 2.3 which corresponds to 355.6 mm (14.0") blank diameter, then for 2.54 mm (0.100") thick blank the required max. punch force is calculated to be  $F_d=79.0$  tons, and required blankholding force is estimated to be  $F_b=57.0$  tons. In total, 136.0 tons of slide force is required to form this cup, which is possible to obtain in Minster press.

### Final Design

A set of tooling is designed and manufactured to form the cup, whose dimensions are given in Table G.2, in 160 ton double action hydraulic Minster press. A sketch of the press is shown in Figure 7.1. Also, specifications of the press are given in Table 7.1. Based on these overall dimensions and the desired cup geometry, the necessary tooling is designed and built to carry out single stroke draw operation. Assembly drawing of the tooling is shown in Figure G.2.

In Figure G.2, working space of the press frame between ram, (11), and bolster, (7), is shown together with the tooling in their assembled position. Upper die assembly is attached to the upper die shoe, (1), which is attached to the ram, (11), and lower die assembly is attached to the lower die shoe, (18), which is attached to the bolster, (7). Guide pins, (13), and bushings, (6), which are attached to the upper and lower die shoes, (1) and (18) respectively, are used for locating purposes during the assembly process, but because of the length and low stiffness of the guide pins, (13), they can not be used for locating

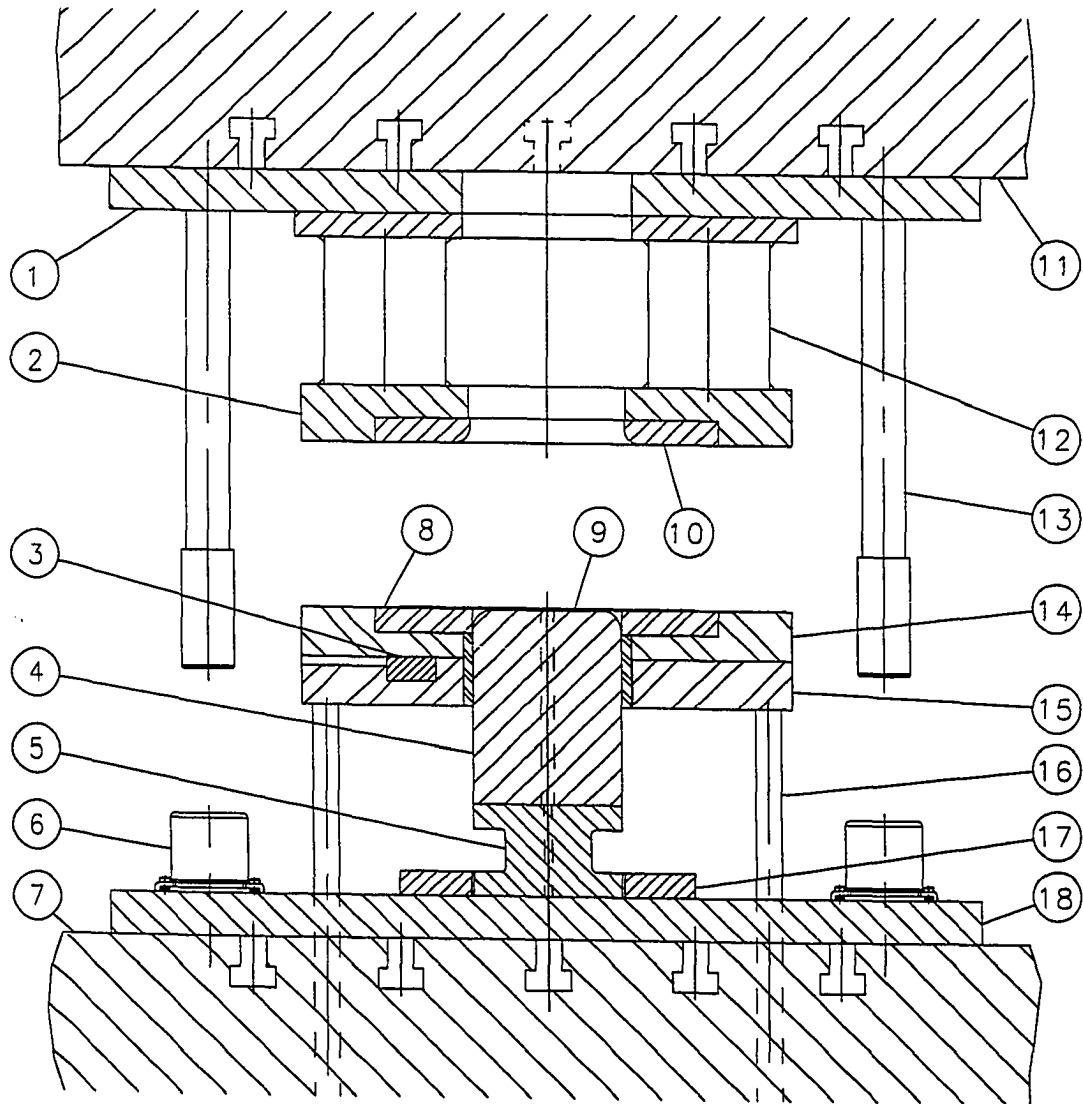


Figure G.2: Assembly drawing of the die set for deep drawing of a round cup in Minster press.



purposes during the forming process. Several holes are opened in the lower die shoe, (18), to allow the penetration of the cushion pins, (16), to support the loadcell container ring, (15).

Axisymmetric punch, (4), is located on top of an inline loadcell, (5), which is attached to the lower die shoe, (18). This loadcell is used to measure the punch load during the deformation. A round spacer, (17), with a slot machined on it, is placed around the lower part of load cell to prevent an accidental damage of the loadcell wire. A hole is drilled in the center of the punch, (4), to let the air go inside to prevent vacuum when the formed part is removed from the punch.

The blankholder assembly including load cell container ring, (15), blankholder container ring, (14), blankholder, (8), and three button loadcells, (3), is placed on top of twelve cushion pins, (16). Usually one ring is enough to contain the blankholder by selecting the thickness of the ring according to the maximum blankholding load. However, in the current design, we have two rings. The second ring under the blankholder container ring, (14), is called loadcell container ring, (15). Three equally spaced button loadcells, (3), which are used to measure the blankholder load during the forming process, are placed inside the pockets machined in this ring, (15). The blankholder container ring, (14), sits on the three loadcells, (3), and it does not touch the loadcell container ring, (15), to obtain accurate force measurements during the forming process. For maintenance purposes and to eliminate separation between container rings, four strips are used to bolt them together. The

length of the strips and the distance between elliptical holes are arranged so that no preload is applied to the loadcells.

A bushing is press fitted to the inside diameter of the blankholder container ring, (14). This bushing should have been made from bronze or cast iron but, in the current design, because of availability, it is made from soft steel. Container rings, (14) and (15), are guided using the interface between bushing and the punch, (4). Inside diameter of the blankholder is made 0.254 mm (0.010") bigger than the inside diameter of the bushing, and it is used to strip the formed part out from the punch.

Sheet metal blank, (9), is located on top of the blankholder, (8), before the deformation starts. A step is machined on the blankholder, (8), to locate the blank, (9). The height of this step should be lower than the minimum thickness of the sheet metal blanks which will be used in the experiments.

Looking at the position of the cushion pins, (16), twelve of them are selected to support the blankholder assembly. The orientation of these supporting cushion pins are shown in Figure G.3. Remaining pins are removed from the press. Maximum stroke of the cushion pins is limited to 190.5 mm (7.5"). Due to the thickness of the lower die shoe, (18), which is 50.8 mm (2"), the available stroke of the cushion pins is reduced by 50.8 mm (2"). This is why the original pins are replaced with 50.8 mm (2") longer ones. Punch, (4), length is also adjusted to allow the maximum travel of the cushion pins, (16).

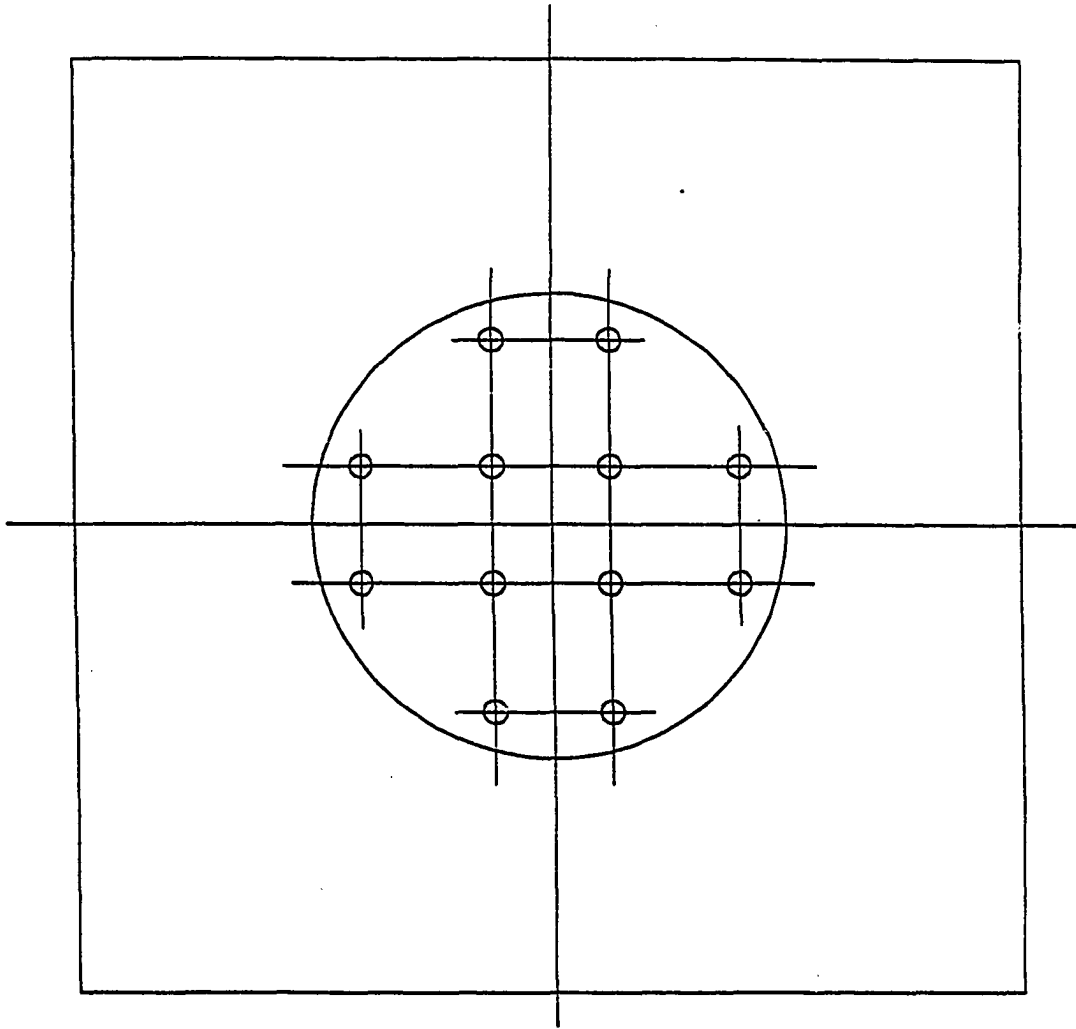


Figure G.3: Orientation of the supporting cushion pins.

Upper die assembly contains die, (10), die holder, (2), and spacer, (12), and it is attached to the upper die shoe, (11). Die, (10), is inserted into the die holder, (2), which is separated from the upper die shoe, (1), by welded spacer, (12), to create enough distance for punch penetration. Another consideration in designing the die assembly is that, in the upper most position of the ram, (11), it should be possible to take the part out of the die after the forming process is completed.

Die, (10), and blankholder, (8), which are in contact with the sheet metal during the forming operation should be made from harder material. In this design, these parts are made such that it is possible to change or modify them for different material or geometry.

Since there is no means of centering die, (10), and the punch, (4), automatically, before starting the forming experiments, die, (10), and the punch, (4), should be centered manually. Punch, (4), and die, (10), are centered in two steps. First, upper die assembly, including parts (2), (10), and (12), is attached and fixed to the upper die shoe, (1). Secondly, punch assembly, including parts (4) and (5), is centered with die, (10), and then fixed to the lower die shoe, (18).

### G.2.3. Operation Sequence

In this section, the operation sequence to carry out the deep drawing operation is explained. All the part numbers referred to in this section are shown in Figure G.2.

Upper and lower halves of the die set is shown at their open position in Figure G.4. At this position, ram, (11), is at its upper most position, and flat sheet metal blank, (9), is placed over the die, (8). Cushion pins, (16), are also extended out. At this position, setup of the press should be completed, i.e. cushion and slide pressures, and the lower limit of the slide position should be set at their desired values.

Upper die assembly driven by ram, (11), moves down, sheet metal, (9), is clamped between die, (10), and the blankholder, (8), Figure G.5. At this position, the load measured in three button loadcells, (3), should show the blankholding force.

Ram, (11), moves further down and forms the sheet metal around the stationary punch, (4), Figure G.6. During this forming stage, punch load is measured by means of inline loadcell, (5). Until the sheet metal leaves the blankholder contact area, it is clamped between the die, (10), and the blankholder, (8), and metal flow can be controlled by the application of blankholding force. Blankholding load is obtained by means of cushion pressure. Cushion pressure can be varied as a function of ram position resulting in a variable blankholding force throughout the forming stroke.

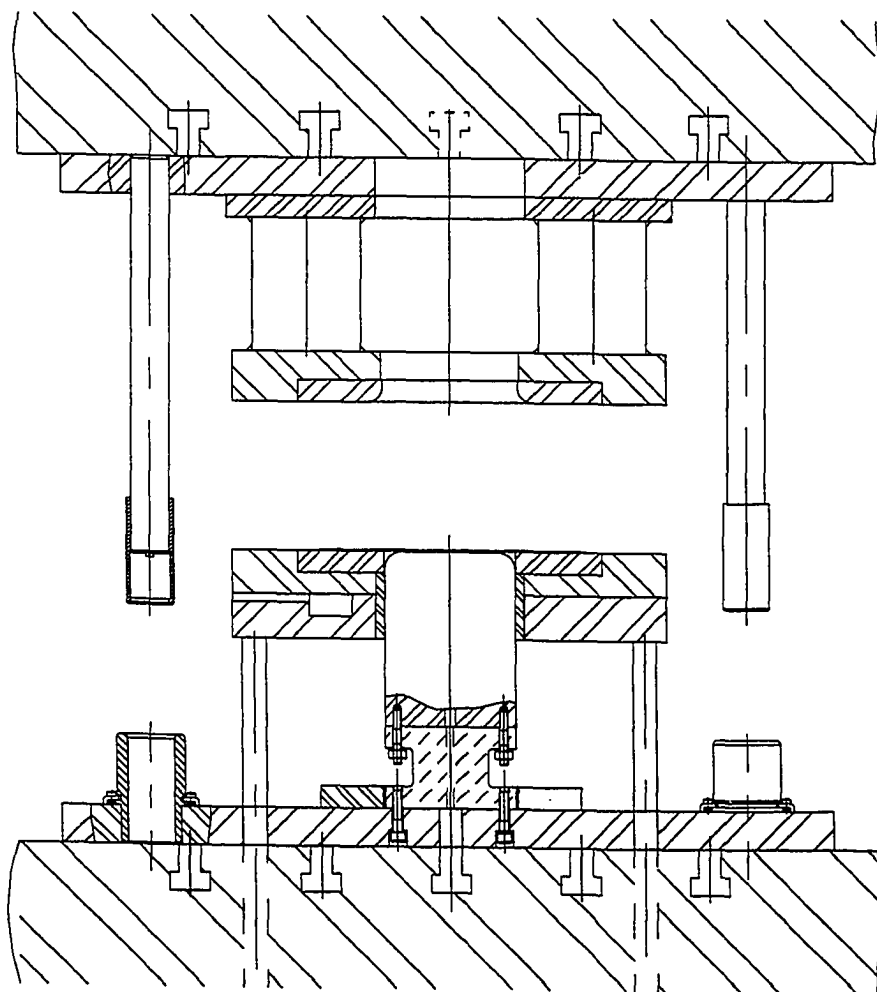


Figure G.4: Open position of the tooling.

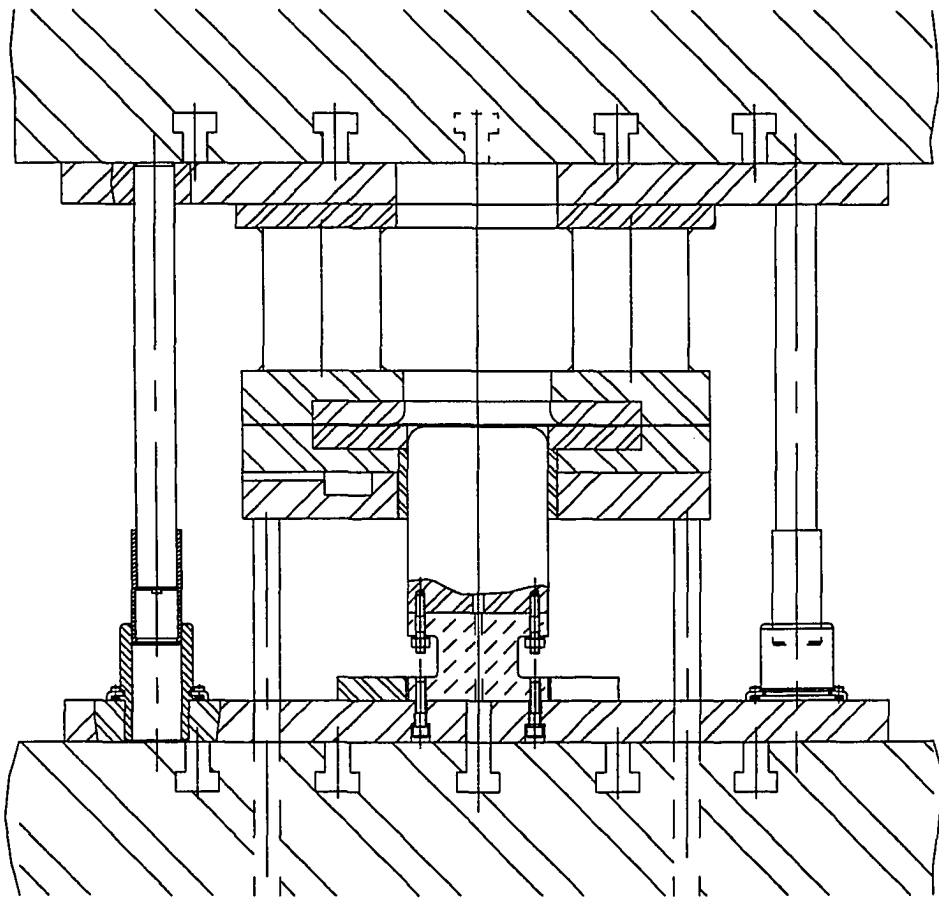


Figure G.5: Clamp position of the tooling.

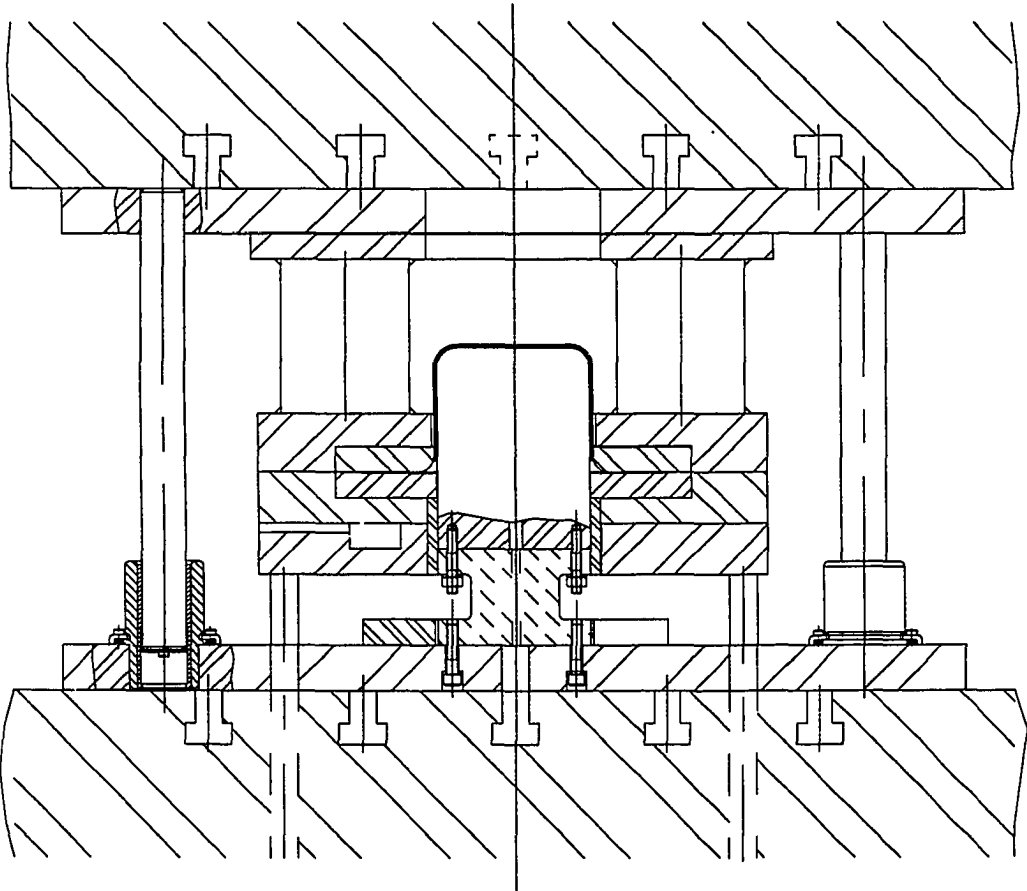


Figure G.6: Formed position of the tooling.



### **G.3. Instrumentation of Tooling**

The Minster press is equipped with various instruments that measure position, pressure and force. These include three blankholder loadcells, punch loadcell, three hydraulic pressure transducers on the slide, die cushion and ejector hydraulic lines, and the string potentiometer attached to the slide.

#### **G.3.1. Hydraulic Pressure Transducers**

The Minster Press was instrumented with hydraulic pressure transducers on the slide, die cushion, and ejector pressure lines. These give the operator of the press some idea about the forces in the tooling without having in-tool instrumentation. The pressure transducers were mounted off of "T" pipe fittings at the dial gages on the front of the press. These fittings were installed by the press manufacturer for their pressure transducers, which they used in the calibration of the press. The pressure transducers mounted on the press were purchased from Sensotec, Inc. They are the bonded foil strain gage type (model LM). They have a full scale capacity of 34.5 MPa (5000 psi) with an output of 2 mv/v and an accuracy of +/- 0.5 %. The pressure transducer's specifications can be seen in Table G.3.

#### **G.3.2. Measurement of The Slide Position**

It is desirable to know the slide position while the load readings are being taken during the deep drawing operation. A number of possible methods

Table G.3: Specifications of LM Pressure Transducer

<b>PERFORMANCE</b>	
Pressure Range .....	0 - 34.5 MPa (0 - 5000 psi)
Accuracy (min) .....	+/- .5% F.S.
Output .....	2.0 mv/v
Resolution .....	Infinite
<b>ENVIRONMENTAL</b>	
Temperature, Operating .....	-54° C - 121° C (-65° F - 250° F)
Temperature, Compensated .....	-16° C - 71° C (60° F - 160° F)
Temperature Effect	
- Zero (max) .....	.018 % F.S./° C (.01 % F.S./° F)
- Span (max) .....	.036 % Rdg./° C (.02 % Rdg./° F)
<b>ELECTRICAL</b>	
Strain Gage Type .....	Bonded Foil
Supply .....	10 VDC
Bridge Resistance .....	350 ohms
Wiring Code (std) .....	#1
Electrical Termination (std) .....	Cable 914 mm (3 ft).
<b>MECHANICAL</b>	
Media .....	Gas, Liquid
Overload-Safe .....	50% > capacity
Pressure Port .....	1/4-18NPT F.
Wetted Parts Material .....	17-4 PH Stainless
Type (Gage, Abs) .....	Gage
Case Material .....	Stainless Steel

were considered, including directly instrumenting the tooling, taking the position readings of the press' encoders (used by the press controller for positioning) or using some device to measure the position of the die cushion directly. It was decided that the best solution for this project would be to attach a string potentiometer to the slide. A string potentiometer was installed on the press slide. In our application, since the slide and die cushion move together, we could use the slide position to determine the die cushion position. The potentiometer is mounted adjacent to the press bed and the end of the string/wire is attached to the slide. The full length of the wire is 762 mm (30.0"). The total travel of the slide is just over 508 mm (20.0"). The specifications of the potentiometer can be seen in Table G.4 (Celesco Transducer Products, Inc.).

### **G.3.3. Loadcells**

The locations of the punch and the blank holder loadcells are shown in the assembly drawing in Figure G.2. These loadcells, and LoadGard system were custom designed, manufactured, and donated to ERC/NSM by Helm Instrument, Co., Maumee, Ohio.

#### 200 Ton Punch Loadcell, (5)<sup>2</sup>

The punch loadcell is 152.4 mm (6.00") in diameter and 95.25 mm (3.75") tall. With a capacity of 200 tons and an overload rating of 244 tons, this loadcell

---

<sup>2</sup> Part numbers are shown in Figure 7.4.

**Table G.4: Specifications of string potentiometer.**

GENERAL	Range	762 mm (30")
	Weight	567 gr (20 oz)
	Case Material	Aluminum
	Sensing System	Precision Potentiometer
	Electrical Connector	MS3102E-14S-6P
ELECTRIC	Input Resistance	500 ohms standard
	Output Resistance	138 ohms max. standard
	Excitation Voltage	25 volts max., AC or DC
PERFORMANCE	Accuracy	+/- .10% F.S. typical
	Resolution	.008% F.S. max.
	Thermal Coefficient of Sensing Element	48.9 P.P.M./°C (88 P.P.M./F)
	Sensitivity	1.23 mV/V/mm (31.26 mV/V/in)
ENVIRONMENTAL	Temperature Range	-18 to +93 °C (0 to +200 F)
	Humidity	up to 90% RH
	Vibration	up to 10 G's to 2000 Hz

can be used for the full capacity of the slide. A drawing of the loadcell can be seen in Figure G.7.

#### 40 Ton BHF Loadcells. (3)

Three loadcells are used to measure the blank holding forces during the deep drawing operation. Each loadcell has a 40.0 ton capacity, with an overload rating of 48.8 tons. They are 50.55 mm (1.99") in diameter, and 25.4 mm

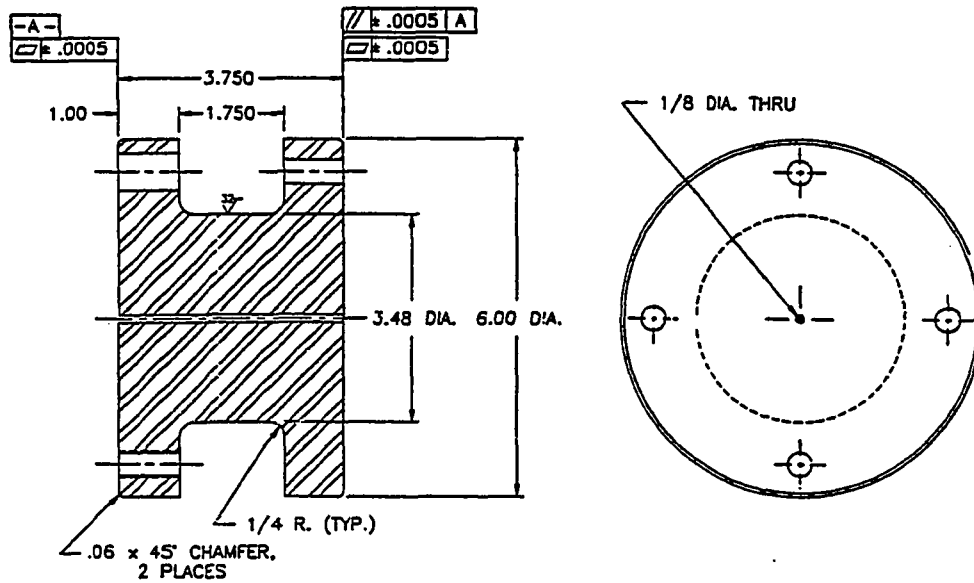


Figure G.7: 200 ton loadcell for measuring punch load in deep drawing tooling on Minster press.

NOTES:

- 1.) NORMAL CAPACITY RANGE IS FROM 4.0 T. ( @ 148  $\mu\epsilon$  ) TO 40.0 T. ( @ 1475  $\mu\epsilon$  ).
- 2.) OVERLOAD RATING IS 48.8 T. ( @ 1800  $\mu\epsilon$  ).

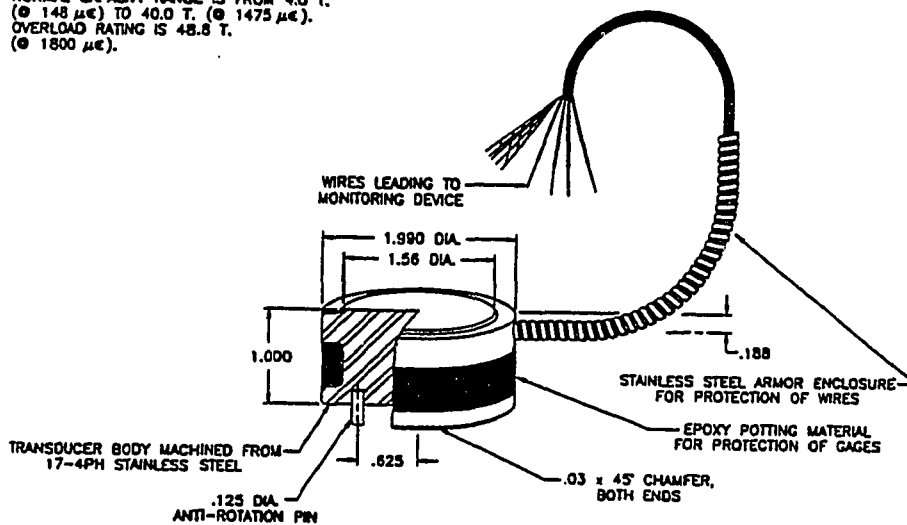


Figure G.8: 40 ton loadcell for measuring blankholder force in deep drawing tooling on Minster press.

(1.00") tall. The loadcells (3) sit evenly spaced below the blank holder ring as seen in Figure G.2. A drawing of the loadcell can be seen in Figure G.8.

When selecting the type of the loadcell for measuring the blank holding forces, a loadcell "ring" was considered. This ring would be in the same location as the current loadcells, and would measure the forces around the entire blank holder ring. This was not done for two reasons. The first is that it would be difficult to use the ring loadcell in future applications, unless it was another deep draw process of similar dimensions. The second is that the ring loadcell would not give us any indication of uneven loading around the blank holder ring.

#### **G.3.4. Data Acquisition**

Installed on the side of the press is the Trend LoadGard System from Helm Instruments. It is a press load monitoring device used to protect the tooling and the machine from damage due to overloading. The deep drawing tooling has three 40 ton loadcells for the die cushion, and one 200 ton loadcell for the punch.

Often, these types of systems are used with machine mounted strain gage transducers to measure press deflection during the forming of parts. In our case, the instrumentation is located in the tooling and not on the press. The

instrument is used to perform signal conditioning from our loadcells. This includes signal filtering and amplification.

A data acquisition system is used to collect signals of punch and blankholding forces, slide displacements. The specifications of this data acquisition system are given in Section F.4.